Non-marine source rocks of petroleum and microbial gas in the Ordos and Qaidam basins, mid-west China

Von der Fakultät für Georessourcen und Materialtechnik der Rheinisch -Westfälischen Technischen Hochschule Aachen

zur Erlangung des akademischen Grades eines

Doktors der Naturwissenschaften

genehmigte Dissertation

vorgelegt von

Jinqi Qiao, M.Sc.

Berichter: Herr Univ. -Prof. Dr. rer. nat. Ralf Littke
Herr Univ. -Prof. Dr. Reinhard Sachsenhofer

Tag der mündlichen Prüfung: 04.11.2021

Diese Dissertation ist auf den Internetseiten der Universitätsbibliothek online verfügbar.

Acknowledgements

Four years of experience studying and living in Germany provided me with an impressive journey in my life. Aachen is the city where I lived the longest since I have left my home when I was 19 years old. My academic career started in this city. I love this beautiful city although the sunshine is rare. Most importantly, there are a lot of people, whom I need to show my sincere thanks at the end of this important period of my life.

First and foremost, I would like to express my most sincere gratitude to my supervisor Prof. Ralf Littke. He gave me the opportunity to conduct my PhD study at the Institute of Geology and Geochemistry of Petroleum and Coal at the RWTH Aachen University. Prof. Littke devoted plenty of time and effort to propose new research ideas, revising my manuscripts and providing valuable advice and guidance through my PhD study. Prof. Littke has broad and profound knowledge which helped me expand my knowledge. In addition, Prof. Littke's rigorous attitude to science and his charming personality taught me how to become a qualified scientist and will inspire me in future studies and life.

I also would like to give my special words of thanks to Prof. Jan Schwarzbauer. He introduced me to work in the laboratory of organic geochemistry.

My special words of thanks should also go to Prof. Reinhard Sachsenhofer (Montanuniversität Leoben). He spent his precious time reviewing my thesis and accepted the task of being the co-examiner of my PhD.

Dr. Laura Zieger, Dr. Sebastian Grohmann and Dr. Reinhard Fink are highly appreciated because of their contributions to my publications. Impressive and intensive discussions with them help me improve my critical thinking as well as scientific writing.

Alireza Baniasad, and Dr. Garri Gaus are thanked for their professional instructions in geochemical and petrophysical experiments, respectively. Dr. Hannes Claes from the Institute of Clay and Interface Mineralogy at RWTH Aachen University is thanked for the XRD analysis.

I sincerely thank Patrick Thelen, a kind technician who was able to solve all kinds of laboratory and IT problems for me. I would like to acknowledge Donka Macherey for the help with sample preparation and Kerstin Windeck for the help with measurements. My heartfelt gratitude goes to Michelle Evertz for the assistance with respect to administrative work and to Annette Schneiderwind and Yvonne Esser for any help in the course of my laboratory work. Dr. Steffen Nolte is acknowledged for translating the abstract to German.

I would like to thank our Chinese colleagues, Tianyu Zheng, Zhongrui Wu and Zibing Zhao. Our friendship makes me feel warm and happy. Felix Froidl, Sebastian Amberg, Linda Burnaz, Ivana Jovancicevic, Nada Vidovic and Christina Schwanen are thanked for creating a friendly working environment.

My special thanks go to my former supervisor, Prof. Luofu Liu (China University of Petroleum, Beijing) for his endless support and encouragement in the past several years. Prof. Zhenxue Jiang, Prof.

ABSTRACT

Source rocks are essential for both conventional and unconventional petroleum and gas resources. This thesis focuses on the characterization of non-marine source rocks covering a wide range of thermal maturity, from immature microbial gas source rocks to overmature source rocks.

In Chapter 2, source rock characterization was performed on 12 gas shale samples collected from Carboniferous Benxi and Permian Shanxi formations from the Yishan Slope of the Ordos Basin, China. These samples were interpreted with regard to mineral composition, thermal maturity, gas storage capacity as well as shale gas potential. The results reveal that the studied shales show low to moderate total organic carbon (TOC) content (0.1% to 2.3 %). Vitrinite reflectance (VR_r) values of 2.3–3.0 % indicate an overmature stage with respect to oil generation. XRD data shows that clays are the major minerals (0–80%) followed by quartz (0–43%) in most samples. Due to their high abundance, clay minerals rather than organic matter control sorption capacity. However, compared to well-studied producing marine shale gas systems with higher TOC contents, the studied shales possess comparatively low gas storage capacities. Sorption has a negligible effect on gas production at pressures of > 10 MPa. This is important for deep reservoirs, where the pore pressure may be high.

In Chapter 3, a comprehensive petrographic and geochemical study was performed on 23 Triassic shale samples collected from 18 wells in the mid-western Ordos Basin. These Chang 7 Member samples were interpreted with regard to the thermal maturity and characteristics of organic matter (OM) as well as the paleo-depositional environment. The results reveal that the studied samples have moderate to very high TOC (0.2–24.8 %) and total sulfur (TS) contents (0.1–6.5 %). The good to very good hydrocarbon generation potential for most of the samples is proven by high S_1 and S_2 values (0.1–3.7 mg HC/g rock and 0.6–92.5 mg HC/g rock, respectively). Organic matter is mainly composed of type II to type III kerogen indicated by Rock-Eval data and supported by petrographical observations. It consists of a mixture of woody, terrigenous (mainly conifers) and aquatic OM. The studied member is a typical clay-rich source rock deposited in a sulphate-poor lacustrine to fluvio-deltaic environment under oxic to sub-oxic conditions. Low salinity is implied by different parameters such as TOC/TS ratios and molecular biomarker data. VR_r values (0.68–0.88%), average Rock-Eval T_{max} values (445 °C), biomarker parameters, and maturity indices based on aromatic compounds all indicate a thermal maturity within the oil window.

In Chapter 4, 30 Pleistocene source rocks from the central Qaidam Basin are described and discussed based on elemental data (TOC, TS, total inorganic carbon (TIC)), organic geochemical and organic petrographic analyses. These thick fine-grained rocks probably act as the main microbial gas source rocks in the region. Two different, lacustrine source rock facies have been identified based on the new data. Organic facies A samples with high TOC (4.1–25.3 %) and moderate TS content (1.5–3.7 %) were mainly deposited under a suboxic to anoxic freshwater column at the lake margins. Although this shallow water fluvial-lacustrine facies only occupies a small part of the whole sedimentary sequence, it has the highest hydrocarbon generation potential. In contrast, organic facies B

samples with low TOC (0.5–1.1 %) and TS contents (0.14–1.0 %) were deposited in more oxygen-rich brackish lake bodies. Rarely, anoxic conditions were present in sediments that were sealed by algal mats. Organic matter is composed of mixed type II-III kerogen derived mainly from aquatic plants. Organic facies A is interpreted to originate from abundant macrophytes (e.g. non-marine algae, submerged angiosperms) at the margin of the lake. In contrast, the OM in organic facies B is related to algae with some additional bacterial contribution. Terrestrial higher plants are subordinate in both organic facies. The cold and dry climatic conditions and very high burial rate favored microbial gas generation.

In chapter 5, the same sediments from the Tibetan Plateau (TP) region of NW China are presented based on other methods in order to obtain information on climate change, environmental conditions and weathering in the area of the Qaidam Basin. Here evidence from specific temperature-sensitive biomarkers (GDGTs), stable isotopes and concentrations of a large number of major and minor chemical elements of the Pleistocene Qigequan Formation was applied. The results confirm that two sediment types exist with completely different organic matter composition, i.e. organic facies A and B. The organic matter accumulation in both organic facies was primarily controlled by the palaeoredox conditions rather than palaeoproductivity. Furthermore, no significant differences between the GDGTs distributions in sediments is observed. Generally, the sediments were deposited under arid/cold conditions with weak chemical weathering, similar to the present-day situation. The Mean Annual Air Temperature was slightly higher than the present temperature. The $R_{i/b}$ (ΣiGDGTs/ΣbGDGTs) values are located between the higher modern $R_{i/b}$ values and the lower Late Miocene $R_{i/b}$ values, indicating neutral to alkaline soils conditions (pH varying between 6 and 10) and a continuous aridification process.

ZUSAMMENFASSUNG

Muttergesteine sind sowohl für konventionelle als auch für unkonventionelle Erdöl- und Erdgasvorkommen von wesentlicher Bedeutung. Diese Dissertation befasst sich mit der Charakterisierung von nicht-marinen Ausgangsgesteinen, welche einen großen Bereich thermischer Reifen abdecken, von unreifen mikrobiellen Gasmuttergesteinen bis zu überreifen Muttergesteinen.

In Kapitel 2 wurden 12 Gasschieferproben aus den karbonischen Benxi- und permischen Shanxi-Formationen am Yishan-Hang des Ordos-Beckens in China untersucht. Diese Proben wurden im Hinblick auf die mineralische Zusammensetzung, die thermische Reife, die Gasspeicherkapazität und das Schiefergaspotenzial ausgewertet. Die Ergebnisse zeigen, dass die untersuchten Sedimentgesteine einen niedrigen bis mäßigen Gehalt an organischem Gesamtkohlenstoff (TOC) aufweisen (0.1% bis 2.3%). Vitrinitreflexionswerte (VR_r) von 2.3-3.0% deuten auf ein überreifes Stadium in Bezug auf die Ölbildung hin. Die XRD-Daten zeigen, dass in den meisten Proben Tone die wichtigsten Mineralien sind (0-80%), gefolgt von Quarz (0-43%). Aufgrund ihres hohen Vorkommens dominieren eher Tonminerale die Sorptionskapazität statt des organischen Materials. Im Vergleich zu gut untersuchten, produzierenden, marinen Schiefergassystemen mit höheren TOC-Gehalten weisen die untersuchten Sedimentgesteine eine vergleichsweise geringe Gasspeicherkapazität auf. Bei Drücken von > 10 MPa hat die Sorption einen vernachlässigbaren Einfluss auf die Gasproduktion. Dies ist wichtig für tiefe Lagerstätten, in denen der Porendruck hoch sein kann.

In Kapitel 3 wurde eine umfassende petrographische und geochemische Untersuchung von 23 triassischen Gesteinsproben durchgeführt, die aus 18 Bohrungen im mitteleren bis westlichen Ordos-Becken entnommen wurden. Die Proben aus der Chang 7 Subformation wurden im Hinblick auf die thermische Reife und die Eigenschaften der organischen Materie (OM), sowie auf das Paläo-Ablagerungsmilieu interpretiert. Die Ergebnisse zeigen, dass die untersuchten Proben mäßige bis sehr hohe TOC (0.2-24.8%) und Gesamtschwefelgehalte (TS) (0.1-6.5%) aufweisen. Das gute bis sehr gute Kohlenwasserstoffbildungspotenzial der meisten Proben wird durch hohe S_1- und S_2-Werte belegt (0.1-3.7 mg HC/g Gestein bzw. 0.6-92.5 mg HC/g Gestein). Die organische Substanz besteht hauptsächlich aus Kerogen des Typs II bis III, wie aus den Rock-Eval-Daten hervorgeht und durch petrographische Beobachtungen bestätigt wird. Sie besteht aus einer Mischung aus holzigem, terrigenem (hauptsächlich Nadelbäume) und aquatischem OM. Die untersuchte Subformation ist ein typisches tonreiches Muttergestein, welches in einer sulfatarmen, lakustrinen bis fluvio-deltaischen Umgebung unter oxischen bis suboxischen Bedingungen abgelagert wurde. Verschiedene Parameter, wie das TOC/TS-Verhältnis und die molekulare Biomarkerdaten, belegen einen niedrigen Salzgehalt. VR_r-Werte (0.68-0.88%), durchschnittliche Rock-Eval-T_{max}-Werte (445 °C), Biomarker-Parameter und Reifeindizes basierend auf aromatische Verbindungen weisen auf eine thermische Reife innerhalb des Ölfensters hin.

In Kapitel 4 werden 30 pleistozäne Muttergesteine aus dem zentralen Qaidam-Becken beschrieben und anhand von Elementardaten (TOC, TS, anorganischer Gesamtkohlenstoff (TIC)), organisch-geochemischen und organisch-petrographischen Analysen diskutiert. Die mächtigen, feinkörnigen

Gesteine sind wahrscheinlich die wichtigsten mikrobiellen Gasquellen in dieser Region. Auf Grundlage der neuen Daten wurden zwei unterschiedliche, lakustrine Muttergesteinsfazies identifiziert. Proben der organischen Fazies A mit hohem TOC (4.1-25.3%) und mäßigem TS-Gehalt (1.5-3.7%) wurden hauptsächlich unter einer suboxischen bis anoxischen Süßwassersäule an den Seeufern abgelagert. Obwohl diese Flachwasser-Fluvial-Lakustrin-Fazies nur einen kleinen Teil der gesamten Sedimentabfolge einnimmt, hat sie das größte Potenzial zur Bildung von Kohlenwasserstoffen. Im Gegensatz dazu wurden die Proben der organischen Fazies B mit niedrigen TOC- (0,5-1,1 %) und TS-Gehalten (0.14-1.0%) in sauerstoffreicheren Brackwasserseen abgelagert. Selten traten anoxische Bedingungen in Sedimenten auf, die dann durch Algenmatten versiegelt waren. Das organische Material besteht aus gemischtem Kerogen vom Typ II-III, welches hauptsächlich von Wasserpflanzen stammt. Es wird davon ausgegangen, dass die organische Fazies A von reichlich vorhandenen Makrophyten (z. B. nicht-marine Algen, submerse Angiospermen) am Rande des Sees stammt. Im Gegensatz dazu ist das OM in der organischen Fazies B auf Algen mit zusätzlichem bakteriellen Beitrag zurückzuführen. Terrestrische, höhere Pflanzen sind in beiden organischen Fazies untergeordnet. Die kalten und trockenen klimatischen Bedingungen und die sehr hohe Sedimentationsrate begünstigten die mikrobielle Gasbildung.

In Kapitel 5 werden dieselben Sedimente aus der Region des Tibetischen Plateaus (TP) im Nordwesten Chinas anhand anderer Methoden vorgestellt, um Informationen über den Klimawandel, die Umweltbedingungen und die Verwitterung im Gebiet des Qaidam-Beckens zu erhalten. Hierzu wurden Indikatoren aus spezifischen, temperatursensitiven Biomarkern (GDGTs), stabilen Isotopen und Konzentrationen einer großen Anzahl von chemischen Haupt- und Spurenelementen der pleistozänen Qigequan-Formation verwendet. Die Ergebnisse bestätigen, dass es zwei Sedimenttypen mit völlig unterschiedlicher Zusammensetzung der organischen Substanz gibt, nämlich die organische Fazies A und B. Die Anreicherung der organischen Substanz in beiden organischen Fazies wurde in erster Linie durch die Paläo-Redoxbedingungen und nicht durch die Paläo-Produktivität gesteuert. Weiterhin wurden keine signifikanten Unterschiede zwischen den GDGT-Verteilungen in den Sedimenten festgestellt. Im Allgemeinen wurden die Sedimente unter trockenen/kalten Bedingungen mit schwacher chemischer Verwitterung abgelagert, ähnlich wie in der gegenwärtigen Situation. Die mittlere Jahreslufttemperatur war etwas höher als die heutige Temperatur. Die $R_{i/b}$-Werte (ΣiGDGTs/ΣbGDGTs) liegen zwischen den höheren modernen $R_{i/b}$-Werten und den niedrigeren spätmiozänen $R_{i/b}$-Werten, was auf neutrale bis alkalische Bodenbedingungen (pH-Wert zwischen 6 und 10) und einen kontinuierlichen Aridifizierungsprozess hindeutet.

Table of Contents

List of Figures

List of Tables

XVII

List of Abbreviations

EIA	U.S Energy Information Administration	C_{28} ααα20S	24-Methyl-5α(H), 14α(H), 17α(H)-cholestane (20S)
XRD	X-ray diffraction	C_{28} αββ20R	24-Methyl-5α(H), 14β(H), 17β(H)-cholestane (20R)
XRF	X-ray fluorescence	C_{28} αββ20S	24-Methyl-5α(H), 14β(H), 17β(H)-cholestane (20S)
CAR	Carbonate content [wt.%]	C_{28} ααα20R	24-Methyl-5a(H), 14a(H), 17a(H)-cholestane (20R)
SIL	Silicate content [wt.%]	C_{29} ααα20S	24-Ethyl-5α(H), 14α(H), 17α(H)-cholestane (20S)
OM	Organic matter	C_{29} αββ20R	24-Ethyl-5α(H), 14β(H), 17β(H)-cholestane (20R)
OM*	Organic matter content before sulfate reduction	C_{29} αββ20S;	24-Ethyl-5α(H), 14β(H), 17β(H)-cholestane (20S)
TOC	Total organic carbon [wt.%]	C_{29} ααα20R	24-Ethyl-5α(H), 14α(H), 17α(H) – cholestane (20R)
TC	Total carbon content	C_{29} neoH	C_{29} neohop-13(18)-ene
TIC	Total inorganic carbon	C_{30} neo H	C_{30} neohop-13(18)-enes
TS	Total sulfur	C_{30} ββ H	C_{30} 17β(H),21β(H)-hopane
S_1	Free and absorbed hydrocarbons [mg HC /g rock]	C_{32} ββ H	C_{32} 17β(H),21β(H)-hopane
S_2	Hydrocarbons generated from pyrolysis [mg HC /g rock]	C_{27} β	C_{27} 17β(H)-22,29,30-trinorhopane
S_3	CO_2 generated from pyrolysis [mg CO_2 /g rock]	N	naphthalene
m_d	Weight of the dry sample [kg]	2-MN	2-methylnaphthalene
m_S	Immersed weights of the saturated samples indeionized water [kg]	1-MN	1-methylnaphthalene
$m_{w\text{-}imm}$	Weight of the water-saturated sample immersed in water [kg]	BP	biphenyls
n_∞	Maximum Langmuir capacity [mol/ kg]	2-EN	2-ethylnaphthalene
n_{excess} (P,T)	Excess sorption amount [mol/ kg]	1-EN	1-ethylnaphthalene
P	Pressure [Pa]	2,6- + 2,7-DMN	2,6 + 2,7-dimethylnaphthalene
P_L (T)	Langmuir pressure [Pa]	1,3- + 1,7-DMN	1,3 + 1,7-dimethylnaphthalene
T	Temperature [K]	1,6-DMN	1,6-dimethylnaphthalene
V_{bulk}	Bulk volume [m³]	1,4- + 2,3-DMN	1,4- + 2,3-dimethylnaphthalene
V_p	Pore volume [m³]	1,5-DMN	1,5-dimethylnaphthalene

ρ_a	Adsorbed gas densities [kg/m³]	1,2-DMN	1,2-dimethylnaphthalene
$\rho_g(P,T)$	Free gas densities [kg/m³]	2-MBP	2-methylbiphenyl
ρ_b	Bulk densities [kg/m³]	DPM	Diphenylmethane
m_w	Saturated sample mass [kg]	3-MBP	3-methylbiphenyl
ρ_w	Density of deionized water at laboratory conditions [0.99 kg/m³]	4-MBP	4-methylbiphenyl
V_v	Void volume [m³]	DBF	Dibenzofuran
ΔS	Molar entropy	1,3,7-TMN	1,3,7-trimethylnaphthalene
P^0	Pressure at the perfect-gas reference state [0.1 MPa]	1,3,6-TMN	1,3,6-trimethylnaphthalene
n_{excess}	Excess amount sorbed [mol/kg]	1,4,6- + 1,3,5-TMN	1,4,6- + 1,3,5-trimethylnaphthalene
n_{pore}	Gas storage capacities in pore [mol/kg]	2,3,6-TMN	2,3,6-trimethylnaphthalene
n_{sorbed}	Sorbed gas storage capacities [mol/kg]	1,2,7- + 1,6,7-TMN	1,2,7- + 1,6,7-trimethylnaphthalene
m_{excess}	Gibbs surface excess [kg]	1,2,6-TMN	1,2,6-trimethylnaphthalene
HI	Hydrogen index [mg HC /g TOC]	1,2,4-TMN	1,2,4-trimethylnaphthalene
OI	Oxygen index [mg CO_2 /g TOC]	1,2,5-TMN	1,2,5-trimethylnaphthalene
PI	Production index	1,2,3-TMN	1,2,3-trimethylnaphthalene
T_{max}	Temperature of maximum pyrolysis yield [°C]	1,3,5,7-TeMN	1,3,5,7-tetramethylnaphthalene
HC	Hydrocarbons	1,3,6,7-TeMN	1,3,6,7-tetramethylnaphthalene
ASE	Accelerated solvent extraction	1,4,6,7- + 1,2,4,6- + 1,2,4,7-TeMN	1,4,6,7- + 1,2,4,6- + 1,2,4,7-tetramethylnaphthalene
GC-FID	Gas chromatography-flame-ionization detector	1,2,5,7-TeMN	1,2,5,7-tetramethylnaphthalene
GC-MS	Gas chromatography-mass spectrometry	2,3,6,7-TeMN	2,3,6,7-tetramethylnaphthalene
HPHT	High-pressure/temperature manometric sorption set-up	1,2,6,7-TeMN	1,2,6,7-tetramethylnaphthalene
MS	Mass spectrometry	1,2,3,7-TeMN	1,2,3,7-tetramethylnaphthalene
SEM	Scanning electron microscope	1,2,3,6-TeMN	1,2,3,6-tetramethylnaphthalene
CPI	Carbon Preference Index	1,2,5,6- + 1,2,3,5-TeMN	1,2,5,6- + 1,2,3,5-tetramethylnaphthalene
DBT	Dibenzothiophene	DBT	Dibenzothiophene
GP	Generation potential	PHE	Phenanthrene
DCM	Dichloromethane	4-MDBT	4-methyldibenzothiophene
NSO	Nitrogen, sulphur and oxygen compounds	2 + 3-MDBT	2 + 3-methyldibenzothiophene
MN	Methylnaphthalene	1-MDBT	1-methyldibenzothiophene
MNR	Ratio of 2-methylnaphthalene/1-methylnaphthalene	3-MP	3-methylphenanthrene

MP	Methylphenanthrene	2-MP	2-methylphenanthrene
MPI	Methylphenanthrene index	9-MP	9-methylphenanthrene
OEP	Odd-even Predominace	1-MP	1-methylphenanthrene
Pr	Pristane	4,6-DMDBT	4,6-dimethyldibenzothiophene
Ph	Phytane	2,4-DMDBT	2,4-dimethyldibenzothiophene
PHE	Phenanthrene	2,6-DMDBT	2,6-dimethyldibenzothiophene
RC	Reference cell	3,6-DMDBT	3,6-dimethyldibenzothiophene
SC	Sample cell	2,7- + 3,7- + 2,8- DMDBT	2,7- + 3,7- + 2,8-dimethyldibenzothiophene
ρ_{gr}	Grain densities [kg/m^3]	1,4- + 1,6- + 1,8-DMDBT	1,4- + 1,6- + 1,8-dimethyldibenzothiophene
SPV	Specific pore volume [m³/kg]	1,3- + 3,4-DMDBT	1,3- + 3,4-dimethyldibenzothiophene
ΔH	Molar enthalpy	1,7-DMDBT	1,7-dimethyldibenzothiophene
Q_{st}	Isosteric heat	2,3- + 1,9-DMDBT	2,3- + 1,9-dimethyldibenzothiophene
R	Molar gas constant [8.314 J/mol/K]	1,2-DMDBT	1,2-dimethyldibenzothiophene
M_{CH_4}	Molality of methane [mol/kg]	3-EP	3-ethylphenanthrene
n_a	Absolute gas storage capacity [mmol/g]	9 + 2 + 3,6-DMP	9 + 2 + 3,6-dimethylphenanthrene
n_{free}	Free gas storage capacity [mol/kg]	1-EP	1-ethylphenanthrene
n_{total}	Total gas storage capacities [mol/kg]	2,6 + 3,5-DMP	2,6 + 3,5-dimethylphenanthrene
$m_{transfer}$	Cumulative sum of the volume of the V_r multiplied with the gas density difference in the RC before and after expansion into the SC [kg]	2,7-DMP	2,7-dimethylphenanthrene
$C_{19}Tri$	C_{19}-tricyclic terpane	1,3 + 3,9 + 3,10 + 2,10-DMP	1,3 + 3,9 + 3,10 + 2,10-dimethylphenanthrene
$C_{20}Tri$	C_{20}-tricyclic terpane	1,6 + 2,9 + 2,5-DMP	1,6 + 2,9 + 2,5-dimethylphenanthrene
$C_{21}Tri$	C_{21}-tricyclic terpane	1,7-DMP	1,7-dimethylphenanthrene
$C_{22}Tri$	C_{22}-tricyclic terpane	1,9 + 4,9 + 4,10-DMP	1,9 + 4,9 + 4,10-dimethylphenanthrene
$C_{23}Tri$	C_{23}-tricyclic terpane	2,3-DMP	2,3-dimethylphenanthrene
$C_{24}Tri$	C_{24}-tricyclic terpane	1,8-DMP	1,8-dimethylphenanthrene
$C_{25}Tri$	C_{25}-tricyclic terpane	1,2-DMP	1,2-dimethylphenanthrene
$C_{24}TeT$	C_{24}-tetracyclic terpane	TNR-1	trimethylnaphthalene ratio 1
$C_{26}Tri\ R$	C_{26}-R tricyclic terpane	TNR-2	Trimethylnaphthalene ratio 2
$C_{26}Tri\ S$	C_{26}-S tricyclic terpane	VR $_{TNR-2}$	Calculated reflectance from TNR-2
$C_{28}Tri\ R$	C_{28}-R tricyclic terpane	TMNR	Trimethylnaphthalene ratio
$C_{28}Tri\ S$	C_{28}-S tricyclic terpane	TeMNr-1:	Tetramethylnaphthalene ratio 1
$C_{29}Tri\ R$	C_{29}-R tricyclic terpane	TeMNr-2	Tetramethylnaphthalene ratio 2

C$_{29}$Tri S	C$_{29}$-S tricyclic terpane	MPI-1	Methylphenanthrene index 1
Ts	18α(H)-22,29,30-trisnorneohopane	VR $_{MPI-1}$	Calculated reflectance from MPI-1
Tm	17α(H)-22,29,30-trisnorhopane	MPDF	Methylphenanthrene distribution fraction
C$_{29}$H	17α(H), 21β(H)-30-norhopane	VR $_{MPDF}$	Calculated reflectance from MPDF
C$_{30}$*DH	15α-methyl-17α(H)-27-norhopane (diahopane)	MBPR	Methylbiphenyl ratio
C$_{29}$M	17β(H), 21α(H)-30-norhopane (normoretane)	MDR	Methyldibenzothiophene ratio
C$_{30}$H	17α(H), 21β(H)-hopane	VR $_{MDR}$	Calculated reflectance from MDR
C$_{30}$M	17β(H), 21α(H)-hopane (moretane)	DMDR	Dimethyldibenzothiophene ratio
C$_{31}$H S	17α(H), 21β(H)-homohopane 30-homohopane (22S)	DMPR	Dimethylphenanthrene ratio
C$_{31}$H R	17α(H), 21β(H)-homohopane 30-homohopane (22R)	VR $_{DMPR}$	Calculated reflectance from DMPR
Gam	Gammacerane	C$_{29}$ *H	C$_{29}$ 17α(H),21β(H)-diahopane
C$_{32}$H S	17α(H), 21β(H)-30,31-dihomohopane (22S)	Ole	Oleanane
C$_{32}$H R	17α(H), 21β(H) -30,31-dihomohopane (22R)	C$_{29}$ ββ H	C$_{29}$ 17β(H),21β(H)-hopane
C$_{33}$H S	17α(H), 21β(H)-30,31,32-trishomohopane (22S)	C$_{31}$ ββ H	C$_{31}$ 17β(H),21β(H)-hopane
C$_{33}$H R	17α(H), 21β(H)-30,31,32-trishomohopane (22R)	C$_{29}$ N	C$_{29}$ 17α(H),21β(H)-25-norhopanes
C$_{34}$H S	17α(H), 21β(H)-30,31,32,33-tetrahomohopane (22S)	SPI	Source potential index [t HC/m^2]
C$_{34}$H R	17α(H), 21β(H)-30,31,32,33-tetrahomohopane (22R)	MAAT	Mean annual air temperature
C$_{35}$H S	17α(H), 21β(H)-30,31,32,33,34-pentahomohopane (22S)	LST	Lake surface temperature
C$_{35}$H R	17α(H), 21β(H)-30,31,32,33,34-pentahomohopane (22R)	GDGT	Glycerol dialkyl glycerol tetraether
pregnane	5α,14β,17β(H)-pregnane (diginane)	CIA	Chemical Index of Alteration
homopregnane	5α,14β,17β(H)-homopregnane (20-methyldiginane)	SLST	Summer surface water temperature
C$_{27}$ βα dia20S	13β(H), 17α(H)-diacholestane (20S)	WLST	Winter surface water temperature
C$_{27}$ βα dia20R	20R-13β(H), 17α(H) -diacholestane	V$_r$	Volume of the reference cell [m^3]
C$_{27}$ αβ dia20S	13α(H), 17β(H)-diacholestane (20S)	V$_s$	Volume of the sample cell [m^3]

C_{27} αβ dia20R	20S-13α(H), 17β(H)-diacholestane	mextracts	Mass of extracted hydrocarbon [kg hydrocarbons]
C_{27} ααα20S	5α(H), 14α(H), 17α(H)-cholestane (20S)	ΔP	Pressure difference [Pa]
C_{27} αββ20R + C_{29} dβα20S	20R-5α(H), 14β(H), 17β(H)-cholestane (20R)+ 13β,17α,20S-diastigmastane	ρ_{bulk}	Bulk density [kg/m^3]
C_{27} αββ20S	5α(H), 14β(H), 17β(H)-cholestane (20S)	$\Phi_{gas-filled}$	Gas-filled porosity [-]
C_{27} ααα20R	5α(H), 14α(H), 17α(H)-cholestane (20R)	Φ_{total}	Total porosity [-]

1 Introduction

1.1 Objectives
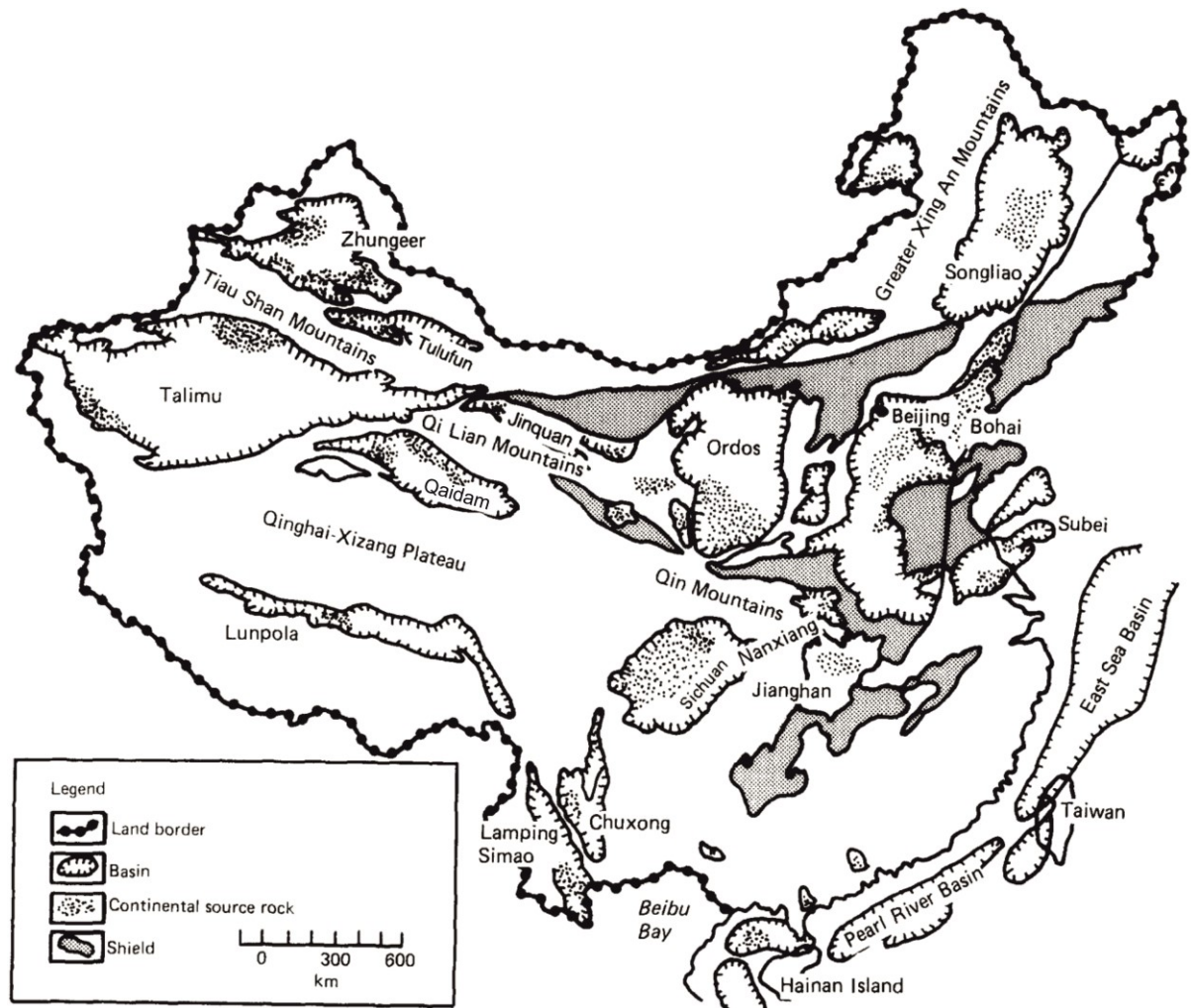
Fig. 1.1. Principal Chinese oil-bearing basins showing the distribution of continental source rocks (modified after Powell, 1986).

Organic matter (OM)-rich shales/mudstones are regarded as important hydrocarbon source rocks in basins. In the past few decades, source rocks have become also targets for unconventional shale-oil and shale-gas production in the world (Montgomery et al., 2005; Ross and Bustin, 2007 and 2009; Jarvie et al., 2007; Gasparik et al., 2014; Li et al., 2018; Qiao et al., 2020 and 2021a). Fine-grained sedimentary rocks, such as clayey siltstones, silty shales, siltstones, and shales, account for more than two-thirds of the world's sedimentary rocks and are formed via different processes in many environments (Stow, 1981; Land et al., 1997), but only a small amount of them is rich in OM. Two key conditions are required for OM-rich sediments to form: (1) surface water is rich in phytoplankton and microorganisms, (2) suitable sedimentary and diagenetic conditions exist for OM preservation and accumulation. As a result, these OM-rich sediments are typically deposited in anoxic sedimentary

1

environments within lakes, lagoons, eutrophic basins, closed embayments, or on a continental shelf below the wave base (Walteret, 1985; Land et al., 1997; Lemons and Chen, 1999).

In many areas of the world, there is a predominance of marine OM rich sediments, i.e. petroleum source rocks. However, OM-rich sediments in China are to a large extent of "transitional" (i.e. paralic) or continental origin (Zou et al., 2010). Since many OM-rich shales/mudstones have been found to be deposited in lake systems, the importance of lacustrine systems for the preservation of hydrocarbon prone OM has been recognized for many years. In China, the preponderance of large petroliferous intermountain basins, i.e., the site of extensive and long-existing lakes, provided the theoretical basis and impetus for the early development of the continental theory of hydrocarbon generation and accumulation (Huang et al., 1984; Zhai et al., 1984). The geographic and stratigraphic distribution of the principal Chinese oil-bearing basins is shown in Fig. 1.1. Compared to well studied marine OM-rich shales from other parts of the world, the non-marine sediments and their related resources in China are only basically understood, and also the geological conditions of different non-marine basins vary significantly. Thus, it is very important to study potential key factors determining the accumulation of OM in non-marine sediments. This thesis focuses on the OM-rich sediments collected from Paleozoic shales in the Yishan Slope of the southeastern Ordos Basin, the Mesozoic Yanchang Formation in the mid-western Ordos Basin and Cenozoic source rocks for microbial gas in the central Qaidam Basin China aiming to:

• i) characterize porosity and sorption capacity of thermally overmature Upper Paleozoic shales from the southeastern Ordos Basin in central China in the context of kerogen quantity, maturity and mineralogy, and furthermore to assess the shale gas potential of these shales;

• ii) reconstruct the depositional environments prevailing during deposition of the Chang 7 member and gain information on the biological precursors of its OM, quantify thermal maturity in the mid-western part of the Ordos Basin, for which almost no such information has been published so far;

• iii) evaluate the quality and quantity of kerogen in the Pleistocene lacustrine deposits in the central Qaidam Basin in northwest China and discuss the enrichment mechanism of OM as a basis for the exploration in the target area. In this context, also the terrestrial OM input needs to be considered. This study provides an example of an integrated approach using multiple proxies to analyze factors controlling OM accumulation in lacustrine environments;

• iv) specifically identify and quantify Pleistocene climate and weathering conditions based on elemental data, isotopes and temperature-sensitive biomarkers (GDGTs).

1.2 Characteristics of non-marine source rocks in China

According to carlsons trophic state index, lake classification can be divided into seven types (Table 1.1). OM-rich sediments in marine basins are controlled by several factors, such as stratified water columns, nutrient supply and recycling, anoxic events, phytoplankton blooms, and rising sea levels

(MacIlvaine and Ross, 1973; Dean et al., 1985; Dimberline et al., 1990; Werne et al., 2002; Bradley, 2003; Macquaker et al., 2003, 2010a and b; Macquaker et al., 2010a; Schieber, 2011). Compared to marine settings, water circulation in lacustrine settings is usually less active, and deep-water overturning is easily inhibited (Fig. 1.2). The formation of OM-rich sediments in lacustrine environment is determined by water depth and stratification, and is improved by rapid burial events due to gravity flows and by addition of trace nutrients. In addition, lacustrine environments are more easily affected by external factors. For example, plenty of terrestrial or volcanic mineral input can dilute organic carbon accumulation but can also provide soluble micronutrients (iron, silicon, phosphorus) to promote algal blooms. Correspondingly, lacustrine OM-rich sediments have different depositional patterns and mechanisms in different basins. Their kerogen types and organic matter contents show large variation.

Table 1.1. Lake classification according to Carlsons trophic state index (Carlson and Simpson, 1996).

TSI	Attributes	Water Supply
<30	**Oligotrophy:** Clear water, oxygen throughout the year in the hypolimnion	Water may be suitable for an unfiltered water supply
30–40	Hypolimnia of shallower lakes may become anoxic	
40–50	**Mesotrophy:** Water moderately clear; increasing probability of hypolimnetic anoxia during summer	Iron, manganese, taste, and odour problems worsen. Raw water turbidity requires filtration
50–60	**Eutrophy:** Anoxic hypolimnia, macrophyte problems possible	
60–70	Blue-green algae dominate, algal scums and macrophyte problems	Episodes of severe taste and odour possible
70–80	**Hypereutrophy:** (light limited productivity). Dense algae and macrophytes	
>80	**Oligotrophy:** Clear water, oxygen throughout the year in the hypolimnion	Water may be suitable for an unfiltered water supply

One of the main conditions for the formation of lacustrine source rocks is that the lacustrine environment must have sufficient scale and duration to facilitate the accumulation of OM. Second, the tectonic environment must provide sufficient burial and thus maturation conditions for the generation of hydrocarbon (Powell, 1986). Actually, the second factor is not very important in some special environments. For example, the immature Pleistocene lacustrine source rocks in the Qaidam Basin generated the largest Quaternary microbial gas field in the world due to its special climate conditions, not requiring very deep burial.

Hutchinson (1957) recognised up to eleven types and some sub-types of lakes in the modern environment. However, only two categories seem to be related to the occurrence of source rocks. These are the alluvial lakes formed on humid flood plains and deltas, and the large tectonic lakes associated with epeirogenic movements. The physical and chemical processes of a lake system are deeply influenced by climate, the physical scale of the lake, and the energy of the river system that flows into the lake.

a

Wind/wave action and morphology

River action

Wind (speed, duration direction) and fetch

R

321

BIOPRODUCTION

Surface currents

Erosion
Transportation

Wave base

Under currents 3

2 1

Accumulation

Bioturbation

0 1 3

'Pelagic' sedimentation

Under currents

Delta sedimentation

Transportation

Slope > 5%

River plume sedimentation

Turbidity currents

Accumulation

3 2 1 0

Turbidity currents

BOTTOM DYNAMICS

1. Erosion (winnowing) — coarse deposits	1. Delta sedimentation — coarse deposits
2. Transportation — coarse and fine deposits	2. River plume sedimentation — coarse and fine deposits
3. Accumulation — fine deposits (—'pelagic' sedimentation)	3. Turbiditic sedimentation — fine and coarse deposits
4. Turbiditic sedimentation — fine deposits	

b

Littoral microflora and macroflora

Pelagic microflora (Phytoplankton) Photosynthesis

Dissolved and particulate organic compounds

Allochthonous dissolved and particulates humic compounds and plant debris

CO_2 and HCO_3^-

Respiration

Oxidation

Aerobic decomposition

Flocculation and adsorption of dissolved organic compounds on $CaCO_3$ and clays

Epilimnion
Hypolimnion

Anaerobic decomposition

$CO_2 + CH_4 + H_2S$

Plant debris

Organic matter in sediments

Anaerobic decomposition

Organic matter in sediments

Fig. 1.2. Physical and biological processes affecting organic matter preservation in lakes (a) Schematic illustration of major sedimentological and bottom dynamic processes in lakes; (b) Processes affecting organic matter preservation in lakes (after Powell, 1986).

Modern lakes developed two modes of OM accumulation (Picard and High, 1981). The increase of OM in offshore sediments is due to sedimentation and preferential preservation under wave-base and hypoxic conditions. The OM accumulation in nearshore sediments is caused by the accumulation of plant remains. The deep anoxic lacustrine facies is characterized by OM-rich shale and marl deposited in the deep water environment under stratified lake conditions. OM is well preserved in anoxic bottom waters. There are also OM-rich sediments related to microbial mats and allochthonous organic debris from higher land plants. The lacustrine source rocks in tectonic lake basins are partly characterized by large thickness with some source rocks up to 700 m thick in China (Li et al., 1984).

Some Chinese authors, e.g. Tlian et al. (1983) and Huang et al. (1984) have categorised lacustrine source facies as well as their depositional setting as follows:

1). Freshwater lakes under humid climates

Subsidence and sedimentation are in equilibrium. The marshes are well developed and terrestrial higher plants flourished. Mudstone, coal, and oil shale alternate vertically, i.e. sedimentary facieses highly variable. These source rocks developed during the Jurassic and Late Triassic in the Ordos Basinand during the Jurassic in the Junggar Basin.

2). Fresh-brackish water lakes in semi-humid climates

The lakes are eutrophic and deep, but they get some OM from the land. The deep lacustrine source rocks are thick and interbedded with oil shale. Examples are the Early Cretaceous of Songliao and Jinquan basins.

3). Saline lakes in semi-arid climates

Black/blue OM-rich mudstones interbedded with thin salt beds, oil shales, and gypsum shales are widespread in the Paleogene, Neogene and Quaternary, e.g. Qaidam Basin. The source rock is formed in a semisaline stage before salt precipitation.

4). Hypersaline lakes under arid climates

In a continuous saline lake, dark mudstone source rock interbedded with thick gypsum as well as salt beds formed. Examples are present in the Eocene and Oligocene of Jianghan Basin.

The freshwater, brackish, and saline lake basins have different patterns of water column stratification (Picard, 1971). Freshwater lakes are generally formed in humid climates and their sediments are dominated by fine-grained sandstone, marlstone and siltstone. The kerogen formed in this type of lake is mainly sapropelic. Bradley (1964) suggested that the water cycle is interrupted in the deepest part of a seasonal freshwater lake, resulting in anoxic bottom water and the formation of thick layers of OM-rich sediments. Brackish and saline lakes are generally formed in dry continental states where debris and carbonate rocks are deposited and dolomitization is strong (Jiang, 1988; Deng and Qian, 1990). Saltwater lakes favor the preservation of OM because salinity-driven stratification tends to be more stable. Brackish lakes are usually connected to external fresh waters with limited water exchange and have a high rate of OM generation. However, these lakes lack reversal of bacterial activity and fragment dilution, which are crucial factors in the formation of OM-rich shales (Surdam and Stanley, 1979). Correspondingly, the OM-rich shales in different basins are controlled by different distribution patterns, sedimentary mechanisms, and OM origins (kerogen types). Thus, the exploration and development of resources in these different basins require different strategies.

The high total organic carbon (TOC) content of black mudstone/shale in deep lake basins can be explained by the water column stratification model. The water depth, oxygen-poor conditions and lake currents control the OM preservation and the distribution of organic-rich shales. In China, high quality lacustrine source rocks are usually associated with tuff beds formed by nearby volcanic eruptions. Volcanic ash is rich in soluble micronutrients (iron, silicon, phosphorus) that promote algal blooms.

Volcanic intercalations are associated with thicker high-quality source rocks. Saline/brackish lacustrine lake basins contain OM-rich dolomite mudstone, which formed mainly when the lake had high salinity, and the stratified water column deprived the underlying water of oxygen, thus preserving large amounts of OM. In summary, the lacustrine systems in China have good potential for oil and gas resources.

North China developed OM-rich shales deposited in marine-nonmarine transitional facies during Carboniferous-Permian periods. Such shales are typically fine-grained sediments deposited in near-shore, paralic environments including coastal marshes, deltas, tidal flats, bays and lagoons (Xiong et al., 2017; Yang et al., 2018). The OM in these shales is mainly originated from terrestrial higher plants in the adjacent depositional areas. The Carboniferous-Permian periods are key periods of geological evolution in China. The palaeogeographic environment changed greatly from marine facies to continental facies where a large number of transitional OM-rich shales was deposited. In North China, the transitional shales appear in the Carboniferous Benxi Formation (C_2b) and the Permian Taiyuan (P_1t) as well as Shanxi (P_1sh) formations. In South China, the transitional shales were deposited in the Permian Liangshan (P_1l) and Longtan (P_3l) formations. These transitional shales are the most important source rocks in the Sichuan and Ordos basins feeding important gas fields (Zou et al., 2019 and Qiao et al., 2020).

After the Middle Triassic period, most of China has been an intracontinental sedimentary system, except the part of the Qinghai-Tibetan region. From Late Triassic to Cenozoic, the landscape features of several large inland lakes in the Ordos, Sichuan, Songliao, Bohai Bay, Qaidam, Junggar, Turpan-Hami and Tarim basins were obvious (Zou et al., 2019). The lacustrine OM-rich shales were mainly deposited in marsh and deep lake environments, where OM preservation and productivity are the most important controlling factors for the formation of OM-rich shales.

All in all, from Permian to Neogene, OM-rich lacustrine shales have been deposited in different freshwater to saltwater lacustrine environments in China.

1.3 Geology of the Ordos Basin

1.3.1 Tectonic evolution

The Ordos Basin is an important basin containing coal, petroleum and gas, covering an area of 26×10^4 km². After the Indochina Movement, the tectonic evolution of China entered a new period, i.e. the marginal pacific tectonic domain and the Tethys tectonic domain evolved. The formation of the marginal pacific tectonic domain is the result of subduction of the Pacific Plate under the Asian Continent. The compression caused by the subduction divided the Paleo-North China Basin into an uplift in the east and the Ordos Basin in the west. The formation of the Tethys tectonic domain is the result of the subduction of the Tethyan oceanic or suboceanic crust under Eurasia. Tectonism caused by subduction not only formed the worldwide largest Indochinese fold area, but also formed large sedimentary basins such as the Sichuan, Ordos, Qaidam and Tarim basins in the margin area of Paleo-

Asian continent. Therefore, the Ordos Basin was the result of the combined action of the Pacific plate and the Tethys oceanic crust on the ancient Asian continent. Besides, based on the analysis of the thickness of Jurassic strata in the western margin of the basin, the Tethys tectonic domain seems to have a greater influence on it.
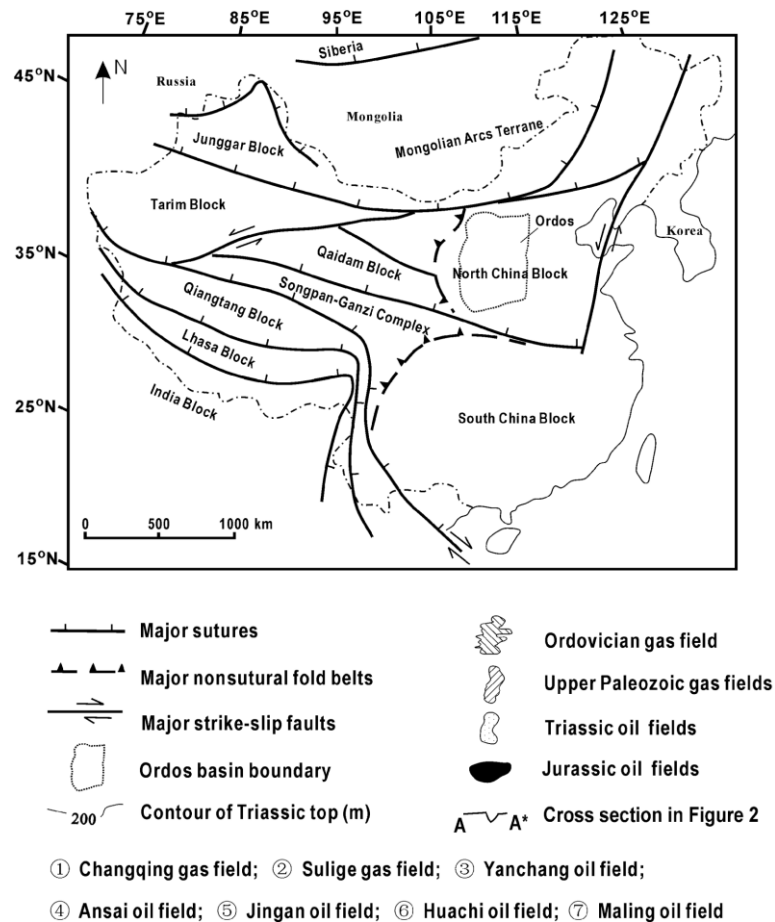
Fig. 1.3. Simplified tectonic map of China, showing major features discussed in the text and location of the Ordos basin (after Yang et al., 2005).

The present Ordos Basin is geographically located in the North China Block (Fig. 1.3), spanning the Shananxi, Shanxi, Ningxia and Gansu provinces as well as the Nei Monggol Autonomous Region. The North China Block includes several microblocks. Some scholars argued that these microblocks merged to form a craton or cratons at 2.5 Ga or earlier (Geng 1998; Zhang,1998; Kusky et al., 2001, 2004 and 2006; Polat et al., 2005 a, b and 2006). However, some others argued that these microblocks did not merge until 1.8 Ga (Zhao et al., 2001a, 2005 and 2006; Liu et al., 2004 and 2006; Guo et al., 2005; Kröner et al., 2005 a and b). Nd T_{DM} models, the initial ratios of terrestrial igneous rocks appeared to lie on the same Nd isotope growth curve as chondritic meteorites (DePaolo and Wasserburg, 1976 a and b), indicate that the main crustal North China Block was formed between 2.9 and 2.7 Ga (Chen and Jahn 1998; Wu et al., 2003a and b).

The craton is separated by the Central Orogenic Belt and can be divided into the Eastern and Western Blocks (also referred to as the Ordos Block). Other blocks, such as the Alashan Block and Jiaoliao Block merged at the time of the collision of the Eastern and Western Blocks at 2.5 Ga. The Ordos Block is a stable part of the craton, with a thick mantle root, low heat flow, and little internal deformation after the Precambrian (Zhai and Liu, 2003). After that, the North China Block entered into an inactive tectonic stage from 2.2 to 1.85 Ga. About 1.9 – 1.8 Ga a granulite event indicates the continent–continent collision between the Ordos Block and Eastern Block (Zhao et al., 2001a, 2005, 2006; Wilde et al.,2003; Kröner et al., 2005a and b). Then there was an important metamorphic event from 1900 to 1800 Ma. So, all cratonic Precambrian rocks experienced the same metamorphic period of 1900-1800 Ma, with intrusion and mixing of crustal molten granite.

During the early Paleozoic, this area was part of the North China Plate. The north, west, and south sides were the Xingmeng and Qinqi troughs (Sun et al., 1989; Yue et al., 2001). During the early Late Paleozoic, the north and south margins of the North China Block experienced oceanic crust subduction and formed a Caledonian fold belt along a continental margin; this resulted in the uplift of North China Block and disappearance of the intraplate shallow sea basin. At the end of the Late Paleozoic, the North China Block began to subside, forming a graben-like inland epeiric sea basin bounding by the Caledonian fold belt in the north and south and connecting with the Qilian Sea. The Qilian Sea on the west side combined with the fold belts on the north and south sides controlled the sedimentary types and accumulation characteristics of the Ordos Basin in the Late Paleozoic. During the Triassic, the basin basically inherited the tectonic framework at the end of the Late Paleozoic. Under the control of sedimentation, the Triassic coal-bearing strata were deposited in Zichang and Hengshan areas. Under the influence of oceanic crust subduction of the Teythys tectonic domain, the western and southwestern margins were strongly uplifted, which made the area became a part of a large dustpan-like inland basin surrounded by folded orogenic belts on the north, west and south sides. The Indosinian movement at the end of Triassic caused the uplift of the whole region, then subjected to denudation and deformation, which turned into a relatively stable depression stage after the Early Jurassic, when the Ordos Basin was formed.

The last stage of Ordos Basin evolution occurred at the Early Cretaceous (Zhao et al., 2011). A large part of the basin received sediment during this period. Since the Late Cretaceous, the basin experienced a uniform, extensive uplift and denudation, resulting in the extensive denudation of Cenozoic strata except for the Neogene red clay and Quaternary loess deposits. During Eocene and Oligocene stages, the disintegration of the Ordos Basin (or block) began to occur, resulting in uplift in source areas and enlargement in depositing thickness and range of sediments. During the early to middle Miocene periods, the uplift area was mainly distributed in all tectonic units except for the Yishan Slope. The eastern part of the Shanbei was uplifted obviously, and the uplift rate is much higher there than in the western part. From the late Miocene to Pliocene period, in the south and east of the basin red clay sediments were widely deposited with large extension and thickness.

During the Quaternary, the basin, due to the south-north compressive stress, has experienced subsidence, uplift, depression and uniform uplift, in turn, before disintegration of the paraplain at an early age. The main river systems of the Loess Plateau, as well as the Yellow River, were formed during 1.67-1.45 Ma. During the middle Quaternary period, structural activities were more frequent, resulting in the main drainage direction of NNW and NW. In the Later Quaternary period, rivers cut downward and the topography gradually formed reaching that of today.

1.3.2 Sedimentary fill

The North China Block includes a large area of locally well-exposed Archaean crust, including c. 3.8-2.5 Ga gneiss, tonalite-trondhjemite-granodiorite (TTG), mica schist, graphite- and sillimanite-bearing gneiss (khondalite), migmatite, granite, ultramafic bodies, amphibolite, banded iron formation (BIF), dolomitic marble, and meta-arkose (Jahn and Zhang, 1984 a and b; Jahn et al., 1987; Bai, 1996; Wang, 1991; Wang and Zhang, 1995; Wang et al., 1997). The Archaean rocks are overlain by conglomerates, quartzites, shales, sandstones, and carbonates of the 1.85-1.40 Ga Mesoproterozoic Great Wall (Changcheng) Series (Li et al., 2000a and b). In some central areas of the North China Block, 2.40-1.90 Ga Palaeoproterozoic sequences deposited in cratonic graben are preserved (Kusky and Li, 2003).

The Late Archaean Qinglong foreland basin and fold-thrust belt are now preserved as several remnant folded sequences (Kusky and Li, 2003; Li and Kusky, 2006). From bottom to top, the sediments can be divided into three subgroups. The lower subgroup, which is composed of quartzite-mudstone-marble, is well preserved in central sections of the Qinglong foreland basin. The middle subgroup and upper subgroup are graded turbidite- and molasse-type sediments, respectively. The western edge of the Qinglong Foreland Basin is strongly affected by thrust folds, and is overthrust by active marginal rocks. The eastern margin of the Qinglong Foreland Basin has less deformation.

During the early Paleozoic period, the North China block tidal-flat and shallow-marine sediments were deposited including oomicrites, minor clastic rocks, and dolomites with a thickness of around 300–600 m in the main area of the basin (Sun et al., 1989).

During the Carboniferous, a transgression occurred on the North China Block. In the middle and eastern parts of the Ordos Basin, a tidal-flat environment developed during the deposition of the Carboniferous Benxi Formation. The depositional environment of the Carboniferous Taiyuan Formation was shallow marine resulting in extensive tidal-flat facies with limited deltaic sand bodies in the northern area of the basin (Fu et al., 2003). The Taiyuan Formation developed black shales interbedded with carbonates, sandstones, and coals with a thickness of about 22–276 m (Yang et al., 2005). During the Early Permian period, the basin received shallow lacustrine and extensive delta sediments (Fu et al., 2003). The Lower Permian succession consists of the Shanxi (37–125 m) and Xiashihezi (100–200 m) formations, which developed swamp and shallow-lacustrine mudstones interbedded with coals and fluvio deltaic sandstones interbedded with mudstones in the central and southern areas and the northern area of the basin, respectively. A small number of marine carbonate

9

rocks and fossils were found in the Lower Permian in the southern area of the basin (Tian and Zhang, 1997), indicating a small-scale transgression. During the Upper Permian–Middle Triassic period, the basin mainly developed red deltaic, fluvial, and shallow-lacustrine clastic rocks under an arid climate (Zhai, 1990). The Early–Middle Triassic strata in the southwestern part of the Ordos Basin experienced the transgression of the Songpan-Ganzi residual ocean basin, which is characterized by thin layers of shallow marine sandstone, mudstone and carbonate rocks containing marine fossil debris (Zhang, 1997).
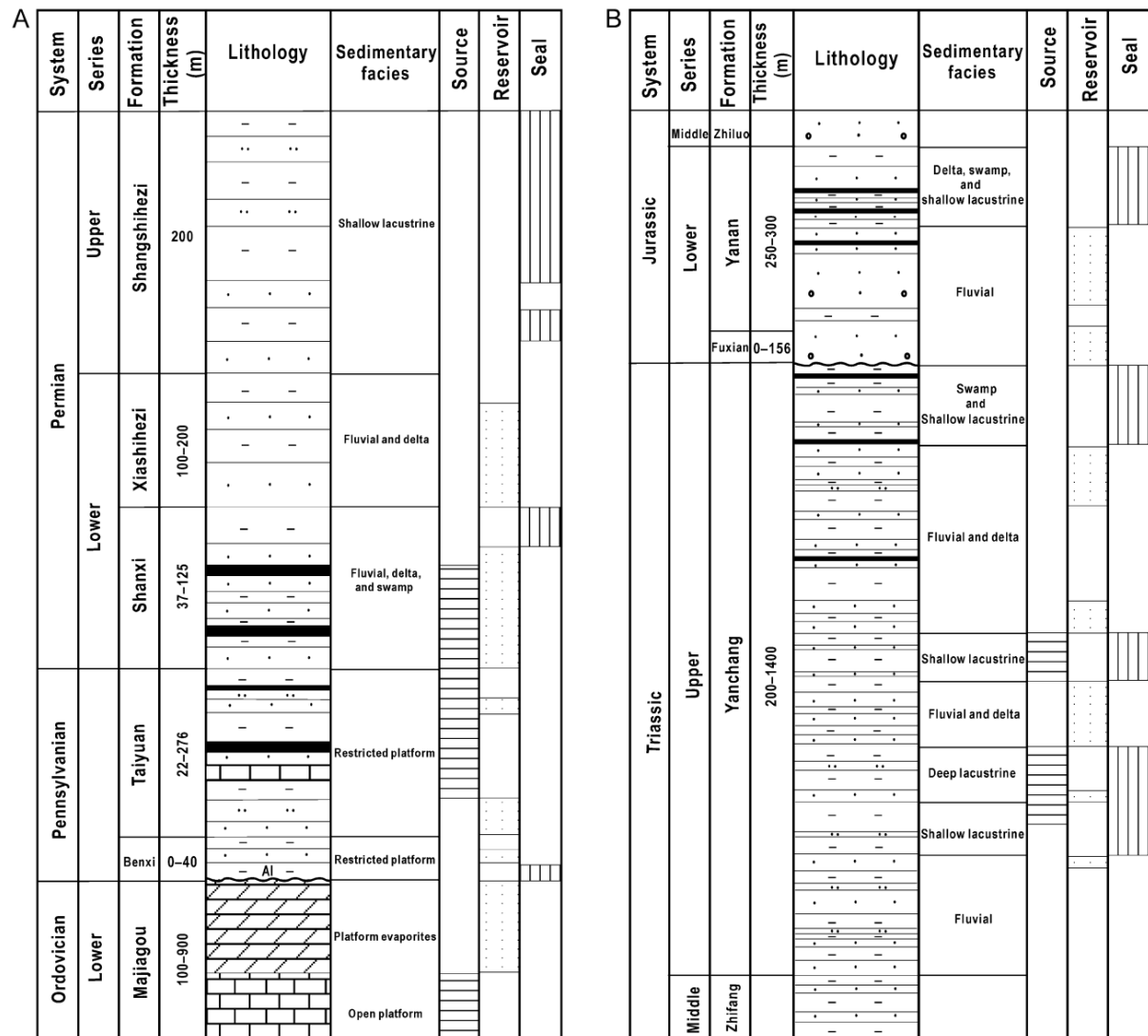
Fig. 1.4. Stratigraphic columns, depositional environments, and source-reservoir-seal associations in the Ordos basin (A) for the Lower Ordovician–Upper Permian; (B) for the Upper Triassic–Lower Jurassic (after Yang et al., 2005).

In the Late Triassic, the Ordos Basin developed the southwest fan delta and the northern delta. The clastic wedges deposited in the southwestern foreland depression of the Ordos Basin are more than 3,000 m thick and gradually tapering to 1000 m to the east (Li et al., 1995). The upper Yanchang Formation was deposited under extensive shallow lacustrine lake and swamp environments with a thickness of around 100 m.

10

The Fuxian Formation of the Lower Jurassic was formed on the erosion surface of the pre-Jurassic. It mainly consist of conglomerate and sandstone of the incised braided channel system (Wu and Xue, 1992). The lower section of the Yanan Formation is mainly composed of sandstones deposited in the incised valleys, and then the meandering river point bars were directly deposited on the erosive terrace (Wu and Xue, 1992). The upper section of the Yanan Formation was deposited in marsh and extensive shallow lake environments with a thickness of around 40-90 m.

The lower and middle sections of the Middle Jurassic mainly consists of fluvial, coarse-grained feldspar-bearing sandstones, while the upper part consists of lacustrine mudstones, with a thickness of about 300-500 m (Guo et al., 1994). Most areas of the Ordos Basin show limited and thin Upper Jurassic deposits (Zhai, 1990). The Lower Cretaceous consists of fluvial and lacustrine sediments with a thickness of 200-1000 m (Sun et al., 1989) (Fig. 1.4).

The Paleogene composes of only the Qingshuiying Formation distributed in the western Ordos Basin and has unconformable contact with the underlying parallel formations. The Miocene Baode Formation, Pliocene Jingle Formation and Quaternary sediments are widely distributed in the Ordos Basin.

1.4 Geology of the Qaidam Basin

1.4.1 Tectonic evolution

The Qaidam Basin is part of a basin-range system that is located at the northern edge of the Tibetan Plateau covering an area of around 120,000 km^2, with an altitude up to 2.7–3.5 km above sea level (Fig. 1.5). During the Paleoarchean, the continental nucleus including the Yangtze, North China, and Tarim cratons were formed, except for the Qinghai-Tibetan Plateau. The basement of the Qaidam Basin formed during Meso- to Neoarchean in relation to the ocean–continent transition during the Mesoarchean to Proterozoic and the post-Cryogenian rift. After that, the thick platform cover formed, i.e. clastic sedimentation and carbonate platform formed a stable crustal tectonic unit.

The Mesozoic and Cenozoic tectonic evolution of the Qaidam Basin can be divided into three tectonic-sedimentary stages: (1) piedmont fault depression stage in the Mesozoic; (2) unified depression stage from Palaogene to Neogene; and (3) subsiding depression in the east and cyclic folding in the center and west during the Quaternary based on the comprehensive analysis of regional tectonic setting, tectonic movement, unconformities, stratigraphic distribution, sedimentary characteristics and tectonic evolution history.

1. Piedmont fault depression stage in the Mesozoic.

In the Early Jurassic, the basin was formed in the interior of the Qaidam Block. During the early and middle Jurassic (after the Indosinian Movement and before the collage of the Gangdise block and Eurasia), the whole northwest region of China including the Qaidam Basin was affected by intense extensional tectonics. During this period, the Qaidam Basin was in an extensional tectonic setting,

related to the Late Indosinian period. The early Yanshanian tectonic event in the Middle Jurassic led to the first tectonic inversion. After that, the basin entered into the stage of compression and uplift.
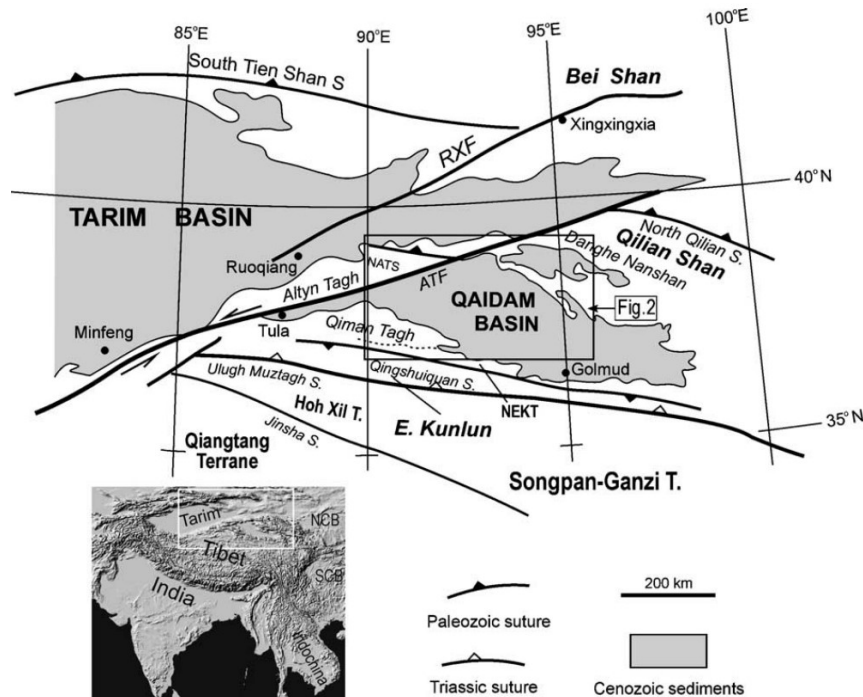
Fig. 1.5. Regional tectonic outline of the northern part of Qinghai–Tibet Plateau, showing current relationship between the Qaidam Basin and neighbouring Altyn Tagh Fault and Tarim Basin (after Zhou et al., 2006). ATF, Altyn Tagh Fault; RXF, Ruoqiang–Xingxingxia Fault; NATS, Northern Altyn Tagh Suture; NCB, North China Block; SCB, South China Block; S, suture; T, terrane.

2. Cretaceous compression and uplift stage

During the Late Cretaceous, Central Asia including the Qaidam Basin did not receive much sediment, suggesting that Central Asia was a vast plateau during this period and the Qaidam Basin entered the stage of compression and uplift. Due to the continuous northward movement of the Indian Plate and intracontinental subduction during Paleogene, the Qaidam Basin was in a compression stage. During Oligocene (Upper Ganchaigou Stage) and early Miocene (Lower Youshashan Stage), compression continued with the intensification of intracontinental subduction of the Tibetan Plateau.

3. Subsiding depression in the east and cyclic folding in the center and west during the Quaternary.

During the Middle and Late Himalayas periods, the intracontinental subduction of the Tibetan Plateau was further intensified, and the basin was further squeezed. During the Late Himalaya-Neotectonic Movement, the western and northern Qaidam Basin was affected by strong tectonic activities, resulting in a large number of folds and faults. The central and eastern Qaidam Basin further subsided under the influence of compression, and the Quaternary subsidence center migrated to the Sanhu area.

1.4.2 Sedimentary fill

Erathem	System	Series	Formation	Symbol	Thickness (m)	Age (Ma)	Lithologic section
Cenozoic	Quaternary	Pleistocene	Qigequan	Q_{1+2}	0 — 3500		
						2.6	
	Neogene	Pliocene	Shizigou	N_2^3	300 — 2000		
						5.1	
		Miocene	Upper Youshashan	N_2^2	300 — 2000		
						12.0	
			Lower Youshashan	N_2^1	600 — 2300		
						24.6	
	Paleogene	Oligocene	Upper Ganchaigou	N_1	500 — 1200		
						40.5	
		Eocene + Paleocene	Lower member of Lower ganchaigou	E_3^2	500		
			Uper member of Lower ganchaigou	E_3^1	3100		
						52.5	
			Lulehe	E_{1+2}	300 — 1000		
						66.0	
Mesozoic	Cretaceous		Quanyagou	K	200 — 1317		
	Jurassic	Upper Jurassic	Hongshuigou Caishiling	J_3	550 — 1200		
						145	
		Middle Jurassic	Dameigou	J_2	1000		
		Lower Jurassic	Xiaomeigou	J_1	140	201	
			Baement rock				

Fig. 1.6. Stratigraphic division, lithology, and source rocks in the Qaidam Basin (changed after Guo et al., 2017).

The Qaidam Basin is filled with Mesozoic–Cenozoic sediments with a thickness of more than 16,000 m originating from the surrounding mountains. All sediments developed on the top of the pre-Mesozoic basement comprising igneous and metamorphic rocks (Fig. 1.6). The Mesozoic deposits in the basin include the Jurassic System and Cretaceous System (Quanyagou Formation). From the bottom

to the up, the Jurassic System can be divided into the Xiaomeigou Formation (J_1) of the Lower Jurassic, the Dameigou Formation (J_2) of the Middle Jurassic, and the Caishiling and Hongshuigou formations (J_3) of the Upper Jurassic (Fig. 1.6). The Lower Jurassic sediments are mainly distributed in the western segment of the northern margin of the Qaidam Basin and the intersection area of the Qilian Mountains and the Altun Mountains, with a distribution area of 22,000 km^2 and a maximum thickness of 2,200 m. The deposition centers were located at Kunte Yi, Yibei and Lenghu areas. The north-west spreading Yibei fault depression and Kunteyi fault depression were connected, with an area of 5,400 km^2 and a maximum thickness of 2,000 m. Renghu fault depression is nearly north-south spreading, with an area of 600 km^2 and a maximum thickness of 2,200 m. During the Middle Jurassic, the sedimentary range migrated eastward and extended to the front of the Qilian Mountains. The Delingha Sag in the eastern part of the basin covers an area of 9,600 km^2 with a maximum thickness of 900 m. Due to the influence of the late tectonic movement, the southern strata in the western area of the northern margin of the Qaidam Basin suffered serious denudation. The Middle Jurassic sediments are mainly distributed along with the Saishiteng-Yuka, covering an area of 4,200 km^2, and the thickest area was located in the Yuka area with 800 m. From Late Jurassic to Early Cretaceous, a set of red molasse deposits dominated by alluvial-fluvial, littoral and shallow lacustrine facies was formed under the control of arid palaeoclimate, which was the product of the compression-depression evolution of the basin. From Late Jurassic to Early Cretaceous, the sediments range was relatively large compared to that in Early Jurassic and Middle Jurassic, which is characterized by gradually expanding from the western and northwestern margins of the basin to the inner basin.

Cenozoic sedimentation began in Paleocene and was synchronized with the India-Asia collision. From the bottom to the top strata, the Cenozoic sediments can be divided into Lulehe Formation (E_{1+2}), the lower member of the lower Ganchaigou Formation (E_{31}), the upper member of the lower Ganchaigou Formation (E_{32}), the upper Ganchaigou Formation (N_1), the lower Youshashan Formation (N_{21}), the upper Youshashan Formation (N_{22}), the Shizigou Formation (N_{23}), and the Quaternary Qigequan Formation (Q_{1+2}). The E_{1+2} and E_{31} formations were deposited in the early filling stage before the weak depression stage, which consists of a set of coarse-grained to fine-grained brown-red and brown sandstone and mudstone. E_{32} Formation was deposited during the depression stage. The main depression was located in Mangya sag and Yiliping sag. The distribution center of the N_1 and N_{21} formations is located at Yiliping depression. The basin is distributed in a rhomb-shape. The regional unconformities at the bottom of the N_{22} Formation are widely distributed in the periphery of the basin, and the strata under it were strongly denudated. This stage is the strike-slip thrust deformation stage of the basin, and the thrust is mainly caused by the south-side compression. As a result, dextral strike-slip occurred in the west of the basin, and a series of linear structural belts were formed. These linear structural belts first developed in the western part of the basin, and then gradually extended to the eastern part of the basin, resulting in the subsidence of the whole basin and the gradual eastward migration of the sedimentary center. The N_{23} Formation was deposited during the period of lake level decline. During

this period, the lake area was the smallest and the water body was generally shallow. The fluvial inundation facies is widely distributed in the basin, while the normal lacustrine facies is limited and distributed in the Sanhu area and Yiliping area in the east of the basin. During the Quaternary, the Qaidam Basin developed a large, shallow, saltwater lake with no obvious topographic break. The Quaternary Qaidam Basin is a typical inland mountain basin without outlets. The Quaternary strata are unconformably overlying Neogene strata with a maximum thickness of more than 3 km. The sedimentary characteristics record the process of lake development and climate change from humid to dry.

1.5 Chapter overview

This thesis consists of a general introduction, three main chapters and a general outlook chapter listed as follows:

Chapter 2: *Controls on gas storage characteristics of Upper Paleozoic shales from the southeastern Ordos Basin.*

This chapter mainly comprises of elemental analyses, organic petrography, XRD and petrophysical information on the Upper Paleozoic shales in the Southern Ordos Basin, which provides insights on the porosity and sorption capacity of these shales in the context of kerogen quantity, thermal maturity and mineralogy. The results of this study can be used to assess shale gas potential of these rocks under variable temperature and pressure conditions. It was published in the "Marine and Petroleum Geology" in 2020.

Chapter 3: *Paleo-depositional environment, origin and characteristics of organic matter of the Triassic Chang 7 Member of the Yanchang Formation throughout the mid-western part of the Ordos Basin, China.*

This chapter contains primarily organic petrography, carbon and sulfur contents, Rock-Eval pyrolysis and molecular organic geochemistry on aliphatic and aromatic hydrocarbons results from 23 clay-rich source rocks samples collected from 18 wells located in mid-western part of the Ordos Basin, China, to i) reconstruct the depositional environments prevailing during deposition of the Chang 7 member and gain information on the biological precursors of its OM and ii) to quantify thermal maturity. It was published in the "International Journal of Coal Geology" in 2021.

Chapter 4: *High microbial gas potential of Pleistocene lacustrine deposits in the central Qaidam Basin.*

This chapter investigates the interpretation of elemental data on organic and inorganic carbon as well as total sulfur, organic geochemical and organic petrographic analysis of Pleistocene source rocks in the central Qaidam Basin. The quality and quantity of kerogen in the source rocks have been evaluated and the enrichment mechanism of OM as a basis for the exploration in the target area is discussed. In this context, also the terrestrial OM input needs to be considered. This study documents a

case for such depositional settings and provides an example of an integrated approach using multiple proxies to analyze factors controlling OM accumulation in lacustrine environments. It was published in the "International Journal of Coal Geology" in 2021.

Chapter 5: *Climatic conditions during the Pleistocene in the Central Qaidam Basin, NE Tibetan Plateau: Evidence from GDGTs, stable isotopes and elements of the Qigequan Formation.*

This chapter investigates the interpretation of GDGTs, stable isotopes and chemical elements of Pleistocene sediments in the central Qaidam Basin. The origin of organic matter and GDGTs, as well as depositional environments were analyzed and the controlling factors of the OM accumulation in the target area are discussed. In addition, the paleo-climate conditions of the Tibetan Plateau during the Pleistocene were interpreted. This study fills a gap in the climate research of the Tibetan Plateau. The characteristics of the Pleistocene GDGTs are analyzed for the first time. It will be submitted to a journal in 2021.

2 Controls on gas storage characteristics of Upper Paleozoic shales from the southeastern Ordos Basin.

2.1 Abstract

Potential shale gas resources in China are not only of marine but also of marine-terrigenous transitional and continental origins. To analyze the controls on gas storage capacity of shales from the Carboniferous Benxi and Permian Shanxi formations, high-pressure/temperature methane sorption isotherms (up to 25 MPa and 120 °C) and porosity have been measured on 12 samples from the Yishan slope. Total organic carbon (TOC) content of Shanxi and Benxi shales are low to moderate from 0.1% to < 2.3%. All samples have reached the over-mature stage as indicated by vitrinite reflectance values between 2.35% and 2.97% and show lithologic variation where clays are the major minerals (0%–80%) followed by quartz (0%–43%) in most samples. The largest fraction of gas (> 80%) is stored on clay minerals (illite/smectite mixed layer and kaolinite) controlling both sorption capacity and porosity. TOC content, due to its low values, is of minor importance. Benxi and Shanxi shales possess comparatively low gas storage capacities compared to producing marine shale gas systems. Combined with the large amount of clay minerals that make hydraulic fracturing more difficult they are regarded unfavourable for shale gas exploitation. Although a substantial amount of gas can be stored sorbed in excess of the free gas in gas shales, methane sorption has a negligible effect on gas production at pressures above 10 MPa. This has major implications for deep reservoirs where pore pressures in the matrix may not be reduced sufficiently before production ceases.

2.2 Introduction

Compared to crude oil and coal, natural gas produces less carbon dioxide upon combustion and is regarded as an ecologically more favorable fossil fuel. Thus, exploration for and research on shale gas reservoirs became more important during the last two decades and has expanded from marine (Montgomery et al., 2005; Ross and Bustin, 2007, 2009; Jarvie et al., 2007; Gasparik et al., 2014) to terrestrial (Katz and Lin, 2014; Merkel et al., 2016) and marine-terrigenous transitional (herein called "transitional") shales. Such shales are typically fine-grained sediments deposited in near-shore, paralic environments including coastal marshes, deltas, tidal flats, bays and lagoons (Xiong et al., 2017; Yang et al., 2018). Gas storage in these rocks depends on thermal maturity, type and quantity of organic matter (OM), but also on source rock properties such as lithology-dependent petrophysical characteristics like porosity, pore size distribution and sorption capacity (Chalmers and Bustin, 2007; Bustin et al., 2008; Ross and Bustin, 2007, 2009; Ji et al., 2012; Zhang et al., 2012; Yang et al., 2015; Fink et al., 2018).
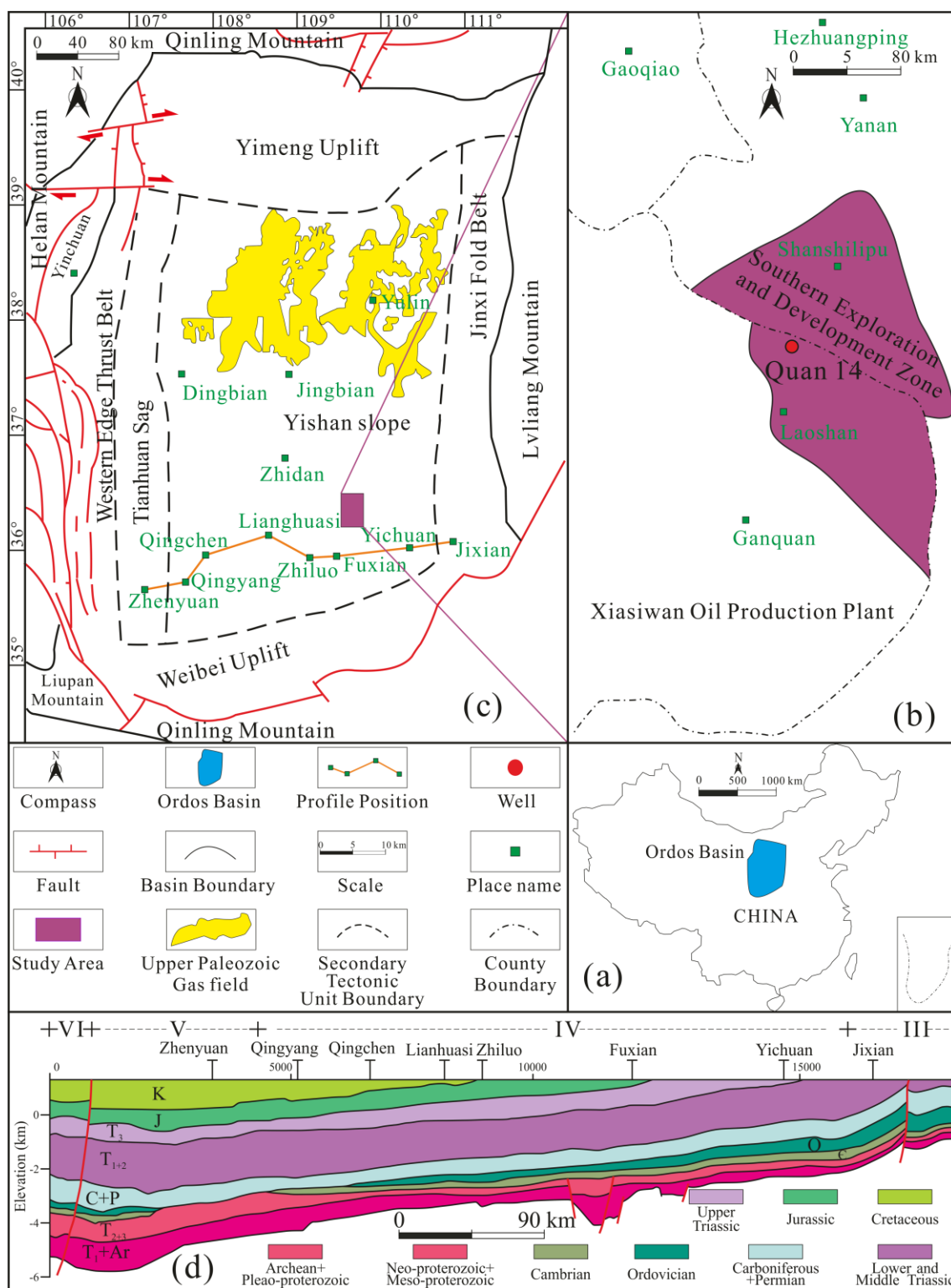
Fig. 2.1. Schematic map showing the location of the Ordos Basin (a), study area (b, the Upper Paleozoic Gas field modified after Yang et al. (2016) and Wu et al. (2017)), sampled well (c, after Xiong et al. (2017)) and a transect (d, modified after Yu et al. (2017)).

In the United States, natural gas production from fine grained rocks, rich in overmature kerogen increased dramatically over the last decade; now more than half of total gas production is derived from such rocks (EIA, 2019, 2020). Usually, the term "shale" is applied, although these rock's lithologies

range from carbonates to siliceous shales (Bustin et al., 2008; Uffmann et al., 2012). China is also an emerging gas producing country with significant potential for shale gas production. For example, in the Sichuan Basin, the Weiyuan-Changning and Fuling marine shale gas fields have reached industrial-scale shale gas production. However, gas-shale plays in China are not only of marine but also of transitional or continental origin (Zou et al., 2010). Examples for such plays are the Palaeozoic shales of the Ordos Basin which are studied here (Fig. 2.1a).

In shales, gas is partly stored as free gas in fractures and pores, partly adsorbed on the surface of OM and clay particles, but also occurs dissolved in kerogen, asphaltenes, residual water and liquid hydrocarbons (Curtis, 2002; Jarvie et al., 2007). It is difficult to distinguish between adsorbed gas and dissolved gas using commonly applied experimental procedures. Hence, the term "sorption" is referred to indicate both adsorbed gas and dissolved gas (Montgomery et al., 2005). The storage capacities of sorbed gas differs in shales, with the sorbed gas accounting for 20%–85% of the total gas (Curtis, 2002). In principle, TOC content, which positively correlates with the increase of micro-porosity in shales, is considered as the main control on methane sorption capacity, since gas is preferentially sorbed in micro-pores due to their great sorption potential and large internal surface areas (e.g. Chalmers and Bustin, 2007; Ross and Bustin, 2007; Gasparik et al., 2014; Yang et al., 2015), whereas the type of OM and its maturity are of less importance (Ross and Bustin, 2009; Zhang et al., 2012). Further, sorption capacity is affected by the content of clay minerals (Ross andBustin, 2007, 2009; Ji et al., 2012; Liu et al., 2013; Fan et al., 2014), micro-nano pore structure, moisture content (Ross and Bustin, 2007; Merkel et al., 2015, 2016; Yang et al., 2017a; Shabani et al., 2018), pressure and temperature conditions (Gasparik et al., 2012; Zhanget al., 2012; Yang et al., 2015) and effective overburden pressure (Gaus et al., 2021).

In this study, Upper Paleozoic shales from the Quan 14 well, drilled in the Southern Exploration and Development Zone (Fig. 2.1b) were sampled and studied by means of elemental analyses, organic petrography, XRD and petrophysical measurements. The major goal of this study is to characterize porosity and sorption capacity of these shales in the context of kerogen quantity, thermal maturity and mineralogy. The results of this study can be used to assess shale gas potential of these rocks under variable temperature and pressure conditions.

2.3 Geological setting

The Ordos Basin is situated in the central part of the North China Plate with an area of 26×10^4 km² (Fig. 2.1a) and is surrounded by the Yin Mountains, Qinling Mountain, Helan Mountains, Liupan Mountain and Lvliang Mountain (Fig. 2.1c) (Yang et al., 2005). The basin can be divided into six structural units (Fig. 2.1c): the eastern Jinxi Fold Belt, the western Tianhuan Sag and the western Edge Thrust Belt, the southern Weibei Uplift, the northern Yimeng Uplift, and the center Yishan Slope (Yang et al., 2016). The basin is a large asymmetric syncline which includes a narrow, steeply dipping western limb and a broad, gently dipping eastern limb, forming an axis in the Tianhuan Sag. The study area is

located in the southeastern Yishan Slope (Fig. 2.1c). Here, the strata are generally dipping below 1° to the west into the basin (Fig. 2.1d).

The evolution of the basin took place during five tectonic-sedimentary stages: (1) rifting stage in the Middle-Late Proterozoic Era; (2) shallow marine platform stage during the Early Paleozoic Era; (3) littoral plain stage in the Late Paleozoic Era; (4) hinterland basin stage during the Mesozoic Era; and (5) peripheral faulted basin in the Cenozoic Era (Yang et al., 2005).

Generally, the study area was a broad, gentle, and west-dipping monocline during the Late Paleozoic period (Ding et al., 2013). During the deposition of the Carboniferous Benxi Formation, an extensive tidal flat-lagoon environment led to the deposition of basal bauxitic mud-stones interbedded with thin limestones and sandstones (Yang et al., 2005, 2017b; Ding et al., 2013). During the Early Permian, the Shanxi Formation developed with peat deposits, shallow-lacustrine mudstones and minor marine carbonates (Yang et al., 2005; Ding et al., 2013).

2.4 Samples
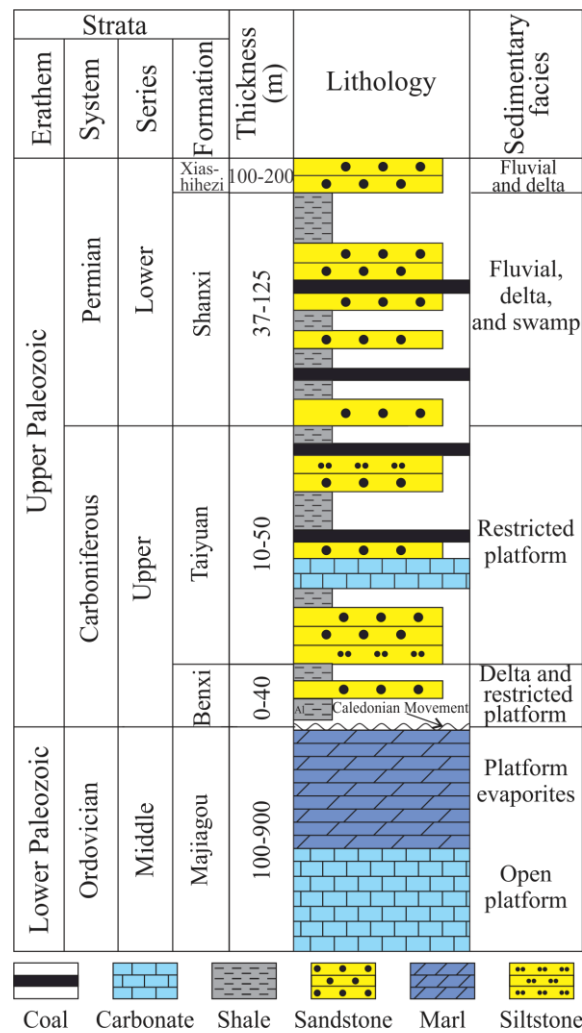
Fig. 2.2. Generalized Paleozoic chrono- and lithostratigraphic chart with corresponding depositional environments of the study area (modified after Ding et al. (2013)).

In order to investigate the effect of lithology on sorption capacity, twelve core samples with great lithologic variation including shales and carbonates from well Quan 14 (Fig. 2.1b) were sampled from the Carboniferous Benxi Formation (3226–3250 m depth) and Permian Shanxi Formation (3160–3176 m depth) (Fig. 2.2).

2.4.1 Benxi Formation

The Benxi Formation is dominated by delta facies as well as restricted platform facies including shelf, lagoon and barrier coast and contains two relatively thin shale layers (cumulative thickness is approximately 30 m) with interbedded thin sandstones in the study area (Ding et al., 2013).

The TOC content of the Benxi Formation ranges between 0.07 and 9.92% (Xiong et al., 2017). The maturity of the Benxi Formation reached over-maturity with vitrinite reflectance (VR_r) ranging from2.44 to 3.12% (Xiong et al., 2017).

The Benxi shales are dominated by clay minerals with mean values of around 67% followed by quartz (mean values are about 22%) and pyrite (Ding et al., 2013; Xiong et al., 2017).

2.4.2 Shanxi Formation

The Shanxi Formation consists of fluvio-deltaic deposits containing two to four sets of grey-black shale with a rather consistent cumulative thickness ranging from 90 to 110 m. These shales are interbedded with thin sandstone, siltstone and coal beds with highly variable TOC contents (Fig. 2.2) (Ding et al., 2013; Yang et al., 2017b).

Throughout the southeastern Yishan Slope, the maturity of the Shanxi Formation is slightly lower than that of the Benxi Formation with VR_r ranging from 2.3 to 3.1% (Ding et al., 2013; Xiong et al., 2017; Yang et al., 2017b).

In terms of mineralogy, the Shanxi Formation shales are mostly composed of clay minerals (mean values are around 60%), followed by quartz with mean values of about 36%, along with smaller amounts of siderite and pyrite (Ding et al., 2013; Xiong et al., 2017; Yang et al.,2017b). Because of the low TOC contents and the grain size, meso-pores and macro-pores rather than micro-pores contribute to the porosity of the Shanxi Formation shales (Xiong et al., 2017; Yang et al., 2017b). Fluvio-deltaic shales are often characterized by grain sizes between 2 and 20 μm, representing fine-grained siltstones rather than claystones (Scheidt and Littke, 1989; Littke et al., 1997).

2.5 Methods

2.5.1 Elemental composition (TOC, TIC and TS)

TOC and inorganic carbon (TIC) contents were measured with a Liqui TOC II analyzer (Elementar Analysen System GmbH, Germany) in one run. About 0.1 g of powder was combusted in an oxygen current in two subsequent heating stages (550 °C for 600 s followed by 1000 °C for 400 s). TOC and TIC contents were assessed by quantifying the amounts of CO_2 released at 550 °C and 1000 °C during this procedure, respectively.

The total sulfur (TS) content was measured using a Leco S 200 sulfur analyzer (precision is < 5% error, detection limit 0.001%).

2.5.2 Organic petrography

VR_r measurement was performed on a Zeiss Axioplan microscope innon-polarized light at a wavelength of 546 nm using a Zeiss Epiplan-Neofluar oil immersion objective (50×) (refraction index ne= 1.518 at 23 °C). A mineral standard of known reflectance was used for calibration. Here, the instrument was calibrated with a gadoli–nium–gallium–garnet (1.72% reflectance) prior to each measurement. Whenever possible, at least 100 vitrinite particles were measured on each sample and the mean random reflectance values were calculated using the DISKUS Fossil software (Technisches Büro Hilgers).

The maceral composition was observed using a Zeiss Axio Imager. M2m microscope and microphotographs were taken with the same instrument. Samples were analyzed in oil immersion with 500× total magnification and Fossil (Hilgers) was used as processing software. Details on preparation of polished samples and microscopic equipment are found in Zieger and Littke (2019).

2.5.3 X-ray diffraction (XRD)

Measurements on randomly oriented powders were performed on a Huber MC9300 diffractometer using Co Kα-radiation (45 kv, 35 mA). During the analysis, an immobile divergence slit (1.8 mm, 1.45°), agraphite monochromator, and 58 mm and 0.3 mm spacing soller slits are used to illuminate the sample. The diffracted beam was measured via a scintillation detector with 0.02° 2θ step size and 20 s step counting time. A scan rate of 2θ/min was used in the testing angle range of 2–76° for recording of diffractograms. Rietveld refinement was used for quantitative phase analysis. BGMN software and customized clay mineral structure models were applied after Ufer et al. (2008).

Powders were prepared by manually grinding sample material in a mortar and milling to a fraction size of less than 200 mesh. After adding 20 wt% of Al_2O_3 as an internal standard, each sample was put into a McCrone Micronising mill for 20 min to assure uniform crystallite sizes. In order to avoid dissolution of water-soluble components and strain damage, milling was done in ethanol.

2.5.4 Porosity and specific pore volume

In this study, porosity (Φ) was determined on irregularly shaped samples by combining grain densities from helium expansion (pycnometry) experiments and bulk densities measured by the buoyancy method (Archimedes method):

$$\Phi = (1 - \frac{\rho_b}{\rho_{gr}}) \quad (2.1)$$

Here, ρ_b (kg/m^3) and ρ_{gr} (kg/m^3) are the bulk and grain densities, respectively.

Samples werefirst cut into irregular shaped blocks with bulk volumes between 5 and 20 cm^3 and dried in a vacuum oven at 105 °C for 24 h to remove moisture and other sorbed fluids. Then, grain densities were measured on a self-costomized He-Pycnometer. Details on the experimental set-up, procedure and evaluation are in detail given by Ghanizadeh et al. (2014).

For the buoyancy method, the dry sample weights md (g) were first measured, then the saturated sample mass mw (g) was determined after evacuating and saturating them with deionized water for more than oneweek. Finally, the immersed weights ms (g) of the saturated samples indeionized water were measured. Based on this, $\rho_b$was calculated with:

$$\rho_b \ = \ \frac{m_d \cdot \rho_w}{m_s - m_w} \ (2.2)$$

Here, ρ_w(0.99 g/cm³) is the density of deionized water at laboratory conditions.

Specific pore volume (SPV) which is pore volume normalized to unitsample mass can be expressed as:

$$SPV \ = \ \frac{V_p}{m_d} \ = \ \frac{1}{\rho_b} \ - \ \frac{1}{\rho_{gr}} (2.3)$$

2.5.5 High-pressure methane sorption experiments

2.5.5.1 High-pressure/temperature manometric sorption setup

A scheme of the manometric setup designed to measure sorption isotherms up to 25 MPa and 120 °C is shown in Fig. 2.3. The used experimental set-ups, calibration, and measuring procedure have been described in detail by Gasparik et al. (2014). The high-pressure/temperature manometric sorption set-up (HPHT) consists of a reference cell (RC) and a sample cell (SC). RC and SC are placed within a low (45 °C) and high-temperature zone (up to 120 °C), respectively, to keep the temperature-sensitive parts offthe high-temperatures. The volumes ofthe RC and SC were calibrated as a function of temperature using tungsten carbide balls with certified volumes.
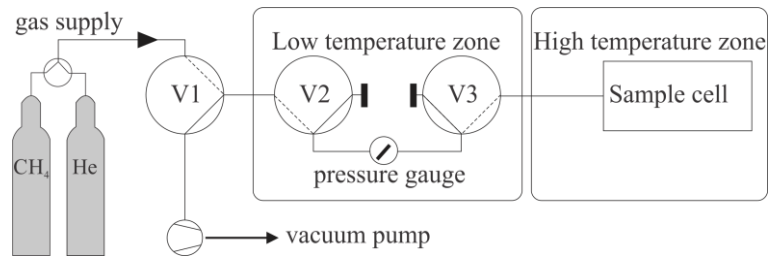
Fig. 2.3. Schematic diagram of the high-pressure/temperature manometric sorption setup (modified after Gasparik et al. (2014)).

2.5.5.2 Methane excess sorption experiments

Methane excess sorption isotherms were measured at 45 °C on 12 powdered samples. Besides, four shale samples were selected from the two formations for experiments at elevated temperatures of 70 °C, 95 °C and 120 °C. Methane of ultra-high purity (99.999%) was used as the sorbate. The procedure consists of the following steps:

1. Drying samples in a vacuum oven at 105 °C for 24 h to remove moisture and other sorbed fluids.

2. Installation of samples in SC.

3. Leak testing (< 5 mbar per hour at 200 bar).

4. Void volume (Vv) calibration with helium used as a non-sorbing reference gas by helium expansion. Vv(m^3) denotes the void volumein the SC. Then the whole setup was evacuated to remove previous helium via the vacuum pump before starting the methane sorption experiment.

5. Methane sorption experiment after evacuation. In a manometric sorption measurement, the excess sorption m$_{excess}$ (also denoted Gibbs surface excess (Sircar, 1999)) is then stepwise calculated from the difference of the total amount of gas transferred into the SC (m$_{transfer}$) and the storage capacity of Vv (non-sorption case):

$$m_{excess} = m_{transfer} - \rho_g(P,T) \cdot V_v \ (2.4)$$

m$_{transfer}$ is a cumulative sum of the volume of the reference cell (V$_r$) multiplied with the gas density difference in the RC before and after expansion into the SC:

$$m_{transfer} = \sum_{j=1}^{n} V_r \ (\rho_{RC}^{j} - \rho_{RC}^{j+1}) \cdot V_r \ (2.5)$$

Helium and methane densities were calculated using the GERG equation of state (Kunz and Wagner, 2012). Results are then presentedin molar units normalized to sample mass (mmol/g).

2.5.5.3 Blank test

A blank test can be used to reduce unknown errors that depend oneach individual device. These errors can originate from systematic errors in the pressure and temperature reading, errors in the equation of state and the calibration (Gasparik et al., 2014). For all setups, blank sorption tests with the measuring gas were performed on non-sorbing tungsten carbide balls at the corresponding temperatures. "Raw" excess sorption isotherms were "blank" corrected by subtracting the "blank" isotherms at an equivalent V$_v$. For details, the reader is referred to Gasparik et al. (2014).

2.5.5.4 Parameterisation of excess sorption isotherms

Excess sorption isotherms werefitted with a 3-parameter Langmuir-type model:

$$n_{excess}(P,T) = n_{\infty} \cdot \frac{P}{P + P_L(T)} \cdot \left(1 - \frac{\rho_g(P,T)}{\rho_a}\right) (2.6)$$

Here n$_{excess}$ (mmol/g) corresponds to the excess sorbed amount at a given T (K) and P (MPa). n$_{\infty}$ (mmol/g) represents the Langmuir methane sorption capacity at full occupancy of all sorption sites (infinite pressure) and P$_L$ (MPa) denotes the Langmuir pressure at which half the sorption capacity is reached. ρ_g (kg/m^3) and ρ_a (kg/m^3) are the free and sorbed phase densities of methane, respectively.

2.5.5.5 Thermodynamics of methane sorption

For constant absolute sorption, the relationship between required equilibrium P and sorption T can be used to calculate its thermodynamic parameters including ΔH (molar enthalpy), ΔS (molar entropy) and Q$_{st}$ (isoteric heat) according to equation 2.7.

$$\ln(P_L) = \frac{\Delta H}{R \cdot T} - \frac{\Delta S}{R} + \ln(P^0) = -\frac{Q_{st}}{R \cdot T} - \frac{\Delta S}{R} + \ln(P^0) (2.7)$$

here P^0, taken as 0.1 MPa, is the pressure at the perfect-gas reference state (Myers and Monson, 2002), ΔH (-Qst) and ΔS are determined from the slope and the y-axis intercept values of regression line on the plot of ln(P) versus 1/T, respectively (Zhang et al., 2012).

4.5.6 Calculation of total gas and free gas storage capacity

Gas storage capacity estimates of shale need to consider free and sorbed gas. For high-pressure gas sorption, it is important to realize that the sorbed phase occupies a non-negligible volume. There are two ways of considering the gas stored in the sorbed volume Vsin gas storage calculations: (1) by subtracting V_s from the pore volume or (2) by subtracting the gas stored in V_s (at the free gas pressure) from the absolute sorbed amount (Gasparik et al., 2015). With this, it becomes evident that one has to precisely define free and sorbed gas, which historically leads to some confusion. The main problem in approach (2.1) is in the usage of the absolute sorption n_a:

$$n_{\text{total}} = n_a + n_{\text{free}} \quad (2.8)$$

Here, the free gas storage capacity n_{free} is equal to the bulk methane density multiplied by the pore volume and subtracting it by the volume of the sorbed phase. However, on a molecular scale there is no sharp boundary between the densities of the free and sorbed gas phase because the gas is supercritical (Sakurovs et al., 2008). Moreover, the absolute sorption and the sorbed volume cannot be derived experimentally in high-pressure sorption experiments and need to be estimated using an unknown sorbed phase density (Krooss et al., 2002).

However, the total gas storage capacity can be derived in a simplerway using approach (2.2) based on the Gibbs definition as the sum of the excess sorbed storage capacity and a product of the entire pore volumeof the shale with the bulk gas phase density. This is practical as allparameters (SPV and excess sorption capacity) are directly measurable.

$$n_{\text{total}} = n_{\text{pore}} + n_{\text{excess}} = SPV \cdot \rho_g (P, T) + n_{\text{excess}} \quad (2.9)$$

Gas storage capacities can be transformed into various units and the conversions are given in the Appendix.

In this definition, sorption is expressed as the amount of gas that can be stored in excess of the storage capacity of a sample with no sorption. This approach highlights also that it is not possible to distinguish between "free" and "sorbed" gas as in practice as each individual gas molecule can continuously transform from a gaseous "free" into asorbed state and vice versa.

Gas storage capacity estimates based on dry data are maximum values as partial water saturation decreases both, the excess sorption and pore volume (Gasparik et al., 2014; Bruns et al., 2016; Shabaniet al., 2018). Therefore, the water saturation is a critical control that needs to be assessed independently. Moreover, over burden stress will additionally decrease the excess sorption capacity and pore volume of gas shales (Fink et al., 2018; Gaus et al., 2021).

2.6 Results

2.6.1 Mineralogy and organic petrology

TOC contents of the Shanxi Formation range from 0.77 to 1.98% and of the Benxi Formation from 0.06 to 2.25% (Table 2.1). TS contents are < 0.25% in the Shanxi Formation and significantly larger with up to 10.6% in the Benxi Formation.

Table 2.1. Total organic and inorganic carbon (TOC, TIC), total sulphur content (TS), vitrinite reflectance (VR_r), grain and bulk densities (ρ_{gr} based on He-pycnometry and ρ_b based on Archimedes), SPV (specific pore volume), for samples from well Quan 14.

Fm.	Sample ID	Depth (m)	TOC (%)	TIC (%)	TS (%)	VR_r (%)	ρ_{gr} (kg/m^3)	ρ_b (kg/m^3)	SPV (m^3/kg)
Shanxi	S-1	3161.20	0.82	0.01	0.07	2.49	2695	2527	$2.47 \cdot 10^{-5}$
	S-2	3161.56	1.97	0.02	0.21	2.35	2722	2530	$2.79 \cdot 10^{-5}$
	S-3	3162.45	1.38	0.02	0.09	2.40	2737	2583	$2.18 \cdot 10^{-5}$
	S-4	3164.78	1.89	0.02	0.07	2.51	2689	2516	$2.56 \cdot 10^{-5}$
	S-5	3175.45	0.77	0.07	0.06	2.42	2768	2629	$1.91 \cdot 10^{-5}$
	S-6	3176.09	1.06	1.23	0.06	2.37	2777	2665	$1.51 \cdot 10^{-5}$
Benxi	B-1	3228.43	0.88	0.03	0.19	2.71	2706	2522	$2.70 \cdot 10^{-5}$
	B-2	3230.87	0.57	0.02	0.13	2.61	2760	2549	$3.00 \cdot 10^{-5}$
	B-3	3232.45	2.25	7.22	10.59	2.52	2751	2737	$1.87 \cdot 10^{-6}$
	B-4	3243.85	1.61	11.11	1.10	2.41	2694	2673	$2.99 \cdot 10^{-6}$
	B-5	3245.87	0.06	0.02	1.26	2.97	2784	2674	$1.48 \cdot 10^{-5}$
	B-6	3246.87	1.47	0.02	0.74	2.60	2740	2585	$2.19 \cdot 10^{-5}$

Table 2.2. Mineralogy based on XRD measurements. Qua – Quartz; Fel – Feldspar group kaolinite; Cal – Calcite; Dol/Ank – Dolomite/Ankerite; Siderite – Sid; Car – Carbonates (Cal + D/A + S); Kao – Kaolinite; Chl – Chlorite; I/S – Illite-smectite mixed layer; C – Clay minerals (Kao + Chl + I/S); Hal – Halite; Pyr – Pyrite; Ana – Anatase; Ver – Vermiculite; others (Hal + Pyr + Ana + Ver).

Sample ID	Qua	Fel	Qua+Fel	Cal	Dol/Ank	Sid	Car	Kao	Chl	I/S	C	Hal	Pyr	Ana	Ver	Others
S-1	27	1	**29**					8	3	58	**70**			1		**1**
S-2	28	2	**30**					7	4	58	**69**			1		**1**
S-3	27	2	**29**					5	2	64	**70**			1		**1**
S-4	29	4	**32**					5	3	58	**66**			1		**1**
S-5	43	7	**50**			5	5	1	2	41	**44**			1		**1**
S-6	37	3	**40**	7	4	7	18	0	2	41	**42**			0		**0**
B-1	15	3	**17**			1	1	36	2	42	**80**			2		**2**
B-2	14	3	**16**			3	3	35	2	43	**79**			2		**2**
B-3	1		**1**	95	1		97		0	0			2			**2**
B-4	0		**0**	94			94	4	0	0	**4**		2			**2**
B-5	23	3	**26**					47	4	19	**70**		2	2		**4**
B-6	1	3	**5**			9	9	57	0	21	**77**	1	1	2	5	**9**
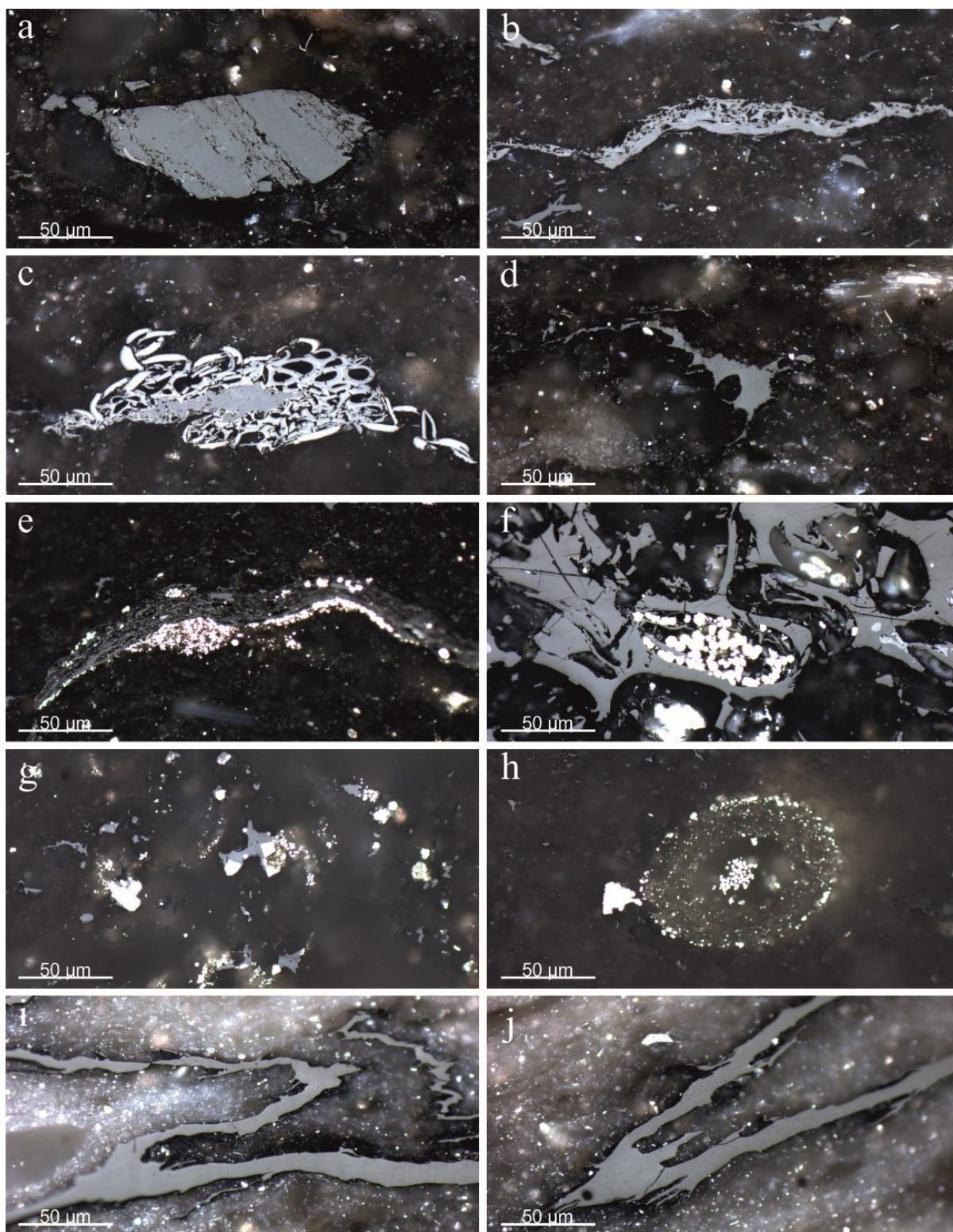
Fig. 2.4. Microscopic observations of identified macerals in the Shanxi (a-c) and Benxi (d-i) formations. Vitrinite and inertinite particles (a), semifusinite and fusinite (b, c), solid bitumen in intergranular spaces (d), structured inertinite and vitrinite (e, f), solid bitumen in intergranular spaces, and partly replaced by secondary, euhedral pyrite (g), framboidal pyrite aggregates and large isolated euhedral pyrite crystals or as small crystals within fossil structures (e, f, g, h). Vitrinite-like structures (possibly rootlets) with several mm length (i, j).

Samples S-1 to S-4 from the Shanxi Formation are silica-rich argillaceous mudstones with clay contents between 66 and 70% and quartz contents between 29 and 32% whereas samples S-5 and S-6 are silicious-argillaceous mudstones with significantly lower clay content around 43%, higher quartz content and a significant fraction of carbonates (Table 2.2). For all Shanxi shales, illite/smectite (I/S) mixed layer is the dominant clay mineral phase.

The Benxi shales can be subdivided into a silica-rich argillaceous (B-1, B-2, B-3, B-6) and carbonate dominated lithotype (B-4, B-5; carbonate content > 94%). Compared to the Shanxi Formation, the silica-rich argillaceous shales have even higher clay (70–80%) and smaller quartz contents (1–15%). Moreover, clay mineralogy significantly differs compared to the Shanxi shales with increased kaolinite content between 35 and 57% (Table 2.2).
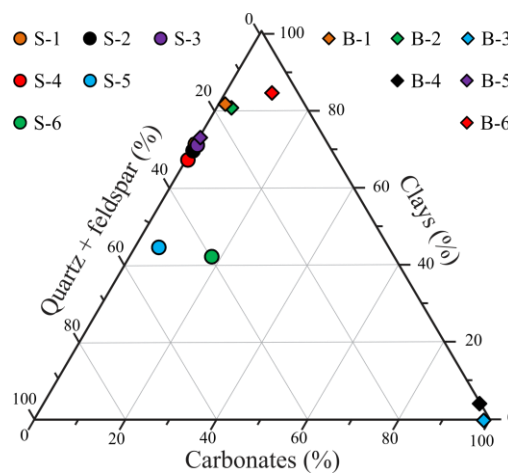
Fig. 2.5. Ternary diagram illustrating the normalized mineralogical composition for the samples from the Shanxi Formation and Benxi Formation in the Ordos Basin. Mineralogy is normalized to quartz + feldspar, clays (kaolinite, mixed layer illite-smectite, and chlorite) and carbonates (calcite, dolomite and siderite).

VR_r of the shales from the Shanxi Formation varies between 2.35 and 2.51% among the samples with an average value of 2.43%. With values ranging from 2.41 to 2.97% (mean = 2.64%) in the Benxi Formation, variance among samples is higher (Table 2.1). OM in shales from the Shanxi Formation is characterized by abundant vitrinite and inertinite particles, and even coal fragments (Fig. 2.4a). Structured inertinite such as semifusinite and fusinite (Fig. 2.4b and c) is common. Pyrite is less abundant as compared to the Benxi Formation samples, which is also supported by the XRD data (Table 2.2, Fig. 2.5). Pyrite is most often represented by small euhedral crystals. Solid bitumen can also be observed in intergranular spaces (Fig. 2.4d). Besides structured inertinite and vitrinite (Fig. 2.4e and f), the Benxi shales show solid bitumen in intergranular spaces, in some cases partly replaced by secondary, euhedral pyrite (Fig. 2.4g). The in some cases high TS values (Table 2.1) are mirrored by the presence of either framboidal pyrite aggregates and large isolated euhedral pyrite crystals or as small crystals within fossil structures (Fig. 2.4e, f, g and h). Sample B-6 shows several mm long vitrinite-like structures that presumably represent rootlets (Fig. 2.4i and j).

2.6.2 Porosity and SPV

The ρ_{gr} and ρ_b values as well as porosities of the samples are listed in Table 2.1. The porosity of the Shanxi Formation samples ranges from 4.1 to 7.1%, and of the Benxi Formation samples from 0.5 to 7.7% (Table 2.3). The ρ_{gr} ranges from 2689 to 2777 kg/m^3 for the Shanxi Formation and between 2694 and 2784 kg/m^3 for the Benxi Formation. The SPV values of the Shanxi Formation are between $1.51 \cdot 10^{-5}$ and $2.79 \cdot 10^{-5}$ m^3/kg, and of the Benxi Formation between $1.87 \cdot 10^{-6}$ and $3.00 \cdot 10^{-5}$ m^3/kg.

Table 2.3. Results of porosity and methane high-pressure sorption measurements on shale samples from the Shanxi and Benxi formations (45 ℃).

Fm.	Sample ID	Porosity (%)	Maximum n_{excess} (mmol/g rock)	3-parameter Langmuir-type model		
				n_∞ (mmol/g rock)	P_L (MPa)	ρ_a (kg/m^3)
Shanxi	S-1	6.2	0.048	0.10	7.2	345
	S-2	7.1	0.058	0.11	5.0	363
	S-3	5.6	0.057	0.11	5.7	370
	S-4	6.4	0.068	0.12	4.5	393
	S-5	5.0	0.034	0.07	6.7	367
	S-6	4.1	0.029	0.06	7.8	320
Benxi	B-1	6.8	0.057	0.12	7.2	335
	B-2	7.7	0.055	0.12	7.6	322
	B-3	0.5	0.007	0.01	4.4	371
	B-4	0.8	0.027	0.04	2.7	347
	B-5	3.9	0.026	0.06	8.4	332
	B-6	5.7	0.047	0.10	7.5	321

2.6.3 High-pressure excess methane sorption isotherms
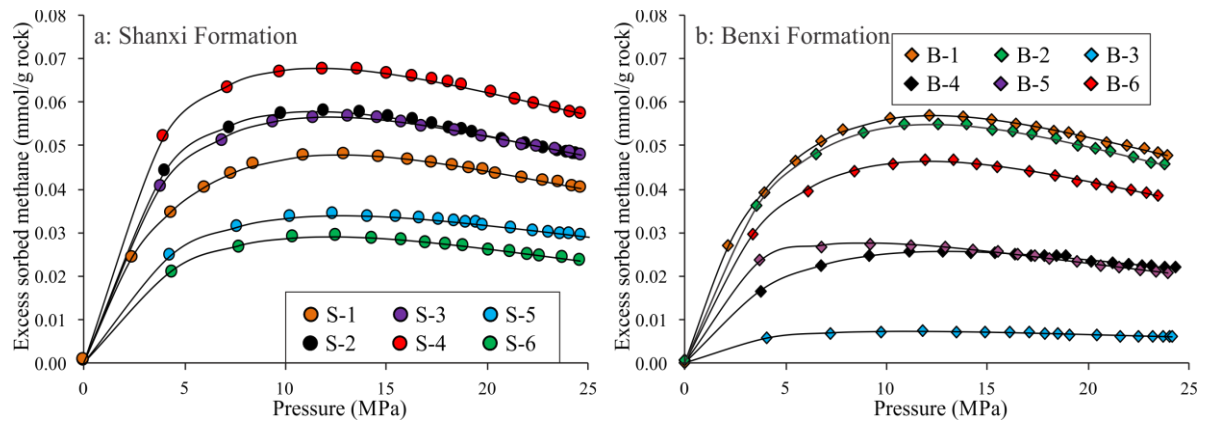
Fig. 2.6. Methane excess sorption isotherms at 45 °C for samples from the Shanxi (a) and Benxi (b) formation.

High-pressure excess methane sorption isotherms (45 °C) (Fig. 2.6) illustrate a large variety of sorption capacities with a maximum mostly at approximately 10 MPa.

Sorption parameters fitted with the 3-parameter Langmuir-type model are listed in Table 2.3. For the samples from the Shanxi Formation, the fitted values of n_∞ for the isotherms at 45 °C range from 0.06 to 0.12 mmol/g rock (Table 2.3); fitted ρ_a values are in the range of 320–393 kg/m^3; fitted Langmuir

29

pressures values range from 4.5 to 7.8 MPa; and the maximum n_{excess} values vary from 0.029 to 0.068 mmol/g rock. For the samples from Benxi Formation, the fitted n_∞ values for the isotherms at 45 °C range from 0.01 to 0.12 mmol/grock (Table 2.3); the fitted ρ_a values are in the range of 321–371 kg/m³, quite consistent with the values of the Shanxi Formation; the fitted Langmuir pressure values vary from 2.7 to 8.4 MPa; and the maximum n_{excess} values vary between 0.007 and 0.057 mmol/g rock.
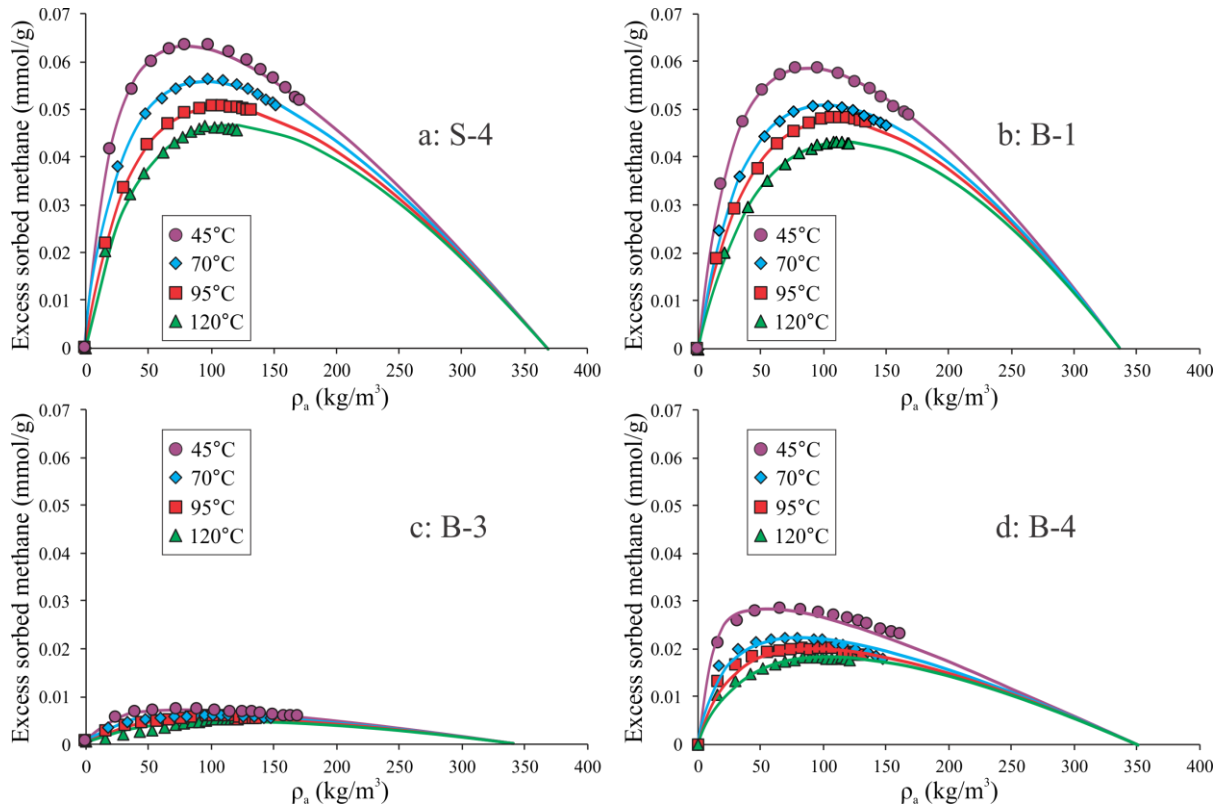
Fig. 2.7. Excess sorption isotherms for selected samples from the Shanxi and Benxi formations of the southeastern Ordos Basin measured at temperatures from 45 to 120 °C.

From the 12 samples measured at 45 °C four end-member samples with the highest and lowest sorption capacities were selected for the high temperature measurements. The maxima of the excess isotherms of He samples show the typically decreasing trend of excess sorption capacity and increasing trend of pronounced maxima pressure with increasing temperature (Fig. 2.7). The pronounced excess sorption maxima occur at pressures between 9.68 and 12.89 MPa at 45 °C and increase to values between 21.57 and 24.91 MPa at 120 °C. Here, the excess sorption maxima at these pressures decreased between 0.002 mmol/g (B-3) and 0.017 mmol/g (S-4) (Table 2.4).

Langmuir parameters for the selected samples are shown in Table 2.4. All parameters were obtained for one sample by simultaneously fitting the 3-parameter Langmuir-based excess sorption function to all four isotherms measured at different temperatures (Gasparik et al., 2015).

Table 2.4. Results from high-pressure methane sorption measurements at 45 to 120 °C on four selected samples. ΔH and ΔS are molar enthalpy and entropy, respectively.

Sample ID	Temperature (°C)	Maximum n_{excess} (mmol/g rock)	Corresponding pressure of Maximum n_{excess} (MPa)	3-parameter Langmuir model				
				n_∞ (mmol/g rock)	P_L (MPa)	ρ_a (kg/m³)	ΔS (J/mol/K)	ΔH (KJ/mol)
S-4	45	0.063	11.56		5.2			
	70	0.056	15.68		8.8			
	95	0.051	19.78	0.12	12.5	369	-84.00	-16.23
	120	0.046	21.57		16.6			
B-1	45	0.058	11.33		7.7			
	70	0.051	16.82		12.4			
	95	0.048	21.65	0.13	15.9	336	-80.74	-14.12
	120	0.043	24.91		21.9			
B-3	45	0.007	12.89		4.9			
	70	0.006	17.45		9.1			
	95	0.006	20.88	0.01	13.0	340	-91.46	-18.62
	120	0.005	23.95		20.0			
B-4	45	0.028	9.68		2.1			
	70	0.022	12.79		6.0			
	95	0.020	17.42	0.04	9.1	350	-104.22	-24.69
	120	0.018	22.99		13.1			

2.7 Discussion

2.7.1 Thermal maturity and depositional conditions

At high levels of sedimentary diagenesis, VR_r is probably the best and most widely used parameter for thermal maturity, because most organic geochemical parameters cannot be applied. VR_r values measured on our sample set are similar to those reported before on both the Shanxi and Benxi formations, which have reached the dry gas petroleum generation stage. TOC values are variable, but partly smaller than reported before (Yang et al., 2016, 2017b; Xiong et al., 2017), which might be related to the location of well Quan 14 at a marginal position on the southeastern Yishan slope.

Both in terms of lithology and mineral content, rocks show strong variability, related to variable depositional settings. This fact is also reflected by highly variable TS contents. In paralic environments, freshwater with little sulfate predominates, but from time to time, transgressive intrusion of seawater provides a massive source of sulfur, while abundant metal ions (in particular iron) and terrestrial OM can be provided by the terrestrial environment, leading to precipitation of iron sulfides as soon as reducing conditions are established in the pore water. Generally, the stronger the intrusion of seawater, the higher the TS content in shales. The processes and depth ranges of microbial sulfate reduction as well as its influence on OM quality have been described in Berner (1984) and Lückge et al. (1999) in great detail. The ratio of TOC to TS can be used to distinguish marine mudstones (0.5 < TOC/TS < 5) and non-marine water-bottom environments (TOC/TS > 10) (Berner, 1984). The values of TOC/TS of

the samples studied cover a wide range and indicate the shift from marine to terrigenous environments as well (Fig. 2.8).
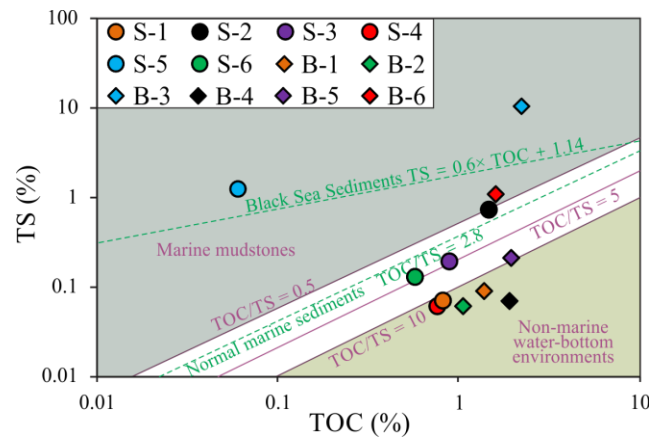
Fig. 2.8. Total sulfur (TS) vs. total organic carbon (TOC) indicating environments of deposition of the Shanxi and Benxi formations of the southeastern Ordos Basin, China.

The observation of abundant vitrinite and inertinite particles, and even coal fragments and roots (Fig. 2.4a, e and f), indicates the terrestrial origin of most OM. This material certainly represents a former type III kerogen, now strongly converted towards carbon-rich residues, which is consistent with conclusions from previous studies (Yang et al., 2016, 2017b; Xiong et al., 2017).

While most samples have a high content of clay minerals, samples B-3 and B-4 show high contents of carbonate. These samples also have low TOC/TS ratios indicating a marine depositional environment. For our sample set, strong marine influence is indicated for Benxi Formation (in agreement with e.g. Ding et al. (2013) and Xiong et al.(2013)) see also Fig. 2.2), but not for Shanxi Formation where the studied samples do not show any marine influence. Clay minerals are clearly dominated by I/S mixed layer in Shanxi Formation, while Benxi Formation shales are characterized by a mixture of both I/S mixed layer and kaolinite. This non-uniform distribution of clay minerals is consistent with previously published data (Ding et al., 2013; Yang et al., 2016, 2017b; Xiong et al., 2017).

2.7.2 Mineralogical controls on porosity and methane sorption capacity

For the Shanxi and Benxi shales there is no relationship between TOC content and porosity (Fig. 2.9a). OM is usually not the controlling factor of porosity when TOC content is less than 2.0% (Ghanizadeh et al., 2015; Chukwuma et al., 2018; Fink et al., 2018). In theory, the evolution of porosity with maturity in OM-rich shales follows a non-linear, trough-shaped path that is primarily controlled by compaction, hydrocarbon generation and development of organic porosity during secondary cracking in the over-mature stage (Mastalerz et al., 2013). For Benxi and Shanxi shales, porosity and the total clays for the studied samples show a good correlation indicating that most of the pores reside within the clay fraction (Fig. 2.9a) (see also Yang et al., 2016; Xiong et al., 2017; Yang et al., 2017b).
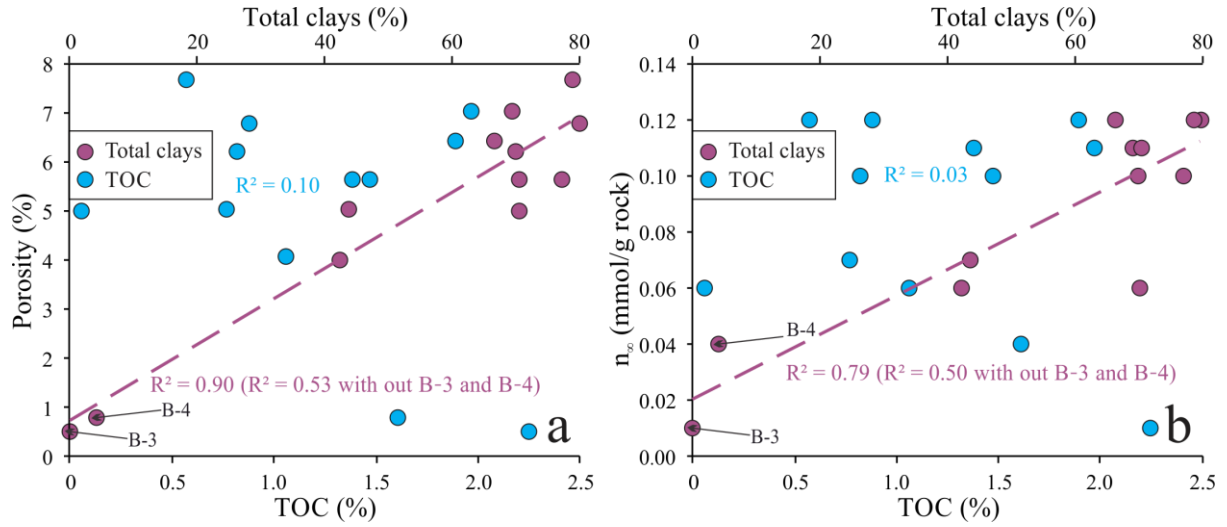
Fig. 2.9. Total organic carbon (TOC) and total clays as a function of porosity (a) andas a function of Langmuir sorption capacity (b).

For many organic-rich shale lithologies, Langmuir sorption capacity is controlled by TOC content due to its high micro-porosity that pro-vides abundant surface area and sorption sides (Chalmers and Bustin, 2008). In our dataset, there is no relationship between TOC content and Langmuir sorption capacity (Fig. 2.9b). This suggests that TOC content is not the main factor controlling Langmuir sorption capacity of Benxi and Shanxi shales where the overall TOC content is low. Clay minerals can possess comparatively large Langmuir sorption capacities with a rough order of smectite > I/S mixed layer ≥ kaolinite > chlorite ≥ illite (Table 2.5, Ji et al., 2012; Liu et al., 2013; Fan et al., 2014). Smectite content in over-mature gas shales is usually negligible as it is converted to illite and I/S mixed layer with increasing temperatures during diagenesis at depths exceeding 1600–2600 m (Chen et al., 2009) and temperatures exceeding 60–120 °C (Lindgren et al., 1991; Strixrude and Peacor, 2002; Peltonen et al., 2009). Both I/S mixed layer and kaolinite are abundant in Benxi and Shanxi shales, and sorption capacity is positively related to clay content (Fig. 2.9b).

To assess the contribution of clays (I/S mixed layer, kaolinite) and organics to sorption capacity/porosity a linear combination approach was used to predict the Langmuir sorption capacity/SPV of each individual mineral constituent. The Langmuir sorption capacity/SPV is expressed as the sum of the individual components on a mass-fraction base (Yang et al., 2015):

$$n_\infty = \sum_{i=1}^{n} n_i\, w_i\ (i = 1,2,3,\dots,n)\ (2.10)$$

$$\Phi = \sum_{i=1}^{n} \rho_{bulk}\, SPV_i\, w_i\ (i = 1,2,3,\dots,n)\ (2.11)$$

Here w_i is the mass fraction, n_i the Langmuir sorption capacity andthe product of both the Langmuir sorption capacity of the sample. The calculation of porosity can only be performed on a mass basis of the individual component as the volume fractions are unknown. Therefore, we use the specific pore volume of each individual component (SPV_i).With this, similar to sorption the contribution of an individual fraction to porosity can be obtained by multiplying the contribution of the SPVwith the samples bulk density.

Table 2.5. Value of Langmuir sorption capacity of individual clay minerals and isolated kerogen.

Variable	Value (mmol/g)	References
Type I kerogen	1.140	
Type II kerogen	1.210	Zhang et al. (2012)
Type III kerogen	1.400	
Smectite	0.380	Ji et al. (2012)
	0.268	Liu et al. (2013)
	0.179	Fan et al. (2014)
I-S mixed layer	0.182	Ji et al. (2012)
	0.138	Fan et al. (2014)
Kaolinite	0.120	Ji et al. (2012)
	0.173	Liu et al. (2013)
	0.155	Fan et al. (2014)
Illite	0.080	Ji et al. (2012)
	0.099	Liu et al. (2013)
	0.154	Fan et al. (2014)
Chlorite	0.100	Ji et al. (2012)
	0.039	Fan et al. (2014)

Considering for Benxi and Shanxi shales that TOC, I/S mixed layerand kaolinite are the main contributors, the following equations are obtained:

$$n_\infty = n_{TOC} \cdot w_{TOC} + n_{I/S} \cdot w_{I/S} + n_{Kaolinite} \cdot w_{Kaolinite} + 0 \cdot w_{Framework} \quad (2.12)$$

$$\Phi = \rho_{bulk} \cdot \left(w_{TOC} \cdot SPV_{TOC} + w_{I/S} \cdot SPV_{I/S} + w_{Kaolinite} \cdot \overline{S}_{Kaolinite} + 0 \cdot w_{Framework} \right) \quad (2.13)$$

Here W_{OM}, $W_{I/S}$, and $W_{Kaolinite}$are the mass fractions of OM, I/S mixed layer, and kaolinite, respectively, n_{TOC}, $n_{I/S}$, and $n_{Kaolinite}$ (mmol/g) are the sorption capacity of OM, I/S mixed layer, and kaolinite, respectively, and SPV_{TOC}, $SPV_{I/S}$, and $SPV_{Kaolinite}$ (cm^3/g) are the SPV of OM, I/S mixed layer, and kaolinite, respectively.

We use linear regression analysis to minimize the Langmuir sorption capacity/porosity of the calculated values with the measured values simultaneously for the whole sample set. With this, the Langmuir sorption capacity/SPV of each component can be determined by using them as a fitting factor. The approach is able to match the measured data reasonably well (Fig. 2.10a and b). The resulting SPV is 0.081 cm^3/g for TOC, 0.036 cm^3/g for I/S mixed layer and 0.026 cm^3/g for kaolinite. Except for the carbonates (B-3 and B-4), which have almost no porosity, porosity is controlled by the clay minerals where more than 90% of the pore volume occurs (Fig. 2.10c). This shows that OM, in contrast to other shale systems, has a negligible effect on the volumetric gas storage in Benxi and Shanxi shales.
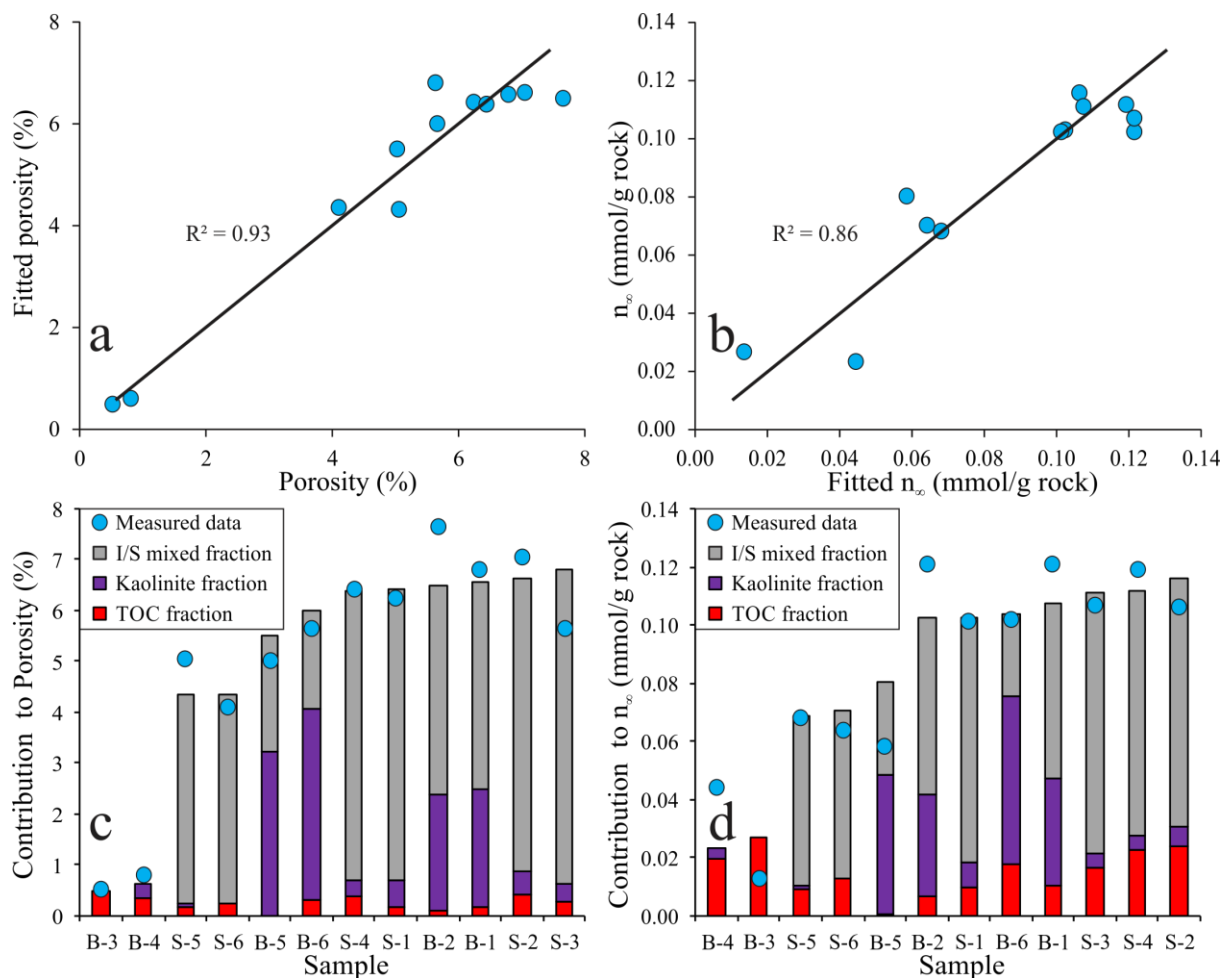
Fig. 2.10. Fitted porosity (a) and Langmuir sorption capacity (b) values (n_∞) using a linear combination approach vs. measured values, and the overall contribution of individual components (c and d).

Similarly, the obtained Langmuir sorption capacities match the measured values reasonably well and we obtained 1.20 mmol/g for TOC, 0.14 mmol/g for I/S mixed layer and 0.10 mmol/g for kaolinite. Our Langmuir sorption capacities of TOC are close to the sorption capacity of isolated kerogen (between 1.14 and 1.4 mmol/g) measured by Zhang et al. (2012). For the clay minerals, they are in good agreement with results from measurements on pure clay minerals (Illite and I/S mixed layer between 0.08 and 0.18 mmol/g, kaolinite between 0.12 and 0.17 mmol/g) (Table 2.5). Sorptive storage in Benxi and Shanxishales mostly occurs in the clay fraction with 80–99% of the overallsorption capacity (excluding the carbonates). In all clay-rich shales, organics contribute very little with less than 20% (Fig. 2.10d).

Compared to other over-mature ($VR_r > 1.3\%$) shale formations Benxi and Shanxi shales possess comparatively low sorption capacities (< 0.13 mmol/g) due to their low TOC content (Fig. 2.11a). Although the high clay content increases the sorption capacity in comparison to other organic-lean shales (< 2.5% TOC), organic-rich shales possess significantly larger sorption capacities resulting in an overall positive trend between TOC content and Langmuir sorption capacity.
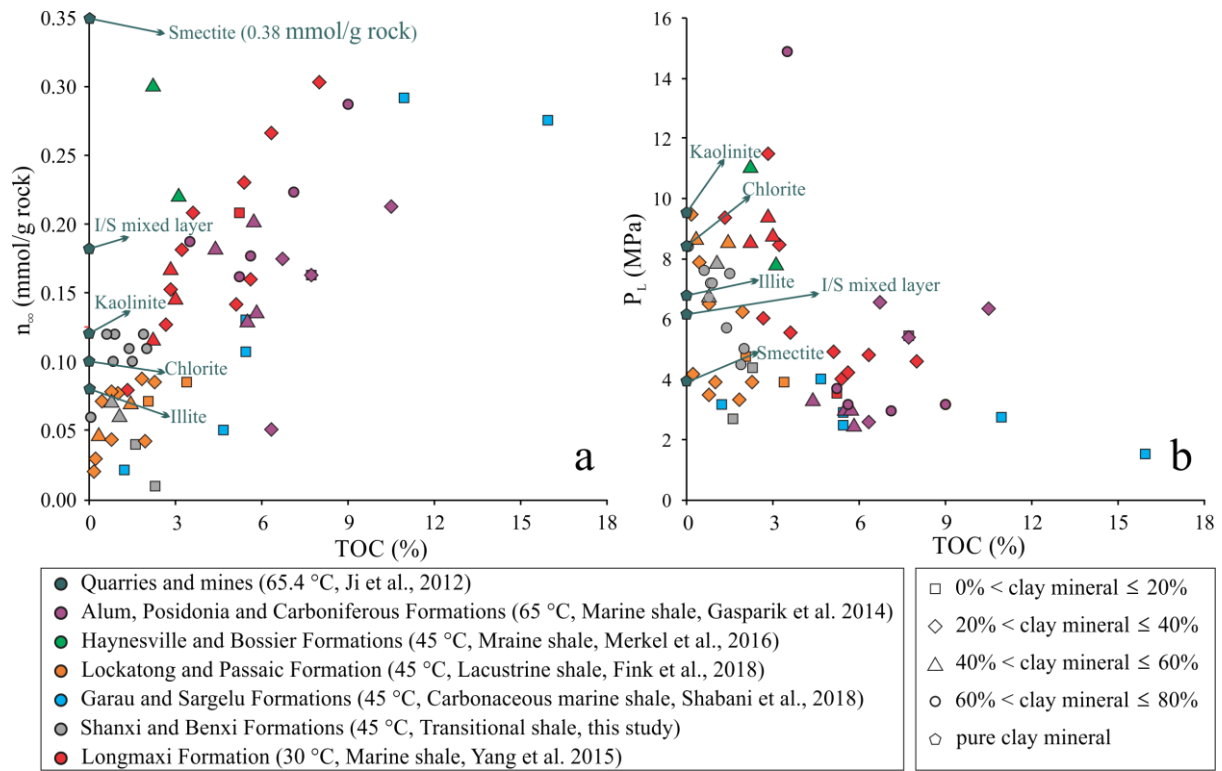
Fig. 2.11. Comparison of sorption capacity (a) and Langmuir pressure (b) of Benxi and Shanxi shales with over-mature (VR$_r$ > 1.3%) lacustrine and marine shales. All data was measured at dry condition between 30 °C and 65.4 °C.

Langmuir pressures of overmature shales range mostly between 2 and 10 MPa at laboratory conditions (dry condition, 30 °C–65.4 °C) (Fig. 2.11b). The scatter in P$_L$ values is very large below 4% TOC and significantly decreases with increasing TOC. The reason is presumably that at low TOC contents the P$_L$ values result from sorption on strongly varying mixtures of clay minerals and organics. Here, samples with relatively high organic and low clay mineral content have tentatively lower P$_L$ values and vice versa (Fig. 2.11b) as the P$_L$ values of pure clays issignificantly larger compared to pure organics.

2.7.3 Effect of temperature

Thermodynamic parameters describing the sorption process can beobtained by analyzing the temperature dependence of the P$_L$ based onequation (7) (Fig. 2.12). Sorption entropy ΔS varies from −14.12 to −24.69 kJ/mol and isosteric heat ΔH from −80.74 to −104.22 J/mol/K (Table 2.4). A linear relationship exists between the ΔH and ΔS (Fig. 2.13) which is caused by the nature of physical (Van-der-Waals) bonding of the gas and the solid (Gasparik et al., 2013). Compared to previously published data on pure clays and kerogen (Ji et al., 2012;Zhang et al.,2012; Rexer et al., 2014), Benxi and Shanxi shales plot between type III kerogen and I/S mixed layer. The thermodynamic parameters closely resemble the mineralogy of the samples. Samples where sorption is dominated by I/S mixed layer and kaolinite plot close to the pure clays whereas samples with little clay mineral content show thermodynamic properties of kerogen type II and III (Fig. 2.13).
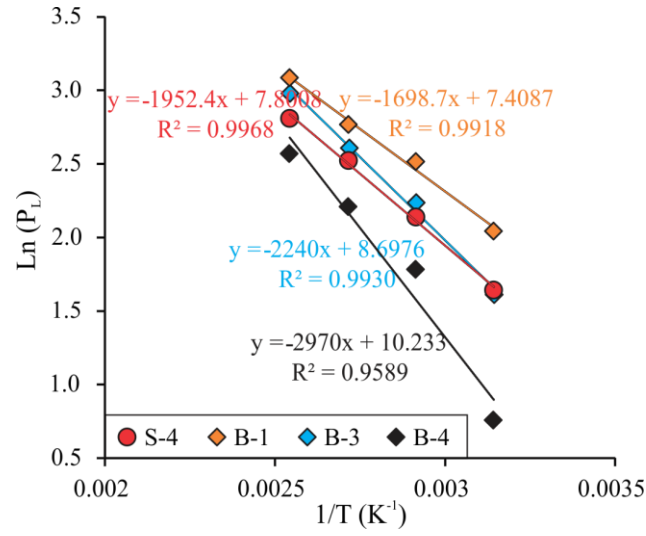
Fig. 2.12. Determination of sorption enthalpy and entropy of the selected shale samples from the Shanxi and Benxi Formations.
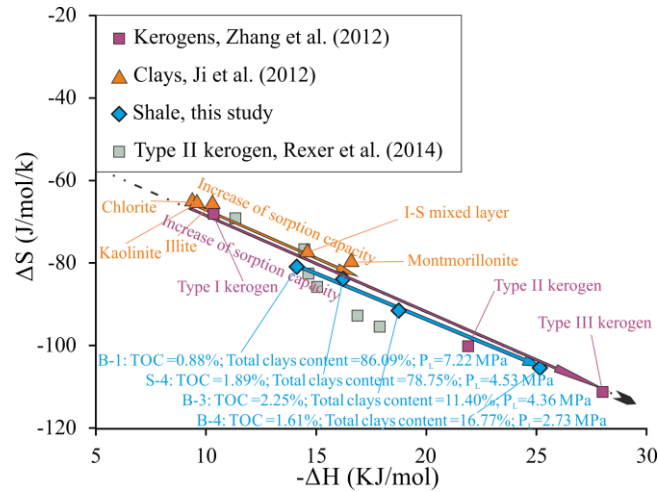
Fig. 2.13. Plot of isosteric heat vs. molar entropy for the selected samples from the Shanxi and Benxi formations of the southeastern Ordos Basin and for the pure clay minerals as well as kerogens.

2.7.4 Gas storage capacity

2.7.4.1 Depth-dependence of gas storage capacity

Sorption capacity, free gas storage capacity and total gas storagecapacity at a certain depth can be estimated by equation (9). Here, it is considered that the shales are dry (0% water saturation), the formationis over consolidated and uplifted to the current depth with no changes inporosity. Moreover, we use a surface temperature of 15 °C and a geo-thermal gradient of 2.8 °C/100 m based on data fromYu et al. (2017).

Gas storage capacity increases with depth up to 0.32 mmol/g for sample S-4, which possesses the largest storage capacity among the Benxi and Shanxi samples (Fig. 2.14). At shallow depths, the excess sorbed gas storage generally dominates the total storage capacity of Benxi and Shanxi shales, whereas

the free storage capacity become sincreasingly important with depth. For all samples, the excess sorbed gas storage capacity decreases after it reaches its maximum value (< 1000m), and the corresponding depth of the maximum of the sorbedgas storage capacity is positively related to the $P_L$value.
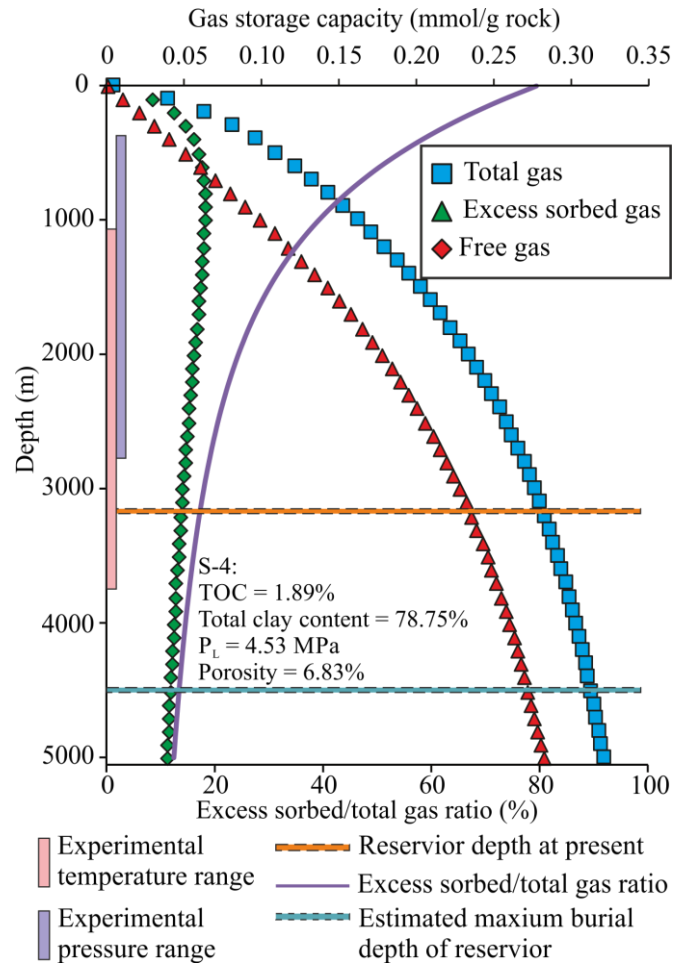
Fig. 2.14. Excess sorbed, free and total gas storage capacity and excess sorbed/total gas ratio as a function of depth. Depth trends are exemplarily shown on the basis of the sample possessing the largest sorption capacity (S-4).

Maximum burial of the Shanxi and Benxi shales in the study area occurred in the Middle Cretaceous (Yu et al., 2017) where they were buried to a depth of up to 5000 m and experienced temperatures up to 140 °C. Gas generation ceased in the Late Cretaceous (100 My) after uplift to 2900 m. The formation subsided again to 3200 m after the Middle Pliocene to the present depth (Ding et al., 2013; Yu et al., 2017).

At current reservoir conditions (Pore pressure = 30 MPa, T = 100 °C) more than 80% of the gas is estimated to be stored as free gas whereas only 20% is stored as excess sorbed gas. Therefore, sorptive gas storage for such deep reservoirs is of minor importance. Further considering that already small amounts of reservoir water considerably decrease the sorption capacity of shales by competitive sorption, sorbedgas storage capacity for Benxi and Shanxi shales may even be in the range of the uncertainty of free gas storage estimates (Merkel et al.,2015, 2016; Shabani et al., 2018).

2.7.4.2 Changes in free and excess sorbed gas during production from theshale matrix

During the production of a shale gas reservoir the pressure in theshale matrix, where most of the shale gas is stored, is gradually reduced. This leads to changes in the ratio between "free" and "excess sorbed" gas in the nano-pores. As physisorption is a fast and reversible process, it is not possible to differentiate between individual "sorbed" and "free" methane molecules and an equilibrium between the sorbed and free phase upon changes in the P-T conditions will occur almost in-stantaneously. Using the reservoir conditions (P = 30 MPa and T = 373.15 K), the gas production and changes in "free" and "excess sorbed" gas can be calculated (Fig. 2.15). During depletion of a given matrix block, the "excess sorbed" gas content changes almost insignificantly until a pressure of around 10 MPa below which the "excess sorbed" gas content will be reduced. Therefore, sorption does not add any significant benefit in shale gas production at high pressure. Fig. 2.15 illustrates that the increase of produced gas amount is negligible at highpressure where some of the free gas even translates into "excess sorbed" gas during the early time of gas production. Only when the pore pressure in the matrix is reduced significantly, below roughly 10 MPa will "excess sorbed" gas contribute to production. Additionally, a matrixblock with high excess sorption compared to a sample with no sorption (only free gas) will release less gas at high pressure due to the transfer of "free" into the "excess sorbed" phase (maximum in the excess sorption isotherms). Thus, it is very important to forecast the reduction of gas pressure in each part of the matrix to judge the relevance of sorption during production. However, depending on the production behavior of a given reservoirs pore pressures may be too high within thematrix and release of "excess sorbed" gas does not significantly add to overall production.
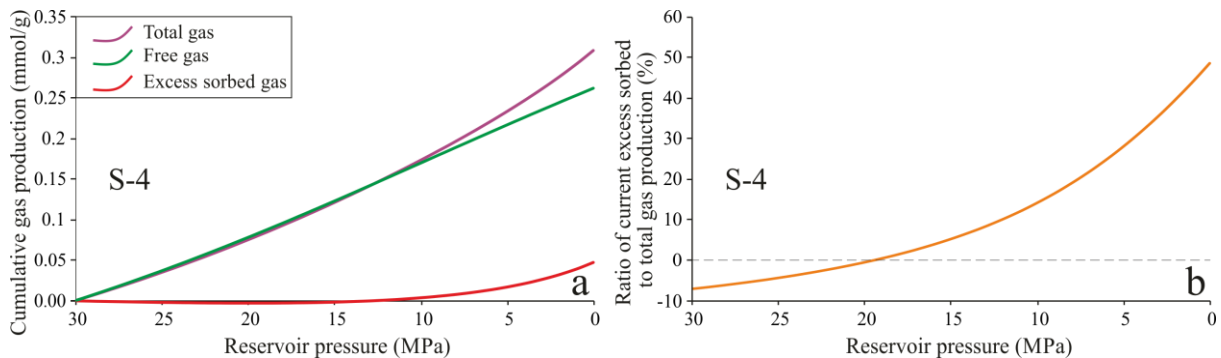
Fig. 2.15. Cumulative gas production from a matrix block of a reservoir at 3000 m depth and 100 °C upon depletion. During production at high pressures (>12 MPa) the change in "excess sorbed" gas content is negative and only the free gas content changes (a). The ratio of the current change of "excess sorbed" gas to the total gas is negative at pressures above the maximum in the excess sorption isotherm (20 MPa). Upon pore pressure reduction below these values will "excess sorbed" gas start contributing to total gas production. The curves were calculated based on the experimental results of sample S-4 (b).

2.8 Conclusions

1) Porosity and excess sorption capacity of over-mature Shanxi and Benxi shales are controlled by their high clay mineral content (up to 80%). In contrast to other shales, TOC due to its low content (< 2.3%), has a negligible effect on gas storage properties.

2) Excess sorptive storage generally dominates the storage capacity of Benxi and Shanxi reservoirs at shallow depths whereas the volumetric "free" gas storage prevails in deeper reservoirs.

3) Methane sorption does not have a positive effect on gas production at high pressure. Only when the pore pressure in the matrix is reduced significantly will "excess sorbed" gas contribute to production. This has major implications for deep reservoirs where pore pressures in the matrix may not be sufficiently reduced before production ceases.

4) Both Benxi and Shanxi shales are characterized by comparatively low porosities, sorption capacities and gas storage capacities compared to producing marine shale gas systems. Combined with the large amount of clay minerals that make hydraulic fracturing more difficult they are regarded unfavourable for shale gas exploitation.

2.9 Appendix

Table A2.1. Gas storage capacities transformed into mol CH$_4$/m^3 rock.

Measurement conditions	Fm.	Sample	Depth (m)	Test temperature (°C)	Sorbed storage capacity at 25 MPa (mol CH$_4$/ m^3 rock)	Freel storage capacity at 25 MPa (mol CH$_4$/ m^3 rock)	Total storage capacity at 25 MPa (mol CH$_4$/ m^3 rock)	n_∞ (mol CH$_4$/ m^3 rock
Sorption measurement at same temperature	Shanxi	S-1	3161.20	45	106.98	680.10	787.08	252.70
		S-2	3161.56	45	126.33	741.30	867.63	278.30
		S-3	3162.45	45	128.05	592.80	720.85	284.13
		S-4	3164.78	45	150.14	677.38	827.51	301.92
		S-5	3175.45	45	73.32	530.53	603.85	184.03
		S-6	3176.09	45	65.47	422.66	488.13	159.90
	Benxi	B-1	3228.43	45	123.06	714.52	837.58	302.64
		B-2	3230.87	45	122.50	803.90	926.40	305.88
		B-3	3232.45	45	16.26	53.26	69.52	27.37
		B-4	3243.85	45	53.11	84.58	137.70	106.92
		B-5	3245.87	45	62.61	528.19	590.80	160.44
		B-6	3246.87	45	105.20	594.28	699.48	258.50
Sorption measurement at different temperature	Shanxi	S-4	3164.78	45	134.31	678.03	812.34	301.17
				70	132.38	601.10	733.48	
				95	129.60	541.88	671.48	
				120	117.39	494.94	612.33	
	Benxi	B-1	3228.43	45	117.32	717.09	834.41	302.66
				70	117.76	636.73	754.49	
				95	120.33	573.40	693.73	
				120	126.60	524.29	650.88	
		B-3	3232.45	45	15.29	53.59	68.88	27.44
				70	14.68	47.72	62.40	
				95	15.78	43.07	58.85	
				120	14.86	39.89	54.75	
		B-4	3243.85	45	62.06	84.41	146.47	106.78
				70	48.26	74.42	122.68	
				95	49.17	67.41	116.58	
				120	46.32	62.07	108.39	

Conversion formula

$$n_{\text{sorbed}} \left(\frac{mol\ (CH4)}{m^3\ (rock)}\right) = n_{\text{excess}} \, (\text{mmol/g}) \cdot \rho_b (\text{kg/m}^3) \quad (2.12)$$

$$n_{\text{total}} \left(\frac{\text{mol}}{\text{m}^3\ (\text{rock})}\right) = \left[\frac{\text{SPV}\,(\text{m}^3/\text{kg}) \cdot \rho_g\,(\text{kg/m}^3)}{M_{CH_4}\,(\text{kg/mol})} + n_{\text{excess}}\,(\text{mmol/g})\right] \cdot \rho_b(\text{kg/m}^3) \quad (2.12)$$

Here n_{sorbed} and n_{total} corresponds to thesorbed and total gas storage capacities, respectively. n_{excess} (mmol/g) corresponds to the excess amount sorbed at T (K) and P (MPa). ρ_b (kg/m^3) is the bulk densities. ρ_g (kg/m^3) is the free phase densities of methane. SPV (Specific pore volume) is pore volume normalized to unit sample mass. M_{CH_4} is the molality of methane.

3 Paleo-depositional environment, origin and characteristics of organic matter of the Triassic Chang 7 Member of the Yanchang Formation throughout the mid-western part of the Ordos Basin, China

3.1 Abstract

A comprehensive geochemical and petrographic study was performed on 23 clay-rich shale samples collected from 18 wells drilled in the mid-western part of the Ordos Basin to investigate the characteristics and thermal maturity of organic matter as well as the paleo-depositional environment of the Chang 7 Member within the Triassic Yanchang Formation. The samples are characterized by moderate to very high organic carbon (TOC) contents ranging from 0.24% to more than 24.83% (2.72% on average) and total sulfur (TS) contents of 0.06% to 6.51%. Rock-Eval S_1 and S_2 values range from 0.13 to 3.70 mg HC/g rock and 0.62 to 92.50 mg HC/g rock, respectively, implying good to very good hydrocarbon generation potential for most of the samples. Rock-Eval data and petrographical observations reveal that the kerogen is mainly composed of type II to type III, consisting of a mixture of aquatic and terrigenous organic matter. The aliphatic fractions show variable monomodal to bimodal distributions of normal alkanes. Different parameters such as TOC/TS and molecular biomarker data imply that the Chang 7 member is a typical clay-rich source rock deposited in a sulphate-poor lacustrine to fluvio-deltaic environment under oxic to sub-oxic conditions with substantial input of organic matter derived from higher land plants, mainly conifers. Low values of gammacerane further indicate a low salinity of the paleo-lake. Average T_{max} values of 445 °C, vitrinite reflectance values between 0.68% and 0.88%, biomarker parameters, such as sterane ratios of C_{29} ααα 20S/(20S +20R) and C_{29} ββ/(ββ +αα), and maturity indices based on aromatic compounds, indicate a thermal maturity within the oil window for the studied samples, showing some regional variability within the mid-western Ordos Basin.

3.2 Introduction

Source rocks are increasingly being regarded as hosts for commercial unconventional hydrocarbons reservoirs, i.e. gas- and oil-shale reservoirs. One prominent example for such a resource is the lacustrine Chang 7 Member in the Ordos Basin, China. Compared to marine settings, lacustrine environments are more complex regarding their deposetting and are prone to be affected by terrestrial material. On the one hand, the depositional facies, depositional environment and organic matter (OM) composition are more diverse and are easy to be disturbed by terrestrial input due to the small scale of lake systems as compared to marine settings. On the other hand, seasonal/periodic paleo-climates can trigger changes in water chemistry and salinity in lake systems over short periods of time, whereas salinity and water chemistry are quite persistent in marine settings. In fact, the paleo-depositional environment exerts a major control on the abundance and quality of OM preserved in sediments, making it an important factor in quantifying the hydrocarbon potential of source rocks on a basin scale (Jones

and Manning, 1994). In turn, thermal maturity of a source rock plays a critical role in the transformation of OM into mobile hydrocarbons.
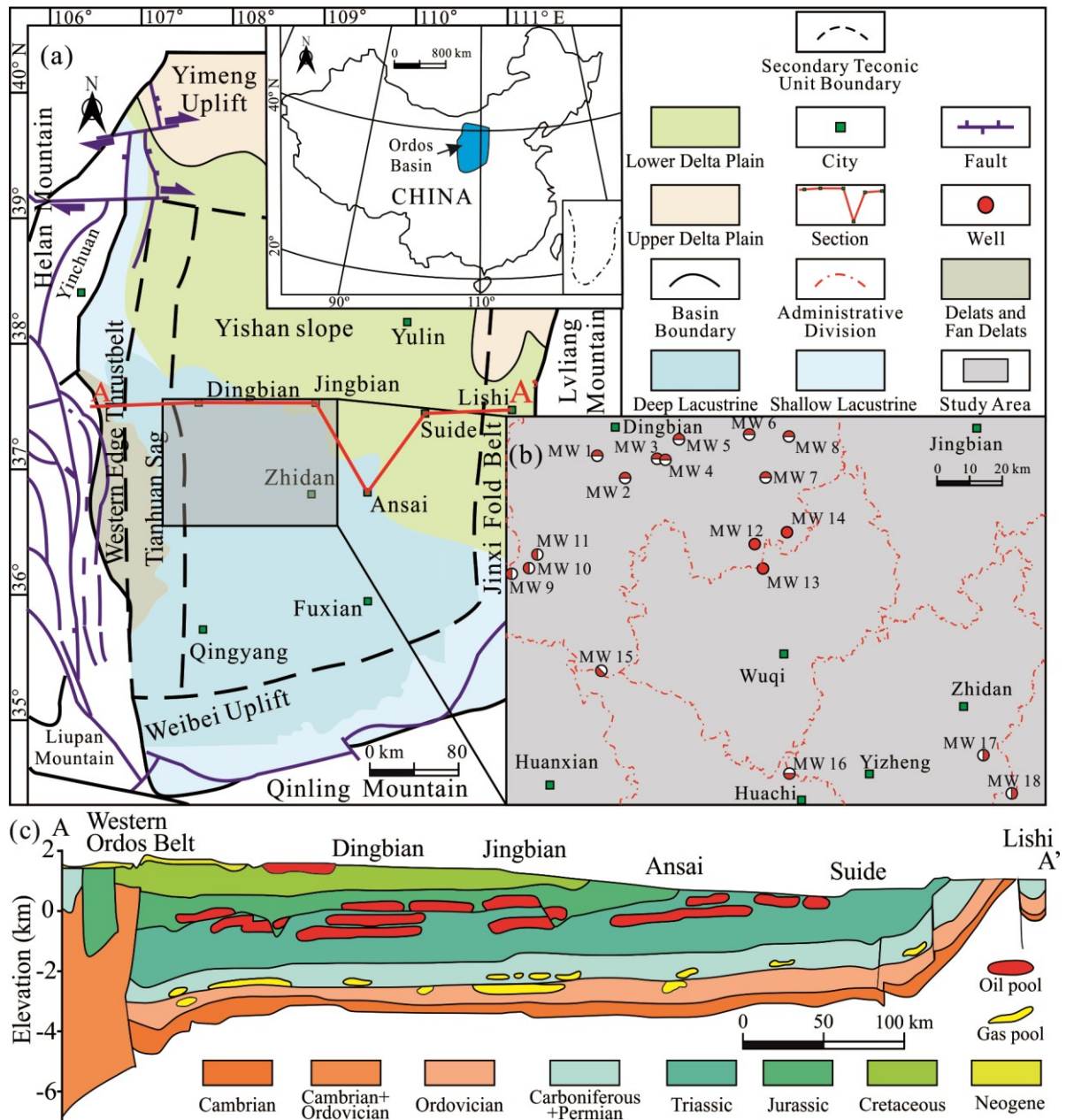
Fig. 3.1. Schematic map showing (a) the Ordos Basin with facies boundaries of the Upper Triassic (after Qiao et al., 2020 and Chen et al., 2017), (b) the study area and well locations (note the different symbols depending on well location, e.g. north, west), and (c) a cross section from west to east of the central Ordos Basin (see a) for position; after Hanson et al. (2007).

The Ordos Basin is the second largest sedimentary basin in China (Li et al., 2016), and has a long depositional history from the Lower Paleozoic to Mesozoic and Cenozoic. It developed on Precambrian metamorphic basement. Following the dry climate of the Permian, plants began to flourish again in the Late-Middle Triassic in the region of the today's Ordos Basin and the most important source rocks of the basin were deposited during the Late Triassic. Triassic hydrocarbon deposits were first discovered

in the 1980ies with the Triassic Chang 7 Member of the Yanchang Formation being regarded as the most important source rock for these accumulations (Hanson et al., 2007; Duan et al., 2008). Although there have been numerous publications on the Chang 7 Member (e.g., Yang et al., 2008; Zhang et al., 2017; Xu et al., 2019; Chen et al., 2019a, Chen et al., 2019b), there is still a lack of detailed information on organic geochemical parameters. Further, there are some controversies related to the depositional environment prevailing during the deposition of the Chang 7 Member which need to be clarified. For example, there are significant differences between the reported geochemical characteristics e.g., with respect to the isoprenoids/n-alkane ratios, terpanes and gammacerane (Gam) indices and sterane data (Duan et al., 2008; Li et al., 2017; Pan et al., 2017; Xu et al., 2019). As a result, there are different interpretations of depositional environment, type of kerogen, redox conditions as well as salinity of the paleo-lake. These differences might be caused by the extensive regional distribution of the Chang 7 member and thus heterogeneity of rock properties indicating the necessity of systematic regional studies. The area selected for the study presented here is located in the major hydrocarbon exploitation area in the mid-western Yishan Slope (Fig. 3.1a). The area is characterized by a low level of tectonic deformation, i.e. there is little faulting and folding (Yang, 2002).

The goal of this study is to apply organic petrography, carbon and sulfur contents, Rock-Eval pyrolysis and molecular organic geochemistry on aliphatic and aromatic hydrocarbons in order to i) reconstruct the depositional environments prevailing during deposition of the Chang 7 member and gain information on the biological precursors of its OM and ii) to quantify thermal maturity in the mid-western part of the Ordos Basin (Fig. 3.1b), for which almost no such information has been published so far. Besides, this study contributes to the understanding of OM-rich Late Triassic rocks, which are less widespread and have been less studied than those of Carboniferous, Jurassic, Cretaceous, and Cenozoic times.

3.3 Geological setting

The Ordos Basin, a sedimentary basin with a complex, long-lasting subsidence, several phases of uplift and erosion interrupting polycyclic sedimentary deposition, is situated in the central part of the North China Plate covering an area of 26×10^4 km^2 where it developed on an Archean–Early Proterozoic rigid crystalline basement (Yang et al., 2005). It is surrounded by the Yin Mountain to the north, the Qinling Mountain to the south, the Helan Mountains to the northwest, the Liupan Mountain to the southwest, and the Lvliang Mountain to the east (Fig. 3.1a). The basin is divided into six structural units based on the geological evolution history and the characteristics of the Mesozoic geological structures; the eastern Jinxi Fold Belt, the western Tianhuan Sag and the Western Edge Thrust belt, the southern Weibei Uplift, the northern Yimeng Uplift, and the central Yishan Slope (Fig. 3.1a). The evolution of the basin took place during five tectonic-sedimentary stages: (1) the aulacogen stage in the Middle-Late Proterozoic; (2) the shallow marine platform stage during the Early Paleozoic; (3) the

45

littoral plain stage in the Late Paleozoic; (4) the hinterland basin stage during the Mesozoic; and (5) the peripheral faulted basin stage in the Cenozoic (Yang et al., 2005). Corresponding sedimentary rocks include shallow-marine clastic-carbonate deposits, epicontinental sea carbonate platform deposits, coastal carbonate-continental clastic platform deposits, and intra-continental lacustrine-fluvial deposits (Meso- and Cenozoic). During the Late Triassic, the tectonic evolution of the basin was controlled by Indosinian Plate movements which resulted in a persistent regression and the development of an inland basin (Yang et al., 2005).
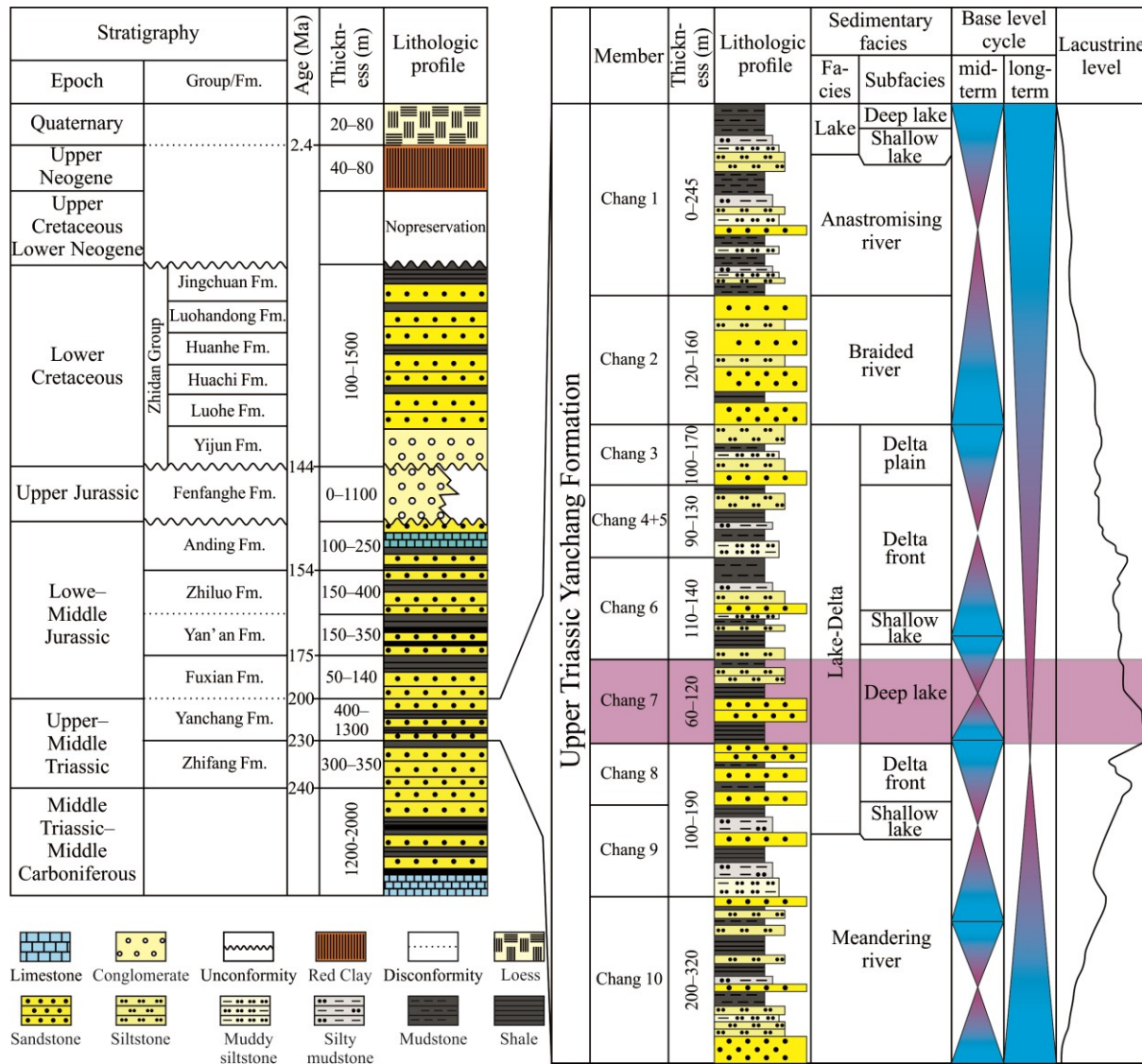
Fig. 3.2. Simplified stratigraphy of the Ordos Basin and the Upper Triassic Yanchang Formation lithologies and their corresponding depositional environment (modified after Zhao et al., 2015).

The Ordos Basin is considered as a Mesozoic and Cenozoic freshwater continental sedimentary system. The stratigraphic sequence comprises of Middle-Upper Triassic to Quaternary strata wherein the Mesozoic strata constitute the majority of the sediments (Figs. 1c and 2). This sequence overlies a crystalline basement of Archean and Lower Proterozoic age (Watson et al., 1987). The whole basin was

filled with lacustrine and fluvial sediments during the Triassic period, but only the lacustrine deposits are considered to possess hydrocarbon generation potential (Zhang et al., 2015). The Yanchang Formation, which is sub-divided into ten members (Chang 1 to Chang 10), underlies the Jurassic Fuxian Formation and overlies the Middle Triassic Zhifang Formation (Fig. 3.2). The Yanchang Formation first experienced a lacustrine transgression leading to deepening of the water column (Chang 9-Chang 7 periods), followed by successive shallowing of the paleo-lake (Chang 6- Chang 1 periods; Fig. 3.2). The Chang 7 Member was deposited at the deepest and most expansive stage of the Triassic Yanchang Ordos Lake. The thickness of this member varies between 60 and 120 m with the cumulative thickness of the source rocks ranging from 15 to 100 m (Li et al., 2020); it is regarded as an important marker bed in the Yanchang Formation corresponding to the Maximum Flooding Surface (MFS). Lithologically, it is composed of mudstone, siltstone and sandstone (Fig. 3.2). OM-rich successions were deposited in the shallow to deep lake water environments and are restricted to the lower 10 to 40 m of the Chang 7 member in an area of more than 50×10^3 km^2 (Chen et al., 2017, Fig. 3.1a).

3.4 Samples and methods

3.4.1 Samples and sample preparation

Table 3.1. TOC, TIC, and TS data, as well as the three major primary sedimentary components calculated for the studied samples from the Chang 7 Member of the Midwestern Ordos Basin, China.

Sample ID	Well	Depth (m)	TOC (%)	TIC (%)	TS (%)	CAR (%)	OM* (%)	SIL (%)
MW 1-1	MW 1	2702.50	0.76	0.04	0.11	0.33	0.97	98.70
MW 1-2		2702.00	4.50	0.06	0.34	0.50	6.10	93.40
MW 2	MW 2	2540.00	1.63	0.02	0.14	0.17	2.22	97.61
MW 3	MW 3	2512.28	0.39	0.87	----	----	----	----
MW 4	MW 4	2393.20	0.44	0.32	0.09	2.67	0.56	96.77
MW 5	MW 5	2284.00	2.64	0.10	0.13	0.83	3.51	95.66
MW 6	MW 6	1512.73	0.67	0.04	0.12	0.33	0.86	98.81
MW 7	MW 7	1873.00	0.50	0.06	0.10	0.50	0.73	98.77
MW 8	MW 8	1982.40	1.45	0.10	0.27	0.83	2.12	97.05
MW 9	MW 9	2566.00	0.33	0.04	----	----	----	----
MW 10-1	MW 10	2570.00	4.73	0.10	0.42	0.85	6.46	92.69
MW 10-2		2571.60	24.83	1.38	6.51	11.50	38.09	50.41
MW 11-1	MW 11	2675.00	0.83	0.06	0.09	0.50	1.06	98.44
MW 11-2		2673.00	1.32	0.06	0.09	0.50	1.78	97.72
MW 12	MW 12	1950.00	0.69	0.03	0.10	0.25	0.88	98.87
MW 13	MW 13	1950.00	1.76	0.05	0.12	0.42	2.37	97.21
MW 14	MW 14	2597.00	0.51	0.32	----	----	----	----
MW 15	MW 15	2668.00	0.24	0.06	----	----	----	----
MW 16-1		1979.24	1.27	0.99	0.06	8.25	1.69	90.06
MW 16-2	MW 16	1981.50	4.76	0.31	1.27	2.58	7.32	90.10
MW 16-3		1981.72	2.16	0.18	1.60	1.50	4.31	94.19
MW 17	MW 17	1332.69	4.25	0.10	0.62	0.83	6.04	93.13
MW 18	MW 18	1445.00	2.00	0.33	0.12	2.75	2.68	94.57

A total of 23 clay-rich core samples usually shales or siltstones (see Xu et al., 2019; Li et al., 2020) has been collected from 18 wells drilled at several locations in the mid-western Ordos Basin at a depth interval between 1332.69 m and 2702.50 m (well positions are shown in Fig. 3.1b, Table 3.1). Macroscopically, the fine- to medium grained shale samples show fine lamination with alternating dark and lighter grey layers (Fig. 3.3).

Each sample was cut into two halves with a diamond rotation saw and subsequently dried at room temperature. One half was ground to fine powder as preparation for elemental carbon and sulfur analyses, Rock-Eval pyrolysis, and biomarker analysis. The second half was used to prepare polished sections for incident light microscopy. Polished sections were prepared on rock pieces cut perpendicular to bedding by following the procedures described in detail by Zieger and Littke (2019).
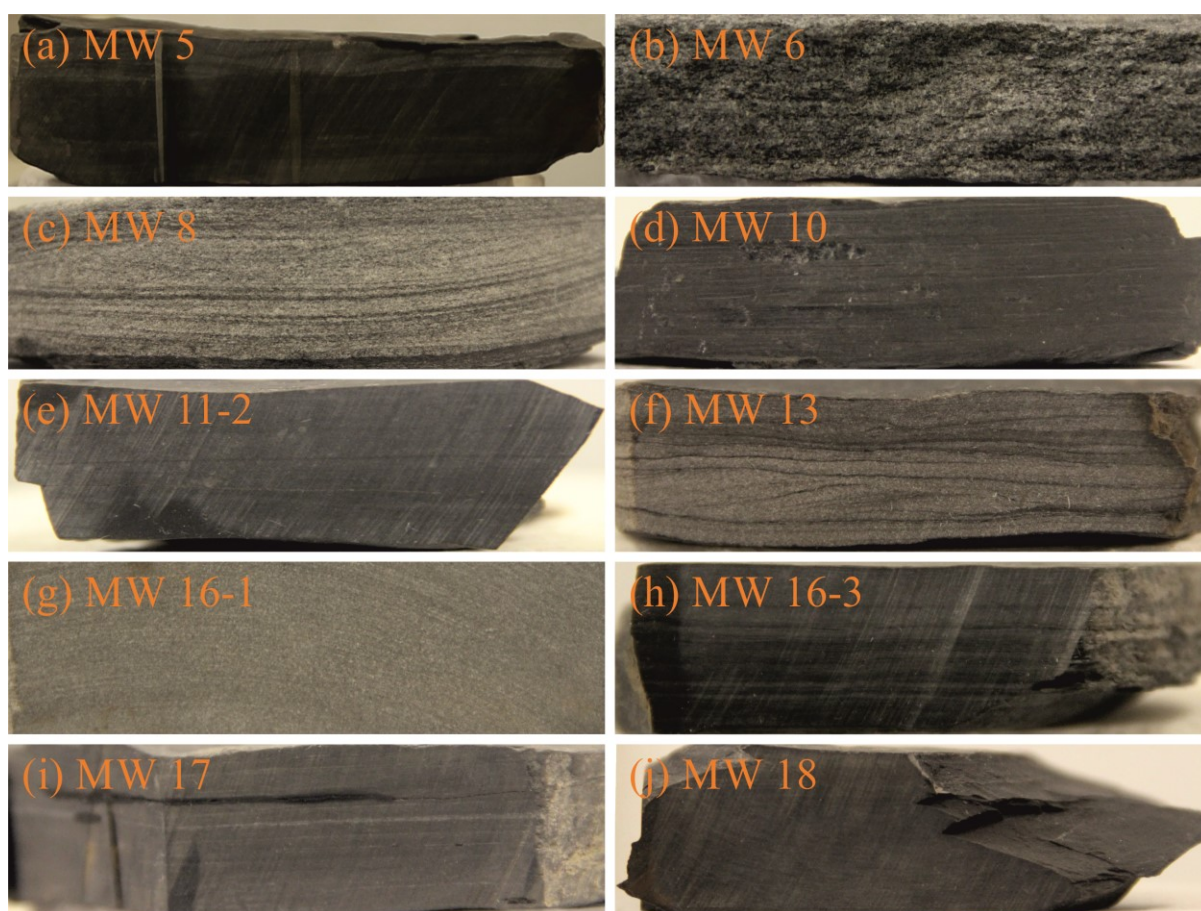
Fig. 3.3. Photographs of selected representative core samples. See text for description.

3.4.2 Elemental carbon and sulfur analysis

TOC and TIC contents were measured on all samples using a liquid TOC II analyzer (Elementar). Aliquots of 100 mg powdered sample were first heated to 550 °C applying a heating rate of 300 °C/min and then kept isothermal for 600 s during which the TOC contents were measured. The temperature was then increased to 1000 °C and remained constant for 400 s to measure the TIC contents. TOC and TIC contents were measured with a non-dispersive infrared detector (NDIR) (detection limit 10 ppm;

TOC error 0.6%; TIC error 1.7%) by recording the amounts of carbon dioxide (CO_2). The TS contents were measured by combusting 100 mg of powdered sample using a Leco S 200 sulfur analyzer (precision is <5% error, detection limit 0.001%). More detailed information on the devices and measuring procedures can be found in Prinz et al. (2017) and Grohmann et al. (2019).

3.4.3 Rock-Eval pyrolysis

Rock-Eval pyrolysis was performed using a Rock-Eval VI instrument (Vinci Technologies) following the procedure described in detail in Behar et al. (2001).

The measured parameters including S_1 (volatile hydrocarbon con-tent, mg HC/g rock), S_2 (remaining hydrocarbon generative potential, mg HC/g rock), S_3 (CO_2 formed by thermal breakdown of kerogen, mg CO_2/g rock), and T_{max} (temperature of maximum pyrolysis yield, °C) were used to calculate the hydrogen index (HI $=S_2$/TOC, mg HC/g TOC), oxygen index (OI $=S_3$/TOC, mg CO_2/g TOC) and production index (PI $=S_1/(S_1 +S_2)$).

3.4.4 Organic petrography

Maceral point counting was performed on a Zeiss Axio Imager inci-dent light microscope operated with DISKUS Fossil software (Hilgers) both in white light and in a fluorescence mode at 500 times magnifi-cation (50×oil immersion objective). Before each vitrinite reflectance (VR_r) measurement, a yttrium-aluminum-garnet standard (0.889% reflectance) was used to calibrate the instrument. 100 randomly ori-ented vitrinite particles were measured per sample whenever possible, according to ISO 7404-5. The maceral composition was determined based on the principles described in Taylor et al. (1998), with macerals being assigned according to the ICCP system 1994 (ICCP, 1998; ICCP, 2001; Pickel et al., 2017). On the same microscope, diameters of all present pyrite framboids were measured on 10 representative areas of 250 ×150 μm per sample by using a digital measuring device imple-mented in the Fossil software.

3.4.5 Molecular geochemistry

Based on TOC contents, 4–6 g of pulverized sample was extracted by accelerated solvent extraction (ASE) with dichloromethane (DCM, 40 mL). Activated copper and sodium sulfate were used to reduce the elemental sulfur and water contents prior to fractionation. Extracts were separated into three fractions by column chromatography using an activated micro column packed with silica gel (2 g) and eluents of different polarity: 5 mL *n*-pentane for the aliphatic hydrocarbons and 5 mL *n*-pentane/DCM (40:60, v:v) for the aromatic hydrocarbons.

Gas chromatography (GC) was performed on aliphatic and aromatic fractions using a Fisons Instruments GC 8000 series, equipped with a flame ionization detector (FID), and a 30 m × 0.25 mm i.d Zebron ZB-1 fused silica column (0.25 μm film thickness). Hydrogen was used as carrier gas with a velocity of approx. 40 cm/s. Chromatographic conditions were set to 270 °C injector temperature, 1 μL split injection at an initial oven temperature of 60 °C, which was then programmed to 310 °C at a heating rate of 5 °C/min, with a final isothermal hold for 20 min.

The GC–MS analysis was performed using a quadrupol mass spec-trometer Trace MS (Thermoquest) linked to a Mega Series HRGC 5160 gas chromatograph (Carlo Erba, IT) equipped with a 30 m × 0.25 mm i. d. x 0.25 μm film Zebron ZB-5 fused silica capillary column. The MS was operated in electron ionization (EI+) mode with an ionization energy of 70 eV and an ion source temperature of 200 °C. Fragmentograms were obtained by selective ion monitoring (SIM) applying 11 and 14 different masses for aliphatic and aromatic fractions, respectively. Helium was used as carrier gas with a velocity of 30 cm/s. The chromatographic conditions for the aliphatic fraction were 270 °C injector temperature, 1 μL splitless injection (splitless time of 60 s) at 80 °C (isothermal time 3 min) then programmed at 10 °C/min to 160 °C, then heating to 320 °C with a rate of 3 °C/min, 20 min isothermal hold. For the aromatic fraction, the temperature program started at 80 °C (isothermal time 3 min), followed by heating to 320 °C at a rate of 3 °C/min, then keeping this temperature for 20 min.

All biomarker ratios were calculated from peak areas of specific ion chromatograms. Identification of individual compounds was based on the retention properties of standards and comparison of elution orders with published gas chromatograms. Evaluations were performed for terpanes (m/z 191) and steranes (m/z 217) in the aliphatic fraction as well as naphthalenes (m/z 128 +142 +156 +170 +184), phenanthrenes (PHE, m/z 178 +192 +206), dibenzothiophenes (DBT, m/z 184 +198 +212), methylbiphenyls (m/z 168), biphenyl (BP, m/z 154), diphenylmethane (DPM, m/z 168), and dibenzofurane (DBF, m/z 168) in the aromatic fractions.

3.5 Results

3.5.1 Elemental carbon and sulfur composition

The TOC contents of the samples range from 0.24% to 24.83% (mean value =2.72%, Table 3.1) and TIC and TS contents from 0.02 to 1.38% (avg. 0.24%) and 0.06 to 6.51% (avg. 0.65%), respectively (Table 3.1). Based on elemental carbon and sulfur contents, the three major sedi-mentary components including original OM (OM* =OM before sulfate reduction), carbonate (CAR) and silicate (SIL) were calculated according to the following formulas originally presented by Littke (1993):

CAR = TIC × 8.333, assumingthat carbonateis presentas calcite (3.1)

Corg* = TOC + 2 × TS × MC/MS (3.2)

OM* = Corg* × 100/COM (3.3)

SIL = 100 − (OM* + CAR) (3.4)

Where Corg* is the original organic carbon weight percentage prior to sulfate reduction; MC and MS are the molecular masses of carbon and sulfur, respectively; and COM corresponds to the carbon content of primary OM (here: 78%; Littke 1993). The results indicate that the analyzed shales are clearly dominated by silicates with values ranging from 50.4% to 98.87% (93.4% on average), whereas carbonate and OM* contents range from 0.17 to 11.5% (avg. 2.0%) and from 0.56 to 38.1% (avg. 4.72%), respectively (Table 3.1).

3.5.2 Rock-Eval pyrolysis
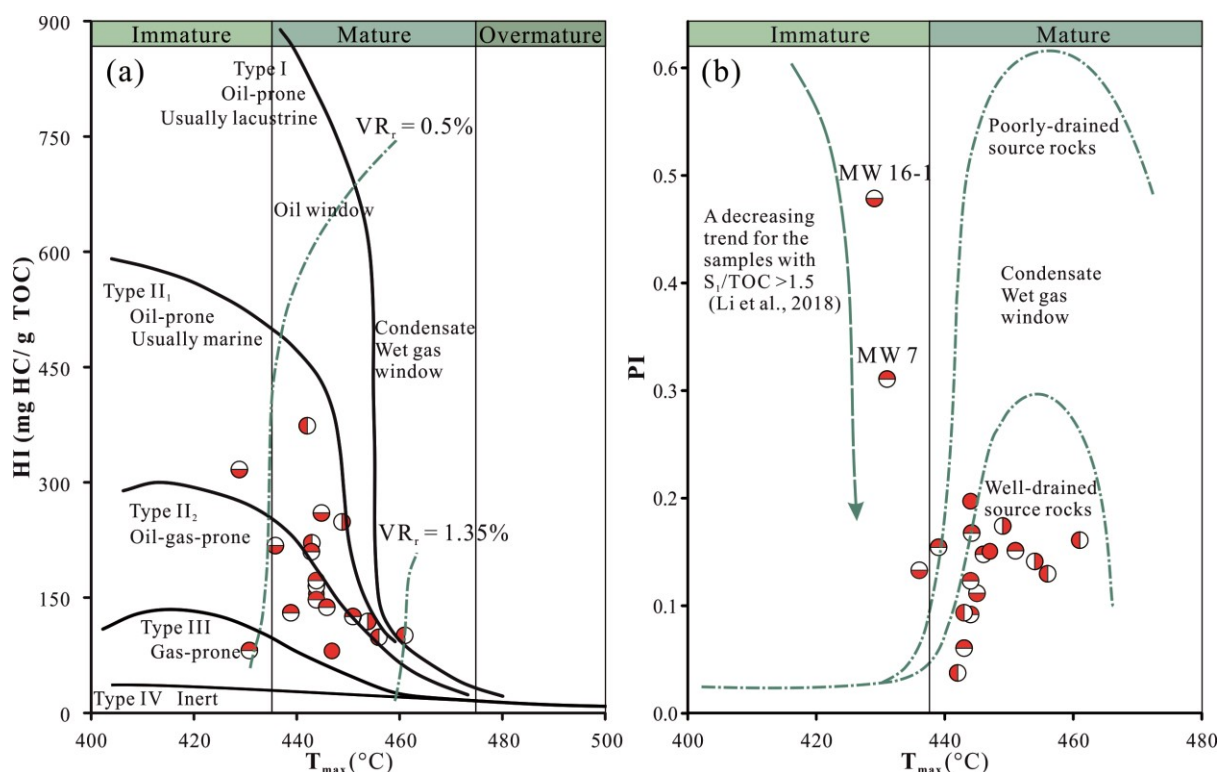
Fig. 3.4. Plots of T_{max} versus HI (a) and PI (b), showing kerogen types and hydrocarbon potential for the samples from the Chang 7 Member.

Table 3.2. Rock-Eval pyrolysis data of the Chang 7 Member samples.

Sample ID	S_1 (mg HC/g rock)	S_2 (mg HC/g rock)	S_3 (mg CO_2/g rock)	PI	T_{max} (ºC)	HI (mg HC/g TOC)	OI (mg CO_2/g TOC)
MW 1-1	0.14	0.79	0.21	0.15	451	126	27
MW 1-2	0.78	7.73	0.14	0.09	444	172	3
MW 2	0.22	3.40	0.24	0.06	443	209	15
MW 3	----	----	----	----	----	----	----
MW 4	0.13	0.65	0.11	0.17	444	147	26
MW 5	0.63	3.45	0.38	0.15	439	131	14
MW 6	0.16	0.93	0.09	0.15	446	138	13
MW 7	0.28	0.62	0.20	0.31	431	80	10
MW 8	0.34	2.42	0.14	0.12	444	167	10
MW 9	----	----	----	----	----	----	----
MW 10-1	1.07	10.47	0.45	0.09	443	222	4
MW 10-2	3.61	92.50	1.09	0.04	442	373	4
MW 11-1	0.16	0.84	0.15	0.16	461	101	18
MW 11-2	0.19	1.28	0.21	0.13	456	97	16
MW 12	0.26	1.06	0.11	0.20	444	154	17
MW 13	0.26	1.49	0.41	0.15	447	84	23
MW 14	----	----	----	----	----	----	----
MW 15	----	----	----	----	----	----	----
MW 16-1	3.70	4.03	0.20	0.48	429	317	15
MW 16-2	1.59	10.39	0.23	0.13	436	218	5
MW 16-3	0.70	5.63	0.15	0.11	445	261	7
MW 17	2.23	10.59	0.25	0.17	449	249	6
MW 18	0.39	2.39	0.28	0.14	454	120	14

51

Rock-Eval pyrolysis is generally used to evaluate kerogen characteristics including hydrocarbon generation potential, kerogen type, and thermal maturity (Fig. 3.4, Lafargue et al., 1998). For the samples studied, S_1 and S_2 values range from 0.13 to 3.70 (mean value = 0.89 mg HC/g rock) and from 0.62 to 92.50 (mean value = 8.46 mg HC/g rock; Table 3.2), respectively. S_3 values range from 0.09 to 1.09 mg CO_2/g rock (0.27 on average). Hydrogen index (HI) values which are affected by the type and maturity of OM and, in turn, indicate the quality of kerogen, vary between 80 and 373 mg HC/g TOC with an average value of 177. T_{max} values of the studied samples range between 429 °C and 461 °C with an average of 445 °C indicating thermal maturity within the oil window. PI values, indicating both maturity and impregnation or migration loss for source rocks, vary from 0.04 to 0.48 (mean = 0.16).

3.5.3 Organic petrography

Table 3.3. VR_r values, maceral compositions (percentages based on whole rock samples), and minimum (min.), maximum (max.) as well as average (ø) diameters of pyrite framboids of the Chang 7 Member samples. Std = standard deviation, sk = skewness, n = number of framboids measured.

Sample ID	VR_r (%)	Maceral composition (vol.%)					Framboidal pyrite diameters (µm)					
		Vitrinite	Liptinite	Inertinite	Solid bitumen	Total OM	min.	max.	ø	std	sk	n
MW 1-1	0.88	1.7	0.2	0.3	0.1	2.2	----	----	----	----	----	----
MW 1-2	0.88	4.8	0.2	0.1	0.0	5.1	2.5	32.1	11.5	4.3	1.0	313
MW 2	0.69	8.9	0.4	0.6	1.3	11.2	4.1	37.1	14.9	10.2	0.9	221
MW 4	0.80	1.0	0.1	0.1	0.0	1.2	3.0	44.2	9.1	4.4	2.7	213
MW 5	0.71	0.8	0.1	0.3	0.3	1.6	2.2	29.1	8.9	4.6	1.6	214
MW 6	0.80	1.4	0.0	0.3	0.0	1.7	2.3	19.3	7.5	3.2	1.4	206
MW 7	0.70	1.1	0.1	0.1	0.2	1.6	----	----	----	----	----	----
MW 8	0.70	2.2	0.3	0.8	0.1	3.4	2.6	37.9	10.1	6.0	2.2	214
MW 10-1	0.76	1.3	0.5	0.4	0.1	2.3	2.4	35.0	10.4	6.3	0.8	224
MW 10-2	0.77	31.4	5.1	0.2	2.1	38.8	1.8	34.0	9.8	4.8	1.4	242
MW 11-1	0.82	2.1	0.2	0.1	0.0	2.5	2.6	43.2	7.6	4.0	4.3	222
MW 11-2	0.82	4.6	0.2	0.2	1.1	6.2	3.2	27.2	10.9	4.7	1.0	242
MW 12	0.68	1.6	0.3	0.0	0.2	2.1	----	----	----	----	----	----
MW 13	0.85	2.8	0.0	0.9	0.5	4.3	----	----	----	----	----	----
MW 16-1	0.70	0.2	0.0	0.1	0.2	0.5	----	----	----	----	----	----
MW 16-2	0.71	3.1	0.2	0.0	0.0	3.3	2.9	31.7	11.8	5.8	0.8	325
MW 16-3	0.78	1.0	0.4	0.2	0.1	1.6	1.9	17.9	6.0	2.9	1.4	211
MW 17	0.78	2.6	2.2	1.1	0.5	6.4	2.8	40.9	12.3	5.9	1.5	273
MW 18	0.84	3.5	0.5	0.2	0.2	4.4	3.7	28.1	8.1	2.9	2.5	216

The analyzed samples are rich in autochthonous vitrinite particles which were used to measure vitrinite reflectance (VR_r) and thus to assess thermal maturity. VR_r of the studied samples varies between 0.68% and 0.88% VR_r (0.77% VR_r on average, Table 3.3). The volumetric percentage of OM observed in the samples varies between 0.5 vol% (MW 16–1) and 38.8 vol% (MW 10–2). Sample MW 10–2 is especially rich in vitrinite (31.4 vol% of the whole rock, Table 3.3). Vitrinite particles (Fig. 3.5a) are abundant in all the samples analyzed, accounting for between 40.0% and 94.1% of the total macerals counted. The input of OM with terrestrial plant origin is further illustrated by the presence of inertinite in most samples (Fig. 3.5b and c), occurring as small detrital particles or in form of semifusinite or fusinite. Solid bitumen occurs either in-between mineral grains or as fillings of empty cell lumens in structured inertinite particles (Fig. 3.5c) and is observed almost in all samples, but not in high quantity. Liptinite is mainly submicroscopic, finely dispersed within the mineral matrix, showing a slight yellowish fluorescence. The liptinite macerals accounting for the determined volumetric percentages

are either liptodetrinite or lamalginite (Fig. 3.5d). A common feature of the samples are calcareous fossil shell remains with varying shapes. Some of these are perfectly round (Fig. 3.5e and f). Pyrite is abundant in all Chang 7 Member samples (Fig. 3.5a, c and e), occurring either as assemblages of recrystallized framboids (Fig. 3.5c, upper left corner), as framboidal pyrites surrounded by OM (Fig. 3.5a) or as euhedral crystals. The variation in sizes of pyrite framboids is large, with diameters ranging from around 2 μm to > 40 μm (6.0–14.9 μm on average; Table 3.3).
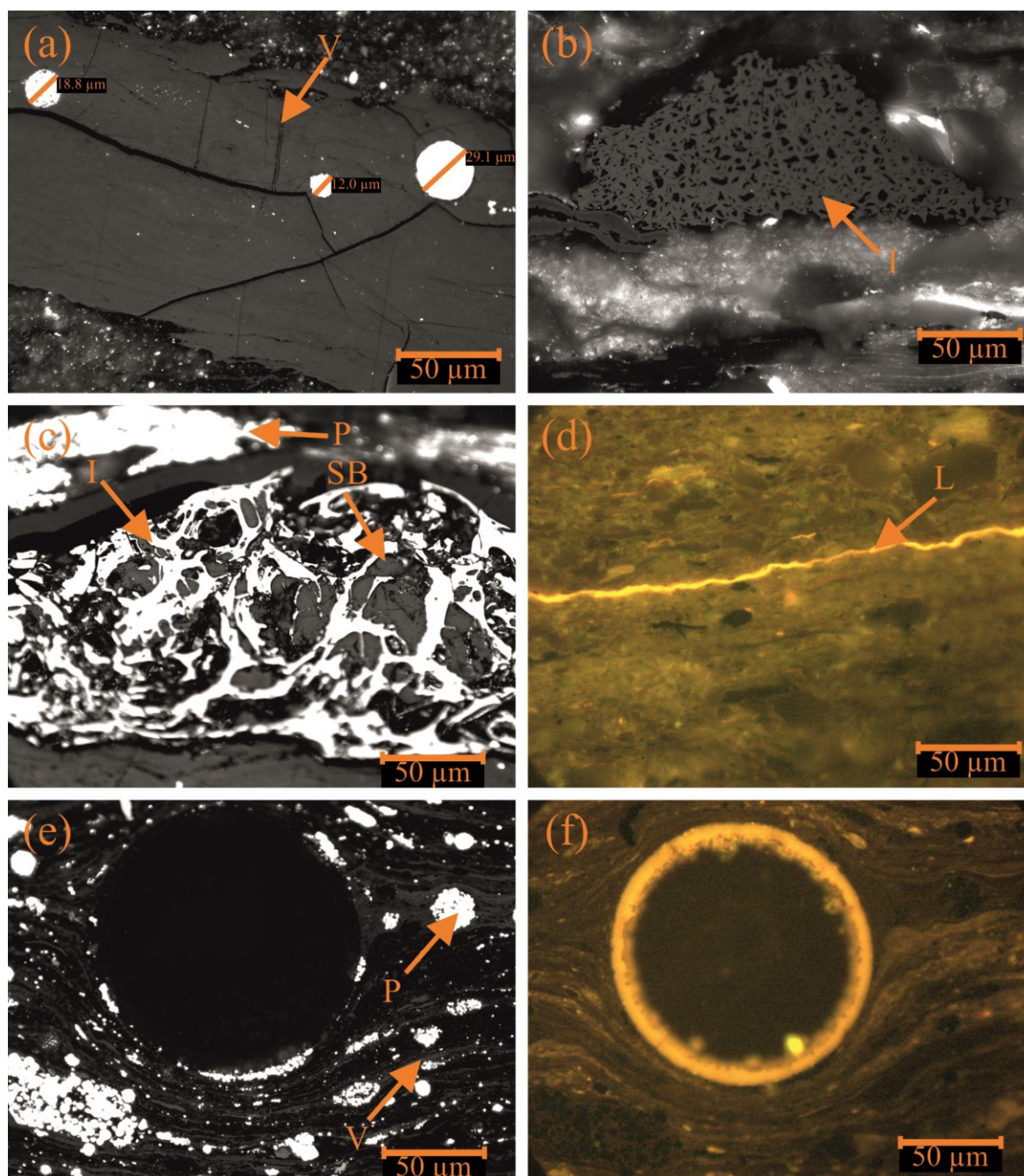
Fig. 3.5. Photomicrographs representative of the organic matter in the Chang 7 Member source rocks under incident white light (a, b, c, e) and in fluorescence mode (d, f). Showing (a) vitrinite (V) with framboidal pyrite (P) (MW 1-2), (b) semifusinite (I) (MW 13), (c) fusinite (I) with solid bitumen (SB) filling empty cell lumens, (d) lamalginite (L) and finely dispersed liptinite within the mineral matrix, (e) circular, calcareous fossil remains in white light and (f) in fluorescence mode.

3.5.4 Molecular geochemistry

3.5.4.1 Acyclic alkanes
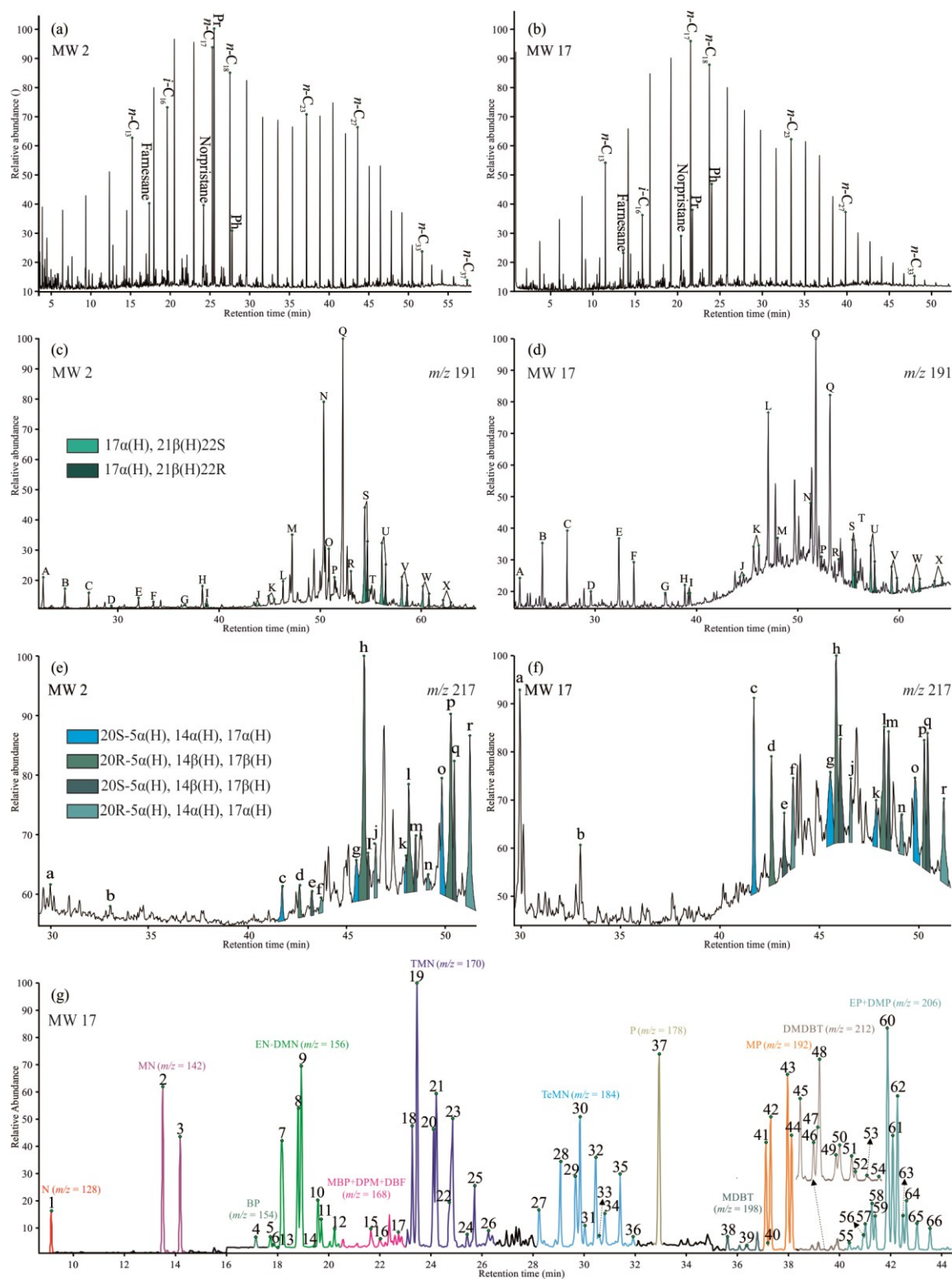
Fig. 3.6. (a, b) Gas chromatograms; (c, d) m/z 191 mass fragmentograms (hopanoids); (e, f) m/z 217 mass fragmentograms (steranes) of the aliphatic fractions (samples MW 2 and MW 17), and (g) total ion chromatogram (TIC) of the aromatic fraction (sample MW 17). See Appendix (Table A3.1) for detailed peak identification.

Acyclic alkanes in the range of n-C_9 to n-C_{37} are characterized by bimodal distributions in most samples (Fig. 3.6a and b), but some samples show unimodal distributions with higher proportions in the low- molecular weight n-alkanes (Fig. 3.7a) with maximum peaks occurring at n-C_{15} and n-C_{17} for most samples (Fig. 3.6a, b; Table 3.4).

Table 3.4. Biomarker parameters of acyclic alkanes of the source rocks from the Chang 7 Member. Pr = pristane; Ph = phytane; CPI = 2 ×∑odd n-C23–29/(∑even n-C22–28 + ∑even n-C24–30); OEP = (n-C21 + 6 × n-C23 + n-C25)/(4 × n-C22 + 4 × n-C24); WI= ∑n-C21-31/∑n-C15-20; TAR = (n-C27 + n-C29 + n-C31)/(n-C15 + n-C17 + n-C19); Paq = (n-C23 + n-C25)/(n-C23 + n-C25 + n-C29 + n-C31).

Sample ID	Distribution of n-alkanes (%)			Pr/ Ph	Pr/ n-C_{17}	Ph/ n-C_{18}	n-C_{17}/ n-C_{27}	CPI	OEP	WI	TAR	P_{aq}
	n-C_{10-20}	n-C_{21-25}	n-C_{26-35}									
MW 1-1	76	15	9	1.99	0.40	0.30	4.71	1.15	1.04	0.50	0.13	0.81
MW 1-2	64	22	14	4.01	0.93	0.26	2.05	1.15	0.96	1.04	0.34	0.75
MW 2	52	24	24	5.03	1.64	0.35	1.36	1.23	1.04	1.27	0.57	0.63
MW 4	60	20	20	1.81	0.46	0.39	2.50	1.11	1.06	0.81	0.32	0.71
MW 5	76	15	9	1.78	0.48	0.39	5.79	1.16	1.03	0.41	0.13	0.72
MW 6	79	13	7	1.82	0.43	0.40	5.51	1.19	1.09	0.46	0.13	0.77
MW 7	61	24	15	1.60	0.60	0.46	2.19	1.17	1.02	1.02	0.34	0.77
MW 8	86	9	6	1.70	0.44	0.44	12.01	1.10	1.10	0.22	0.07	0.72
MW 10-1	87	9	4	1.26	0.22	0.21	10.02	1.33	0.98	0.34	0.32	0.10
MW 10-2	90	7	2	1.07	0.15	0.19	28.08	1.14	1.05	0.22	0.04	0.73
MW 11-1	72	18	10	1.19	0.30	0.27	2.70	1.22	1.01	0.84	0.29	0.73
MW 11-2	75	16	9	2.23	0.62	0.38	4.11	1.26	1.02	0.60	0.18	0.76
MW 12	30	35	35	2.65	0.98	0.51	0.75	1.27	1.03	0.71	0.25	0.72
MW 13	85	11	4	2.16	0.50	0.36	14.83	1.22	1.04	0.27	0.05	0.84
MW 16-1	67	20	13	0.48	0.67	1.10	3.34	1.17	1.06	2.18	1.09	0.62
MW 16-2	75	19	7	0.81	0.52	0.75	6.14	1.16	1.07	0.53	0.11	0.82
MW 16-3	62	26	13	0.79	0.44	0.63	3.30	1.18	1.03	0.82	0.22	0.80
MW 17	66	24	10	1.46	0.26	0.19	4.23	1.11	1.04	0.65	0.16	0.80
MW 18	87	10	3	3.63	0.43	0.15	12.23	1.11	1.03	0.29	0.05	0.84

CPI values (carbon preference index; Bray and Evans 1961) vary from 1.10 to 1.33 and OEP values (odd-to-even predominance; Peters and Moldowan 1993) range from 0.96 to 1.10 (Table 3.4). Pristane (Pr) and phytane (Ph) are the dominant acyclic isoprenoids. The Pr/Ph ratio ranges from 0.48 to 5.03 (Table 3.4; Peters et al., 2005). Their concentrations are in most cases lower than those of the adjacent n-alkanes, i.e. Pr/n-C_{17} and Ph/n-C_{18} values are in the range of 0.15–1.64 and 0.15–1.10, respectively (Table 3.4). The iso-alkanes norpristane and farnesane are also abundant in all samples (Figs. 6a, b). The n-C_{17}/n-C_{27} ratios, indicating the relative abundance of marine/aquatic over higher land plant derived OM (Eglinton and Hamilton 1967; Guenther et al., 2013; Rodrigues et al., 2016), varies from 0.75 to 28.08 (Table 3.4). Correspondingly, the terrigenous/aquatic ratio (TAR; Bourbonniere and Meyers, 1996) is lower than 1.00 (0.04–0.57) except for sample MW 16–1 (TAR = 1.09; Table 3.4). The proxy ratio on the relative input of submerged/floating macrophytes compared to phytoplankton plus higher land plants (Paq; Ficken et al., 2000) varies between 0.10 and 0.84 (0.72 on average, Table 3.4). The waxiness index (WI; Peters et al., 2005) reflecting the contribution of terrestrial plants to the OM ranges between 0.22 and 2.18 (Table 3.4).
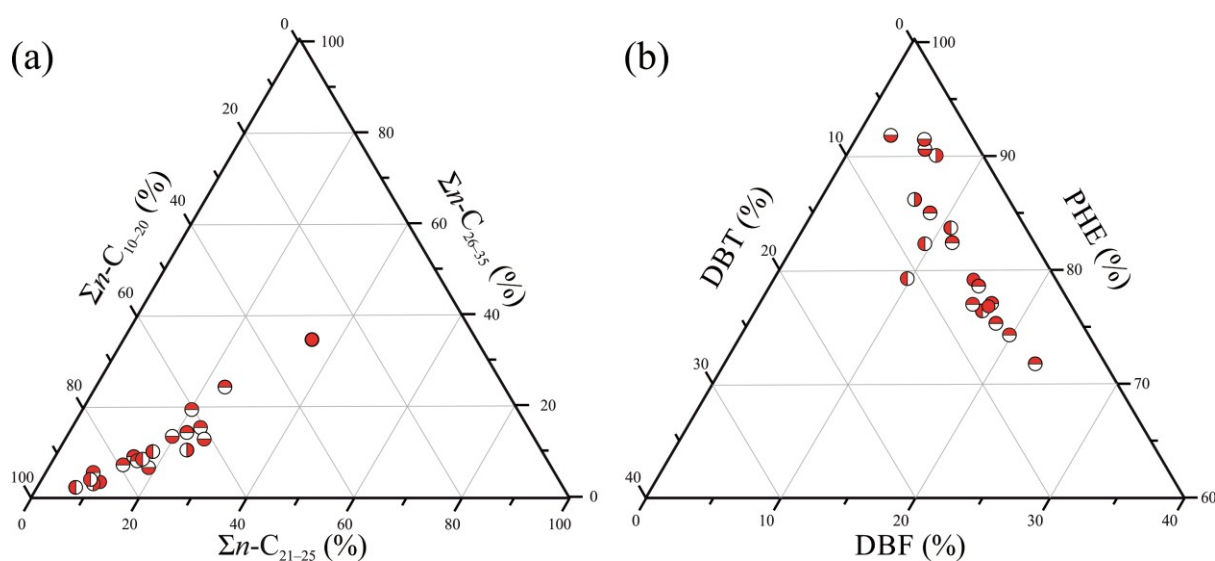
Fig. 3.7. Ternary diagrams showing (a) the n-alkane distributions and (b) the proportions of phenanthrene (PHE), dibenzofuran (DBF), and dibenzothiophene (DBT) of the Chang 7 Member samples.

3.5.4.2 Terpanes

Tricyclic terpanes (C_{19}-C_{26} Tri), C_{24} tetracyclic terpane (C_{24} Tet) and pentacyclic terpanes (hopanes) are widely distributed in all samples (Fig. 3.6c and d). The concentrations of C_{19} Tri and C_{24} Tet show large variations compared to the C_{19}/C_{23} Tri and the C_{24} Tet/(C_{24} Tet +C_{23} Tri) ratios, ranging from 0.23 to 2.42 and from 0.19 to 0.72, respectively (Table 3.5). The C_{22}/C_{21} Tri (0.15–3.32) and the C_{24}/C_{23} Tri (0.47–0.87) ratios are rather variable (Table 3.5). Large variations between the sam-ples are further observed in the ratio of C_{26}/C_{25} Tri (1.03–7.83).

The Ts/(Ts +Tm) ratio, applied as a thermal maturity parameter (Seifert and Moldowan 1978), ranges from 0.24 to 0.90. Besides Ts, other diahopanes, especially C_{30} diahopane (C_{30}* DH), are observed in the source rocks studied (Fig. 3.6c, d). Nor-moretane (C_{29} M) and moretane (C_{30} M) are thermally less stable than C_{29} nor-hopane (C_{29} H) and C_{30} hopane (C_{30} H) (George et al., 2001). The ratios of C_{30} H/(C_{30} H +C_{30} M) (0.89–0.95) and of C_{29} H/(C_{29} H +C_{29} M) (0.81–0.94) are close to or even exceed the respective equilibrium level (George et al., 2001). The Gam content is generally low as reflected by Gam/C_{30} hopane ratios < 0.20 (Fig. 3.6c and d, Table 3.5).

The 22S/(22S +22R) ratios for C_{31} and C_{32} homohopanes range from 0.44 to 0.61 and from 0.56 to 0.65, respectively (Table 3.5).

C_{30} H is more abundant than C_{31} 22R hopanes; i.e. ratios of C_{31} 22R/ C_{30} hopane (0.11–0.42) are <1 for the samples analyzed (Fig. 3.6c and d; Table 3.5). The samples are characterized by low C_{35} homohopane con-tents as indicated by homohopane index values (HHI, C_{35}/$\sum C_{31-35}$ 22S and 22R homohopanes; Peters and Moldowan 1991) and C_{35}/C_{34} 22S and 22R homohopane ratios of less than one (Table 3.5).

Table. 3.5 Biomarker parameters of tricyclic and tetracyclic terpanes, hopanes, and steranes of the source rocks from the Chang 7 Member in the mid-western Ordos Basin. Tri = tricyclic terpanes, Tet = tetracyclic terpanes, H = hopane, DH = diahopane, M = moretane, Gam = Gammacerane; HHI = homohopane index, steranes/hopanes = C_{27}–C_{29} regular steranes/C_{29}–C_{35} 17α-hopanes.

	Tricyclic and tetracyclic terpanes						Hopanes										Steranes						Sterane $\alpha\alpha\alpha$20R distribution (%)		
Sample ID	C_{19}/C_{23} Tri	C_{24}/C_{23} Tri	C_{22}/C_{21} Tri	C_{26}/C_{25} Tri	$C_{20}/(C_{23}$ Tri)	C_{24} Tet/(C_{24} Tet + C_{23} Tri)	Ts/(Tm+Ts)	$C_{30}H/(C_{30}H+C_{30}M)$	$C_{29}H/(C_{29}H+C_{30}H)$	$C_{30}DH/C_{30}H$	$C_{30}*/C_{30}H$	Gam/$C_{30}H$	$C_{31}H$ 22S/22(S+R)	$C_{32}H$ 22S/22(S+R)	$C_{35}/C_{34}H$	HHI	Steranes/hopanes	Pregnane/Homopregnane	$C_{21-22}/(C_{21-22}$+regular steranes)	C_{27}dia/(diasteranes+regular steranes)	C_{29}S/(R+S)	$C_{29}\beta\beta/(\beta\beta+\alpha\alpha)$	C_{27}	C_{28}	C_{29}
MW 1-1	1.69	0.54	0.21	1.03	0.89	0.20	0.55	0.89	0.90	0.15	0.13	0.17	0.57	0.62	0.41	0.03	0.19	3.63	0.20	0.25	0.42	0.42	33	25	42
MW 1-2	0.39	0.51	0.25	1.77	1.23	0.36	0.59	0.93	0.62	0.42	0.01	0.19	0.60	0.62	0.21	0.01	0.25	2.81	0.13	0.29	0.54	0.45	24	21	55
MW 2	0.49	0.51	0.36	6.19	1.19	0.72	0.24	0.89	0.59	0.19	0.05	0.28	0.58	0.59	0.42	0.04	0.17	1.72	0.01	0.16	0.38	0.50	20	9	71
MW 4	1.23	0.54	0.31	1.20	0.66	0.19	0.59	0.91	0.60	0.15	0.11	0.16	0.57	0.61	0.60	0.06	0.35	2.95	0.17	0.28	0.47	0.43	35	24	41
MW 5	0.36	0.60	0.33	1.53	0.83	0.32	0.59	0.88	0.58	0.27	0.11	0.18	0.58	0.62	0.50	0.06	0.23	2.99	0.09	0.39	0.61	0.50	25	21	54
MW 6	0.84	0.56	0.23	1.25	0.84	0.32	0.83	0.92	0.56	0.06	0.04	0.16	0.56	0.59	0.45	0.02	0.32	2.72	0.17	0.23	0.46	0.51	26	25	49
MW 7	0.23	0.55	0.26	1.16	0.81	0.22	0.85	0.92	0.60	0.27	0.14	0.22	0.58	0.60	0.68	0.08	0.28	2.36	0.18	0.26	0.46	0.43	25	34	41
MW 8	0.63	0.47	0.16	2.70	1.28	0.32	0.63	0.93	0.89	0.12	0.02	0.15	0.59	0.60	0.29	0.02	0.13	3.62	0.33	0.39	0.57	0.44	28	18	54
MW 10-1	0.49	0.66	0.22	3.74	1.27	0.61	0.55	0.90	0.90	0.12	0.05	0.17	0.56	0.58	0.46	0.04	0.14	2.05	0.15	0.16	0.50	0.51	21	28	51
MW 10-2	0.52	0.69	0.22	3.32	0.90	0.39	0.39	0.90	0.95	0.08	0.02	0.12	0.56	0.58	0.24	0.03	0.18	2.11	0.19	0.27	0.50	0.58	24	28	48
MW 11-1	0.35	0.76	0.23	7.83	0.58	0.34	0.54	0.90	0.93	0.12	0.07	0.11	0.56	0.62	0.70	0.07	0.52	2.43	0.04	0.31	0.53	0.58	19	31	50
MW 11-2	2.42	0.56	0.24	1.35	1.19	0.31	0.44	0.87	0.91	0.21	0.06	0.24	0.57	0.59	0.39	0.03	0.31	2.44	0.19	0.22	0.50	0.50	26	25	49
MW 12	0.66	0.57	0.26	2.16	1.07	0.48	0.27	0.89	0.91	0.13	0.08	0.25	0.61	0.61	0.47	0.04	0.21	2.14	0.05	0.25	0.52	0.53	14	18	68
MW 13	0.79	0.53	0.21	1.42	1.07	0.23	0.52	0.94	0.93	0.10	0.05	0.18	0.53	0.65	0.35	0.02	0.46	3.70	0.18	0.21	0.47	0.56	24	13	63
MW 16-1	0.59	0.77	0.15	1.87	0.64	0.35	0.55	0.93	0.89	0.17	0.07	0.11	0.54	0.59	0.72	0.04	0.35	4.24	0.04	0.25	0.60	0.53	22	30	48
MW 16-2	0.84	0.87	0.37	1.64	1.00	0.43	0.81	0.89	0.93	0.10	0.05	0.31	0.48	0.60	0.34	0.04	0.44	3.34	0.07	0.21	0.61	0.60	23	27	50
MW 16-3	1.37	0.70	0.41	1.35	0.67	0.34	0.84	0.89	0.89	0.36	0.10	0.42	0.48	0.60	0.44	0.04	0.48	3.59	0.16	0.42	0.48	0.54	23	19	58
MW 17	0.42	0.62	0.23	1.70	0.73	0.21	0.87	0.82	0.89	0.19	0.10	0.29	0.49	0.56	0.59	0.06	0.46	3.29	0.08	0.41	0.49	0.54	23	24	53
MW 18	0.92	0.69	0.31	1.28	1.12	0.37	0.83	0.86	0.89	1.42	0.16	0.29	0.52	0.64	0.19	0.02	0.61	3.02	0.61	0.39	0.44	0.54	21	13	66

3.5.4.3 Steroids

The concentration of steranes is lower than that of hopanes with the steranes/hopanes ratio ranging from 0.13 to 0.61 (Table 3.5). The sterane distributions are shown in Fig. 3.6e and f; they are characterized by higher proportions of C_{29} (41–71%) compared to C_{27} (14–35%) and C_{28} (9–31%) $\alpha\alpha\alpha$ 20R steranes (Table 3.5). The C_{29} $\alpha\alpha\alpha$ 20S/(20S +20R) ratio (Seifert and Moldowan 1986) ranges from 0.38 to 0.61 (Table 3.5).

The C_{29} $\beta\beta/(\beta\beta +\alpha\alpha)$ ratio ranges from 0.42 to 0.60 (Table 3.5). Equilibrium point for this ratio is reached at values of 0.67–0.71 cor-responding to around 0.9% VR_r (Seifert and Moldowan 1986).

C_{27} diasteranes are recognized in all samples but their abundances show large variations; the C_{27} diasteranes/(diasteranes +regular ster-anes) ratio varies from 0.15 to 0.43 (Fig. 3.6e and f; Table 3.5). Sample MW 17, for example, with a high abundance of C_{27} diasteranes also shows a marked contribution of short-chain $C_{21–C22}$ steroids (pregnane and homopregnane) in comparison to sample MW 2 (Fig. 3.6e and f). Pregnane is here more abundant than homopregnane with pregnane/homopreg-nane ratio values ranging from 1.72 to 4.24 (Table 3.5).

3.5.4.4 Aromatic hydrocarbons

The selected mass fragmentograms of the aromatic fraction from sample MW 17 are exemplarily shown in Fig. 3.6g. The samples are characterized by the predominant presence of 2-methylnaphthalene (2-MN), phenanthrene (PHE) and/or trimethylnaphthalenes (TMNs), whereas the proportions of sulfur-containing compounds such as dibenzothiophene (DBT) are low (DBT/PHE ratios are 0.01–0.14; Table 3.6).

The distributions of methylnaphthalenes, ethylnaphthalene (EN) and dimethylnaphthalene (DMN) isomers show that 1-MN is less abundant than 2-MN in all samples (Fig. 3.6g). There is a predominance of 2-EN over 1-EN. The most predominant compound in the TMN homologues is 1,3,6- TMN, while 1,2,4-TMN and 1,4,5-TMN have the lowest abundances in most samples. The tetramethylnaphthalenes (TeMNs) distribution is characterized by the predominance of 1,3,6,7-TeMN and 1,2,5,7- +1,3,6,8-TeMN. The methylphenanthrenes (MPs) distribution indicates that 9-MP is dominant while a predominance of 2-MP can be observed in some samples. With respect to dimethylphenanthrenes (DMPs), the studied samples are characterized by a relatively high abundance of 1,3- +3,9- +3,10-+2,10-DMP. The distribution of methylbiphenyls (MBPs) in all samples is similar: 3-MBP is most abundant followed by 4-MBP. The distribution of dimethyldibenzothiophenes (DMDBTs) shows that 3,6- DMDBT is present in relatively high amounts in most samples, but 2,7- +3,7- +2,8-DMDBT or 4,6-DMDPT are predominant in individual samples such as MW 2, MW 7 and MW 11–2.

The normalized distribution of PHE, DBF, and DBT shows that PHE occurs in highest relative concentration (71.63%–91.63%) followed by DBF (2.42%–23.15%) and DBT (3.43%–10.95%) (Fig. 3.7b; Table 3.6).

Table 3.6. Parameters of the aromatic fractions and corresponding calculated vitrinite reflectances for the Chang 7 Member samples.

Sample ID	Log MP (1/9,3+3,10 +2,10 +3,10 DMP)	Log (1,7/1,3+3,9 /1,3,7 TMN)	Log (1,2,7 /1,3,7 TMN)	Log (1,2,5 /1,3,6 TMN)	DBT /PHE	DBT	DBF	PHE	DM PR (%) MPR-1	VR_D MPI (%) MPI-1	MPI VR (%) R	MD MDR R (%)	VR TN MDR R-2	TN R-1	VR TNR-2 (%)	TM NR R-1	Te MN MN R-1	Te MN MN R-2	MP DF MPDF (%)	VR R	MBP DM DR
MW 1-1	-0.12	-0.39	-0.74	-0.51	0.08	6.25	18.38	75.37	0.23	0.67	0.75	0.85	5.18	0.89	1.59	0.97	0.98	0.68	0.90	0.64	0.50	0.96	46.37	0.51
MW 1-2	-0.09	-0.35	-0.65	-0.38	0.08	5.83	19.91	74.26	0.30	0.80	0.74	0.84	5.51	0.91	1.46	1.03	1.02	0.65	1.12	0.60	0.51	0.97	61.91	0.43
MW 2	-0.12	-0.43	-0.51	-0.07	0.08	5.78	17.24	76.99	0.16	0.47	0.61	0.77	3.36	0.76	1.04	0.89	0.93	0.47	0.42	0.34	0.49	0.94	31.41	0.42
MW 4	-0.12	-0.32	-0.48	-0.26	0.08	5.99	15.51	78.51	0.29	0.77	0.75	0.85	3.53	0.77	1.26	0.87	0.92	0.53	0.68	0.51	0.50	0.96	30.31	0.46
MW 5	-0.13	-0.21	-0.52	-0.22	0.07	6.05	11.65	82.30	0.24	0.68	0.72	0.83	3.64	0.78	1.11	0.82	0.89	0.51	0.55	0.45	0.50	0.96	25.29	0.45
MW 6	-0.13	-0.12	-0.49	-0.33	0.10	7.33	15.57	77.10	0.20	0.59	0.66	0.80	2.99	0.73	1.12	0.63	0.78	0.45	0.22	0.52	0.45	0.85	27.54	0.27
MW 7	-0.13	-0.37	-0.65	-0.47	0.07	5.22	23.15	71.63	0.30	0.80	0.68	0.81	5.50	0.91	1.52	1.05	1.03	0.70	0.45	0.50	0.50	0.97	52.55	0.46
MW 8	-0.15	-0.25	-0.64	-0.39	0.08	6.39	8.71	84.90	0.24	0.69	0.70	0.82	4.59	0.84	1.31	0.83	0.90	0.58	0.80	0.53	0.47	0.89	30.44	0.41
MW 10-1	-0.21	-0.23	-0.34	-0.34	0.07	5.51	10.90	83.59	0.15	0.43	0.71	0.83	4.98	0.87	0.65	0.60	0.76	0.55	0.40	0.61	0.43	0.80	14.00	0.37
MW 10-2	-0.12	-0.17	-0.65	-0.44	0.10	8.14	9.67	82.20	0.18	0.55	0.71	0.82	5.08	0.88	0.79	0.60	0.76	0.56	0.40	0.60	0.42	0.78	14.90	0.41
MW 11-1	-0.10	-0.32	-0.94	-0.86	0.14	10.95	9.88	79.17	0.30	0.80	0.86	0.92	8.33	1.12	1.86	1.09	1.05	0.84	2.26	0.78	0.51	0.98	81.93	0.50
MW 11-2	-0.12	-0.08	-0.50	-0.38	0.09	6.83	16.68	76.50	0.18	0.54	0.46	0.68	2.97	0.73	1.62	1.05	1.03	0.64	1.10	0.59	0.43	0.81	51.68	0.45
MW 12	-0.12	-0.08	-0.60	-0.29	0.08	6.13	17.13	76.75	0.18	0.54	0.60	0.76	2.97	0.73	1.22	0.71	0.83	0.46	0.31	0.55	0.43	0.81	15.34	0.31
MW 13	-0.14	-0.32	-0.58	-0.36	0.08	6.11	14.64	79.25	0.31	0.81	0.80	0.88	4.18	0.82	1.43	0.94	0.97	0.60	0.73	0.55	0.52	1.00	44.50	0.39
MW 16-1	-0.19	-0.16	-0.64	-0.63	0.06	5.94	2.42	91.63	0.20	0.59	0.95	0.97	4.61	0.85	1.28	0.69	0.81	0.64	0.51	0.58	0.45	0.85	33.54	0.36
MW 16-2	-0.19	-0.34	-0.62	-0.66	0.04	3.61	5.08	91.31	0.20	0.58	0.80	0.88	8.39	1.12	1.14	0.71	0.83	0.69	0.62	0.54	0.44	0.82	23.10	0.58
MW 16-3	-0.18	-0.34	-0.78	-0.64	0.04	4.00	5.55	90.46	0.19	0.57	0.74	0.85	7.41	1.05	0.97	0.78	0.87	0.74	1.49	0.64	0.42	0.78	20.51	0.54
MW 17	-0.18	-0.25	-0.48	-0.63	0.04	3.43	6.66	89.91	0.21	0.62	0.79	0.87	5.60	0.92	1.13	0.68	0.81	0.66	0.65	0.56	0.45	0.83	24.26	0.51
MW 18	-0.12	-0.29	-0.88	-1.04	0.08	6.95	6.98	86.07	0.30	0.80	0.96	0.98	9.50	1.20	1.64	0.89	0.93	0.86	0.23	0.76	0.53	1.01	25.39	0.43

TNR-1: trimethylnaphthalene ratio 1 (2,3,6-TMN/[1,4,6- + 1,3,5-TMN]). Alexander et al., 1985.

TNR-2: trimethylnaphthalene ratio 2 (2,3,6- + 1,3,7-TMN/[1,4,6- + 1,3,5- + 1,3,6-TMN]). Radke et al., 1986.

VR_{TNR-2}: calculated reflectance from TNR-2 (0.60 × TNR-2 + 0.40). Radke et al., 1994.

TMNR: trimethylnaphthalene ratio (1,3,7-TMN/[1,3,7-TMN + 1,2,5-TMN]). van Aarssen et al., 1999.

TeMNr-1: tetramethylnaphthalene ratio 1 (2,3,6,7-TeMN/1,2,3,6-TeMN). George et al., 1996.

TeMNr-2: tetramethylnaphthalene ratio 2 (1,3,6,7-TeMN/[1,3,6,7- + 1,2,5,6-TeMN]). van Aarssen et al., 1999.

MPI-1: methylphenanthrene index 1 (1.89 × [3-MP + 2-MP]/[P + 1.26 × (9-MP + 1-MP)]). Cassani et al., 1988.

VR_{MPI-1}: calculated reflectance from MPI-1 (0.60 × MPI-1 + 0.40). Radke and Welte, 1983.

MPDF: methylphenanthrene distribution fraction ([3-MP + 2-MP]/RMPs). Cassani et al., 1988.

VR_{MPDF}: calculated reflectance from MPDF (2.242 × MPDF-0.16). Kvalheim et al., 1987.

MBPR: methylbiphenyl ratio (3-MBP/2-MBP). Alexander et al., 1986.

MDR: methyldibenzothiophene ratio (4-MDBT/1-MDBT). Radke et al., 1986.

VR_{MDR}: calculated reflectance from MDR (0.073 × MDR + 0.51). Kvalheim et al., 1987.

DMDR: dimethyldibenzothiophene ratio (4,6-DMDBT/[3,6- + 2,6-DMDBT]). George et al., 2001.

DMPR: dimethylphenanthrene ratio ([3,5- + 2,6- + 2,7-DMP]/[1,3- + 3,9- + 2,10- + 3,10 + 1,6- + 2,9- + 2,5-DMP]). Radke et al., 1982.

VR_{DMPR}: calculated reflectance from DMPR (1.17 × log10 DMPR + 1.14). Radke 1984.

Moreover, trimethylphenanthrenes (TMPs, $m/z = 220$); 4-ring polycyclic aromatic PAHs including fluoranthene and pyrene ($m/z = 202$), methylfluoranthenes, benzo[a]fluorene, benzo[b]fluorene, 2-methylpyrene, 4-methylpyrene and 1-methylpyrene ($m/z = 216$); 5-ring PAHs including chrysene ($m/z = 228$); benzo[e]pyrene, benzo[a] pyrene, and perylene ($m/z = 252$); and 6-ring PAHs including indeno [1,2,3-cd]pyrene and benzo[ghi]perylene ($m/z = 276$) are observed (Appendix Figure A.3.1).

Various specific aromatic indices which are representative of plant species, depositional environment, and thermal maturity are given in Table 3.6 and are discussed in more detail in the following sections.

3.6 Discussion

3.6.1 Paleo-depositional environment

The TOC/TS ratios in the Chang 7 Member indicate a non-marine/ freshwater depositional environment (Fig. 3.8; after Berner 1984), which is consistent with other data, such as high C_{26}/C_{25} Tri ratios and low C_{31} 22R/C_{30} H ratios (Peters et al., 2005; Table 3.5). The low amount of gammacerane along with Pr/Ph ratios >1 (except for the samples from MW 16 well; Table 3.4) further indicate freshwater conditions without any salinity stratification during the deposition of the Chang 7 Member (ten Haven et al., 1987; Sinninghe Damst´e et al., 1995a; Peters et al., 2005). The relatively low C_{28} steroid proportion is typical of limnic environments (Volkman, 1986; Peters et al., 2005) and the low steranes/hopanes ratio of <1 (Peters et al., 2005) is in agreement with the above stated findings. The high abundance of DBF compared to both DBT (Fan et al., 1990, 1991) and MDBTs (Hughes 1984) as well as the predominance of MPs over MDBTs (Radke et al., 2000) also indicates that the studied samples were deposited under conditions not affected by marine waters. The presence of sufficient iron, limiting the sulfurization of OM can be visualized by comparing TS values and DBT/PHE ratios (Fig. 3.9a; Song et al., 2017). The low organic sulfur contents as reflected by low DBT/PHE ratios of the Chang 7 Member shales (Table 3.6) can be explained by the low sulfurization of OM due to the presence of iron leading to the utilization of sulfur in the formation of pyrite, which is typically most pronounced in freshwater containing little sulfate. Such pattern is often observed in clay-rich source rocks while high organic sulfur contents have been reported for carbonate source rocks (Rullk¨otter et al., 1990; Hughes et al., 1995; Barakat and Rullk¨otter, 1999; Grohmann et al., 2019).

Applying the paleo-depositional plot after Hughes et al., (1995), which sets the amount of organic sulfur in relation to the OM's origin, allows for the classification of depositional setting based on data from well-studied source rocks. Fig. 3.9b shows that the analyzed samples of the Chang 7 Member plot in the sulfate-poor environments typical for shales deposited as lake sediments. However, Pr/Ph ratios reveal some differences for the sample-set analyzed in this study. Samples taken from the well drilled in the central part of the former lake (MW 16 well) show distinctly lower values than those originating from wells further north (MW 1 and MW 2 wells; Figs. 1b, 9b) which show fluvio-deltaic characteristics.

61
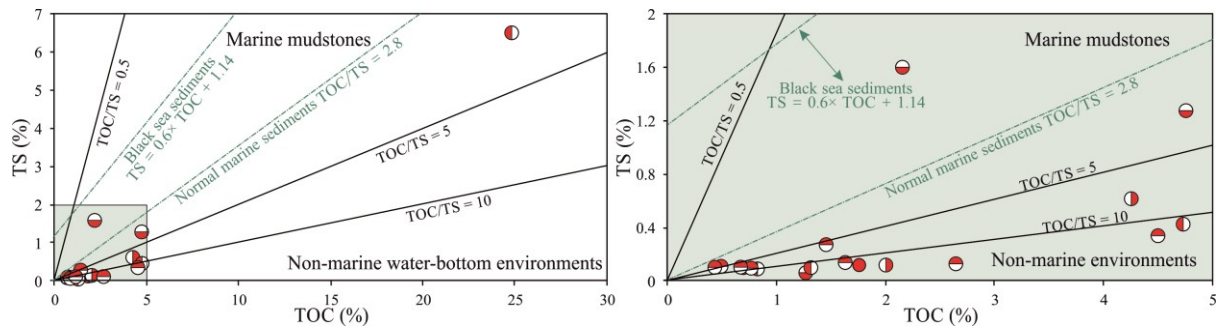
Fig. 3.8. TS vs. TOC indicating depositional environments of the Chang 7 Member source rocks. Data of normal marine sediments and Black Sea sediments from Berner and Raiswell, 1983 and Leventhal 1983, respectively.

Unlike in marine environments where the TOC content is commonly negatively related to the carbonate content but shows positive correla-tion to silicate contents (Sachse et al., 2012a; Bou Daher et al., 2015; Ghassal et al., 2018), organic-rich shales which are dominated by silicate minerals with sufficient nutrient supply often show a positive relation-ship between TOC values and carbonate contents (Rippen et al., 2013). In the shales of the Chang 7 Member, Corg* shows an unclear relationship with CaCO3 content (both calculated from measured TOC, TS and TIC), indicating that calcareous plankton/bacteria had only little contribution to the OM (Appendix Figure A3.2).
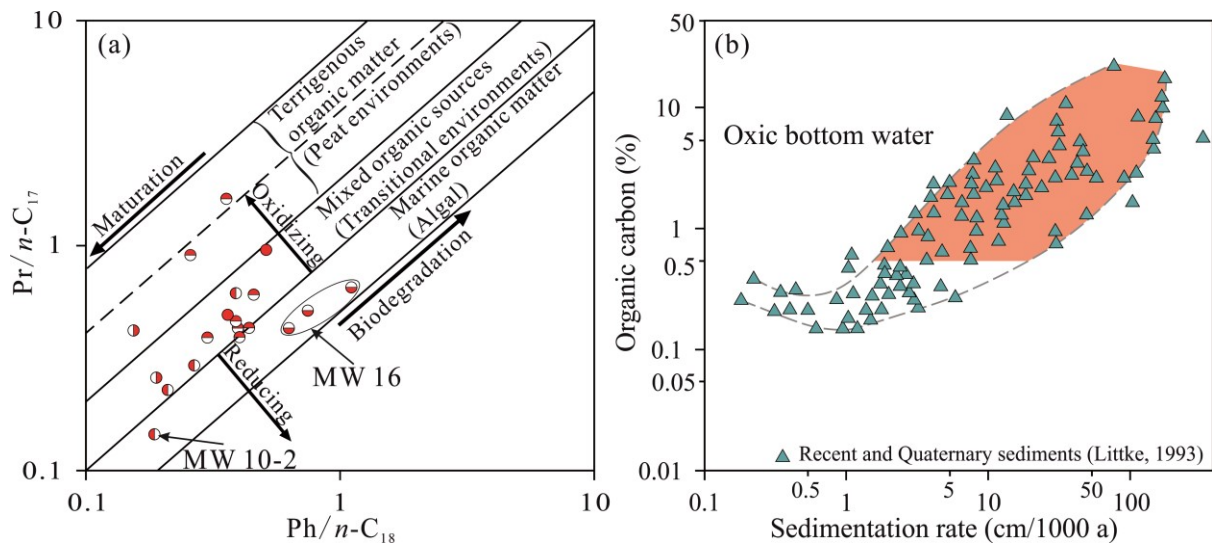
Fig. 3.9. Plots of pristane/n-C$_{17}$ vs. phytane/n-C$_{18}$ reflecting kerogen type, maturity, and depositional environment (after Shanmugam, 1985) (a) and organic carbon content vs. sedimentation rate (modified after Littke, 1993) (b). The range of sedimentation rates for the Chang 7 member samples is marked by the red area.

Oxygenated bottom water depositional conditions are supported by the high Pr over Ph ratios (Didyk et al., 1978) in most areas except the central part of the studied part of the Ordos Basin, represented by sample MW 16 (Fig. 3.1c). The ratio is related to different anaerobic and aerobic degradation pathways of the chlorophyll side-chain, but should always be used in combination with

other redox proxies, such as TOC/TS ratios (Sachse et al., 2011; Rippen et al., 2013; Song et al., 2014; Ghassal et al., 2018). An oxygenated and/or sulfate-depleted depositional environment is further indicated by high TOC/TS ratios (1.35–21.17; Fig. 3.8) as well as very low values of HHI and C_{35}/C_{34} 22S and 22R homohopane (Table 3.5; Köster et al., 1997; Peters et al., 2005; Sachse et al., 2012b). Classically, the occurrence of $C_{30}*$ DH ($C_{30}*$ DH/C_{30} H ratios are 0.06–1.42; Table 3.5) indicates deposition in clay-rich settings under oxic or suboxic conditions (Nytoft et al., 2006; Li et al., 2009; Baydjanova and George 2019). Such a depositional environment is also demonstrated by the positions of the analyzed samples in the Pr/n-C_{17} vs. Ph/n-C_{18} diagram (Fig. 3.10a). The samples NW 10–2 and NW 16 close to the field of reducing conditions in Fig. 3.10a also show the highest HI values.
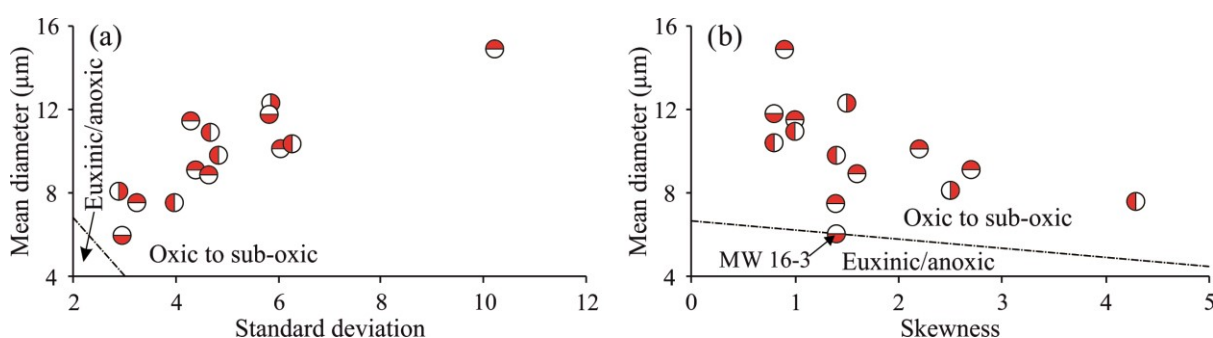
Fig. 3.10. Results of the pyrite framboids size distribution showing (a) mean framboid diameters vs. standard deviation and (b) skewness of diameter distribution (plot after Wilkin et al., 1996).

The presence of large framboidal pyrites (Figs. 5a, 11) with a general skewness towards larger diameters and framboidal pyrite aggregation (Figs. 5c, e) are further indicators of rather oxic conditions during the sedimentation of the Chang 7 Member shales (Wilkin et al., 1996). These framboidal pyrites can be observed in almost all samples except samples MW–12 and MW–13 (Fig. 3.11). The rather large framboidal pyrites as well as fine, dot-like pyrites inserted in or next to OM (Fig. 3.5a) indicate a formation during local reducing conditions caused by oxygen depletion via OM degradation at the early diagenesis stage (Canfield et al., 1992). Similar findings on shales from the Chang 7 Member have been made on other samples from the southwestern Ordos Basin by Yuan et al. (2017), who reported average diameters of 10.6 μm to 13.8 μm.

The paleo-redox conditions concluded from the data presented here are in line with findings made by Chen et al. (2019a) who also indicated sub-oxic to oxic conditions during the formation of organic-rich shales of the Chang 7 Member based on the isotopic composition of nitrogen.

Usually, in oxic to sub-oxic sub-aquatic environments, a high concentration of well preserved OM can only occur in rather calm waters and at high sedimentation rates (Meyers and Ishiwatari 1993; Pichevin et al., 2004). The relationship between organic carbon content and sedimentation rate in recent and Quaternary sediments is shown in Fig. 3.10b (Littke 1993). For the Chang 7 Member samples, considering the original organic carbon content (see eq. 1), sedimentation rates ranging from at least 1.5 cm/1000 years to more than 1 m/1000 years are expected (red area in Fig. 3.10b). This is consistent

with the large range between moderate to high sedimentation rates suggested by Chen et al. (2019b) for the Chang 7 Member in the Triassic Ordos Basin. The low HHI values and the decreasing trend from C_{31} to C_{35} homohopane contents further support a clastic depositional environment for the Chang 7 Member (Peters and Moldowan 1991; Sinninghe Damsté et al., 1995; Waseda and Nishita 1998).
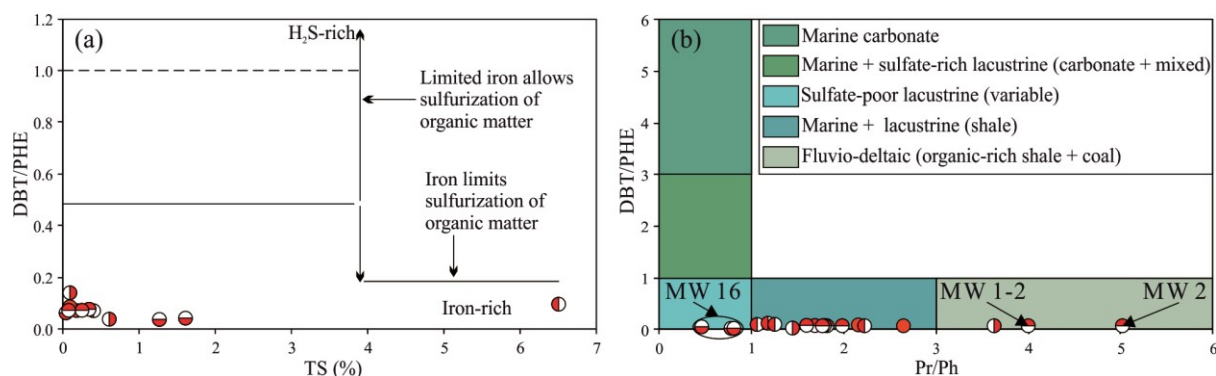
Fig. 3.11. Dibenzothiophene/phenanthrene ratio vs. TS values (after Song et al., 2017) (a) and Pr/Ph (after Hughes et al., 1995) (b), reflecting depositional environment and lithology of the Chang 7 Member samples.

3.6.2 Origin of organic matter

Microscopy data shows that the OM in the Chang 7 Member is mainly composed of fragments (from about 1 to >200 μm) of fusinite and vitrinite (Fig. 3.5a-c) with a small number of algae-derived OM, mainly in form of lamalginite (L) and finely dispersed liptodetrinite within the mineral matrix (Fig. 3.5d). Comparing the volumetric percentages of counted macerals with TOC values, it gets obvious that almost all OM is visible in the form of macerals and very little is submicroscopically small. This observation is in accordance with the classification of OM as type II-III kerogen derived from Rock-Eval results (Fig. 3.4a). The contribution of terrestrial derived OM to the Chang 7 Member shales has been reported before, as palynomorphs including bisaccate pollen and an Asseretospora-Walchiites assemblage (Ji and Meng, 2006; Ji et al., 2010).

On the other hand, the studied samples are characterized on a molecular level by the predominance of short-chain alkanes (n-$C_{10–20}$) with n-C_{17} and n-C_{18} being most pronounced, which is typically attributed to algae and cyanobacteria (Hunt 1996), while the relative contribution of long-chained n-alkanes (n-$C_{26–35}$) derived from waxes of higher land plants (Eglinton and Hamilton 1967; Killops and Killops 2005) is relatively low. Further, the high proportion of short-chain n-alkanes and the absence of an unresolved complex mixture in gas chromatograms (Fig. 3.6a, b) indicate that no significant biodegradation took place (Hedges et al., 2000; Song et al., 2015a; Ghassal et al., 2018). Only minor terrigenous input of OM is expected based on the n-C_{17}/n-C_{27} ratios and TAR values (Brooks et al., 1969; Connan and Cassou, 1980; Bourbonniere and Meyers, 1996), and only some of the samples show moderate to high (>0.8) WI values which are used as a proxy of a substantial contribution of terrestrial OM (Table 3.4). The high Paq values (>0.4; Table 3.4) related to the concentrations of mid molecular

weight n-alkanes (n-$C_{21–25}$) and the second-largest peak of n-C_{23} and n-C_{25} in part of the samples (Fig. 3.6a, b) indicate that submerged macrophytes indeed contributed to the accu-mulated OM. Fig. 3.6a and b indicates that emergent aquatic plants (typically producing C_{25}, C_{27} or C_{29} n-alkanes during diagenesis) and conifers (C_{27} or C_{29} n-alkanes) are relatively more important than other woody terrestrial vegetation and mangroves (typically producing C_{29}, C_{31} or C_{33} n-alkanes; He et al., 2020). However, these conclusions drawn by the evaluation of GC-FID data should be taken with caution, since the n-alkane distribution is easily affected by maturity (Peters et al., 2005). Furthermore, the source information from n-alkanes is not always conclusive due to their relatively simple structure and the complexity of other components present in waxes (Kolattukudy 1976). For example, the extracts of conifer waxes show n-alkanes varying between C_{16} and C_{35} with peak carbon varying from C_{23} to C_{33} (Oros et al., 1999), and terrigenous OM producing predominantly short chain n-alkanes has been observed in some immature to early mature Cod′o Formation samples in the S̃ao Luís Basin in Brazil (Gonzales et al., 2020). Finally, CPI values of the samples studied here (Table 3.4) are consistent with terrestrial OM input, if the maturity stage is considered. Thus, the distribution of n-alkanes (e.g. Fig. 3.6a) fits well with type II-III kerogen. In fact, for the samples analyzed here, petrographic data (maceral composition; Table 3.3) and only moderate HI values not exceeding 400 mg HC/g TOC (Table 3.2) do not support such conclusions; the same holds true for the low sterane/hopane ratios (Table 3.5). Steranes originate mainly from algae and higher plants, and hopanes originate from the cell material of bacteria (Rohmer and Ourisson 1976). In samples dominated by terrigenous OM, there is commonly also a high amount of (submi-croscopic) bacterial biomass; therefore sterane/hopane ratios are low. The presence of steranes and diasteranes is further regarded as evidence for eukaryotic input (cf. Summons et al., 2006). A predominance of C_{27} steranes is characteristic of algal input (Volkman, 2003), whereas a strong contribution of C_{29} steranes is usually associated with terrestrial higher plant (Huang and Meinschein, 1979; Moldowan et al., 1986; Volkman, 2003). As shown in Fig. 3.12a, most samples are characterized as clay-rich source rocks deposited under oxic conditions with significant terrigenous OM input. The ternary diagram of the C_{27}, C_{28} and C_{29} ααα 20R steranes distributions (Fig. 3.12b; Huang and Meinschein 1979) indicates a mixed OM origin from algae, higher land plants and bacteria deposited in a terrestrial environment. Samples interpreted to be deposited under bay/estuary environments are mainly concentrated in the northwestern study area, such as samples MW 1–1, MW 4, and MW 7 (planktonic/bacterial; Fig. 3.12b). High proportions of C_{19} and C_{20} Tri further point towards a substantial terrestrial OM input into the basin (Peters et al., 2005), whereas C_{23} Tri is predominant in a reducing marine carbonate settings with high contribution of marine OM (Waples and Machihara, 1991; Tao et al., 2015). Large variations of C_{19}/C_{23} Tri and C_{24} Tet/(C_{24} Tet +C_{23} Tri) ratios are indicative of a mixed lacustrine aquatic algal-bacterial and terrestrial OM, which is consistent with the low to moderate ratios of C_{24}/C_{23} Tri and low of C_{22}/C_{21} Tri (Table 3.5) (Peters and Moldowan, 1993; Preston and Edwards, 2000; Peters et al., 2005; Volk et al., 2005; Adegoke et al., 2014).
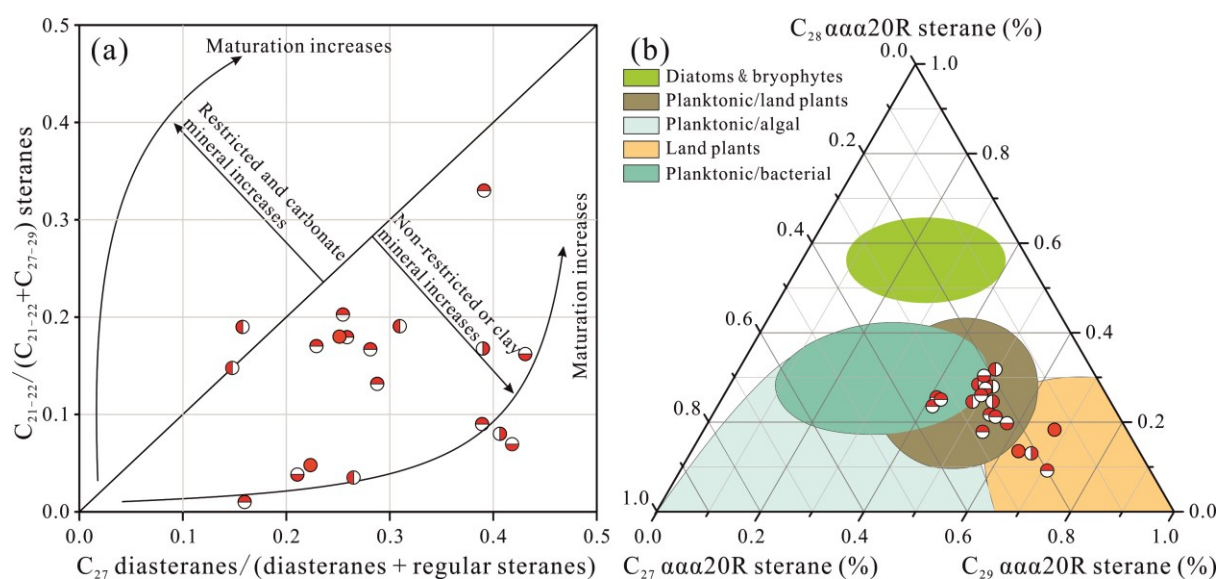
Fig. 3.12. Plot of (a) $C_{21-22}/(C_{21-22} + C_{27-29})$ sterane vs. C_{27} diasteranes/(diasteranes + regular steranes) (modified after Wang et al., 2015) and (b) ternary diagram showing the distribution of C_{27}, C_{28} and C_{29} steranes (modified after Huang and Meinschein, 1979).

Aromatic hydrocarbons such as 1,7-DMP, 1-MP, and 1,2,5-TMN can originate from conifers, such as Araucariaceae resins (Alexander et al., 1988). Such species might have been the primary source for the terrestrial OM input into the paleo-lake during the deposition of the Chang 7 Member. The high abundances of these compounds in analyzed shales indicate a strong contribution of coniferous plant species (Fig. 3.6g). This interpretation is consistent with the assumption that forests surrounding the area were indeed dominated by conifers in the mid-latitudes of eastern Asia during the Late Triassic–Early Jurassic (Pole et al., 2016). In addition, the palynoflora was found to be dominated by bisaccate pollen produced by conifers in the Yanchang Formation (Ji and Meng, 2006). Additionally, values of the log (1,2,7-TMN/1,3,7-TMN) ratio (see Table 3.6) suggest a lack of contribution of plant matter originated from angiosperm species (Strachan, 1988), which is in agreement with the biological evolution suggested for the surrounding area at the time of the formation of the Chang 7 Member. However, log ratios of 1-MP/9-MP, 1,2,5-TMN/1,3,6-TMN and 1,7- DMP/(1,3- +3,9- +2,10- +3,10- DMP) which were used as indicators of OM input from coniferous higher plants are well below the threshold values suggested by Alexander (1988) (Table 3.6). This might be explained by the vulnerability of these parameters to thermal alteration (van Aarssen et al., 1999; Arouri and McKirdy, 2005), lithology or OM sources (Grice et al., 2007; Alexander et al., 1995; van Aarssen et al., 1999). The presence of abundant 1,6-DMN, 1,2,5-TMN and 1,7-DMP is further prove of land plant OM input (Romero-Sarmiento et al., 2011). These compounds show high abundances in the Chang 7 Member sam-ples (Fig. 3.6g), and the presence of abundant naphthalene, TMPs, chrysene and perylene, etc. are typically indicative of terrigenous higher plant input (Chaffee and Johns 1983; Chaffee and Fookes 1988). The terrestrial nature of the OM is further indicated by PHE relative abun-dances (compared to DBF and DBT) exceeding 70% (Table 3.6 and Fig. 3.7b; Radke et al., 2000).

The occurrence of PAHs including pyrene, fluoranthene, and chrys-ene can be related to the significant presence of fusinite macerals, most particularly pyrofusinite, in the OM (Romero-Sarmiento et al., 2011). Inertinite contents of 10.3% on average (on a mineral matter-free basis, calculated from Table 3.3), presented by mainly structured, oxidized particles (Figs. 5b,c) in the samples analyzed here, combined with the identification of compounds such as benzo[a]pyrene, benzo[e]pyrene, benzo[b]fluoranthene, perylene, indeno[1,2,3-cd]pyrene, and benzo [ghi]perylene indicate that wildfires occurred close to the examined area (Killops and Massoud 1992; Lima et al., 2005; Huang et al., 2015; Jar-oszewicz et al., 2018). These events may be partly related to frequent volcanic eruptions that reportedly occurred during the corresponding period of the Chang 7 member deposition in the Qinling Mountain area in the southern part of the basin (Fig. 3.1b; Zhang et al., 2017, Zhang et al., 2020). Moreover, the in part high OM contents of the Chang 7 shales may also be related to re-occurring volcanic eruptions and volcanic ash, promoting the prosperity of bacteria and algae resulting in an increased primary bio-productivity (Erbacher et al., 1996; Duggen et al., 2007; Olgun et al., 2013). In summary, the source-related characteristics of the Chang 7 Member samples indicate a strong contribution of terrestrial-derived OM, to a great extent originating from gymnosperms (conifers) as well as the contribution of algal-bacterial-macrophytic OM deposited at rather high sedimentation rates in a siliciclastic lake environment. Proxies for redox conditions reveal a sulfate poor-lacustrine environment in the central part of the basin (MW 16 well) and fluvio-deltaic environments northwestward (MW 1 well). The central part of the study area (location of MW 16 well) shows slightly more reducing bottom water characteristics during deposition (Figs. 1b, 8, 10a).

3.6.3 Thermal maturity and source rock characteristics

The VR_r and Rock-Eval T_{max} values (Fig. 3.13a) indicate a maturity of the samples within the oil window, while the shales have not yet reached 50% conversion to petroleum (Fig. 3.4). This interpretation is consistent with the following molecular thermal maturity parameters derived from data of the aliphatic as well as aromatic fractions. A comparison of the ratios of C_{29} $\alpha\alpha\alpha$ 20S/(20S +20R) and C_{29} $\beta\beta/(\beta\beta +\alpha\alpha)$ as well as of the terpane ratios of C_{31} and C_{32} homohopanes 22S/(22S +22R) illustrate a thermal maturity between the early and main oil window (Fig. 3.13b and c; Peters et al., 2005). Similar maturity conditions can be recognized from the plots of C_{29} $\alpha\beta/(\alpha\beta +\beta\alpha)$ hopane vs. C_{30} $\alpha\beta/(\alpha\beta +\beta\alpha)$ hopane and CPI vs. OEP (Fig. 3.13d, e). The steroid pregnane has a higher abundance than homopregnane (Fig. 3.6f), which is consistent with a peak oil window maturity (George et al., 2008). This relatively homogeneous maturity over a wide area corresponds to the rather equal thickness of the Triassic Yanchang Formation along the whole Yishan Slope (Fig. 3.1c) and later a rather consistent burial over large areas during the Jurassic and Early Cretaceous. The ratio of Ts/(Ts +Tm) vs. C_{27} diasteranes/ (diasteranes +regular steranes) (Fig. 3.13f) may indicate a larger variability of maturity, but both parameters can be affected by variations in the OM facies (Farrimond et al., 1998; Song et al., 2015b; Peters et al., 2005; Sachse et al., 2011; Baniasad et al., 2017).
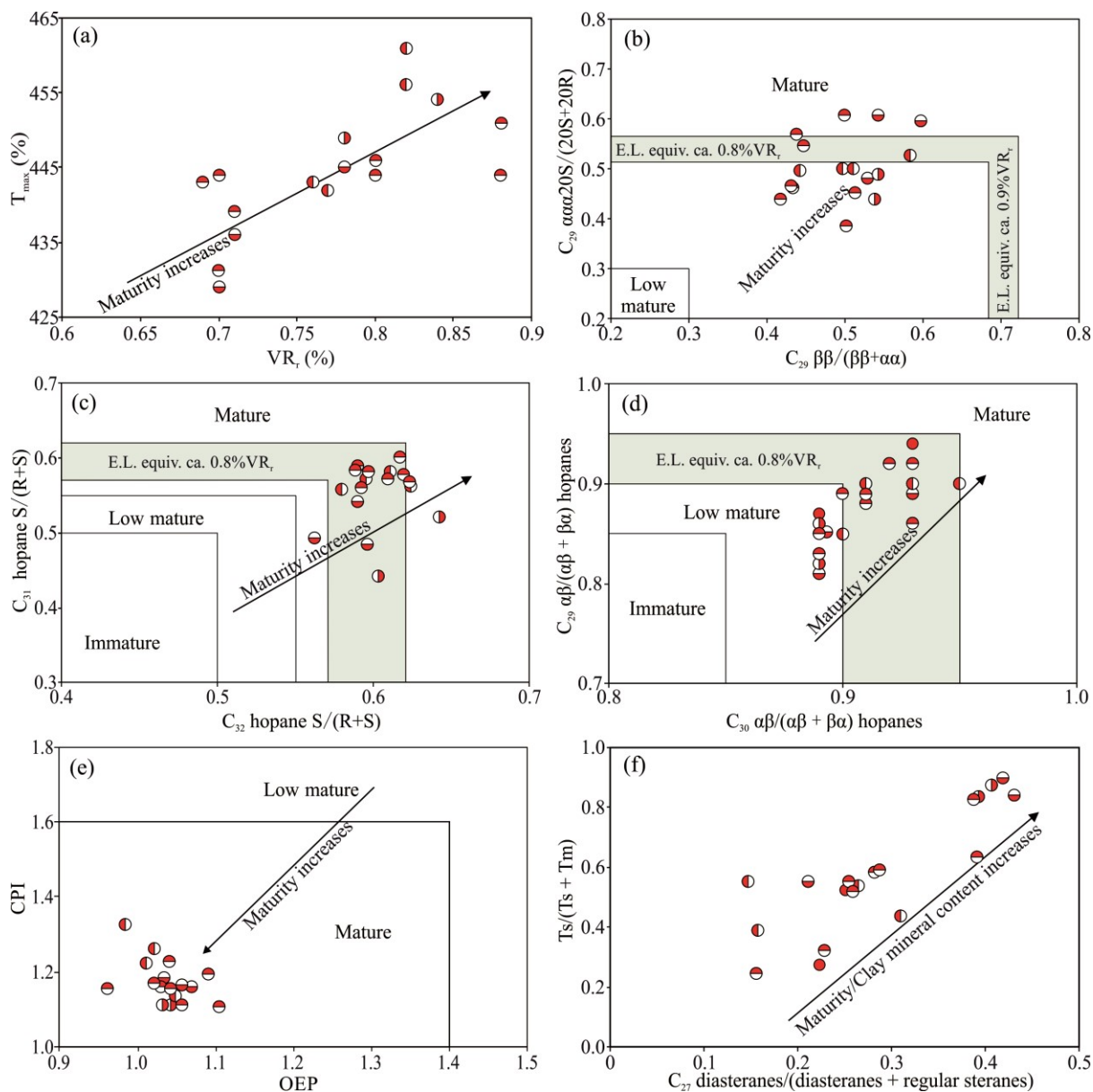
Fig. 3.13. Rock-Eval T$_{max}$, vitrinite reflectance and molecular thermal maturity indicators of the Chang 7 Member samples. (a) T$_{max}$ vs. VR$_r$, (b) C$_{29}$ ααα 20S/(20S + 20R) vs. C$_{29}$ ββ/(ββ+αα), (c) C$_{31}$ homohopane 22S/(22S + 22R) vs. C$_{32}$ homohopane 22S/(22S + 22R), (d) C$_{29}$ αβ/(αβ+βα) hopanes vs. C$_{30}$ αβ/(αβ + βα) hopanes (after George et al., 2001), (e) CPI vs. OEP, and (f) Ts/(Ts + Tm) vs. C$_{27}$ diasteranes/(diasteranes + regular steranes). E.L. equiv. = equilibration levels equivalent to vitrinite reflectance values (taken from Peters et al., 2005).

Aromatic maturity parameters including MPI-1 (Radke and Welte, 1983), TNR-2 (Radke et al., 1994) and MDR (Radke et al., 1986) (Table 3.6) indicate that the samples are at the main stage of oil generation, while TMNR, TeMNR-1, TeMNR-2 and DMPR indicate somewhat lower, early to peak oil window maturities (Table 3.6; van Aarssen et al., 1999; George and Ahmed, 2002) which is in better agreement with the VR$_r$ and Rock- Eval T$_{max}$ data. The MBPR is based on published calibrations (Cumbers et al., 1987) and the low values of DMDR based on MDBT are consistent with early to peak oil window maturities (Radke 1988; George and Ahmed, 2002). The TNR-1 and MPDF ratios also

indicate a peak to late oil window maturity (George and Ahmed, 2002). In summary, various aromatic indicators show slight discrepancies, although all values are in line with an oil window maturity (George and Ahmed 2002).

In summary, the thermal maturity data are remarkably uniform within the early oil window stage, although the samples were taken from the entire, large western Ordos Basin. Obviously, burial history within this area was quite consistent, affecting marginal and central parts in a similar way.

Regarding their moderate to very high TOC contents and HI values, most samples are characterized as good to excellent source rocks, while few samples have poor to fair source rock potential (TOC content <1.0% and $S_1 + S_2$ content <6 mg/g). The quality of the source rocks is not as good as previously reported (e.g. Xu et al., 2019), which might be caused by the sampling locations further towards the margin of the basin. Best source rock properties are expected in the area of the former central lake. T_{max} values and PI ratios (Table 3.2, Fig. 3.4b) imply that most samples can be considered as well-drained source rocks which expelled generated hy-drocarbons efficiently to the coarse grained sandstone/siltstone intervals nearby (Raji et al., 2015). Unlike other samples, MW 6 and MW 16–1 have lower T_{max} but high PI values (Fig. 3.4b), which might be caused by natural or artificial impregnation. Moreover, high PI values can be caused by the early generation of hetero-compounds (Curiale, 1986), which decrease with increasing thermal maturity (Lewan, 1994). In a poorly-drained system, expelled hydrocarbons can impregnate the coarser grained laminae (Jarvie 2012; Chen and Jiang 2016; Li et al., 2018). In general, the Chang 7 Member is a clay-rich shaly rock (clay mineral contents of more than 40%), where sandstone intervals occur in direct vicinity within the same member and have been proven as important tight-oil reservoirs (Cui et al., 2019; Xu et al., 2019). The shaly intervals might also act as potential shale-oil reservoirs (Chen et al., 2019b).

3.7 Conclusions

This study presents new data on organic geochemistry, elemental carbon and sulfur composition, Rock-Eval pyrolysis and organic petrography on the Triassic Chang 7 Member in the Yanchang Forma-tion, an important petroleum source rock in the mid-western Ordos Basin, China. Samples from 18 different wells have been studied in order to achieve an overview on regional heterogeneity over a large area. Thus, this study gives insight into variability of resource potential, paleo-depositional environment, as well as origin and maturity of organic matter.

Multiple parameters, such as TOC/TS, sizes of pyrite framboids and molecular biomarker data indicate that the Chang 7 member is a typical clay-rich source rock deposited and preserved in a sulphate-poor lacustrine environment in the center of the basin (MW 16 well) and a fluvio-deltaic environment northwestward (MW 1 well) under fresh water and oxic to sub-oxic conditions. The MW 16 well situated close to the center of the former lake shows, however, slightly reducing conditions. Organic matter is composed of a Type II-III kerogen. A mixture of lacustrine aquatic algal-bacterial-

macrophytic organisms and terrigenous higher plants (mainly composed of conifers) was the main source of organic matter based on combined organic petrography and biomarkers results.

The thermal maturity of the Chang 7 Member source rocks reaches the main phase of oil generation based on vitrinite reflectance, Rock-Eval and most molecular geochemical data. This small range of maturity accords with the thickness distribution of the Triassic, Jurassic and Lower Cretaceous rocks in the study area. The study reveals that these source rocks possess good to very good potential for liquid hydrocarbon generation, based on the moderate to very high total organic matter content, thickness (up to 100 m of source rock within the 60–120 m Chang 7 Member) and Rock-Eval results.

3.8 Appendix
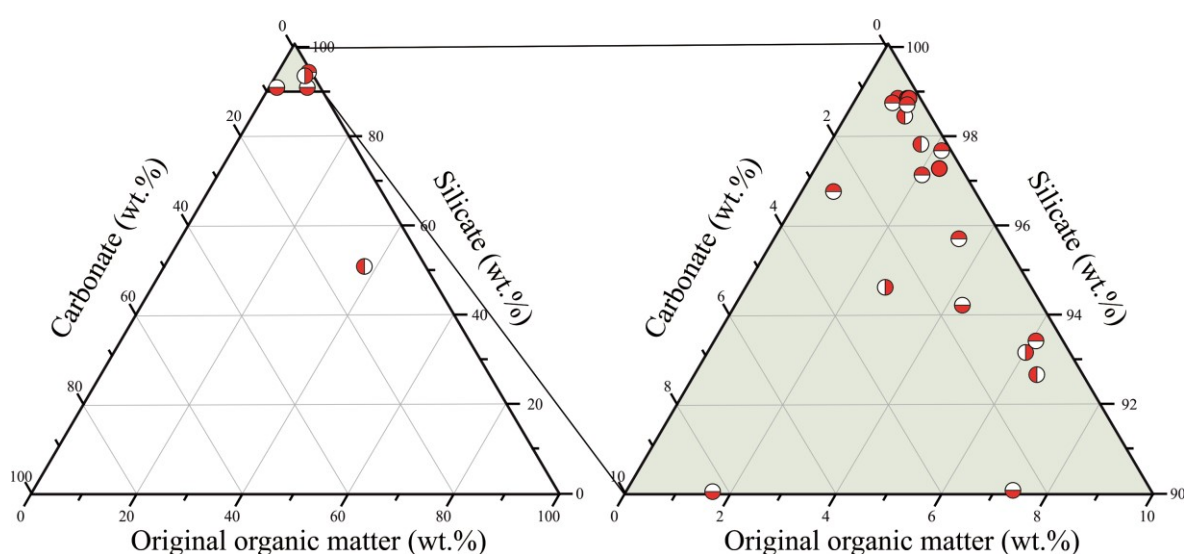
Figure A3.1. Ion chromatograms (m/z 202, 216, 220, 228, 252, and 276) for representative samples of the Chang 7 Member, showing the relative distributions of ≥3 ring aromatic hydrocarbons.
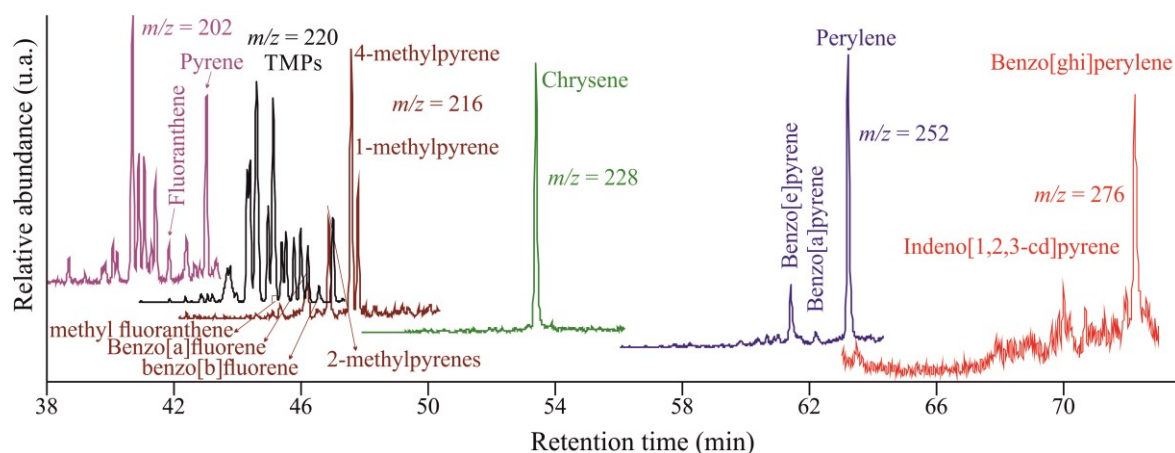
Figure A3.2. Triangular plot of the three major sedimentary components (carbonate, silicate, original organic matter) of the Chang 7 Member samples.

Table A3.1. Identification of terpanes, steranes and aromatic compounds in Fig. 3.6.

Compound group	Peak	Abbreviation	Biomarker	*m/z*
Terpane	A	C_{19}Tri	C_{19}-tricyclic terpane	
	B	C_{20}Tri	C_{20}-tricyclic terpane	
	C	C_{21}Tri	C_{21}-tricyclic terpane	
	D	C_{22}Tri	C_{22}-tricyclic terpane	
	E	C_{23}Tri	C_{23}-tricyclic terpane	
	F	C_{24}Tri	C_{24}-tricyclic terpane	
	G	C_{25}Tri	C_{25}-tricyclic terpane	
	H	C_{24}TeT	C_{24}-tetracyclic terpane	
	I	C_{26}Tri R	C_{26}-R tricyclic terpane	
		C_{26}Tri S	C_{26}-S tricyclic terpane	
	J	C_{28}Tri R	C_{28}-R tricyclic terpane	
		C_{28}Tri S	C_{28}-S tricyclic terpane	
	K	C_{29}Tri R	C_{29}-R tricyclic terpane	
		C_{29}Tri S	C_{29}-S tricyclic terpane	
	L	Ts	C_{27}-18α-22,29,30-trisnorneohopane	
	M	Tm	C_{27}-17α-22,29,30-trisnorhopane	191
Hopanes	N	C_{29}H	C_{29}-17α(H),21β(H)-hopane	
	O	C_{30}*DH	C_{30}-17α(H),21β(H)-diahopane	
	P	C_{29}M	C_{29}-17β(H),21α(H)-hopane	
	Q	C_{30}H	C_{30}-17α(H),21β(H)-hopane	
	R	C_{30}M	C_{30}-17β(H),21α(H)-hopane	
	S	C_{31}H S	C_{31}-17α(H),21β(H)22S-hopane	
		C_{31}H R	C_{31}-17α(H),21β(H),22R-hopane	
	T	Gam	Gammacerane	
	U	C_{32}H S	C_{32}-17α(H),21β(H),22S-hopane	
		C_{32}H R	C_{32}-17α(H),21β(H),22R-hopane	
	V	C_{33}H S	C_{33}-17α(H),21β(H),22S-hopane	
		C_{33}H R	C_{33}-17α(H),21β(H),22R-hopane	
	W	C_{34}H S	C_{34}-17α(H),21β(H),22S-hopane	
		C_{34}H R	C_{34}-17α(H),21β(H),22R-hopane	
	X	C_{35}H S	C_{35}-17α(H),21β(H),22S-hopane	
		C_{35}H R	C_{35}-17α(H),21β(H),22R-hopane	
Steranes	a	pregnane	5α,14β,17β(H)-pregnane (diginane)	
	b	homopregnane	5α,14β,17β(H)-homopregnane (20-methyldiginane)	
	c	C_{27} βα dia20S	20S-13β(H), 17α(H)-diacholestane	
	d	C_{27} βα dia20R	20R-13β(H), 17α(H) -diacholestane	
	e	C_{27} αβ dia20S	20R-13α(H), 17β(H)-diacholestane	
	f	C_{27} αβ dia20R	20S-13α(H), 17β(H)-diacholestane	
	g	C_{27} ααα20S	20S-5α(H), 14α(H), 17α(H)-cholestane	217
	h	C_{27} αββ20R + C_{29}dβα20S	20R-5α(H), 14β(H), 17β(H)-cholestane+ 13β,17α,20S-diastigmastane	
	i	C_{27} αββ20S	20S-5α(H), 14β(H), 17β(H)-cholestane	
	j	C_{27} ααα20R	20R-5α(H), 14α(H), 17α(H)-cholestane	
	k	C_{28} ααα20S	20S-24-Methyl-5α(H), 14α(H), 17α(H)-cholestane	
	l	C_{28} αββ20R	20R-24-Methyl-5α(H), 14β(H), 17β(H)-cholestane	

	m	C$_{28}$ αββ20S	20S-24-Methyl-5α(H), 14β(H), 17β(H)-cholestane	
	n	C$_{28}$ ααα20R	20R-24-Methyl-5a(H), 14a(H), 17a(H)-cholestane	
	o	C$_{29}$ ααα20S	20S-24-Ethyl-5α(H), 14α(H), 17α(H)-cholestane	
	p	C$_{29}$ αββ20R	20R-24-Ethyl-5α(H), 14β(H), 17β(H)-cholestane	
	q	C$_{29}$ αββ20S;	20S-24-Ethyl-5α(H), 14β(H), 17β(H)-cholestane	
	r	C$_{29}$ ααα20R	20R-24-Ethyl-5α(H), 14α(H), 17α(H) -cholestane	
	1	N	naphthalene	128
	2	2-MN	2-methylnaphthalene	142
	3	1-MN	1-methylnaphthalene	
	4	BP	biphenyls	154
	5	2-EN	2-ethylnaphthalene	
	6	1-EN	1-ethylnaphthalene	
	7	2,6- + 2,7-DMN	2,6- + 2,7-dimethylnaphthalene	
	8	1,3- + 1,7-DMN	1,3- + 1,7-dimethylnaphthalene	156
	9	1,6-DMN	1,6-dimethylnaphthalene	
	10	1,4- + 2,3-DMN	1,4- + 2,3-dimethylnaphthalene	
	11	1,5-DMN	1,5-dimethylnaphthalene	
	12	1,2-DMN;	1,2-dimethylnaphthalene	
	13	2-MBp	2-methylbiphenyl	
	14	DPM	diphenylmethane	
	15	3-MBp	3-methylbiphenyl	168
	16	4-MBp	4-methylbiphenyl	
	17	DBF	Dibenzofuran	
	18	1,3,7-TMN	1,3,7-trimethylnaphthalene	
	19	1,3,6-TMN	1,3,6-trimethylnaphthalene	
Aromatic hydrocarbons	20	1,4,6- + 1,3,5-TMN	1,4,6- + 1,3,5-trimethylnaphthalene	
	21	2,3,6-TMN	2,3,6-trimethylnaphthalene	
	22	1,2,7- + 1,6,7-TMN	1,2,7- + 1,6,7-trimethylnaphthalene	170
	23	1,2,6-TMN	1,2,6-trimethylnaphthalene	
	24	1,2,4-TMN	1,2,4-trimethylnaphthalene	
	25	1,2,5-TMN	1,2,5-trimethylnaphthalene	
	26	1,4,5-TMN	1,2,3-trimethylnaphthalene	
	27	1,3,5,7-TeMN	1,3,5,7-tetramethylnaphthalene	
	28	1,3,6,7-TeMN	1,3,6,7-tetramethylnaphthalene	
	29	1,4,6,7- + 1,2,4,6- + 1,2,4,7-TeMN	1,4,6,7- + 1,2,4,6- + 1,2,4,7-tetramethylnaphthalene	
	30	1,2,5,7-TeMN	1,2,5,7-tetramethylnaphthalene	
	31	2,3,6,7-TeMN	2,3,6,7-tetramethylnaphthalene	184
	32	1,2,6,7-TeMN	1,2,6,7-tetramethylnaphthalene	
	33	1,2,3,7-TeMN	1,2,3,7-tetramethylnaphthalene	
	34	1,2,3,6-TeMN	1,2,3,6-tetramethylnaphthalene	
	35	1,2,5,6- + 1,2,3,5-TeMN	1,2,5,6- + 1,2,3,5-tetramethylnaphthalene	
	36	DBT	dibenzothiophene	
	37	PHE	phenanthrene	178
	38	4-MDBT	4-methyldibenzothiophene	198

39	2- + 3-MDBT	2- + 3-methyldibenzothiophene	
40	1-MDBT	1-methyldibenzothiophene	
41	3-MP	3-methylphenanthrene	
42	2-MP	2-methylphenanthrene	192
43	9-MP	9-methylphenanthrene	
44	1-MP	1-methylphenanthrene	
45	4,6-DMDBT	4,6-dimethyldibenzothiophene	
46	2,4-DMDBT	2,4-dimethyldibenzothiophene	
47	2,6-DMDBT	2,6-dimethyldibenzothiophene	
48	3,6-DMDBT	3,6-dimethyldibenzothiophene	
49	2,7- + 3,7- + 2,8-DMDBP	2,7- + 3,7- + 2,8- dimethyldibenzothiophene	212
50	1,4- + 1,6- + 1,8-DMDBP	1,4- + 1,6- + 1,8-dimethyldibenzothiophene	
51	1,3- + 3,4-DMDBP	1,3- + 3,4-dimethyldibenzothiophene	
52	1,7-DMDBP	1,7-dimethyldibenzothiophene	
53	2,3- + 1,9-DMDBP	2,3- + 1,9-dimethyldibenzothiophene	
54	1,2-DMDBP	1,2-dimethyldibenzothiophene	
55	3-EP	3-ethylphenanthrene	
56	9- + 2- + 3,6-DMP	9- + 2- + 3,6- dimethylphenanthrene	
57	1-EP	1-ethylphenanthrene	
58	2,6- + 3,5-DMP	2,6- + 3,5-dimethylphenanthrene	
59	2,7-DMP	2,7-dimethylphenanthrene	
60	1,3- + 3,9- + 3,10- + 2,10-DMP	1,3- + 3,9- + 3,10- + 2,10-dimethylphenanthrene	206
61	1,6- + 2,9- + 2,5-DMP	1,6- + 2,9- + 2,5-dimethylphenanthrene	
62	1,7-DMP	1,7-dimethylphenanthrene	
63	1,9- + 4,9- + 4,10-DMP	1,9- + 4,9- + 4,10-dimethylphenanthrene	
64	2,3-DMP	2,3-dimethylphenanthrene	
65	1,8-DMP	1,8-dimethylphenanthrene	
66	1,2-DMP	1,2-dimethylphenanthrene	

4 High microbial gas potential of Pleistocene lacustrine deposits in the central Qaidam Basin, China

4.1 Abstract

Thick Pleistocene fine-grained rocks in the central Qaidam Basin, China, are regarded as the principal source rocks for microbial gas there. Here, for the first time, a detailed investigation on the organic geochemistry and petrology of this sedimentary sequence is presented. Two different, immature, lacustrine source rocks facies are present in the study area. Organic facies A samples with high TOC (4.1–25.3 wt%) and TS (1.5–3.7 wt%) contents mainly developed under a suboxic to anoxic freshwater column at the lake margins. This shallow water fluviolacustrine facies, accounts for only a small proportion of the whole sedimentary sequence, but has the highest petroleum generation potential. In contrast, organic facies B samples having lower TOC (0.5–1.1 wt%) and TS (0.14–1.0 wt%) contents were deposited in a more oxic, brackish-lacustrine water body. However, exceptionally, anoxic conditions were present in sediments that were sealed by algae mats.

The majority of the interval is comprised of gas prone, mixed type II-III kerogen derived mainly from aquatic plants. Organic facies A is interpreted to be derived from abundant macrophytes (e.g. non-marine algae, submerged angiosperms) around the lake margin. By contrast, the organic matter in organic facies B mainly stems from saltwater algae, with some additional bacterial contribution. Terrestrial higher plants are subordinate in both organic facies. The organic carbon accumulation rate was high compared to organic matter-rich Quaternary marine sediments. Cold and dry climate conditions and high burial rates favored methanogenesis via carbonate reduction in the sediments.

4.2 Introduction

Compared to petroleum and coal, natural gas produces less carbon dioxide during combustion (Gustavsson and Sathre, 2006). Thus, in order to reduce emissions, natural gas accumulations became an even more important exploration target in the past decades. In addition to conventional gas, unconventional natural gas resources such as shale gas, gas hydrates, deep gas, gas in tight sandstones and coal-bed methane got more and more into the focus of research and exploration (Littke et al., 2011; Weniger et al., 2012; Ni et al., 2013; Ghazwani et al., 2018; Oshima et al., 2019; Qiao et al., 2020).

Microbial gas resources account for about 20% of the conventional natural gas reservoirs in the world (Rice and Claypool, 1981) and may dominate in some unconventional natural gas reservoirs, such as gas hydrate (Kvenvolden, 1988) and coal-bed methane (Aravena et al., 2003; Moore, 2012). Generally, microbial gas is considered as the product of anaerobic degradation of organic matter (OM) at low temperatures, and is typically trapped in relatively shallow and immature sediments (Rice and Claypool, 1981). However, the formation of microbial gas under geological settings is a complex

process, which is still poorly understood. One fundamental issue in this context is the characterization of microbial gas source rocks, which are essential for microbial gas exploration but are only rarely documented (Zhang et al., 2014).

The Qaidam Basin in China features the youngest and largest commercial Quaternary accumulation of microbial gas worldwide with a proven reserve of 320×10^9 m^3 (Pang et al., 2005; Dang et al., 2008). This accumulation is regarded as a typical early generation system due to the short depositional time and the young strata (Pang et al., 2005; Dang et al., 2008). Previous climatic studies of the Quaternary of the Qaidam Basin mainly concentrated on the pollen composition of sediments (Wang et al., 1999) and the stable isotopes of carbonate rocks (Rieser et al., 2009), indicating generally cold, extreme evaporative conditions in a closed lacustrine environment, which is further supported by widespread salt deposits (Lehmkuhl and Haselein, 2000). This setting is related to the rapid and significant uplift movement of the Tibetan Plateau (An et al., 2001) and the land-sea redistribution associated with the continental collision of India and Eurasia (Ramstein et al., 1997). Next to tectonic processes, climatic conditions can control erosional and depositional processes, and thus the sediment input into the basin. Deposition of OM-rich lacustrine mudstones - which act as the primary hydrocarbon source rocks in the basin - is closely related to paleoclimatic conditions (Huc, 1988; Jian et al., 2013).

OM is common in fine-grained sediments and derived from either aquatic sources (e.g. algae, cyanobacteria and macrophytic organisms) or terrestrial sources (higher land plants, bacteria) transported to the site of deposition. Abundance of the latter strongly depends on climate (with a humid climate being much more favorable than an arid one) and transport systems (with proximal deposits containing much more terrigenous OM than distal ones). Organic petrology can reveal the presence and size of higher land plant particles and aquatic OM, but not resolve microbes. Organic geochemistry, using the biomarker approach, can give information on the original type of fauna/flora present in the environment, as well as on depositional conditions, such as salinity or temperature (Peters et al., 2005). For these reasons, biomarkers are regularly used in paleoenvironmental studies (Böcker et al., 2013; Song et al., 2015b; Song et al., 2017; Qiao et al., 2021b).

This study focuses on the interpretation of elemental data on organic and inorganic carbon as well as total sulfur, organic geochemical and organic petrographic analysis of Pleistocene source rocks in the central Qaidam Basin. These Quaternary microbial gas source rocks have received little attention so far, and detailed information on OM quality and quantity, depositional environment, kerogen type and the related hydrocarbon generation potential are still missing. The quality and quantity of kerogen in the source rocks have been evaluated and the enrichment mechanism of OM as a basis for the exploration in the target area is discussed. In this context, also the terrestrial OM input needs to be considered. This study documents a case for such depositional settings and provides an example of an integrated approach using multiple proxies to analyze factors controlling OM accumulation in lacustrine environments.

4.3 Geological setting
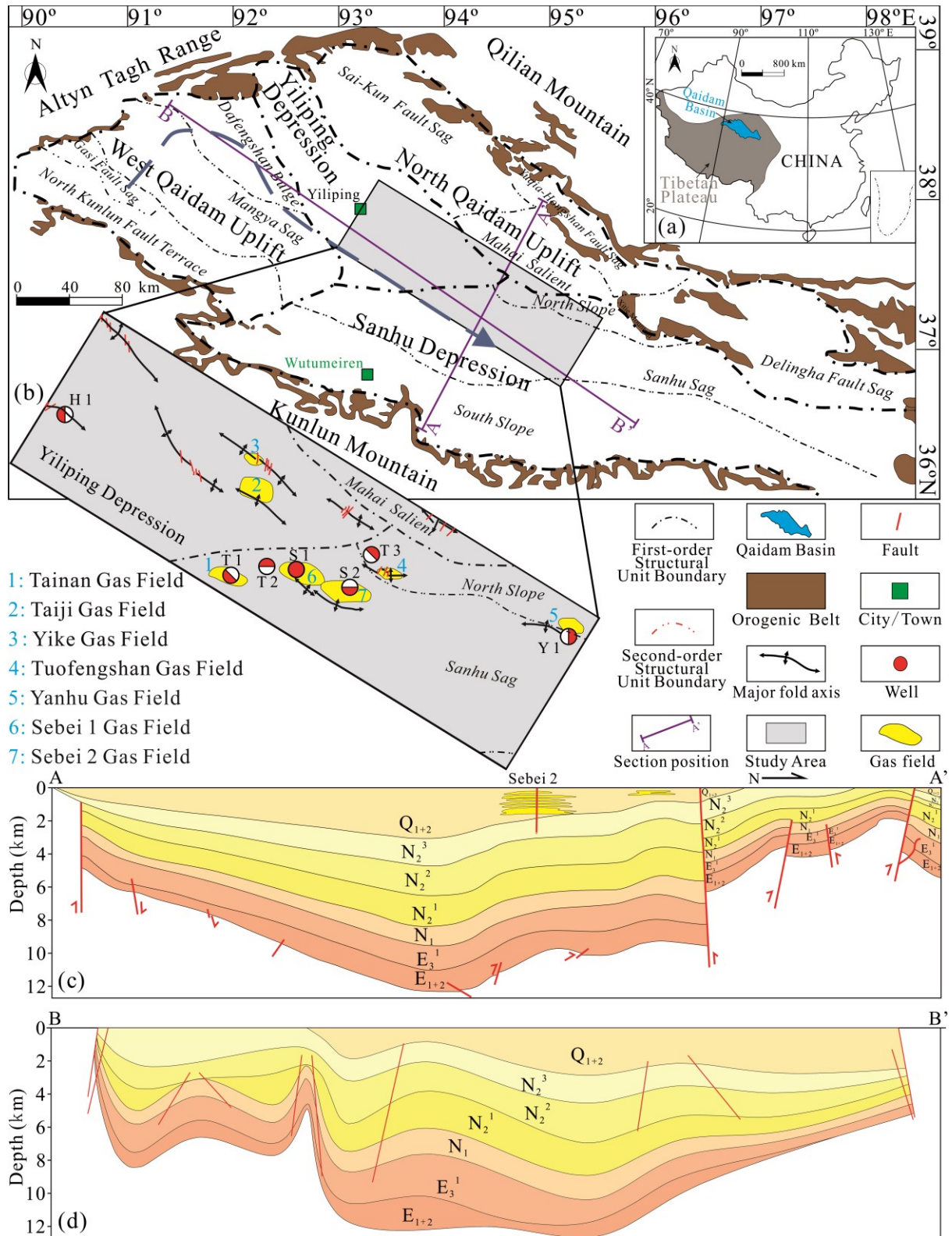
Fig. 4.1. (a) Schematic map showing the location of the Qaidam Basin in China, (b) its geological setting and sample well locations, modified after Bao et al. (2017), and two transects (c and d, modified after Zhang et al., 2013a and Qiu et al., 2003). The dashed line with an arrow illustrates the depocenter shift during the depositional history of the basin.
Note: the different well symbols correspond to the different locations.

The Qaidam Basin is part of a basin-range system that is located at the northern edge of the Tibetan Plateau covering an area of around 120,000 km², with an altitude up to 2.7–3.5 km above sea level. The continental basin formed in the Mesozoic and contains an exceptionally thick Mesozoic-Cenozoic sedimentary succession of 3–16 km (Jian et al., 2013) deposited on the basement consisting of igneous and meta-morphic rocks (Pang et al., 2005). The basin is surrounded by three mountain ranges with altitudes ranging from 4 to over 5 km, which are the Eastern Kunlun Mountain in the south, the Qilian Mountain in the east, and the Altyn Tagh Range in the northwest (Fig. 4.1a). The bound-aries of the basin are represented by large-scale faults creating a high relief towards these surrounding mountain ranges (Fang et al., 2007).

Tapponnier et al. (2001) considered that the formation of the Qaidam Basin is the result of the convergent system in the northeastern Tibetan Plateau. The basin's Mesozoic tectonic settings are affected by the evolution of the Neo-Tethys, Meso-Tethys and the Mongol-Okhotsk Ocean and the collisions of related blocks (Gehrels et al., 2011). In the Cenozoic, the tectonic evolution is related to the India-Eurasia collision as well as to rise, shortening, thickening, and lateral extrusion of the Tibetan Plateau (Harrison et al., 1992; Tapponnier et al., 2001; Royden et al., 2008). In summary, the evolution of the basin took place during three tectonic-sedimentary stages: (1) piedmont fault depression stage in the Mesozoic; (2) unified depression stage from the Palaogene to Neogene; and (3) subsiding depression in the east and cyclic folding in the center and west during the Quaternary (Dang et al., 2008).

Structurally, the western and southern parts are two Cenozoic de-pressions, and the northern part of the basin is a Mesozoic fault-block belt (Pang et al., 2005). During the Jurassic, the depocentres of the basin were located in the northern basin and they shifted to the western area during the deposition of the Paleogene and Neogene. The depo-centres were eastward-moving during the Pleistocene due to the colli-sion with the Indian plate at the end of Neogene (the late Himalayan orogeny) (Pang et al., 2005). Based on the basement structure and the sedimentary sequence, the Qaidam Basin can be divided into four first- order structural units (Fig. 4.1b), which are the north and west Qaidam Uplifts, the Yiliping Depression, and the Sanhu Depression (Bao et al., 2017). Further, eleven second-order structural units can be distin-guished, which are Sai-Kun Fault Sag, North Kunlun Fault Terrace, Mangya Sag, Dafengshan Bulge, South Slope, Sanhu Sag, North Slope, Mahai Salient, Delingha Fault Sag, Yuqia-Hongshan Fault Sag, and Gasi Fault Sag (Bao et al., 2017).

During the early Pleistocene, fluvial-deltaic sediments were depos-ited with abundant terrestrial debris. Afterwards, the lake basin reached its climax, with the deposition of dominantly deep-water fine-grained argillaceous sediments in the middle Pleistocene. Finally, the central area of the basin was continuously elevated due to the influence of the tectonic movement during the late Pleistocene (Dang et al., 2008). Quaternary sediments referred as the Qigequan Formation (Q_{1+2}) mostly range from 1.5 to 2.5 km thick (1.7 km on average, greatest thickness about 3.4 km), with an average sedimentation rate of about 0.65 to 0.8 km/Ma. They were mainly deposited in the Sanhu Depres-sion due to uplift in the

west and a consequent eastward shift of the depocenter (Fig. 4.1c and d; Dang et al., 2008; Shuai et al., 2013; Zhang et al., 2013a).
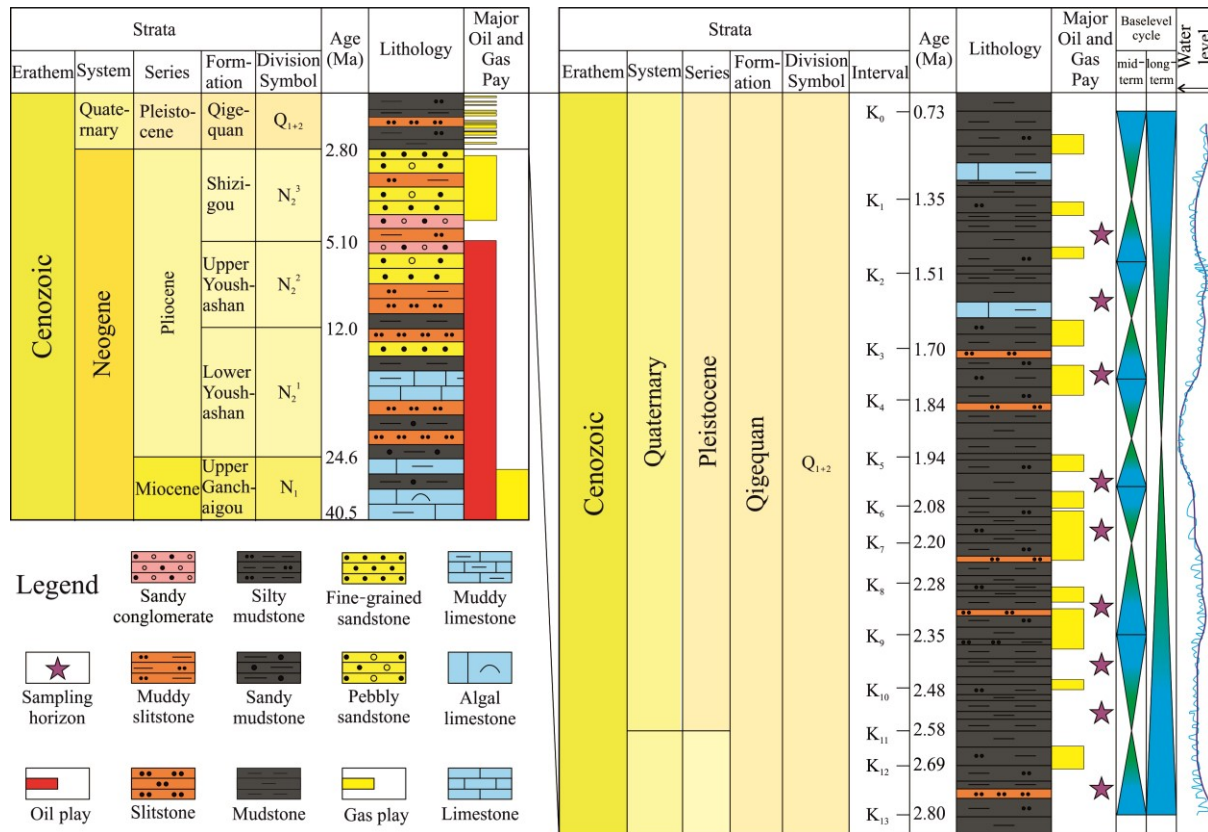
Fig. 4.2. Generalized Pleistocene stratigraphic column for the study area (modified after Jian et al., 2013; Zhang et al., 2013a).

The Q_{1+2} Formation is divided into 12 intervals (K_0–K_{13}, from top to base) based on seismic reflectance features (Zhang et al., 2013a; Fig. 4.2). The middle Pleistocene (K_6–K_7) deposited at the most expansive stage of the Q_{1+2} Formation corresponds to the Maximum Flooding Surface (MFS) of a long-term sequence cycle (Fig. 4.2). The lithology of Q_{1+2} Formation is dominated by mudstones, silty mudstones, muddy lime-stones, and siltstones as well as some thin halite layers varying between 0.1 and 2.0 m thickness. Due to the influence of the tectonic movements in the late Pleistocene, around 0.5 km have been eroded along the Sebei- Tainan gas fields during the Holocene, while slightly less sediment eroded in the southern part of the Sanhu Depression (Zhang et al., 2013a).

The seven largest gas fields were all discovered in the central basin and are sourced from and trapped in Pleistocene, shallow, near-shore, lacustrine sediments (Fig. 4.1b; Shuai et al., 2013; Zhang et al., 2013a; Wang et al., 2015). All these gas fields comprise mainly natural gas produced by microbes in reducing, calcareous environments (Whiticar, 1999).

4.4 Samples and Methods

Seventy-three samples of Pleistocene source rocks were collected from seven wells and 30 samples were selected to be studied in detail, covering nine different stratigraphic intervals (Fig. 4.2). In accordance with observations by Zhang et al. (2014), two main types of source rocks are distinguished in the study area based on TOC (total organic carbon) and TS (total sulfur) contents as well as lithology.

The first type, here defined as organic facies A, comprises samples with high TOC and TS contents that are characterized by coarse grain size, poor gradation, with relatively high quartz and feldspar, but low clay mineral contents. Organic facies A samples are interpreted as a lacustrine-marginal facies, such as shallow water fluvio-lacustrine facies (Zhang et al., 2014).

The second type, here defined as organic facies B, comprises samples with low TOC and TS contents which are commonly characterized by fine grain size, good gradation, with relatively low quartz and feldspar, but high clay mineral contents and about 10–22% of authigenic minerals. Organic facies B samples are interpreted as lacustrine facies (Zhang et al., 2014).

The obtained samples were cut from cores and polished sections were made with a size of around 3–5 cm2. For the geochemical analysis, samples were pulverized using a disc mill.

In order to evaluate porosity and density, two samples from each organic facies were selected to prepare cuboid pieces of known volume.

Facies A and B accounts for approximately 20 and 70% of the whole Pleistocene interval, respectively, while the remaining 10% comprise siltstones, which have not been sampled (Fig. 4.2). Due to the high concentration of OM, all organic facies A samples, but only part of the organic facies B samples containing much less OM were studied in detail.

4.4.1 Elemental analysis

TOC and total inorganic carbon (TIC) contents were determined using a Liqui TOC II analyzer (Elementar Analysen System GmbH, Germany) while TS content was measured using a Leco S 200 sulfur analyzer. Details on the sample preparation, amount of samples, precision and analytical procedure are provided in Qiao et al. (2020). In addition to TOC, TIC, TS, the Fe content was determined using an ARL Perform' X 4200 wavelength-dispersive X-ray fluorescence (WD-XRF) spectrometer.

4.4.2 Rock-Eval pyrolysis

Rock-Eval pyrolysis was performed on a Rock-Eval VI instrument (Vinci Technologies) following the standard bulk rock method described by Behar et al. (2001). In an inert nitrogen atmosphere, the pyrolysis temperature was set to 300 °C and held for 3 min to release the S_1 (volatile hydrocarbon content, mg HC/g rock) fraction. Then the oven was heated to 650 °C at 25∘/min to measure the S_2 (remaining hydrocarbon generative potential, mg HC/g rock) fraction. Before the first sample and after each four samples, standards and blanks were measured.

4.4.3 Organic petrography

The preparation of the polished sections was based on the procedures described in detail by Zieger and Littke (2019). For reflectance measurements and maceral investigation a Zeiss Axio Imager microscope was used. A mineral standard of known reflectance (LEUKO-SAPHIR, 0.592%) was used for calibration before reflectance was measured at 546 nm in oil immersion. Strictly speaking, the maceral group "vitrinite" occurs only from the bituminous coal stage onwards, because the glasslike appearance (vitros (Greek) means glass) is not present at lower maturities. Thus, the term huminite is applied by coal petrologists. However, in geology and the petroleum industry, where vitrinite reflectance is commonly used, the term huminite is hardly known. Thus, in order to avoid confusion, the term huminite is used here when talking about the maceral group and "huminite/vitrinite reflectance (VRr)" when talking about reflectance. On each sample, at least 100 measurements were randomly taken and the mean VRr was calculated using the DISKUS Fossil software (Technisches Büro Carl H. Hilgers). Observations on macerals were not only made in reflected white light but also in a fluorescence mode at 500 times magnification. Maceral identification and counting follows the international standard ICCP system 1994 (ICCP, 1998 and 2001; Pickel et al., 2017; see also Taylor et al., 1998a, 1998b). More detailed parameters and introduction of the instrument and the used software are described in Zieger and Littke (2019).

4.4.4 Biomarkers analysis

4.4.4.1 Extraction and fractionation

About 5 g of each powdered sample was extracted by accelerated solvent extraction (ASE) using a DIONEX ASE 150 instrument (ThermoFischer SCIENTIFIC) with about 10 mL of dichloromethane (DCM) at 100 °C and 10 bar for about 15 min. After extraction, the removal of water and elemental sulfur were achieved by adding anhydrous sodium sulfate and activated copper powder to the extracts.

The extracts were subsequently separated into three fractions via column chromatography using an activated micro column packed with silica gel, which was activated at 200 °C for 12 h prior to the extract separation. Eluents of different polarity were used for fractionation: 5 mL *n*-pentane for the aliphatic hydrocarbons, 5 mL *n*-pentane/DCM (2:3 V:V) for the aromatic hydrocarbons and 5 mL methanol for the NSO components.

4.4.4.2 GC-FID and GC-MS

Aliphatic and aromatic hydrocarbon fractions were analyzed by gas chromatography-flame ionization (GC-FID) and gas chromatography–mass spectrometry (GC–MS).

The GC-FID analysis was performed using a Fisons Instruments GC 8000 series, equipped with a split/splitless injector and a flame ionization detector (FID), using a Zebron ZB-1 capillary column (30 m length, 0.25 mm i.d.) with a 0.25-mm coating. The carrier gas was hydrogen at a velocity of approx. 40 cm/s. GC–MS analyses were performed using a quadrupol mass spectrometer Trace MS (Thermoquest), coupled to a Mega Series HRGC 5160 gas chromatograph (Carlo Erba, IT) equipped with a Zebron ZB-5 fused silica column (30 m × 0.25 mm ID) with a 0.25-mm coating. The MS was

operated in electron ionization (EI+) mode with an ionization energy of 70 eV and a source temperature of 200 °C, scanning from 35 to 700 amu at 1 s/decade with an inter-scan time of 0.1 s. The mass spectrometer was operated at a source temperature of 200 °C. The carrier gas was helium at a velocity of 30 cm/s.

Chromatographic conditions of GC-FID were: 1 µL split injection at an initial oven temperature of 60 °C, then programmed to 310 °C at 5 °C/min, with a final hold at 310 °C for 20 min. For the GC–MS, full scan analysis was operated on all samples. The GC oven temperature started at 80 °C (isothermal time 3 min) with splitless time of 60 s, then heating to 320 °C with a rate of 3∘/min, and finally keeping an isothermal time at 320 °C for 20 min. All biomarker ratios were calculated from peak areas of the specific ion chromatograms.

4.4.5 Porosity and density

In this study, porosity (Φ) was determined on regularly shaped samples by combining grain densities from helium expansion (pycnometry) experiments and bulk densities measured on blocks gauged by high precision vernier calipers. Samples were first cut into regularly shaped blocks and dried in a vacuum oven at 105 °C for 48 h to remove moisture and other sorbed fluids. Then, grain densities were measured on a self-customized He-Pycnometer. Details on the experimental set-up, procedure and evaluation are presented in Ghanizadeh et al. (2014). The bulk densities were determined by the ratio of dry sample weights md (g) and the bulk volumes mv (cm^3).

4.5 Results

4.5.1 Elemental composition

Organic facies A samples have high TOC contents of 4.1–25.3 wt% and high TS contents of 1.5–3.7 wt% while organic facies B samples are characterized by lower TOC contents of 0.5–1.1 wt% and TS contents of 0.14–1.0 wt% (Table 4.1). Average TIC contents are lower in organic facies A than in organic facies B samples (Table 4.1). The Fe_2O_3 of the samples are 2.6–5.2 wt% with an average value of 3.9 wt% (Table 4.1).

4.5.2 Rock-Eval pyrolysis

Both S_1 and S_2 values in organic facies A samples (0.24–4.4 and 6.2–74.4 mg HC/g rock) are higher than those in organic facies B samples (0.08–0.81 and 0.56–3.1 mg HC/g rock). By contrast, both average Hydrogen Index (HI) and Tmax (temperature of maximum pyrolysis yield, °C) values are similar for the two organic facies with HI values varying between 56 and 493 mg HC/g TOC (200 mg HC/g TOC on average) and Tmax values ranging between 341 and 440 °C (411 °C on average). The results of Rock-Eval pyrolysis are shown in Table 4.1.

Table 4.1. Total organic (TOC) and inorganic carbon (TIC), total sulfur (TS), and Rock-Eval data with free hydrocarbons (S_1), hydrocarbon generation potential (S_2), temperature of the highest pyrolysis yield (T_{max}) and Hydrogen Index (HI).

Well	Interval	Sample ID	Depth (m)	Organic Facies	TOC (wt.%)	TIC (wt.%)	TS (wt.%)	Fe (wt.%)	S_1 (mg HC/g rock)	S_2 (mg HC/g rock)	T_{max} (°C)	HI (mg HC/g TOC)
S 1	K4	18-850	794.76	B	0.83	1.31	0.77	4.30	0.81	2.79	401	336
		18-853	801.46	A	12.86	0.67	1.67	2.79	0.87	26.30	423	204
		18-856	811.86	B	0.62	0.55	0.46	4.59	0.51	2.54	431	409
		18-857	820.47	B	0.78	1.19	0.24	3.79	0.08	0.49	433	62
	K9	18-858	1269.00	A	8.86	0.02	1.55	4.26	0.76	25.20	428	284
		18-860	1272.50	B	0.68	1.28	1.02	4.58	0.28	1.46	423	214
		18-861	1279.40	A	25.31	0.02	2.20	2.91	4.42	71.41	412	282
	K10	18-862	1377.50	A	16.73	0.01	3.72	4.97	1.31	30.92	412	184
		18-864	1380.50	A	6.49	0.02	3.50	5.20	0.38	11.52	410	177
T 1	K11	18-867	1697.30	A	4.08	3.86	1.48	2.59	0.24	6.23	433	152
		18-868	1697.50	A	4.15	4.36	1.47	2.77	2.95	4.88	435	118
		18-869	1697.70	A	9.91	0.02	1.77	3.78	0.75	13.68	412	138
Y 1	K 4	18-872	124.69	B	0.64	0.02	0.88	4.62	0.57	3.16	431	493
		18-873	124.99	B	0.52	0.37	0.71	5.08	0.24	0.97	438	186
S 2	K2	18-876	534.40	B	0.71	0.93	0.36	3.45	0.28	1.65	432	232
		18-878	543.80	A	8.19	0.02	1.78	3.42	1.44	11.62	413	141
	K3	18-879	555.10	B	1.11	0.72	0.14	4.82	0.43	3.12	440	280
		18-880	566.10	B	1.10	1.24	0.21	3.95	0.23	1.44	438	130
	K7	18-889	1082.70	B	0.66	0.97	0.78	3.14	0.36	1.76	423	266
	K10	18-892	1313.30	B	0.60	2.11	0.58	3.82	0.64	2.01	428	335
T 2	K6	18-894	1266.70	B	1.00	0.49	0.43	5.06	0.14	0.56	407	56
		18-895	1269.90	B	0.70	3.46	0.76	3.62	0.09	0.58	399	82
H 1	K4	18-897	235.10	B	0.79	2.80	0.33	3.08	0.45	1.08	348	136
		18-898	255.90	B	0.70	3.86	0.27	2.84	0.27	1.14	358	162
		18-899	266.40	B	0.74	2.47	0.22	/	0.34	1.75	361	236
	K13	18-900	982.20	B	0.69	3.38	0.55	3.23	0.25	1.07	421	154
		18-901	985.80	B	0.82	1.86	1.03	3.97	0.13	0.88	415	106
		18-904	1005.90	B	0.85	2.93	0.37	/	0.11	0.78	428	91
T 3	K6	18-915	631.30	B	0.49	0.53	0.66	4.47	0.24	1.15	341	235
		18-916	646.11	B	0.77	1.25	0.16	3.91	0.21	0.96	348	125

HI = hydrogen index ($S_2 \times 100/\text{TOC}$), mg HC/g TOC.

4.5.3 Organic petrography

There are numerous autochthonous huminite particles, which can be used to measure VR_r. The VR_r values vary from 0.25 to 0.43% with an average value of 0.35% (Table 4.2). The volumetric percentage of OM observed is higher in organic facies A sample sections ranging from 5.9 vol% (18–868) to 38.9 vol% (18–861) (Fig. 4.3a-f) and lower in organic facies B sample sections ranging from 1.2 vol% (18–872) to 2.0 vol% (18–901) (Fig. 4.3g-i). Huminite is especially enriched in sample 18–861 (34.2 vol% of the whole rock counted; Table 4.2). Huminite particles are abundant in all the samples analyzed, representing 70 to 92 vol% of the total macerals counted. There are two kinds of huminite in organic facies A samples, i) massive, homogeneous huminite (Fig. 4.3a, b), and ii) huminite mixed with liptinite (Fig. 4.3e, f). The higher plant contribution to OM is further documented by the occurrence of inertinite, either as small detrital particles or as large fusinite (Fig. 4.3c, d) in some samples, although its abundance is usually low (0.0–0.8 vol% of whole rock, Table 4.2). Liptinite mainly occurs as sporinite (yellowish fluorescence; Fig. 4.3e, f) or resinite and fluorinite (greenish-yellow fluorescence;

Fig. 4.3d, f) forming oval to round bodies within densinite (Fig. 4.3f) and fillings of the cell cavities of huminite or fusinite (Fig. 4.3d). In organic facies B samples, the huminite appears more broken (Fig. 4.3g) and inertinite is very rare. As liptinite, only planar lamalginites and liptodetrinite (Fig. 4.3h) with yellow fluorescence color are observed in organic facies B samples.

Table 4.2. TOC content, random huminite reflectance (VR$_r$) and maceral composition (percentages based on whole rock samples).

Well	Interval	Sample ID	Depth (m)	Organic facies	TOC (wt.%)	R$_r$ (%)	Maceral composition (vol.%)			
							Huminite	Inertinite	Liptinite	Total OM
S 1	K 4	18-850	794.76	B	0.83	0.36	1.13	0.30	0.60	2.03
		18-853	801.46	A	12.86	0.25	12.16	1.45	0.60	14.21
		18-857	820.47	B	0.78	0.34	1.17	0.09	0.40	1.66
	K 9	18-858	1269.00	A	8.86	0.34	11.04	0.22	2.49	13.75
		18-860	1272.50	B	0.68	0.38	1.13	0.11	0.49	1.73
		18-861	1279.40	A	25.31	0.32	34.15	0.18	4.54	38.87
	K 10	18-862	1377.50	A	16.73	0.26	21.75	0.00	2.87	24.63
		18-864	1380.50	A	6.49	0.35	9.83	0.92	1.79	12.53
T 1	K11	18-867	1697.30	A	4.08	0.33	6.79	0.19	0.98	7.96
		18-868	1697.50	A	4.15	0.31	5.04	0.05	0.78	5.86
		18-869	1697.70	A	9.91	0.38	15.94	0.29	2.44	18.67
Y 1	K 4	18-872	124.69	B	0.64	0.42	0.79	0.11	0.34	1.24
S 2	K2	18-878	543.80	A	8.19	0.34	9.25	0.22	0.60	10.08
	K3	18-879	555.10	B	1.11	0.36	0.87	0.10	0.80	1.76
		18-880	566.10	B	1.10	0.34	1.54	0.00	0.20	1.74
	K 10	18-892	1313.30	B	0.60	0.37	0.80	0.20	0.59	1.59
T 2	K 6	18-894	1266.70	B	1.00	0.40	1.48	0.12	0.31	1.92
H 1	K 13	18-901	985.80	B	0.82	0.33	1.26	0.59	0.20	2.04
		18-904	1005.90	B	0.85	0.43	1.28	0.10	0.39	1.77

Pyrite is abundant in most organic facies A samples but rare in organic facies B samples, which is consistent with the TS concentration in both organic facies. It occurs either as euhedral crystals (Fig. 4.3a, c, e, g) or as assemblages of recrystallized framboidal pyrites (Fig. 4.3a, g) inserted in huminite or finely dispersed within the mineral matrix.
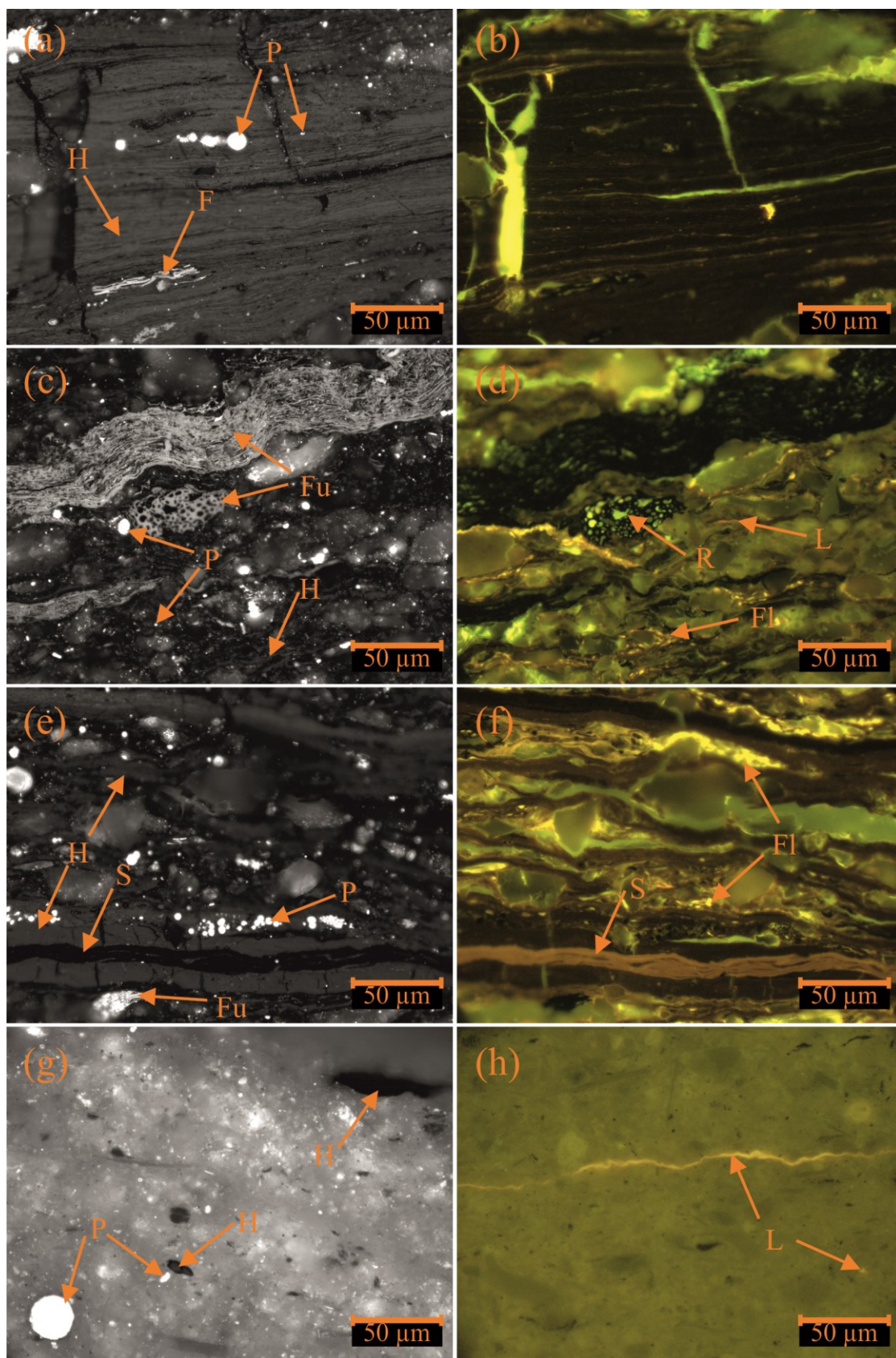
Fig. 4.3. Microphotographs showing macerals in the Pleistocene source rocks under incident reflected white light (left columns) and in fluorescence mode (right columns). a-d: sample 18-964, e-f: sample 18-861, and g-h: sample 18-894. All photomicrographs are at the same scale; the horizontal length is around 300 μm. Huminite-vitrinite, Fu-fusinite, Fl- fluorinite, S-sporinite, R-resinite, L-lamalginite/liptodetrinite, P-pyrite, I-inertinite.

4.5.4 Biomarkers analysis

4.5.4.1 *n*-Alkanes, acyclic isoprenoids and bicyclic alkanes
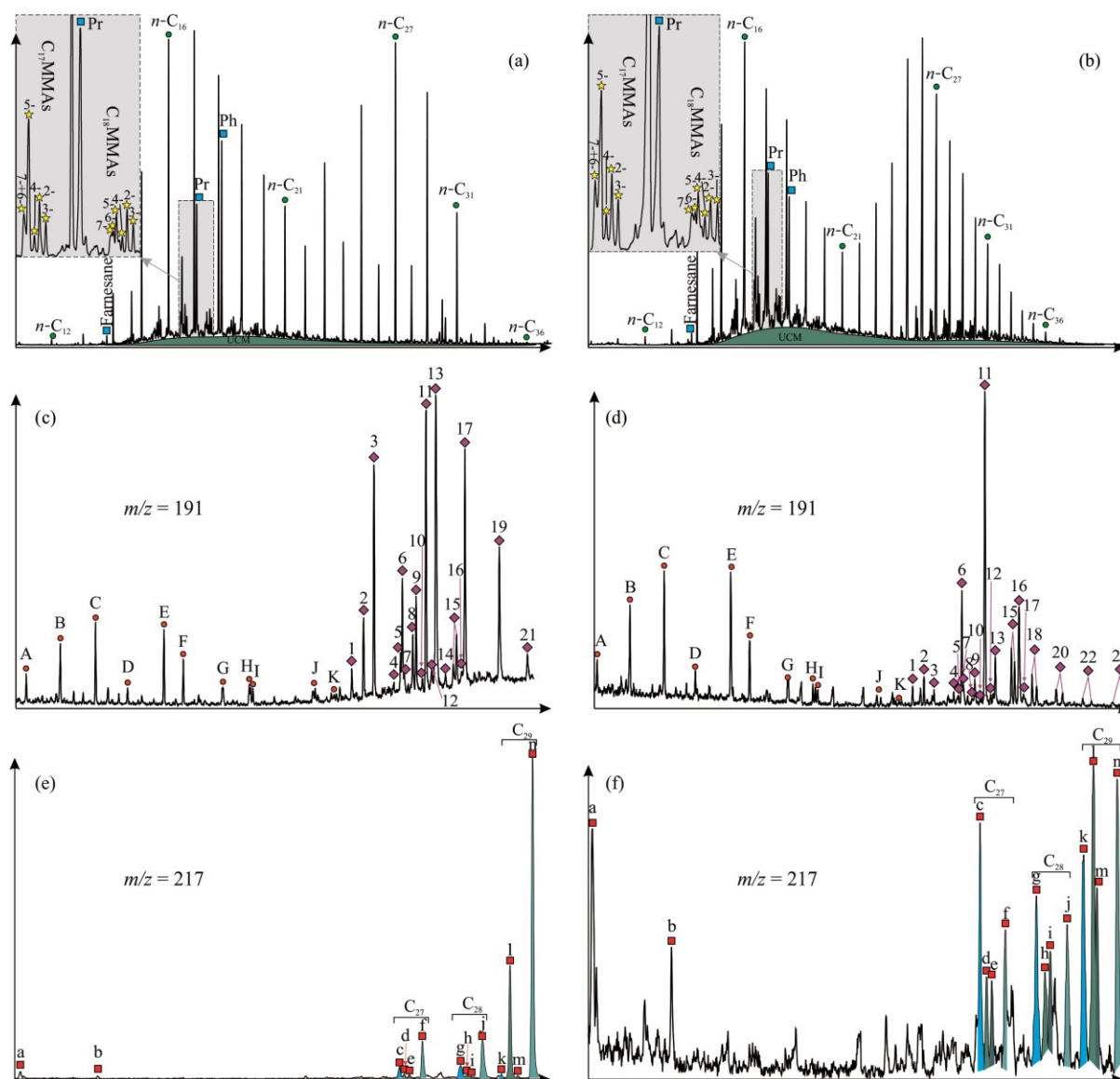
Fig. 4.4. (a, b) Gas chromatograms, (c, d) mass chromatograms of m/z 191 of the aliphatic fraction showing the distribution of terpanes, and (e, f) mass chromatograms of m/z 217 showing the distribution of steranes. See Appendix (Table A4.1) for detailed peak identification.
Figures on the left (a, c, e) represent sample 18-869 (organic facies A), those on the right sample 18-916 (organic facies B).

Acyclic alkanes range from n-C_{10} to n-C_{40} showing a bimodal distribution with maximum concentrations at n-C_{16}, n/i-C_{17} or n-C_{18} for the short-chain homologs (< n-C_{21}) and between n-C_{25} to n-C_{27} for the longchain homologs (> n-C_{25}) in most samples (Fig. 4.4a and b). Organic facies A samples contain a clear odd n-alkane preference with the carbon preference index (CPI; Bray and Evans, 1961) greater than 2.1, while this preference is not obvious in the organic facies B samples (Fig. 4.4a and b; Table 4.3). Besides, some OM source indicators show a large difference between these two organic facies. TAR (terrigenous/aquatic ratio, Bourbonniere and Meyers, 1996) is higher in the TOC-rich

samples, while $n\text{-}C_{17}/(n\text{-}C_{23} + n\text{-}C_{25} + n\text{-}C_{27})$ and Paq ratios (Ficken et al., 2000) are higher in the samples with low TOC contents (Fig. 4.4a and b; Table 4.3).

Table 4.3. Ratios calculated from distributions of n-alkanes and acyclic isoprenoids.

Well	Interval	Sample ID	Organic facies	Pr/ $n\text{-}C_{17}$	Ph/ $n\text{-}C_{18}$	Pr/Ph	CPI	Paq	TAR	$n\text{-}C_{17}/(n\text{-}C_{23}+ n\text{-}C_{25}+ n\text{-}C_{27})$	HD/ D
S 1	K 4	18-853	A	3.08	1.48	1.79	2.11	0.49	4.54	0.09	2.59
		18-857	B	0.71	0.94	0.84	1.20	0.68	0.34	0.92	3.17
	K 9	18-858	A	0.71	0.90	1.36	3.53	0.38	2.81	0.25	2.13
		18-860	B	0.88	0.94	1.72	1.53	0.50	0.08	7.34	3.02
		18-861	A	8.71	14.11	0.70	4.60	0.41	8.23	0.06	1.34
	K 10	18-864	A	1.08	2.05	0.87	3.00	0.46	1.45	0.29	2.33
T 1	K 11	18-867	A	0.98	4.19	0.46	1.66	0.59	1.97	0.14	1.49
		18-868	A	0.87	2.23	0.59	1.96	0.61	2.26	0.16	2.68
		18-869	A	0.69	0.93	0.86	3.08	0.51	1.08	0.40	2.09
Y 1	K 4	18-872	B	0.58	0.55	0.97	1.21	0.72	0.23	1.18	4.71
S 2	K 2	18-878	A	1.25	1.16	1.52	3.32	0.47	3.78	0.13	2.93
	K 3	18-880	B	0.74	0.81	1.37	1.48	0.51	0.33	1.39	3.14
	K 7	18-889	B	0.64	1.01	0.55	1.07	0.65	0.92	0.26	2.98
	K 10	18-892	B	0.79	1.13	1.09	1.50	0.52	0.46	0.98	3.32
T 2	K 10	18-894	B	0.55	0.80	0.94	1.21	0.70	0.42	0.73	8.15
H 1	K 4	18-897	B	0.70	0.64	1.06	1.30	0.57	0.13	3.51	3.81
	K 13	18-900	B	0.64	0.48	1.35	1.18	0.62	1.03	0.32	3.25
		18-904	B	0.52	0.73	1.33	1.63	0.54	0.27	1.67	6.61
T 3	K 6	18-916	B	0.72	0.75	1.42	1.13	0.64	1.02	0.35	3.56

Pr = pristane; Ph = phytane; CPI = $2 \times \sum\text{odd } n\text{-}C_{23–29}/(\sum\text{even } n\text{-}C_{22–28}+ \sum\text{even } n\text{-}C_{24–30})$; TAR = $(n\text{-}C_{27} + n\text{-}C_{29} + n\text{-}C_{31})/(n\text{-}C_{15} + n\text{-}C_{17} + n\text{-}C_{19})$; Paq = $(n\text{-}C_{23} + n\text{-}C_{25})/(n\text{-}C_{23} + n\text{-}C_{25} + n\text{-}C_{29} + n\text{-}C_{31})$; HD/D = 8β-(H)-homodrimane/8β-(H)-drimane.

Pristane (Pr) and phytane (Ph) are the dominating acyclic isoprenoids with the ratio of Pr/Ph ranging from 0.55 to 1.79 (Table 4.3). The ratio of their concentrations to those of their adjacent n-alkanes (Pr/$n\text{-}C_{17}$ and Ph/$n\text{-}C_{18}$) are 0.53–8.71 and 0.55–14.11, respectively. Unresolved complex mixture (UCM; Blumer et al., 1973) concentrations can be observed in all samples (Fig. 4.4a, b), which are sometimes the result of the biodegradation of saturated hydrocarbons (Formolo et al., 2008); however little is known about the chemical composition and origin of UCM (Hedges et al., 2000).

The bicyclic alkanes comprising 8β-(H)-drimane (D) and 8β-(H)-homodrimane (HD) are identified in the *m/z* 123 mass chromatogram with ratios of HD/D of 1.34–8.15.

4.5.4.2 Terpanes

Tricyclic terpanes ranging from C_{19} to C_{29} are identified in all samples. Increasing concentrations can be observed from C_{19} to C_{21} tricyclic terpanes, while decreasing concentrations occur from C_{23} to C_{25} tricyclic terpanes. Besides, C_{22} tricyclic terpane contents are similar to C_{19} and C_{25} tricyclic terpanes contents. Ratios of C_{24} tetracyclic/C_{23} tricyclic terpane range from 0.14–0.31 (Table 4.4).

Table 4.4. Biomarker parameters in the aliphatic fraction.

Well	Interval	Sample ID	Organic facies	Terpanes				Hopanes							Steranes				Normalized sterane $\alpha\alpha\alpha$ 20R distribution (%)		
				$C_{19}/(C_{19}+C_{23})$ tricyclic terpanes	C_{22}/C_{21} tricyclic terpane	C_{24} tetracyclic terpane/C_{23} tricyclic terpane	Terpenes/C_{30} $\alpha\beta$ hopanes	$C_{29}N/C_{30}$ $\alpha\beta$ hopane	C_{29} $\alpha\beta$/($\alpha\beta+\beta\alpha+\beta\beta$)	C_{30} $\alpha\beta$/($\alpha\beta+\beta\alpha+\beta\beta$)	$C_{31}\alpha\beta$ 22S/2(S+R)	$C_{32}\alpha\beta$ 22S/2(S+R)	Gam/C_{30} $\alpha\beta$ hopane	Steranes/hopanoids	C_{21-22} steranes/C_{27-29} steranes	C_{29}/C_{27} regular steranes	C_{29} $\alpha\alpha\alpha$ 20S/(20S+20R)	$C_{27}R$	$C_{28}R$	$C_{29}R$
S 1	K4	18-853	A	0.21	0.21	0.22	2.78	0.05	0.17	0.24	0.33	0.32	0.11	0.25	0.07	4.08	0.14	12.48	25.04	62.48
		18-857	B	0.09	0.26	0.19	3.34	0.27	0.60	0.92	0.57	0.65	0.16	1.00	0.10	1.91	0.15	10.65	15.25	74.10
	K9	18-858	A	0.36	0.17	0.16	1.24	0.04	0.10	0.34	0.23	0.32	0.07	0.57	0.01	6.76	0.02	15.89	21.18	62.93
		18-860	B	0.19	0.22	0.15	10.09	0.53	0.52	0.84	0.55	0.77	0.22	1.77	0.12	2.00	0.09	11.24	15.94	72.81
		18-861	A	0.15	0.16	0.19	0.37	0.02	0.08	0.46	0.18	0.24	0.05	2.90	0.00	4.33	0.00	8.90	13.76	77.34
	K10	18-864	A	0.35	0.22	0.05	2.71	0.01	0.10	0.38	0.18	0.43	0.07	1.49	0.01	6.32	0.01	22.62	29.20	48.18
		18-867	A	0.29	0.43	0.33	1.14	0.13	0.16	0.49	0.23	0.52	0.07	1.58	0.01	3.13	0.03	11.39	22.33	66.28
T 1	K11	18-868	A	0.24	0.17	0.15	3.38	0.14	0.25	0.61	0.20	0.49	0.03	3.29	0.02	3.10	0.02	32.41	25.68	41.90
		18-869	A	0.26	0.23	0.31	1.29	0.03	0.18	0.49	0.32	0.46	0.06	1.53	0.01	8.03	0.02	31.70	31.83	36.47
Y 1	K4	18-872	B	0.22	0.34	0.19	4.52	0.20	0.62	0.90	0.58	0.56	0.17	0.94	0.15	1.57	0.15	16.08	20.25	63.67
	K2	18-878	A	0.20	0.21	0.18	5.11	0.01	0.11	0.27	0.24	0.49	0.10	0.21	0.21	3.79	0.04	24.55	24.05	51.40
S 2	K3	18-880	B	0.18	0.31	0.15	5.59	0.21	0.53	0.89	0.56	0.61	0.25	1.00	0.17	1.16	0.32	34.02	31.51	34.47
	K7	18-889	B	0.11	0.31	0.18	3.06	0.11	0.62	0.91	0.58	0.59	0.26	0.60	0.17	1.35	0.45	38.81	20.03	41.16
	K10	18-892	B	0.13	0.27	0.23	1.70	0.37	0.59	0.84	0.55	0.57	0.18	1.73	0.02	3.06	0.04	19.38	23.56	57.06
T 2	K10	18-894	B	0.20	0.27	0.18	3.92	0.22	0.54	0.90	0.51	0.58	0.31	1.21	0.06	1.91	0.15	36.43	25.94	37.63
	K4	18-897	B	0.10	0.30	0.21	4.45	0.26	0.74	0.87	0.55	0.48	0.22	0.58	0.19	1.07	0.53	19.48	17.20	63.32
H 1	K13	18-900	B	0.15	0.25	0.18	8.25	0.48	0.53	0.88	0.56	0.60	0.10	0.83	0.24	0.99	0.43	20.86	19.10	60.05
		18-904	B	0.13	0.31	0.23	7.29	0.49	0.64	0.79	0.54	0.66	0.30	0.62	0.22	1.06	0.32	19.26	20.92	59.82
T 3	K6	18-916	B	0.22	0.24	0.14	1.90	0.05	0.59	0.96	0.58	0.57	0.42	0.67	0.13	2.33	0.10	22.53	22.08	55.39

Sterane/hopanes = C_{27-29} regular steranes/C_{29-35} 17α-hopanes.

A series of hopanes, ranging from C_{27} to C_{35} except for C_{28}, was observed in the studied samples and includes multiple stereoisomers (Fig. 4.4c, d). The distribution of hopanes varies in the different organic facies. For organic facies A, the identified hopanes include C_{27}-C_{31} ββ (even to C_{32} ββ in some samples), C_{29}-C_{30} βα, and C_{27}-C_{32} αβ with C_{29} ββ being the dominant compound. Besides, C_{27}-17β(H)-22,29,30-trisnorhopane (C_{27}β) and hopenes including C_{29}-C_{30} neohop-13(18)-enes, and C_{30} hop-17(21)-ene are observed. C_{29}N (25-Norhorpane) is present in all samples, although with different concentrations (Fig. 4.4) with C_{29}N/C_{30}H ratios clearly higher in facies B (avg. 0.29) than in facies A (avg. 0.05) (Table 4.4). Moreover, no other compounds such as gammacerane or C_{33}, C_{34} or C_{35} homohopanes have been found in significant abundance. In organic facies B samples, gammacerane occurs and C_{32}-C_{35} αβ homohopanes are more abundant, while hopenes and ββ hopanes are missing.

4.5.4.3 *Steroids*

Steranes and diasteranes were observed by monitoring the *m/z* 217 ion (Fig. 4.4e, f). In organic facies A, steranes are dominated by the C_{29} ααα20R-sterane, followed by C_{29} αββ-sterane which co-elutes with βββ(R)-sterane (Fig. 4.4e and f). Additionally, pregnane and homopregnane were also detected in low abundances. However, high contents of pregnane and homopregnane can be observed in organic facies B samples (Fig. 4.4f). In these samples, besides the contents of the C_{27}-C_{29} ααα20R-steranes, the contents of other steranes and diasteranes are high as well (Table 4.4).

4.5.4.4 Aromatic hydrocarbons

The distribution of aromatic hydrocarbons concerned is shown in Fig. 4.5 (a and b). Unlike aliphatic hydrocarbons, parameters based on aromatic hydrocarbons show little differences between the two organic facies. This is expected due to the low to marginal maturity of studied samples. The most abundant peak is phenanthrene (P; *m/z* 178) followed by dibenzofuran (DBF; *m/z* 168), methylphenanthrenes (MPs; *m/z* 192) and ethylphenanthrenes + dimethylphenanthrenes (EPs + DMPs; 206). Among DMPs, 1,3- + 3,9- + 2,10- + 3,10-DMP is the most abundant peak with 1,7-DMP/(1,3-+3,9- + 2,10- + 3,10-DMP) ratios of 0.36–0.55 in most samples except for sample 18–878 (Table 4.5). Further, a positive relationship between 1,7-DMP/(1,3- + 3,9- + 2,10- + 3,10-DMP) and 1-MP/9-MP ratios (0.60–1.73, 0.87 on average) can be observed. Trimethylnaphthalenes (TMNs; *m/z* 170), tetramethylnaphthalenes + dibenzothiophene (TeMNs + DBT; *m/z* 184), and fluorene (FL; *m/z* 166) show small abundances compared to above compounds. DBT, a compound containing sulfur, shows relatively low contents in the normalized distribution of FL, DBF and DBT (Fig. 4.6a) and compared to P (Fig. 4.6b). Among TMNs, the 1,3,6-TMN is the most abundant compound with 1,2,5-TMN/1,3,6-TMN ratios of 0.27–0.82 and 1,2,7-TMN showing small concentrations with 1,2,7-TMN/1,3,7-TMN ratios of 0.49–1.73. Other aromatic hydrocarbons with biological origin such as of cadalene (Cad; *m/z* 183) and diterpenoids including retene (Ret; *m/z* 219), 19- + 18-norabieta-8,11,13-trienes (*m/z* 241), tetrahydroretene (Tet; *m/z* 223), dehydroabietane (Deh; *m/z* 255), simonellite (Sim; *m/z* 237) and 9- + 2-methylretenes (Mrets; *m/z* 233) occur in small concentrations (Fig. 4.5).
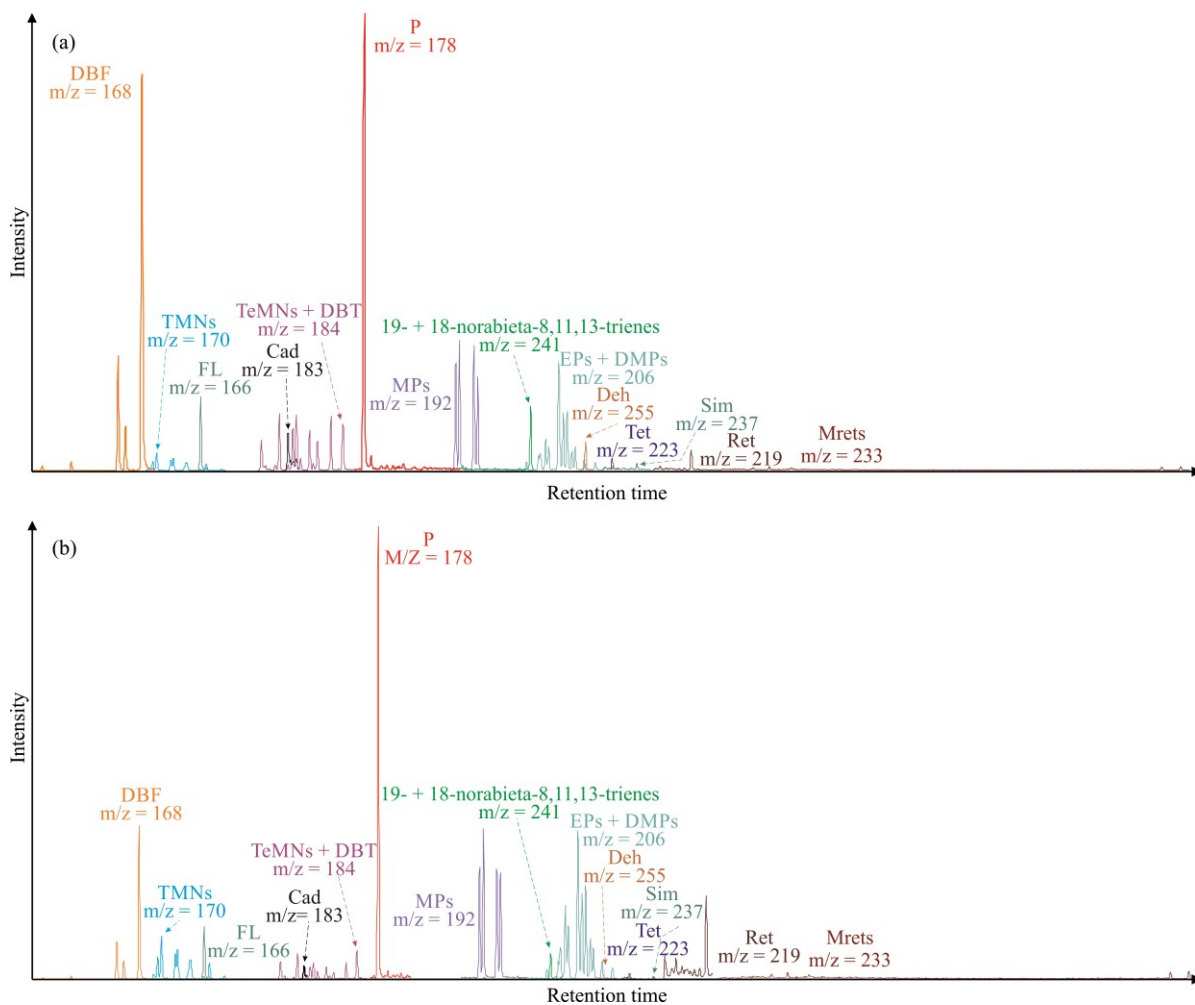
Fig. 4.5 Aromatic hydrocarbons of (a) sample 18-869 (organic facies A) and (b) sample 18-916 (organic facies B).
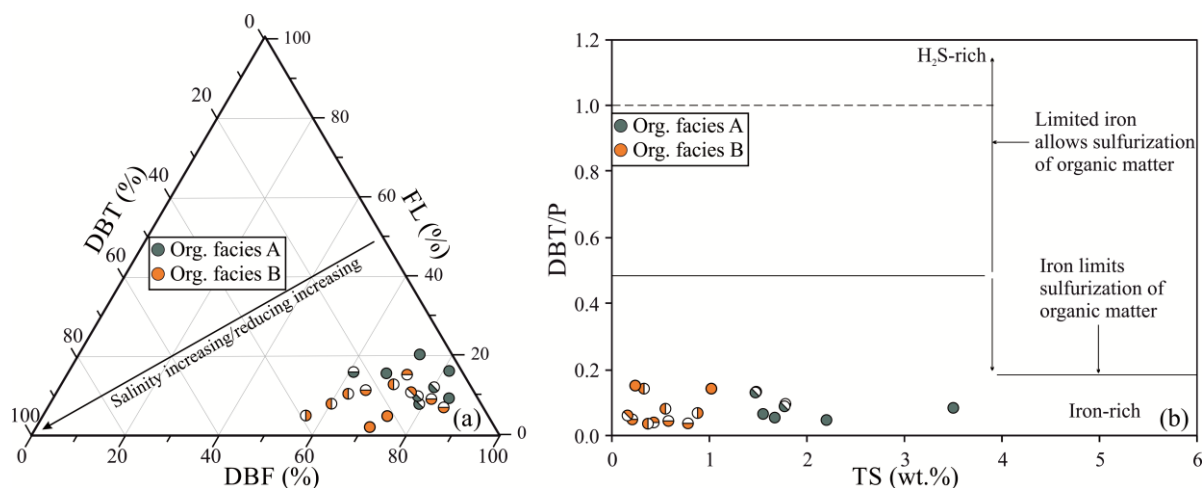
Fig. 4.6. Relative proportions of (a) fluorene (FL), dibenzofuran (DBF), and dibenzothiophene (DBT), and (b) DBT/phenanthrene (P) ratio vs. total sulfur (TS). Note: symbols represent sample locations (see Fig. 4.1b).

Table 4.5. Geochemical parameters in the aromatic fraction.

Well	Inte-rval	Sample ID	Organic facies	1,2,5-TMN/ 1,3,6-TMN	1,2,7-TMN/ 1,3,7-TMN	1-MP/ 9-MP	1,7-DMP/(1, 3- + 3,9- + 2,10- + 3,10-DMP)	Retene /9-MP	DBT /P	Normalized distribution of DBT, DBF and FL (%)		
										DBT	FL	DBF
S 1	K 4	18-853	A	0.52	0.99	0.88	0.45	0.24	0.05	6.69	20.35	72.96
		18-857	B	0.39	1.38	0.90	0.53	0.44	0.15	21.37	4.90	73.73
	K 9	18-858	A	0.32	1.15	0.78	0.42	0.13	0.07	5.91	9.33	84.76
		18-860	B	0.32	1.33	0.91	0.44	0.12	0.14	26.50	2.14	71.36
		18-861	A	0.55	0.49	0.60	0.35	0.11	0.05	2.44	16.19	81.37
	K 10	18-864	A	0.31	1.03	0.80	0.50	0.48	0.08	16.16	15.64	68.19
T 1	K 11	18-867	A	0.46	1.01	0.79	0.38	0.19	0.13	13.02	7.94	79.05
		18-868	A	0.29	1.22	0.73	0.36	0.23	0.13	12.34	9.86	77.80
		18-869	A	0.42	0.94	0.73	0.45	0.17	0.09	7.70	12.15	80.15
Y 1	K 4	18-872	B	0.59	0.85	0.66	0.44	0.20	0.07	38.76	5.03	56.22
S 2	K 2	18-878	A	0.51	1.15	1.73	2.17	1.85	0.10	23.04	15.98	60.98
	K 3	18-880	B	0.30	1.07	0.82	0.45	0.00	0.05	9.78	9.14	81.08
	K 7	18-889	B	0.46	1.01	0.91	0.47	0.13	0.04	22.75	11.39	65.86
	K 10	18-892	B	0.27	1.15	0.86	0.42	0.26	0.04	8.18	7.06	84.76
T 2	K 10	18-894	B	0.49	0.95	0.85	0.45	0.16	0.04	11.94	15.27	72.79
H 1	K 4	18-897	B	0.42	1.01	1.03	0.52	0.15	0.14	26.95	10.46	62.59
	K 13	18-900	B	0.74	1.36	1.02	0.51	0.30	0.08	31.78	7.98	60.24
		18-904	B	0.82	0.78	0.63	0.45	0.18	0.04	16.04	12.84	71.11
T 3	K 6	18-916	B	0.49	0.76	0.96	0.55	0.83	0.06	13.28	10.87	75.85

TMN: trimethylnaphthalene; MP: methylphenanthrene; DMP: dimethylphenanthrene; DBT: dibenzothiophene; P: phenanthrene; FL: fluorene; DBF: dibenzofuran.

4.5.5 Porosity and density

The mean wet bulk density (WBD) value is 2.10 g/cm^3 for organic facies A samples and 2.22 g/cm^3 for organic facies B samples. The mean porosities (Po) are 39.59% and 37.28% for organic facies A and B samples, respectively.

4.6 Discussion

4.6.1 Thermal maturity of organic matter

Both the T_{max} and VR_r values illustrate that the source rocks are thermally immature with average values of 411 °C and 0.33%, respectively. This is consistent with the following molecular parameters.

In organic facies A samples, the high abundances of $C_{27}\beta$, 17β(H),21β(H)-hopanes, neohop-13(18)-enes and C_{30} hop-17(21)-ene (Mackenzie et al., 1980; ten Haven et al., 1986; Sinninghe Damsté et al., 2014; Volkman et al., 2015) indicate an immature stage. The low abundances of these compounds in organic facies B suggest a different source material rather than a different maturity compared to organic facies A. The same conclusion can be deduced from other parameters based on steranes and

hopanes including the C_{29} ααα 20S/(20S + 20R) ratios and C_{29} vs. C_{30} αβ/(αβ + βα + ββ) ratios (Fig. 4.7). It is thus clear that the studied samples are immature.
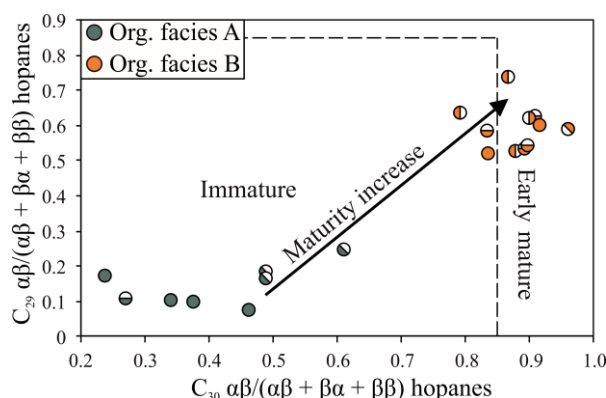
Fig. 4.7. C_{30} αβ/(αβ + βα + ββ) vs. C_{29} αβ/(αβ + βα + ββ) hopanes diagram, indicating maturity. Note: symbols represent sample locations (see Fig. 4.1b).

4.6.2 Origin of organic matter

The majority of the analyzed samples comprise gas prone mixed type II-III kerogen (Fig. 4.8a, Pepper and Corvi, 1995). Here, there is no clear distinction between these two organic facies samples. Actually, the kerogen type of organic facies B cannot be determined accurately based on Rock-Eval data (Fig. 4.8a), since samples with low TOC contents are affected by the mineral matrix effect (MME) in laboratory pyrolysis (Katz, 1983; Espitalié et al., 1985; Grohmann et al., 2019; Beti et al., 2021), i.e. this effect dramatically lowers the true S_2 and thus HI value of samples with TOC contents <3 wt%. As a result, the low S_2 values of organic facies B samples are partly due to the MME; i.e. the type III kerogen character is not due to abundant higher plants OM in these samples as also proven by microscopy investigations. Microscopic observation shows that the OM in organic facies A samples is mainly composed of large fragments (from about 1 to >200 μm) of fusinite and huminite as well as sporinite and resinite/fluorinite (Fig. 4.3a-f) with little algae-derived OM. However, smaller huminite particles and algaederived OM such as thin lamalginite and liptodetrinite are commonly observed in organic facies B samples. There is a very good positive relationship between volumetric percentages of OM and TOC contents ($R^2 = 0.97$) for organic facies A samples (Fig. 4.8b) indicating that most of the organic material is visible in the form of macerals derived from higher plants. This is in agreement with the Rock-Eval results showing type II-III kerogen (Fig. 4.8a). For organic facies B samples, the relationship between TOC and volume percentage of macerals is less clear with a correlation coefficient of only 0.2 implying that part of the OM is submicroscopic, which is consistent with the presence of very small liptodetrinite and very thin lamalginite (Fig. 4.3h). This observation might indicate a pronounced microbial input. This mixed OM is thus interpreted to originate from microbes and higher plants.

This pyrolytic and microscopic information is further supported by molecular geochemical data. Abundant OM input is proposed to originate from plants living close to or in the water. Paq > 0.4

indicates a major input of submerged/floating species (Ficken et al., 2000; He et al., 2020) for organic facies A samples, which probably grew in freshwater environments at the lake margin, close to land. This marginal environment is also indicated by the petrographic data (large huminite and fusinite fragments) as well as by the abundant odd-numbered long-chain n-alkanes (e.g. n-C_{27}; Fig. 4.4a). Abundant middle-chain odd-numbered nalkanes correspond not only to Sphagnum mosses (Nichols et al., 2006; Bingham et al., 2010), Chara (Mead et al., 2005) and freshwater algae (Riboulleau et al., 2007), but also aquatic angiosperms, such as freshwater Nymphaea (Coetzee, 1967) and Ruppia (Mead et al., 2005; He et al., 2020). The odd-numbered long-chain n-alkanes leading to high CPI values (up to 4.7) might indicate higher land plants. They would also be in accordance with the occurrence of Botryococcus braunii, race A (Derenne et al., 1997), although these algae were not detected microscopically. Moreover, the higher concentration of hop-17(21)-enes might represent several eukaryotic phyta (e.g., ferns, mosses, lichens, fungi) (Bottari et al., 1972; Wakeham, 1990; Bechtel et al., 2007) in organic facies A. The interpretation of such an assemblage of OM goes along with the mixed occurrence of huminite, sporinite, fluorinite, and fusinite (Fig. 4.3a-f).
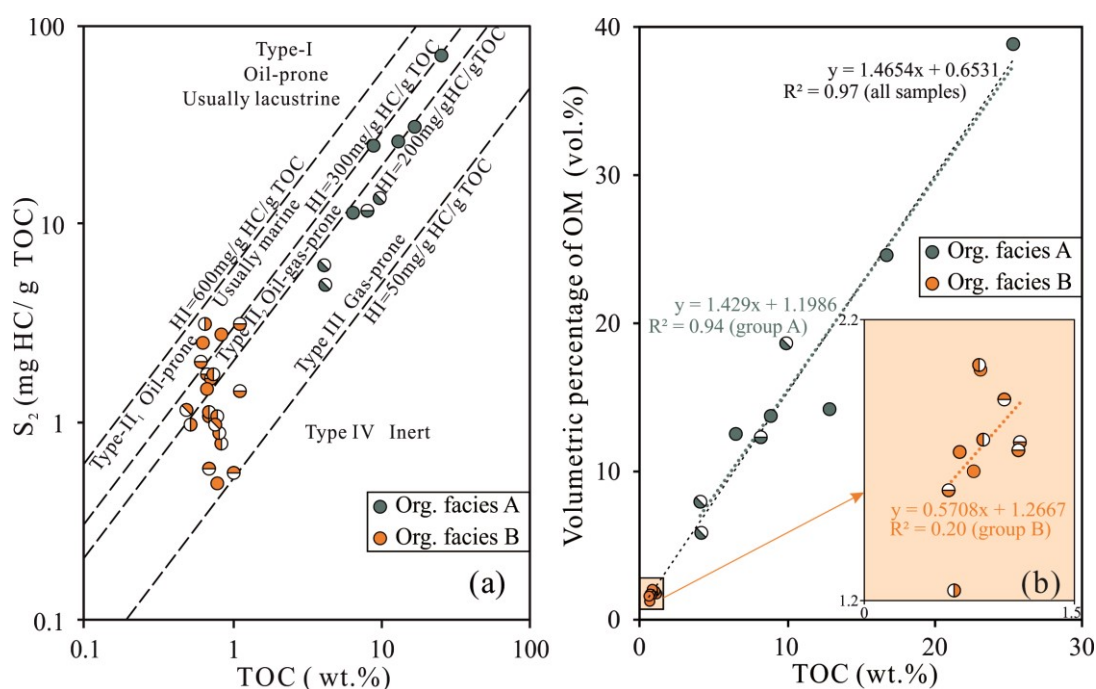
Fig. 4.8. (a) Plots of total organic carbon (TOC) vs. S_2 indicating kerogen types and (b) TOC vs. volumetric percentage of OM indicating that most OM is well visible as macerals (see Fig. 4.3). Note: symbols represent sample locations (see Fig. 4.1b).

By contrast, algae/phytoplankton or cyanobacteria contribute much more to the total OM in organic facies B samples. On a molecular level, this is confirmed by a higher concentration of n-C_{17} (mainly derived from stearic acid in algae; Riboulleau et al., 2007) compared to concentrations of n-C_{23}, n-C_{25} and n-C_{27} alkanes (Table 4.3). This observation is consistent with the presences of planar lamalginite and liptodetrinite (Fig. 4.3h). The occurrence of monomethylalkanes (MMAs), having a methyl group at position 4, 5, 6 or 7 (Fig. 4.4a and b) indicates the input from cyanobacteria living in

microbial mats found in both salt and freshwater environments (Kenig, 2000; Bauersachs et al., 2009; Pawlowska et al., 2013); these compounds are present in both organic facies.

Terrestrial plant input is probably not derived mainly from trees/shrubs/ferns and mangroves, as they typically produce very low Paq values of <0.3 (Ficken et al., 2000; Mead et al., 2005; He et al., 2020) and a distribution of long chain n-alkanes maximizing at C_{29}, C_{31} or C_{33} (Mead et al., 2005; Volkman et al., 2015; He et al., 2020); such a pattern is not observed in the studied samples. The absences of diploptene and fernenes argue also for the lack of ferns (Bottari et al., 1972). This conclusion is further supported by the relatively low C_{24} tetracyclic terpane/C_{23} tricyclic terpane (0.05–0.33) and $C_{19}/(C_{19} + C_{23})$ tricyclic terpane (0.09–0.36) ratios (Table 4.4) (Peters and Moldowan, 1993; Peters et al., 2005; Volk et al., 2005; Volkman et al., 2015) as well as low 1-MP abundances (Alexander et al., 1988). The low oleanane abundance indicates a minor contribution from angiosperms (Moldowan et al., 1994) (Fig. 4.4c and d). It should be noted that this interpretation is not inconsistent with the high content of C_{29} steranes in organic facies A samples (Fig. 4.4e) as these compounds are not only associated with terrestrial higher plants (Volkman, 2003) but can be evolved from some aquatic plants and algae enrich in C_{29} β2 sitosterol and C_{29} stigmasterol (Huang and Meinschein, 1979; Moldowan et al., 1986; Volkman, 2003; Volkman et al., 2015).

1,2,7-TMN used as a marker of angiosperm input (Peters et al., 2005) and 1,2,5-TMN associated with both conifers (Alexander et al., 1988) and angiosperms (Strachan et al., 1988) are present, but seemingly lower in concentration compared to Upper Cretaceous source rocks from e.g. the Gippsland Basin, Australia where both angiosperms and gymnosperms are important precursors of the OM (Jiang and George, 2019). Retene and 1,7-DMP related to conifers (Strachan et al., 1988; van Aarssen et al., 2000) and other aromatic conifer biomarkers including Cad, Sim, 19- + 18-nor-abieta-8,11,13-triene, Tet, Deh and 9- + 2-Mrets (see Fig. 4.5; Simoneit, 1977; Bastow et al., 2001; Otto and Wilde, 2001; Haberer et al., 2006) are present, but in small concentrations, whereas aromatic triterpenoids related to angiosperms (Haberer et al., 2006; Nakamura et al., 2010) are only present at the detection limit.

In summary, there is a much higher contribution of odd-numbered long-chain n-alkanes (peaking at n-C_{27}) and of higher plants-derived macerals in organic facies A than in organic facies B samples, indicating major input of higher plants OM or macrophytes. However, this material does not seem to be mainly derived from gymnosperm or angiosperm wood. This is consistent with a pollen study indicating the abrupt disappearance of some subtropical and coniferous trees coinciding with a dramatic expansion of drought-tolerant herbaceous plants (e.g. Ephedra, Artemisia, and Chenopodiaceae) and the expansion of the steppe during 2.6–1.83 Ma (Wu et al., 2011).

A microbial contribution was interpreted for both organic facies evidenced by the occurrence of hopanoids, branched alkanes (Shiea et al., 1990) and bicyclic alkanes (Alexander et al., 1983; Alexander et al., 1984) (Fig. 4.4a-b). Furthermore, neohop-13(18)-enes (Fig. 4.4c and d) as well as 1,3,6,7-TeMN (Fig. 4.5), which are typical biomarkers associated to a microbial source of OM (Jiang et al., 1998; Cesar and Grice, 2017; Volkman et al., 2015) were observed in both organic facies. Based on the

steranes/hopanoids ratios, which range from 0.21 to 3.29 (avg. 1.48) and 0.58 to 1.77 (avg. 0.99) in organic facies A and B samples, respectively (Table 4.4), a strong microbial contribution is present, which is slightly more pronounced in organic facies B as compared to organic facies A. Steranes originate mainly from eukaryotic OM (algae and higher plants) (Peters et al., 2005), while hopanoids (e.g. hopanes and hopenes) are generally regarded as biomarkers for aerobic bacteria (Innes et al., 1997), although biohopanoids were identified as well in sulfate-reducing bacteria under strictly anoxic conditions (Blumenberg et al., 2006).

Briefly, OM of organic facies A is dominated by aquatic higher plants, i.e. large plants growing at the margin of the lake and submerged angiosperms, while organic facies B is dominated by saltwater algae. Cyanobacteria made a certain contribution to the kerogen in both organic facies, whereas terrestrial higher land plants account for only a small proportion of the OM. Other microbial contribution is on average slightly more pronounced for organic facies B than organic facies A.

4.6.3 Depositional setting

Changes in water levels in lakes as well as growth rates of plants in the adjacent drainage areas can be triggered by climatic changes (Carroll and Bohacs, 1999; Renaut et al., 2013), which then can affect the paleosalinity and biotic components (Qiao et al., 2021b). During arid periods, water salinity tends to be increased, terrestrial input decreased and a stratified water column may develop. On the contrary, higher precipitation increases the amount of terrestrial OM, sediment and nutrient input into the lake.

4.6.3.1 Paleosalinity

Salinity plays an important role in aquatic organism community composition in lake systems (Romero-Viana et al., 2012). The TOC/TS ratios (Fig. 4.9a; Berner and Raiswell, 1984) indicate that organic facies A samples were deposited in a shallow freshwater environment without stratification, which is consistent with the low abundance of C_{33}, C_{34} and C_{35} homohopanes (Sinninghe Damsté et al., 1995b; Peters et al., 2005). Besides, the high concentration of C_{23}–C_{31} odd n-alkanes is an indication of low salinity during deposition of organic facies A (Fig. 4.4a, Riboulleau et al., 2007). In contrast, organic facies B samples developed in hypersaline depositional environments and partly even in lakes with water column stratification, which is supported by the high pregnane and homopregnane compared to steranes (ten Haven et al., 1985; Requejo et al., 1997), high tricyclic terpanes/C_{30} αβ hopane ratios (Kruge et al., 1990; Peters et al., 2005) (Fig. 4.9b), and no carbon-number preference among the n-C_{24}–n-C_{35} alkanes (Peters et al., 2005; Fig. 4.4b). Such a hypersaline environment is further supported by high gammacerane/C_{30} αβ hopane and homodrimane/drimane (HD/D) ratios as abundant homodrimane is characteristic for calcareous mudstones and probably highly saline conditions, while drimane is usually enriched in most crude oils from the freshwater environments (Fan et al., 1991; Al-Arouri et al., 1998) (Fig. 4.9c). Different paleosalinities during deposition of the two organic facies are also indicated by C_{22}/C_{21} tricyclic terpane ratios (Table 4.4; Peters et al., 2005). Under the influence of the Himalayan

orogeny of this period, the prolonged arid/frigid climatic conditions (Wang et al., 1999; Rieser et al., 2009; Zhang et al., 2013b; Zhuang et al., 2011; Cai et al., 2012) favor a hypersaline lake environment with the primary OM being derived from algal and microbial organisms (organic facies B samples) (Warren, 1986). However, from time to time, freshwater dominated the lakes, possibly due to either more humid time intervals or periods when more glacial meltwater was transported to the lakes. It is also possible that marginal parts of the lakes were more freshwater dominated, due to inflow of rivers, whereas central parts were more saline and possibly stratified. For example, it is known that Botryococcus blooms occur currently in the saline lakes of the arid Coorong region after heavy rain (Cane, 1976; Grice et al., 1998). Meanwhile, modern lakes in the Tibetan Plateau are common home to Chara and Ruppia (Liu et al., 2018). Chara live in the photic zone in freshwater environments (Liu et al., 2013) and would become extinct with rising salinity (Krull et al., 2009). Therefore, their presence in the organic facies A samples, as indicated by the GC–MS results and discussed above, supports the interpretation of a freshwater, lacustrine environment during the deposition of facies A. Organic facies B represents the central area of the lake system with higher salinity.
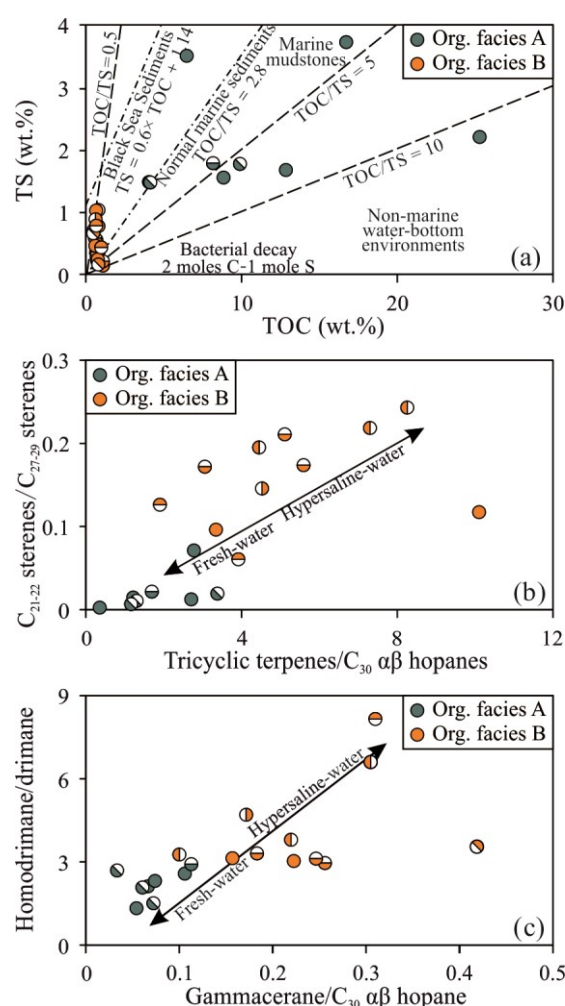
Fig. 4.9. (a) TS vs. TOC, (b) tricyclic terpanes/C_{30} hopane vs. C_{21}-C_{22} steranes/C_{27}-C_{29} steranes, and (c) homodrimane/drimane vs. gammacerane/C_{30} hopane. Note: symbols represent sample locations (see Fig. 4.1b).

4.6.3.2 Paleoredox conditions

In addition to paleosalinity, paleoredox conditions can affect paleoproductivity and OM preservation. The relative concentrations of TOC, TS and iron indicate dysoxic to slightly anoxic bottom water conditions for organic facies A samples and oxic conditions for organic facies B samples (Fig. 4.10a), i.e. there is a major difference between organic facies A and B. The Pr/n-C_{17} vs. Ph/n-C_{18} diagram indicates reducing conditions both for organic facies A and B samples (Fig. 4.10b), with quite some variability for organic facies A. In shallow, hypersaline lakes (Blumenberg et al., 2015; Lee et al., 2019) microbial mats may develop that can provide a seal insulating the under-lying reductive sediments from the overlying oxidizing environment (Pawlowska et al., 2013). Thus, local reducing conditions formed in microenvironments around abundant OM can occur (i.e. "mat-seal effect"; Pawlowska et al., 2013). MMAs (having a methyl group in position 4–7) indicating the presence of microbial mats (Sinninghe Damsté et al., 1995a; Pawlowska et al., 2013) are abundant in the studied samples (Fig. 4.4a and b). Finally, the large sizes of framboidal pyrite in the mineral matrix of the organic facies B samples (Fig. 4.3h) might indicate that the redox interface was very close to the sediment/water interface and not in the water. However, it has to be noted that the amount of framboidal pyrite is rarely high enough to make statistics. Small, dot-like pyrites are abundant, whereas rather large framboidal pyrites can be observed in organic facies A samples as well (Fig. 4.3a, c and e). It should be noticed that dot-like pyrites are randomly distributed over the entire polished sections, but all large framboidal pyrites inserted in or next to OM.
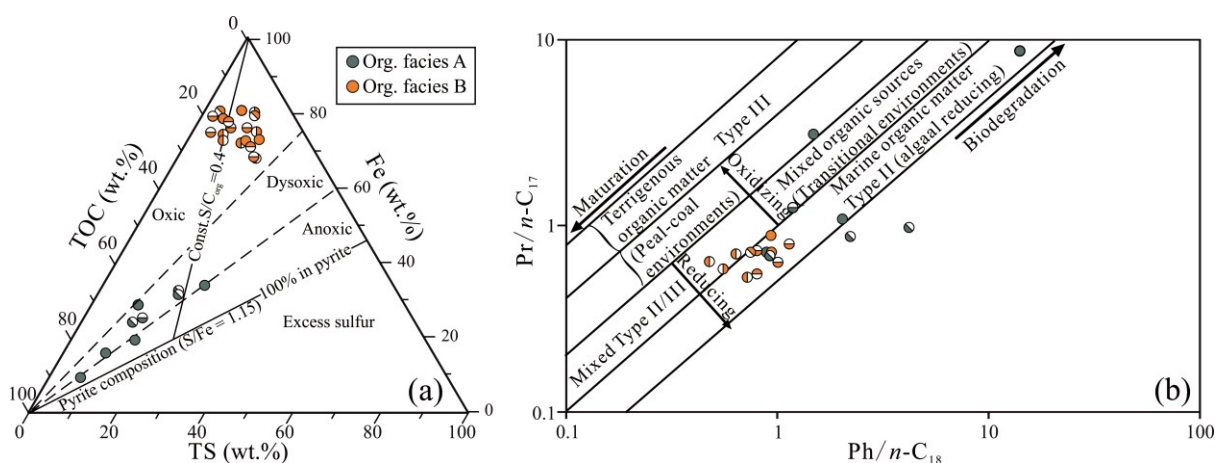
Fig. 4.10. (a) Ternary diagram showing the relative concentration of TOC, TS and Fe. (b) Pristane/n-C_{17} vs. phytane/n-C_{18} reflecting kerogen type, maturity, and depositional environment. Note: symbols represent sample locations (see Fig. 4.1b).

In summary, lake water in marginal areas, where organic facies A was deposited, was less saline than in central areas, represented by organic facies B. Bottom waters were during most times oxygen-depleted but not completely anoxic.

4.6.4 Accumulation rates and methanogenesis

The thermally immature to very early mature stage of the studied samples is a necessary prerequisite for intense microbial methane generation (Schoell, 1980). Both, organic facies A and facies B samples have the potential to generate microbial gas. Organic facies A is clearly more enriched in TOC, which is regarded favorable for microbial gas generation. On the other hand, the larger area of unresolved complex mixture (UCM; Fig. 4.4a and b) and rather high 25-norhopane to hopane ratios in organic facies B indicate that organic facies B samples already underwent slight microbial degradation (Blumer et al., 1973; Peters et al., 2005). This degradation of OM might also explain the abnormally high maturity inferred from biomarkers of organic facies B samples, i.e. steranes are commonly known to be degraded in the order ααα 20R and αββ 20R > ααα 20S and αββ 20S, while the 22S counterparts of the 17α-homohopanes are more stable than their 22R counterparts (Volkman et al., 1983; Peters et al., 2005).

Table 4.6. Age information (Zhang et al., 2013a), depth of the sampled wells and calculated linear sedimentation rates (LSR).

Gas field	Well	Inter-val	Depth top (m)	Depth bottom (m)	Thickness (m)	Age top (Ma)	Age bottom (Ma)	LSR[1] (m/Ma)
Seibei 1	S 1	K 4	680	810	130	1.70	1.84	929
		K 9	1240	1309	69	2.28	2.35	986
		K 10	1309	1435	126	2.35	2.48	969
	T 2	K 6	1245	1400	155	1.70	1.84	1107
Tainan	T 1	K 11	1680	1765	85	2.48	2.58	850
Yanhu	Y 1	K 4	88	148	60	1.70	1.84	429
Seibei 2	S 2	K 2	387	550	163	1.35	1.51	438
		K 3	55	698	643	1.51	1.70	779
		K 7	1052	1152	100	2.08	2.20	833
		K 10	1299	1422	123	2.35	2.48	946
Tuofengshan	T 3	K 6	615	726	111	1.70	1.84	793

[1] Linear Sedimentation Rate; calculated as: LSR = Thickness/(Age top - Age bottom).

Previous isotopic data shows that most microbial gas in the study area is generated in bacterial carbonate reduction environments (Hu et al., 2010; Hu et al., 2015; Pang et al., 2005; Shuai et al., 2016; Zhang et al., 2003; Zhang et al., 2013a). Carbonate reduction as the main methanogenesis pathway in some non-marine freshwater settings has been observed before (Coleman et al., 1988; Schoell, 1988). Low DBT and TS contents in the samples (Fig. 4.6) suggest that microbial sulfate reduction did not contribute to OM degradation in the study area significantly. Thus, OM remained well-preserved before the stage of methanogenesis was reached. Generally, cold climatic conditions along with saline environments, as interpreted for the study area, are favorable for carbonate reducing methanogenis at relatively great depths (Schoell, 1988; Whiticar, 1999; Whiticar, 2020). In this "cold" case, the range of microbial gas generation is shifted to greater depth, which is more favorable for preservation of generated gas than very shallow microbial gas generation. Furthermore, high sedimentation rates are

favorable for microbial gas generation which can be assumed for the Qaidam area. Generally, areas of high paleo bio-productivity do not necessarily coincide with areas of OM enrichment and preservation in sediments (Demaison and Moore, 1980). Within lacustrine systems, primary productivity of OM, redox conditions at the sediment water interface and sedimentation rates are regarded as primary controlling factors for accumulation and preservation of OM (Katz, 2001). Thus, the available data was used to calculate the accumulation rates of bulk sediment as well as organic carbon, carbonates, and clastic minerals based on linear sedimentation rates estimated from the ages and thickness of the different intervals (Fig. 4.2, Table 4.6, Stein, 1991). Calculated sedimentation rates range from 429 to 1107 m/Ma. There are some uncertainties concerning exact stratigraphic boundaries and ages and it is possible that short term non-deposition or erosion affected the area. Even if this effect is neglected, calculated sedimentation rates are high in the entire area, i.e. the organic biomass was rapidly buried, limiting aerobic microbial decay.

Table 4.7. "Determined/calculated" average densities and different accumulation rates (AR) of the sampled intervals.

Gas field	We-ll	Inte-rval	Sample ID	Organic facies	Original TOC (wt.%)	AR[1] (g C m^{-2} a^{-1})			
						Bulk	TOC*	Sil	Carb
Sebei 1 gas field	S 1	K 4	18-850	B	1.41	1704.56	23.99	241.89	186.08
			18-853	A	14.11	1569.38	221.48	151.05	87.62
			18-856	B	0.97	1704.56	16.45	308.08	78.13
			18-857	B	0.96	1704.56	16.36	225.39	169.04
		K 9	18-858	A	10.02	1665.96	166.97	217.87	2.78
			18-860	B	1.43	1809.46	25.88	282.11	193.01
			18-861	A	26.96	1665.96	449.14	155.98	2.78
		K 10	18-862	A	19.51	1638.10	319.51	187.46	1.37
			18-864	A	9.12	1638.10	149.31	228.38	2.73
	T 2	K 6	18-894	A	5.21	1436.59	74.77	120.85	462.10
			18-895	A	5.28	1436.59	75.78	111.80	521.96
Tainan gas field	T 1	K 11	18-867	A	11.26	1436.59	161.76	180.22	2.39
			18-868	B	1.30	724.58	9.42	133.53	1.21
			18-869	B	1.05	786.72	8.28	144.83	24.26
Yanhu gas field	Y 1	K 4	18-872	B	0.98	1870.10	18.33	328.31	144.93
			18-873	A	9.53	1721.79	164.00	206.20	2.87
Sebei 2 gas field	S 2	K 2	18-876	B	1.22	1316.95	16.00	223.46	79.02
			18-878	B	1.26	1429.90	17.98	194.94	147.76
		K 3	18-879	B	1.25	1529.73	19.05	179.32	123.65
			18-880	B	1.04	1736.84	17.98	241.52	305.39
		K 7	18-889	B	1.32	2032.36	26.88	373.81	82.99
		K 10	18-892	B	1.27	3181.85	40.41	350.99	917.43
Tuofengshan gas field	T 3	K 6	18-915	B	0.99	1455.43	14.34	257.44	64.28
			18-916	B	0.89	1455.43	12.95	226.35	151.61

[1] Accumulation rate (AR); calculated as AR =Matter (i.e. TOC, Carbonate and Silicate in %) ×SR × (WBD-1.025Po/100) (after Lückge et al., 1996)

In order to compare ancient sedimentary rocks and recent sediments, accumulation rates rather than sedimentation rates should be used, taking rock densities into account. Accordingly, dry bulk

densities (DBD) and porosities were measured (Table 4.7), in order to calculate WBD. In Table 4.7, accumulation rates are summarized for bulk sediment, TOC, carbonate.

The organic carbon mass accumulation rate of TOC was calculated based on the equation by Lückge et al. (1996):

$$MAR_{TOC} = TOC/100 \times SR \times (WBD - 1.025 \times Po/100) \quad (4.1)$$

where MAR_{TOC} is mass accumulation rate of TOC (g C cm^{-2}a^{-1}), TOC represents total organic carbon (wt%), SR is mean sedimentation rate (cm/a), WBD is wet bulk density based on measured values of samples 18–858, 18–860, 18–867 and 18–915 (2.10 g/cm^3 and 2.22 g/cm^3 for organic facies A and B samples, respectively), and Po represents porosity based on measured values presented above (39.59% and 37.28% for organic facies A and B samples, respectively).

The Qigequan Formation was deposited under rather stable tectonic subsidence, although it was weakly uplifted in the latest Quaternary (Zhang et al., 2013a). The results suggest that the accumulation rates of TOC of both organic facies A samples (74.77–449.14 g C m^{-2}a^{-1} with an average value of 198.08 g C m^{-2}a^{-1}) and organic facies B samples (8.28–40.41 g C m^{-2}a^{-1} with an average value of 18.95 g C m^{-2}a^{-1}) are distinctly higher than e.g. in OM-rich Quaternary marine sediments sites drilled by ODP such as Baffin Bay, Labrador Sea (0.1–3 g C m^{-2}a^{-1}; Stein, 1991). Furthermore, they are greater or close to upwelling areas offshore Peru and Oman (0.4–15.9 g C m^{-2}a^{-1} with an average value of 3.69 g C m^{-2}a^{-1}; Lückge et al., 1996) and open-ocean gyres (0.026–378 g C m^{-2}a^{-1} with an average value of 55.85 g C m^{-2}a^{-1}; Suess, 1980), respectively. This is due to the tectonic setting leading to strong erosion in the hinterland and thus high sediment accumulation rates, combined with lake environments favorable for OM production and preservation. Compared to other lake systems, the values of organic facies B samples are slightly lower and those of facies A are slightly higher than those in Brazilian lakes, such as Feia (43 g C m^{-2}a^{-1}; lake altitude is 850 m) and Agua Preta de Baixo (22 g C m^{-2}a^{-1}; lake altitude is 240 m), where also large populations of floating macrophytes developed during the Holocene (Turcq et al., 2002). It should be noted that organic facies B is generally more prevalent than facies A in the analyzed Pleistocene sequence (about 70 and 20%, respectively) and further both facies are partly interlayered with each other. Since the above mentioned calculations are based on average values for each facies, there is a rather high uncertainty with respect to the absolute values. Nevertheless, even with a total average of about 50.2 g C m^{-2}a^{-1} (taking into account the respective percentage of each facies) there is no doubt about the very high organic carbon accumulation rates in this thick, Pleistocene interval leading to rapid burial of large amounts of kerogen into the zone of methanogenesis. Furthermore, sulphate availability is usually limited in freshwater environments. In case of the Qaidam lake, the marginal areas (organic facies A) were probably less saline than the more central areas represented by organic facies B. Therefore, OM in the freshwater environment (facies A) reached the zone of methanogenesis not only rapidly ut also quite well preserved, whereas organic facies B was more degraded due to higher levels of bacterial sulphate reduction. Temperature critically determines the methanogenesis pathway, i.e., acetate fermentation mainly occurs in sediments at a shallower depth

in warm climates, while greater depth with cold climatic conditions is in favor of the carbonate reduction pathway (Schoell, 1988). Given the above, even though there are minor freshwater microenvironments in marginal lake areas (organic facies A), the cold and dry climate conditions with high burial rate are favorable for carbonate reduction in the Qaidam area. Carbonate reduction as the main methanogenesis pathway in some nonmarine lakewater settings has been observed before (Coleman et al., 1988; Schoell, 1988). Methanogenesis from organic facies A started at much shallower depth (due to limited sulphate availability) and much of this generated methane might have escaped to the surface.

Another area rich in commercial quantities of microbial gas is the southern foreland of the Alps, Italy (Mattavelli et al., 1983), where also rapid sedimentation in the course of mountain building and erosion took place during the Neogene, mainly in freshwater environments.

In summary, the high OM accumulation rate, OM -type and -preservation and its fast burial were the conditions leading to a high microbial gas potential of the Pleistocene lacustrine deposits in the central Qaidam Basin.

4.7 Conclusions

This study combines elemental data including elemental total organic (TOC), inorganic carbon (TIC) and sulfur (TS), as well iron, Rock-Eval pyrolysis, biomarker analysis and microscopic investigation of Pleistocene, microbial gas source rocks in the central Qaidam Basin. The following conclusions concerning thermal maturity of organic matter (OM), its origin and preservation, as well as depositional environment together with paleoclimatic are drawn:

1) Sediments are generally rich in OM, but contain two vastly different organic facies (A and B), which are interlayered with each other. These two facies both represent lacustrine systems.

2) Periodically, shallow freshwater fluvio-lacustrine, environments similar to inundated swamps developed during high water levels at the lake margins with suboxic to anoxic redox conditions in bottom water favoring the development of OM-rich (4.1–25.3 wt% TOC) and sulfur-rich (1.5–3.7 wt% TS) sediments. They represent organic facies A, which, however, accounts for only a small proportion of the whole sedimentary sequence. More common is organic facies B, represented by samples with moderate contents of TOC (0.5–1.1 wt %) and TS (0.14–1.0 wt%), which were deposited under more oxic bottom waters in more distal parts of the lake. However, reducing conditions (indicated by biomarker data) were probably sometimes present in the sediment caused by the "mat-seal effect".

3) The kerogen is classified as gas prone mixed type II-III in most samples, which are thermally immature. A large part of it is derived from aquatic higher plants in sediments representing organic facies A, i.e. macrophytes and submerged angiosperms, that were growing at the lake margin. By contrast, organic facies B samples mainly developed from saltwater algae. Cyanobacteria contributed to the kerogen in both organic facies, while other microbial contribution was more pronounced for

organic facies B than organic facies A. Terrestrial higher land plants only provided a minor part of the kerogen.

4) The calculated organic carbon accumulation rate of both organic facies A (74.77–449.14 g C $m^{-2}a^{-1}$) and organic facies B (8.28–40.41 g C $m^{-2}a^{-1}$) is very high favoring rapid burial of kerogen into the zone of methanogenesis. Furthermore, the cold climatic conditions shifted microbial gas generation to greater depths, where favorable temperatures are present. These factors as well as the low sulphate availability in freshwater, limiting microbial sulphate reduction coupled to OM oxidation, make this sequence an excellent microbial gas exploration and production target.

4.8 Appendix 1

Table A4.1. Identified terpanes and steranes as shown in Fig. 4.5.

Hopanes (*m/z* 191)			Steranes (*m/z* 217)		
Peak	Abbreviation	Biomarker	Peak	Abbreviation	Biomarker
A	C_{19} Tri	C_{19} tricyclic terpane	a	Pregnane	$5\alpha,14\beta,17\beta$(H)-pregnane (diginane)
B	C_{20} Tri	C_{20} tricyclic terpane	b	Homopregnane	$5\alpha,14\beta,17\beta$(H)-homopregnane (20-methyldiginane)
C	C_{21} Tri	C_{21} tricyclic terpane	c	C_{27} $\alpha\alpha\alpha$20S	20S-5α(H), 14α(H), 17α(H)-cholestane
D	C_{22} Tri	C_{22} tricyclic terpane	d	C_{27} $\alpha\beta\beta$20R	20R-5α(H), 14β(H), 17β(H)-cholestane
E	C_{23} Tri	C_{23} tricyclic terpane	e	C_{27} $\alpha\beta\beta$20S	20S-5α(H), 14β(H), 17β(H)-cholestane
F	C_{24} Tri	C_{24} tricyclic terpane	f	C_{27} $\alpha\alpha\alpha$20R	20R-5α(H), 14α(H), 17α(H)-cholestane
G	C_{25} Tri	C_{25} tricyclic terpane	g	C_{28} $\alpha\alpha\alpha$20S	20S-24-Methyl-5α(H), 14α(H), 17α(H)-cholestane
H	C_{24} TeT	C_{24} tetracyclic terpane	h	C_{28} $\alpha\beta\beta$20R	20R-24-Methyl-5α(H), 14β(H), 17β(H)-cholestane
I	C_{26} Tri R	C_{26} R tricyclic terpane	i	C_{28} $\alpha\beta\beta$20S	20S-24-Methyl-5α(H), 14β(H), 17β(H)-cholestane
	C_{26} Tri S	C_{26} S tricyclic terpane	j	C_{28} $\alpha\alpha\alpha$20R	20R-24-Methyl-$5a$(H), $14a$(H), $17a$(H)-cholestane
J	C_{28} Tri R	C_{28} R tricyclic terpane	k	C_{29} $\alpha\alpha\alpha$20S	20S-24-Ethyl-5α(H), 14α(H), 17α(H)- cholestane
	C_{28} Tri S	C_{28} S tricyclic terpane	l[1]	C_{29} $\alpha\beta\beta$20R	20R-24-Ethyl-5α(H), 14β(H), 17β(H)-cholestane
K	C_{29} Tri R	C_{29} R tricyclic terpane	m	C_{29} $\alpha\beta\beta$20S	20S-24-Ethyl-5α(H), 14β(H), 17β(H)- cholestane
	C_{29} Tri S	C_{29} S tricyclic terpane	n	C_{29} $\alpha\alpha\alpha$20R	20R-24-Ethyl-5α(H), 14α(H), 17α(H) -cholestane
1	Ts	C_{27} 18α(H)-22,29,30-trisnorneohopane			
2	Tm	C_{27} 17α(H)-22,29,30-trisnorhopane			

3	C_{27} β	C_{27} 17β(H)-22,29,30-trinorhopane
4	C_{29} N	C_{29} 17α(H),21β(H)-25-norhopanes
5	C_{29} neoH	C_{29} neohop-13(18)-ene
6	C_{29} H	C_{29} 17α(H),21β(H)-30-norhopane
7	C_{29} Ts	C_{29} 18α(H)-30-norneohopane
8	C_{30} H 17(21)	C_{30} hop-17(21)-ene
9	C_{29} M	C_{29} 17β(H),21α(H)-norhopane
10	Ole	Oleanane
11	C_{30} H	C_{30} 17α(H),21β(H)-hopane
12	C_{30} neo H	C_{30} neohop-13(18)-enes
13	C_{29} ββ H	C_{29} 17β(H),21β(H)-norhopane
14	C_{30} M	C_{30} 17β(H),21α(H)-hopane
15	C_{31} H S	C_{31}-17α(H),21β(H)22S-homohopane
	C_{31} H R	C_{31}-17α(H),21β(H),22R-homohopane
16	Gam	Gammacerane
17	C_{30} ββ H	C_{30} 17β(H),21β(H)-hopane
18	C_{32} H S	C_{32} 17α(H),21β(H),22S-homohopane
	C_{32} H R	C_{32} 17α(H),21β(H),22R-homohopane
19	C_{31} ββ H	C_{31} 17β(H),21β(H)-homohopane
20	C_{33} H S	C_{33} 17α(H),21β(H),22S-homohopane
	C_{33} H R	C_{33} 17α(H),21β(H),22R-homohopane
21	C_{32} ββ H	C_{32} 17β(H),21β(H)-homohopane
22	C_{34} H S	C_{34} 17α(H),21β(H),22S-homohopane
	C_{34} H R	C_{34} 17α(H),21β(H),22R-homohopane
23	C_{35} H S	C_{35} 17α(H),21β(H),22S-homohopane
	C_{35} H R	C_{35} 17α(H),21β(H),22R-homohopane

[1] 24-Ethyl-5β(H), 14β(H), 17β(H)-cholestane exists and co-elutes with peaks labeled by l.

5 Climatic conditions during the Pleistocene in the Central Qaidam Basin, NE Tibetan Plateau: Evidence from GDGTs, stable isotopes and major and trace elements of the Qigequan Formation

5.1 Abstract

Sediments in the Tibetan Plateau (TP) region of NW China provide sensitive records of climate change and its impact on past ecosystems. The Qaidam Basin, located in the north-eastern part of the TP contains an exceptionally thick Meso-Cenozoic sedimentary succession; it is also the largest sedimentary basin in the TP. Here, new data on Pleistocene sediments on the TP are reported. Evidence from GDGTs, stable isotopes as well as major and trace elements of the Pleistocene Qigequan Formation was used to decipher depositional conditions within the water column and the origin of kerogen. This information was further applied to interpret factors controlling organic matter (OM) accumulation and climate conditions. In accordance with a previous study, the results show that two completely different organic facies are present, representing vastly different lake environments. OM of organic facies A samples is mainly derived from a mixture of C3 higher plants and phytoplankton, deposited in a shallow freshwater lake environment under dysoxic to anoxic bottom water conditions. In contrast, OM of organic facies B is mainly derived from a hypersaline and more distal lake environments mainly under oxic conditions. OM accumulation in both organic facies was primarily controlled by the paleo-redox conditions rather than paleo-productivity. By contrast, there is no significant difference between organic facies A and B samples with respect to the paleoclimate proxies. Generally, the sediments were deposited under arid/cold conditions with weak chemical weathering during the Pleistocene. The soils on the Tibetan Plateau tended to be alkaline at this time. Combined with the published data, the Pleistocene indices based on GDGT biomarkers indicate a rather continuous cooling and aridification process from Miocene to present. The Pleistocene Mean Annual Air Temperature based on bGDGTs (0.54-4.91 °C, 2.23 °C on average) was slightly higher than the present temperature, and the reconstructed lake surface temperature ranges from 5.7 to 19.6 °C (in winter 2.4-13.7 °C).

5.2 Introduction

Climate change in Asia was affected significantly by altitude changes of the Tibetan Plateau (TP) (Raymo and Ruddiman, 1992; Kutzbach et al., 1993). The TP is not only a controlling factor of the Asian winter and summer monsoons, but also blocks the northward flow of the warm and wet air coming from the Indian Ocean, therefore strongly influencing the climate of continental Asia. Quantitative reconstruction of the paleo-elevation of the TP is of great significance in the study of the process of mountain uplift and in turn its influence on climate and environment (Garzione et al., 2000a, b). For example, strontium isotopes of samples from the Indian Ocean and the Himalayan foreland have been

employed as indicators that suggest links between climate change and topography of the TP (e.g., Edmond, 1992; Derry and France-Lanord, 1996). Further, the evolution of climate and changes in intensity of monsoons is related to the glaciation in the Northern Hemisphere (An et al., 2001). A significant increase in altitude of the TP is thought to have occurred around 11-8 Ma (Harrison et al., 1992; Molnar et al., 1993; Garzione et al., 2000a, b; An et al., 2001; Dettman et al., 2003). The evolution of Asian climate from the Middle Miocene onwards can roughly be divided into three phases and has been reconstructed based on evidence from sediments from continental China and the Indian and North Pacific oceans (Sun et al., 1997, 1998; Rea et al., 1998; An et al., 2001). About 9-8 Ma ago, the Asian interior drought intensified, and the Indian and East Asian monsoons developed. Then, about 3.6-2.6 Ma ago, the East Asian summer and winter monsoons continued to get more intense, and dust transport from direction of the North Pacific increased. Starting with the onset of Pleistocene (2.6 Ma), the variability of the Indian and East Asian summer monsoon increased and its intensity attenuated, while the East Asian winter monsoon got more intense (Sun et al., 1997, 1998; Rea et al., 1998; An et al., 2001).

Sediments, as the products of weathering and sedimentation, hold records of paleo-climatic conditions. With respect to understanding these conditions during the deposition of organic matter (OM)-rich rocks, both inorganic and organic geochemical characteristics can be used. In lacustrine and continent-near marine settings, inorganic geochemical characteristics are largely determined by the composition of source material, weathering, transport distance and -processes as well as by redox conditions and salinity of the bottom water during deposition (Nesbitt, 1979). As a result, some salinity- and redox-sensitive metals can be used as proxies for the evolution of paleo-depositional conditions (Algeo and Maynard, 2004; Abanda and Hannigan, 2006), while other proxies can be used to evaluate weathering intensity and to reconstruct paleo-climatic conditions (Nesbitt et al., 1980; Nesbitt and Young, 1982). For example, biotic processes have an influence on the elemental composition of sedimentary rocks (Algeo and Maynard, 2004; Tribovillard et al., 2006). However, major element data should be used with caution in provenance analysis and the reconstruction of climate due to the mobility of diverse elements during diagenesis (Nesbitt and Young, 1989); the concentration of each element depends on several factors rather than on a single one. Therefore, it is necessary to use multiple proxies to obtain conclusive reconstructions of past environments.

Glycerol dialkyl glycerol tetraether (GDGT) lipids are important components of microbial membrane lipids (Schouten et al., 2013), that are able to record paleo-climatic conditions (Weijers et al., 2007a,b). GDGTs are widely distributed in soils (Weijers et al., 2006a; Liu et al., 2013), peats (Weijers et al., 2006b; Stock et al., 2016), lake sediments (Loomis et al., 2011; Wang et al., 2015; Raberg et al., 2021), and ocean sediments (Schouten et al., 2002, 2003; Liu et al., 2009). The most common GDGT parameters used for reconstruction of paleo-temperatures and redox conditions include isoprenoid GDGTs and branched GDGTs, which are derived from Archaea and Bacteria, respectively (Weijers et al., 2006a). Isoprenoid GDGTs (*i*GDGTs) contain cyclopentane structures, their number

being controlled by the temperature prevailing during archaea growth (Schouten et al., 2002). Branched GDGTs (*b*GDGTs) generally contain two to six methyl branched chain structures and one to two cyclopentane structures. The degree of methylation and cyclisation of the branched tetraethers is related to Mean Annual Air Temperature (MAAT) and pH of soils. The cyclization ratio (CBT) of branched tetraethers is established to indicate paleo-soil pH, while the methylation index (MBT) of branched tetraethers indicates both MAAT and pH; the MBT/CBT is commonly used as a paleo-temperature index (Weijers et al., 2007b). However, there may be a large deviation between the reconstructed regional temperature and the actual temperature in different areas. Thus, it is necessary to establish a regional conversion equation (Yang et al., 2015a). A further application of the MBT/CBT proxy is in paleo-altimetry reconstruction, on the two prerequisites that i) MBT has a good correlation with MAAT and ii) MAAT has a stable temperature lapse rate along a given altitudinal transect (Sinninghe Damsté et al., 2008; Peterse et al., 2009; Anderson et al., 2014; Yang et al., 2015b). At present, only few studies on the relationship between GDGT indices and altitude are available and are regionally concentrated on the Xiangpi Mount region, located southeast of the Qaidam Basin (Liu et al., 2013) and the region north of the Himalayas (Deng et al., 2016).

Climate change can trigger changes in lake levels and plant growth rates in adjacent catchment areas, which causes variation of paleo-salinity and OM composition. During arid periods, terrestrial input tends to be decreased, and water salinity increased with the possible development of stratified water columns. On the contrary, higher precipitation increases the input of terrigenous detrital mineral matter and OM as well as nutrients to the lake (Qiao et al., 2021a, b). $\delta^{13}C_{org}$ values can be used as a criterion for differentiating the origin of OM (Meyers, 1997; Lamb et al., 2006). Furthermore, the TOC/TN ratio can be used to differentiate between terrestrial and aquatic OM input into a lake system (Meyers, 1997). Therefore, combining TOC/TN ratio with $\delta^{13}C_{org}$ values has been used to assess the sources of OM (Lamb et al., 2006).

The Qaidam Basin, located on the north-eastern TP (Fig. 5.1), is a natural experimental field for the study of GDGTs due to its special arid environment. The distributions and the environmental responses of GDGTs in soils and recent lake sediments in the north-eastern TP have been studied thoroughly (Wang et al., 2012, 2013a, b; Liu et al., 2013; Dang et al., 2016; Ding et al., 2016; Li et al., 2016; Sun et al., 2016). However, for older geological periods, it is still necessary to evaluate whether GDGTs can be effectively used as records of paleo-environments. At present, there are only few reports on GDGTs of older strata on the Tibetan Plateau. For example, Xie et al. (2012) studied the tectonic uplifting of the Tibetan Plateau during the Late Miocene by using drought signals recorded by an aridity proxy ($R_{i/b}$; ΣiGDGTs/ΣbGDGTs) in the Zhada Basin. In recent years, new structures (6 methyl isomers, etc.) and new indices of GDGTs have been detected and developed, and a lot of refining has been done on the existing indices (De Jonge et al., 2014; Ding et al., 2016).
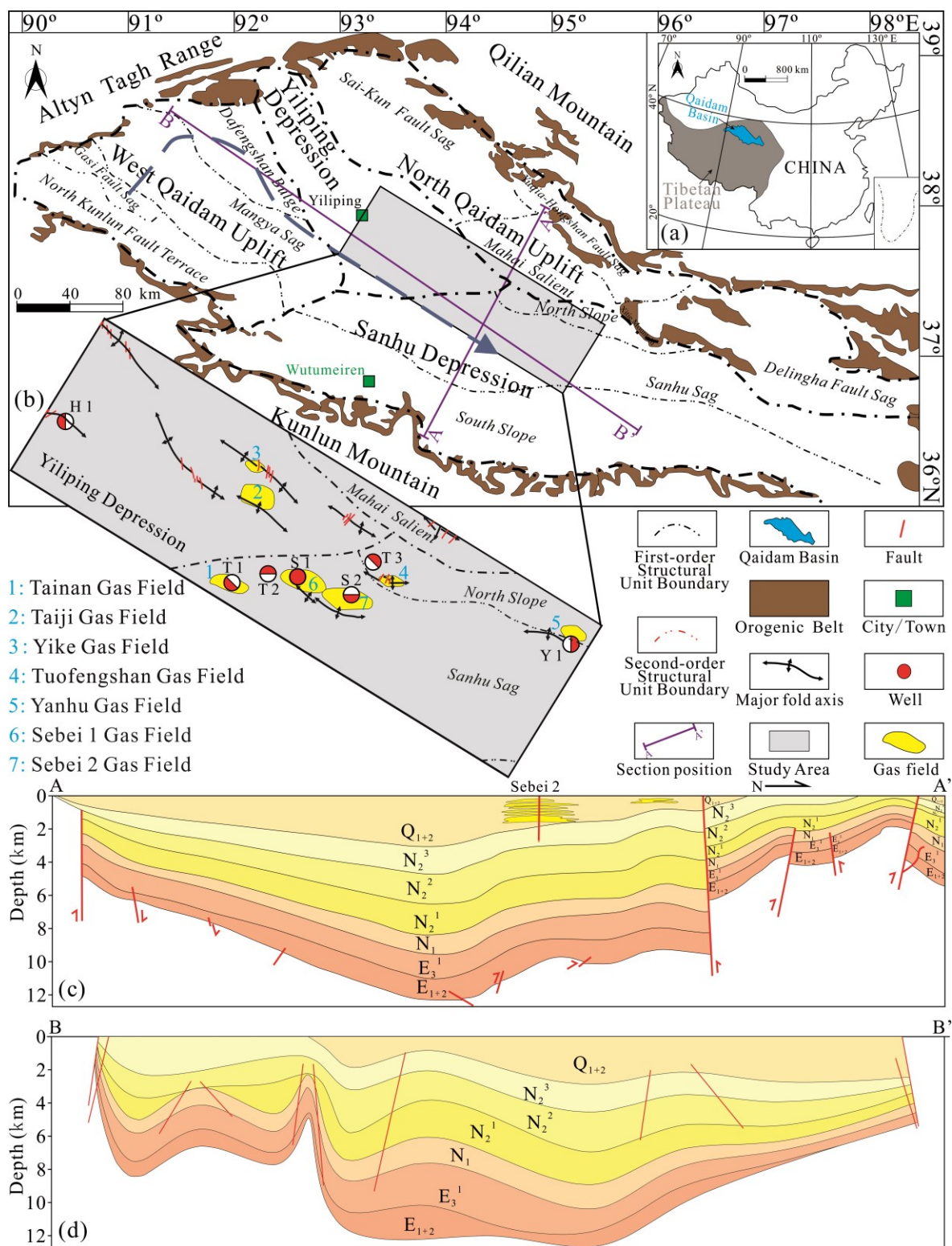
Fig. 5.1. (a) Schematic map showing the location of the Qaidam Basin in China, (b) its geological setting and sample well locations, and (c) cross sections in SE-NE and NW-SE directions (see b for position on the map). The dashed line with an arrow illustrates the depocenter shift during the depositional history of the basin (Qiu et al., 2013).
Note: the different well symbols correspond to the different locations.

This study focuses on the distribution of GDGTs, stable isotopes and major and trace elements of Pleistocene mudstones from the Central Qaidam Basin in the northeast of the Tibetan Plateau, aiming to reconstruct paleo climatic and redox conditions during this episode.

5.3 Geological setting

The Qaidam Basin is located at the northern edge of the Tibetan Plateau covering an area of about 120,000 km^2 at an elevation of 2.7 to 3.5 km. The rhomb-shaped intermontane basin is surrounded by large-scale faults creating a high relief towards three mountain ranges: the Eastern Kunlun Mountain in the south, the Altyn Tagh Range in the northwest, and the Qilian Mountains in the east (Tapponnier et al., 2001; Fang et al., 2007; Fig. 5.1a). During the Mesozoic and Cenozoic a 3 to 16 km thick sedimentary succession, mainly of lacustrine origin, was deposited (Pang et al., 2005; Jian et al., 2013; Qiao et al., 2021a). The Mesozoic tectonic regime was characterized by the evolution of the Tethys and Mongol–Okhotsk Oceans and by the collision of related tectonic units (Gehrels et al., 2011).

The initial formation and evolution of the basin was controlled by syn-sedimentary basement faults during the Mesozoic; each part of the basin evolved into a combined major depression during the Paleogene-Neogene. During the Quaternary, inversion and folding took place in the midwestern part of the basin and subsidence in the eastern part (Dang et al., 2008). The tectonic evolution of the Cenozoic basin is characterized by the collision of the Indian and Eurasian plates. The depocentre moved from the northern part during the Jurassic westwards during the Paleogene-Neogene, and then towards the east during the Pleistocene (Pang et al., 2005). The Qaidam Basin can be divided into four main structural units; the West and North Qaidam Uplifts and the Sanhu and Yiliping Depressions (Fig. 5.1b; Bao et al., 2017). In the Early Pleistocene, a thick succession of fluvial-deltaic sediments was deposited. During the Middle Pleistocene, the paleo-lake reached its maximum depth, leading to deposition of mainly fine-grained argillaceous sediments. Then, in the Late Pleistocene, and under the influence of the recent tectonic movements, the central part of the basin was continuously uplifted (Dang et al., 2008).

The Pleistocene Qigequan Formation (Q$_{1+2}$), which is the subject of this study, reaches thicknesses between 1.7 and 3.4 km, and was deposited at high sedimentation rates of around 650 to 800 m/Ma (Fig. 5.1c, d; Dang et al., 2008; Shuai et al., 2013; Zhang et al., 2013a).

Based on seismic data, the Q$_{1+2}$ can be divided into 14 intervals (K$_0$-K$_{13}$; Fig. 5.2). The lithology of Q$_{1+2}$ Formation is dominated by silty mudstones, mudstones, siltstones, and muddy limestones as well as some thin halite layers of up to 2.0 m thickness. Under the influence of the tectonic movements during the Late Pleistocene, about 500 m of the succession was eroded in the northernmost part of the Sanhu Slope (Fig. 5.1a, b; Zhang et al., 2013a). This study focuses on Pleistocene samples from the central part of the basin, where large gas fields developed, sourced from and trapped in near-shore, shallow, lacustrine sediments (Fig. 5.1b; Shuai et al., 2013; Zhang et al., 2013a; Wang et al., 2015).
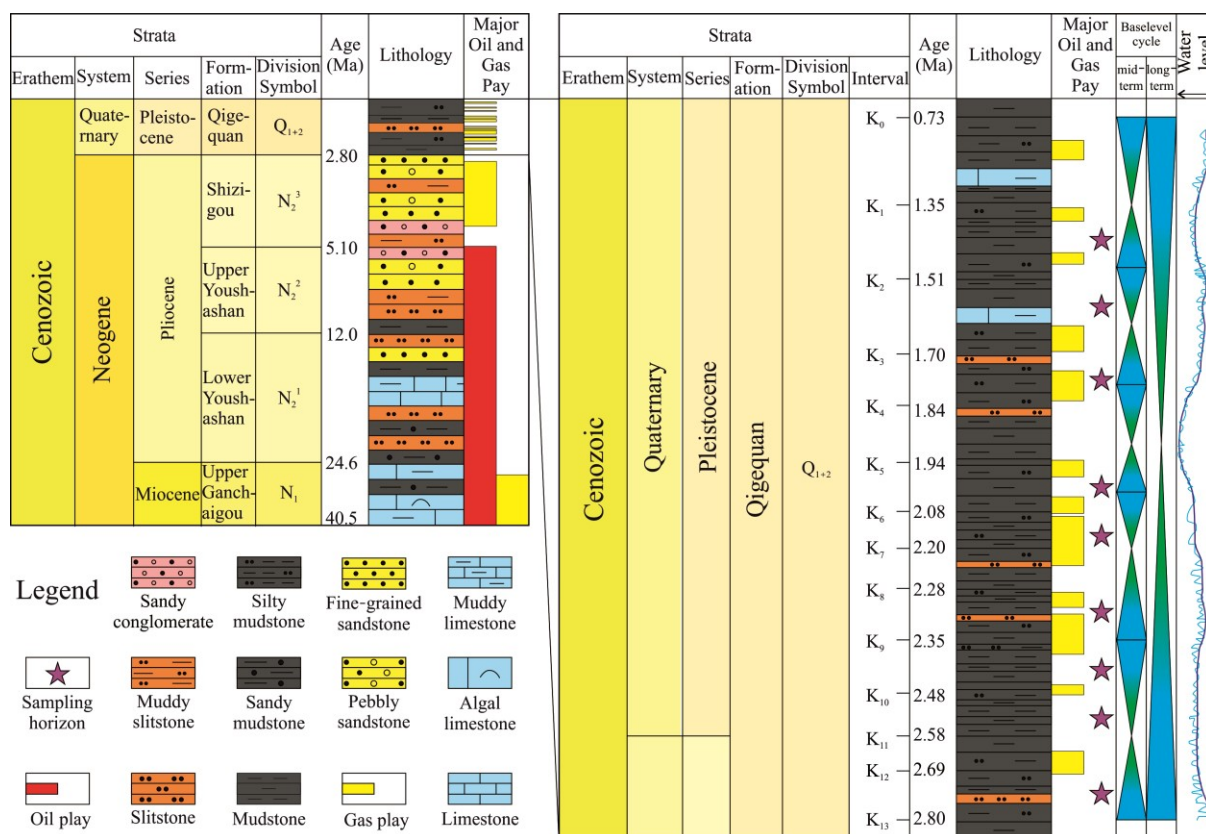
Fig. 5.2. Generalized Pleistocene stratigraphic column for the study area (modified after Jian et al., 2013; Zhang et al., 2013a).

5.4 Material and methods

30 samples have been investigated on which organic geochemical and petrographic characteristics have been studied in detail previously (Fig. 5.1). Two different organic facies (A and B) are distinguished based on these characteristics, indicating completely different depositional environments (for more detailed see Qiao et al., 2021a).

5.4.1 Kerogen Concentration

14 samples were selected to obtain total organic matter concentrates. First, the powdered samples were treated with 32% hydrochloric acid (HCl) to remove carbonates and then were neutralized. Thereafter, concentrated hydrofluoric acid (FH) was used to remove silicates. Finally, the residues were neutralized again with water and air-dried. During the process, the materials were not exposed to oxidizing agents or high temperature.

5.4.2 Elemental analysis

Before the measurement of major and trace elements, fresh core samples were pulverized to a mesh size of < 200 using a tungsten carbide ball mill. Major elements were analyzed using an ARL Perform' X 4200 wavelength-dispersive X-ray fluorescence (WD-XRF) spectrometer. Loss on ignition (LOI) was achieved by heating 1 g of powder at 1100 ºC for one hour. Analytical precision was better than 1%.

The relative concentration of trace elements of bulk rock samples was determined via an ELAN DRC-e inductively coupled plasma mass spectrometer (ICP-MS). Before the insertion into the ICP-MS, powders were digested with a mixed solution of HF/HNO_3 in high-pressure Teflon bombs, and then heated to 190 °C for 48 h. Internal and international standards (BH-VO2, AGV-2, BCR-2 and GSP-1 (USGS)) were used for calibration and three duplicates were analyzed to invest the accuracy of the measurements. Analytical accuracy and precision are 10% and 5%, respectively.

The measurement of total organic (TOC) and inorganic (TIC) carbon contents of the kerogen concentrates were performed using a Liqui TOC II analyzer (Elementar). In addition, total sulfur (TS) content was analyzed using a Leco S 200 sulfur analyzer. Further information on these analyses is published in Qiao et al. (2020 and 2021b). The elemental compositions of kerogen (C, N, H) were analyzed by using a LECO-CHN-628 based on DIN 51732.

5.4.3 Rock-Eval pyrolysis

Rock-Eval pyrolysis was performed on the kerogen concentrates using a Rock-Eval VI instrument (Vinci Technologies) following the procedure describe in detail in Behar et al. (2001). The measured parameters include S_1 (volatile/sorbed hydrocarbon content, mg HC/g rock), S_2 (remaining hydrocarbon generative potential, mg HC/g rock), and T_{max} (temperature of maximum pyrolysis yield, °C). Hydrogen index (HI = S_2/TOC, mg HC/g TOC) was calculated.

5.4.4 Organic geochemical analyses

5.4.4.1 Experimental Methods

Aliquots of 10-15 g of pulverized sample were extracted by ultra-sonication for 15 min and subsequent stirring for 15 min at room temperature. The extraction was performed sequentially using methanol (50 mL), a mixture of methanol and dichloromethane (1:1, vv; 50 mL), and dichloromethane (50 mL), respectively. The combined raw extracts were concentrated using rotary evaporation to a volume of 1 mL, dried by addition of ca. 2 mg of sodium sulfate and evaporated to dryness under a gentle stream of nitrogen at room temperature. Prior to fractionation, the extracts were re-dissolved in a mixture of 0.5 mL of *n*-pentane and 300 µL of DCM. Fractionation was performed by column chromatography using microcolumns with activated silica gel (2 g) and eluents of increasing polarity resulting in three fractions: 5 mL of *n*-pentane/DCM (40:60, v:v); 5 mL of DCM; and 5 mL of methanol/DCM (1:1, v:v). The third fraction, containing the GDGTs, was evaporated to dryness under a gentle stream of nitrogen, re-dissolved in 400 µL of a mixture of *iso*-propanol/*n*-hexane (1:99, v:v), and finally filtered over a 0.4 µm polytetrafluoroethylene (PTFE) filter. Liquid chromatography-mass spectroscopy was conducted with a Thermo Finnigan MAT LCQ-MS equipped with an APCI ion source and a cyanid-column (3µm, 150×3 mm) with a scanning range of 950 to 1450 *m/z*. Nitrogen was used as carrier gas.

5.4.4.2 Calculation of GDGTs proxies

Different indices including the branched isoprenoid tetraether (BIT; Hopmans et al., 2004), the methylation of branched tetraether MBT[(t)] (after Weijers et al., 2007b; Peterse et al., 2012), CBT

(cyclisation of branched tetraether after Weijers et al., 2007b), and the TetraEther index of tetraethers consisting of 86 carbon atoms (TEX$_{86}$; Schouten et al., 2002) were calculated following the equations (5.1)-(5.5).

$$\text{BIT} = \frac{b\text{GDGT III} + b\text{GDGT II} + b\text{GDGT I}}{b\text{GDGT III} + b\text{GDGT II} + b\text{GDGT I} + \text{crenarchaeol}} \ (5.1)$$

$$\text{MBT} = \frac{b\text{GDGT I} + b\text{GDGT Ia} + b\text{GDGT Ib}}{b\text{GDGT I} + b\text{GDGT Ia} + b\text{GDGT Ib} + b\text{GDGT II} + b\text{GDGT IIa} + b\text{GDGT IIb} + b\text{GDGT III} + b\text{GDGT IIIa} + b\text{GDGT IIIb}} \ (5.2)$$

$$\text{MBT}' = \frac{b\text{GDGT I} + b\text{GDGT Ia} + b\text{GDGT Ib}}{b\text{GDGT I} + b\text{GDGT Ia} + b\text{GDGT Ib} + b\text{GDGT II} + b\text{GDGT IIa} + b\text{GDGT IIb} + b\text{GDGT III}} \ (5.3)$$

$$\text{CBT} = -\log \left(\frac{b\text{GDGT Ia} + b\text{GDGT IIa}}{b\text{GDGT I} + b\text{GDGT II}}\right) \ (5.4)$$

$$\text{TEX}_{86} = \frac{i\text{GDGT}-2 + i\text{GDGT}-3 + \text{Cren}\prime}{i\text{GDGT}-1 + i\text{GDGT}-2 + i\text{GDGT}-3 + \text{Cren}'} \ (5.5)$$

Several calibrations for lake surface temperature (LST) and specific calibrations for summer (SLST) and winter lake surface temperature (WLST) from global and regional studies have been proposed, i.e. the equation (5.6)-(5.11) (Powers et al., 2010; Tierney et al., 2010a; Castañeda and Schouten, 2011; Pearson et al., 2011; Sun et al., 2011).

$\text{LST}_{\text{Powers2010}} = 50.8 \times \text{TEX}_{86} - 10.4 \ (5.6)$

$\text{SLST}_{\text{Powers2010}} = 46.6 \times \text{TEX}_{86} - 5.6 \ (5.7)$

$\text{WLST}_{\text{Powers2010}} = 57.3 \times \text{TEX}_{86} - 17.5 \ (5.8)$

$\text{LST}_{\text{Tierney2010}} = 38.87 \times \text{TEX}_{86} - 3.50 \ (5.9)$

$\text{LST}_{\text{Castañeda2011}} = 54.89 \times \text{TEX}_{86} - 13.36 \ (5.10)$

$\text{LST}_{\text{Kim2008}} = 56.2 \times \text{TEX}_{86} - 10.78 \ (5.11)$

MAAT (mean annual air temperature) was calculated based on assumptions and calibrations for both soils and lake sediments. Based on a globally distributed soil calibration (Weijers et al., 2007b), MAAT can be obtained using Eq. 5.12. This calibration was extended and revised with the transfer function (Eq. 5.13) proposed by Peterse et al. (2012). The MAAT proxy based on the distribution of bGDGTs in global soils was calculated following the equation of De Jonge et al. (2014) (5.14 and 5.15). In addition, a calibration for soil-derived GDGTs on the Tibetan Plateau (Günther et al., 2014) was applied (5.16).

$$\text{MAAT}_{\text{Weijers2007 (G)}} = \frac{\text{MBT} - 0.12 - 0.19 \times \text{CBT}}{0.02} \ (5.12)$$

$\text{MAAT}_{\text{Peterse2012}} = 0.81 - 5.67 \times \text{CBT} + 31.0 \times \text{MBT}' \ (5.13)$

$\text{MAAT}_{\text{De Jonge 2014}} = 7.17 + 17.1 \times [\text{I}] + 25.9 \times [\text{Ib}] + 34.4 \times [\text{Ic}] - 28.6 \times [\text{II}] \ (5.14)$

$\text{MAAT}_{\text{De Jonge 2014}'} = -8.15 + 31.45 \times \text{MBT}' \ (5.15)$

$\text{MAAT}_{\text{Günther 2014}} = -3.84 + 9.84 \times \text{CBT} + 5.92 \times \text{MBT}' \ (5.16)$

Several global and regional lake temperature calibration studies have been proposed for African (Tierney et al., 2010a; Loomis et al., 2012), Chinese and Nepalese lakes (Sun et al., 2011) and lakes along a transect from the Scandinavian Arctic to Antarctica (Pearson et al., 2011):

$\text{MAAT}_{\text{Tierney2010}} = 11.84 + 32.54 \times \text{MBT} - 9.32 \times \text{CBT} \ (5.17)$

$\text{MAAT}_{\text{Tierney2010'}} = 50.57 - 74.28 \times [\text{III}] - 31.60 \times [\text{II}] - 34.79 \times [\text{I}]$ (5.18)

$\text{MAAT}_{\text{Sun2011}} = 4.0 + 38.2 \times \text{MBT} - 5.6 \times \text{CBT}$ (5.19)

$\text{MAAT}_{\text{Pearson2011}} = 20.9 + 98.1 \times [\text{Ib}] - 12.0 \times [\text{II}] - 20.5 \times [\text{III}]$ (5.20)

$\text{MAAT}_{\text{Loomis2012}} = 22.77 - 33.58 \times [\text{III}] - 12.88 \times [\text{II}] - 418.53 \times [\text{IIc}] + 86.43 \times [\text{Ib}]$ (5.21)

Moreover, the following equations were applied to calculate soil–pH based on *i*GDGTs from global and regional studies (Tierney et al., 2010a; Sun et al., 2011; De Jonge et al., 2014), including calibrations for the Tibetan Plateau (Günther et al., 2014).

$\text{pH}_{\text{Günther2014}} = 7.97 + 2.78 \times \text{CBT}$ (5.22)

$\text{pH}_{\text{De Jonge2014}} = 7.9 - 1.97 \times \text{CBT}$ (5.23)

$\text{pH}_{\text{Weijers2007}} = (3.33 - \text{CBT})/0.38$ (5.24)

$\text{pH}_{\text{Tierney2010}} = 10.32 - 3.03 \times \text{CBT}$ (5.25)

$\text{pH}_{\text{sun2011}} = 8.98 - 1.72 \times \text{CBT}$ (5.26)

The following equations were used to evaluate aridity conditions:

Aridity proxy R$_{i/b}$ (Xie et al., 2012) $= \Sigma i\text{DGETs}/\Sigma b\text{DGETs}$ (5.27)

#rings$_{\text{tetra}}$ (Sinninghe Damsté, 2016) $= ([\text{Ib}] + 2 \times [\text{Ic}])/([\text{Ia}] + [\text{Ib}] + [\text{Ic}])$ (5.28)

5.4.5 Carbon and nitrogen isotopes

Carbon and nitrogen isotope measurements were carried out on kerogen concentrates. Around 0.05-0.1 mg isolated kerogen was weighed into tin capsules. The measurements were performed on a Delta V Advantage isotope ratio mass spectrometer linked to a Flash EA IsoLink™ combustion elemental analyzer. The $\delta^{13}\text{C}$ and $\delta^{15}\text{N}$ values are given relative to the international VPDB (Vienna Pee Dee Belemnite) and AIR standards. International reference materials USGS 24 and USGS 40 ($\delta^{13}\text{C}$), IAEA N1 and IAEA N$_2$ ($\delta^{15}\text{N}$) were used to monitor analytical performance.

5.5 Results

5.5.1 Elemental composition

The major and trace elemental concentrations of the bulk samples are shown in Table 5.1. Ratios of $\text{SiO}_2/\text{Al}_2\text{O}_3$ (2.67-4.58) and $\text{Fe}_2\text{O}_3/\text{K}_2\text{O}$ (1.27-3.13) (Table 5.2) are in accordance with the typical ratios observed in shales (Herron, 1988). Their compositions normalized to Post-Archean Australian Shale (PAAS) (Taylor and McLennan, 1985) are shown in Fig. 5.3. Compared to the PAAS, the Pleistocene source rocks are depleted in SiO_2, TiO_2, Al_2O_3, Fe_2O_3, K_2O, and enriched in Na_2O. The relative concentrations of CaO and P_2O_5 vary around the PAAS value in two organic facies samples (Fig. 5.3). Relative to the PAAS, Rb, Th, Mn and Ga are depleted only in organic facies A. Sr is enriched in organic facies B and U and Mo in organic facies A. Ba shows a larger variation in organic facies B compared to that in organic facies A (Fig. 5.3). Enrichment factors (EF) for trace elements (X) were calculated as:

$\text{X}_{\text{EF}} = (\text{X/Al})_{\text{sample}}/(\text{X/Al})_{\text{PAAS}}$ (5.29)
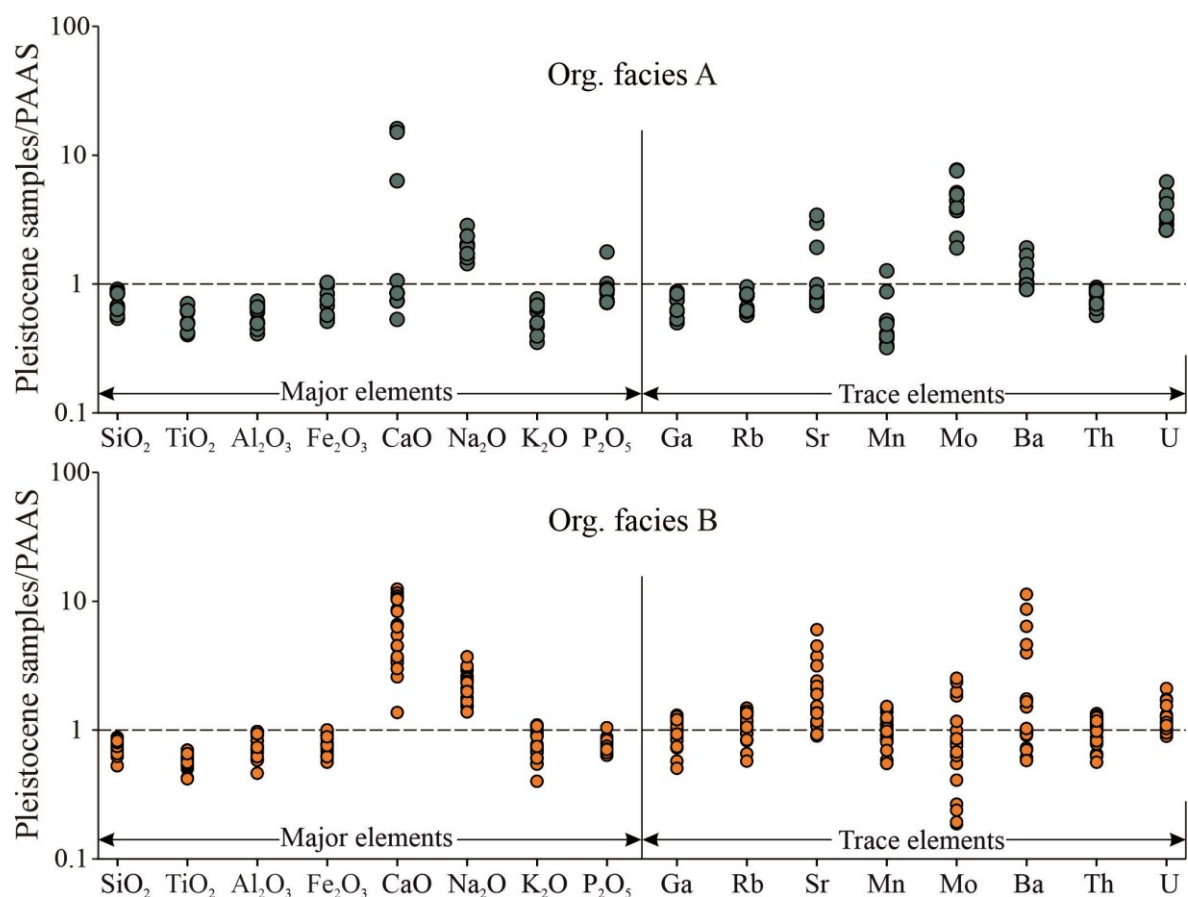
Fig. 5.3. Major and trace elements normalized to Post-Archean Australian Shale (PAAS; Taylor and McLennan, 1985) for the Pleistocene source rocks.

The TOC, TIC, and TS data of the whole rock samples can be found in a previously published study (Qiao et al., 2021a). The elemental composition of the concentrated kerogen are shown in Table 5.3. The TOC and TIC contents of the isolated kerogen for the organic facies A samples are 22.44-48.16 wt.% TOC with an average value of 33.79 % and 0.02-0.07 wt.% TIC with an average of 0.04 wt.%, respectively (Table 5.3). TIC values close to zero are expected after HCl treatment The TS values for organic facies A are 2.17-9.80 wt.% with an avg. of 5.44 wt.%.

Kerogen from organic facies A samples has both high C/N atomic ratios of 25.18-33.76 and C/S atomic ratios of 7.40–40.15 (Table 5.3). H/C atomic ratios of organic facies A are 1.30–1.61 (1.44 on average) and thus in a typical range for kerogen (Table 5.3). TOC, TIC, TS and elemental composition in terms of hydrogen, and nitrogen contents for the organic facies B samples could not be measured accurately due to the poor kerogen concentrations and are thus not reported here.

Table 5.1. Major and trace elements concentrations of the Pleistocene lacustrine mudstone.

Well	Interval	Sample ID	Depth (m)	Organic facies	TOC (%)	Major elements (%)								Trace elements (ppm)							
						SiO_2	TiO_2	Al_2O_3	Fe_2O_3	CaO	Na_2O	K_2O	P_2O_5	Ga	Mn	Rb	Sr	Mo	Ba	Th	U
K4	K4	18-850	794.76	B	0.83	48.80	0.59	14.19	6.14	8.43	2.93	2.86	0.14	19	833	172	418	2	2586	15	4
	K9	18-853	801.46	A	12.86	41.98	0.50	9.63	3.99	8.25	2.41	1.75	0.12	12	443	105	387	14	1085	11	15
	K4	18-856	811.86	B	0.62	50.13	0.61	18.07	6.55	4.33	2.02	3.96	0.11	25	828	222	234	1	4152	19	3
S1	S1	18-857	820.47	B	0.78	53.68	0.62	13.22	5.41	7.09	3.11	2.47	0.14	17	877	149	281	1	1080	14	3
	K9	18-858	1269.00	A	8.86	57.28	0.69	13.08	6.08	1.11	2.46	2.62	0.16	16	323	135	164	10	609	14	15
K9		18-860	1272.50	B	0.68	48.56	0.63	15.59	6.54	8.23	1.82	3.29	0.10	21	590	191	307	2	621	16	4
		18-861	1279.40	A	25.31	40.05	0.49	9.36	4.15	1.11	2.07	1.87	0.12	13	284	100	175	9	592	10	8
K10	K10	18-862	1377.50	A	16.73	42.64	0.50	11.44	7.10	1.11	2.40	2.27	0.12	15	351	129	154	15	1240	12	19
	K10	18-864	1380.50	A	6.49	52.90	0.71	13.94	7.43	0.69	2.33	2.83	0.12	18	273	153	136	7	926	13	13
		18-867	1697.30	A	4.08	36.01	0.42	8.41	3.70	19.69	1.92	1.46	0.28	11	743	98	683	4	762	9	10
K11	K11	18-868	1697.50	A	4.15	34.06	0.41	7.78	3.95	20.91	1.73	1.31	0.14	10	1078	92	596	4	674	8	9
T1	T1	18-869	1697.70	A	9.91	53.23	0.62	12.55	5.40	0.96	2.84	2.53	0.14	17	335	134	144	7	643	13	10
Y1	Y1	18-872	124.69	B	0.64	53.48	0.54	18.43	6.60	1.78	1.88	4.05	0.12	26	687	237	273	5	7352	20	5
	K4	18-873	124.99	B	0.52	50.15	0.56	18.41	7.25	3.91	1.66	4.02	0.11	25	1064	225	271	2	5627	18	3
	K2	18-876	534.40	B	0.71	54.97	0.59	17.56	4.93	3.76	2.99	3.87	0.13	24	469	210	180	0	2997	16	3
		18-878	543.80	A	8.19	54.85	0.61	11.98	4.89	1.38	3.42	2.46	0.15	15	416	131	198	8	782	13	15
S2	S2	18-879	555.10	B	1.11	48.43	0.70	16.97	6.89	5.82	2.52	3.55	0.12	23	1298	206	279	0	982	18	3
K3	K3	18-880	566.10	B	1.10	46.64	0.58	13.63	5.64	8.55	3.49	2.65	0.11	18	924	162	480	1	1132	15	3
	K7	18-889	1082.70	B	0.66	41.17	0.53	11.72	4.49	13.40	4.45	2.24	0.13	10	496	92	630	1	376	8	4
	K10	18-892	1313.30	B	0.60	46.72	0.59	13.91	5.45	10.82	1.99	2.76	0.11	19	956	168	378	1	601	14	4
T2	K6	18-894	1266.70	B	1.00	49.00	0.61	18.39	7.23	4.56	1.83	4.03	0.11	25	1023	226	226	1	664	17	3
		18-895	1269.90	B	0.70	40.38	0.50	11.03	5.17	15.11	2.36	2.03	0.12	15	931	133	898	3	641	11	5
		18-897	235.10	B	0.79	39.55	0.43	11.17	4.40	16.16	3.76	2.23	0.11	15	709	133	1203	5	589	10	7
K4	K4	18-898	255.90	B	0.70	33.06	0.42	8.70	4.06	14.30	2.87	1.48	0.13	11	1251	105	302	4	398	9	5
		18-899	266.40	B	0.74	/	/	/	/	/	/	/	/	/	/	/	/	/	/	/	/
H1		18-900	982.20	B	0.69	39.16	0.52	11.01	4.62	13.70	2.80	2.01	0.13	15	1174	134	437	4	454	12	4
K13	K13	18-901	985.80	B	0.82	44.73	0.56	12.64	5.67	11.23	3.15	2.53	0.13	17	727	152	744	2	470	13	4
		18-904	1005.90	B	0.85	/	/	/	/	/	/	/	/	/	/	/	/	/	/	/	/
T3	K6	18-915	631.30	B	0.49	51.55	0.65	17.69	6.39	4.81	2.39	3.96	0.11	24	775	216	185	2	668	17	3
K6		18-916	646.11	B	0.77	46.35	0.70	15.55	5.59	5.87	2.14	3.35	0.17	21	854	183	216	0	627	16	4

Table 5.2. Calculated elemental ratios of the Pleistocene lacustrine mudstones.

Well	Interval	Sample ID	Depth (m)	Organic Facies	CIA CORRECTED	Ga/Rb	K_2O/Al_2O_3	SiO_2/Al_2O_3	Fe_2O_3/K_2O	U/Th	Sr/Ba	Authigenic U	Mo_{EF}	U_{EF}	Mo/TOC	TS/Fe	Al_2O_3/TOC	TS/Mn	TiO_2/TOC
		18-850	794.76	B	49.87	0.11	0.20	3.44	2.15	0.26	0.16	-1.16	1.06	1.71	1.82	0.18	17.10	9.25	0.71
	K4	18-853	801.46	A	37.34	0.12	0.18	4.36	2.28	1.38	0.36	11.31	14.89	9.43	1.11	0.60	0.75	37.74	0.04
		18-856	811.86	B	60.93	0.11	0.22	2.77	1.66	0.17	0.06	-3.06	0.66	1.08	1.93	0.10	29.15	5.55	0.99
		18-857	820.47	B	51.44	0.11	0.19	4.06	2.19	0.20	0.26	-1.92	0.38	1.28	0.64	0.06	16.95	2.74	0.79
S 1		18-858	1269.00	A	60.91	0.12	0.20	4.38	2.32	1.07	0.27	10.16	7.41	6.87	1.09	0.36	1.48	48.03	0.08
	K9	18-860	1272.50	B	54.89	0.11	0.21	3.11	1.99	0.22	0.49	-1.88	1.20	1.40	2.75	0.22	22.93	16.94	0.93
		18-861	1279.40	A	57.09	0.13	0.20	4.28	2.22	0.79	0.29	4.72	10.05	5.31	0.37	0.76	0.37	77.36	0.02
	K10	18-862	1377.50	A	58.62	0.12	0.20	3.73	3.13	1.57	0.12	15.16	12.68	10.26	0.87	0.74	0.68	105.48	0.03
		18-864	1380.50	A	64.31	0.11	0.20	3.79	2.62	0.26	0.15	8.99	5.05	5.86	1.09	0.67	2.15	128.35	0.11
		18-867	1697.30	A	36.92	0.11	0.17	4.28	2.53	1.06	0.90	6.80	4.29	7.20	0.89	0.58	2.06	20.19	0.10
T 1	K11	18-868	1697.50	A	37.16	0.11	0.17	4.38	3.02	1.08	0.89	6.21	5.51	7.05	1.03	0.54	1.88	13.91	0.10
		18-869	1697.70	A	59.10	0.13	0.20	4.24	2.13	0.80	0.22	6.07	5.92	5.04	0.75	0.48	1.27	53.69	0.06
		18-872	124.69	B	64.18	0.11	0.22	2.90	1.63	0.24	0.04	-1.73	2.58	1.58	7.44	0.19	28.79	12.80	0.85
Y 1	K 4	18-873	124.99	B	61.59	0.11	0.22	2.72	1.80	0.17	0.05	-2.91	0.88	1.05	3.11	0.14	35.40	6.68	1.08
	K2	18-876	534.40	B	64.88	0.11	0.22	3.13	1.27	0.18	0.06	-2.39	0.26	1.02	0.64	0.10	24.73	7.67	0.83
		18-878	543.80	A	53.74	0.11	0.21	4.58	1.99	1.21	0.25	11.01	7.00	7.74	1.02	0.52	1.46	42.79	0.07
	K3	18-879	555.10	B	55.69	0.11	0.21	2.85	1.94	0.18	0.28	-2.76	0.21	1.12	0.32	0.03	15.29	1.08	0.63
S 2		18-880	566.10	B	46.50	0.11	0.19	3.42	2.13	0.24	0.42	-1.45	0.57	1.56	0.70	0.05	12.39	2.27	0.53
	K7	18-889	1082.70	B	29.98	0.11	0.19	3.51	2.01	0.48	1.67	1.19	1.22	2.04	2.16	0.25	17.76	15.72	0.80
	K10	18-892	1313.30	B	54.26	0.11	0.20	3.36	1.98	0.25	0.63	-1.21	0.92	1.56	2.13	0.15	23.18	6.07	0.98
	K6	18-894	1266.70	B	60.19	0.11	0.22	2.66	1.79	0.19	0.34	-2.52	0.56	1.09	1.04	0.08	18.39	4.20	0.61
T 2		18-895	1269.90	B	51.45	0.11	0.18	3.66	2.54	0.47	1.40	1.60	3.15	2.98	4.96	0.21	15.76	8.16	0.72
		18-897	235.10	B	36.75	0.11	0.20	3.54	1.97	0.68	2.04	3.32	4.11	3.55	5.81	0.11	14.14	4.65	0.54
	K4	18-898	255.90	B	57.21	0.11	0.17	3.80	2.73	0.58	0.76	2.23	4.30	3.70	5.35	0.10	12.43	2.16	0.60
		18-899	266.40	B	—	—	—	—	—	—	—	—	—	—	—	—	—	—	—
H 1		18-900	982.20	B	54.87	0.11	0.18	3.56	2.30	0.33	0.96	-0.03	4.06	2.20	6.48	0.17	15.95	4.69	0.75
	K13	18-901	985.80	B	44.50	0.11	0.20	3.54	2.24	0.29	1.58	-0.50	1.30	1.82	2.01	0.26	15.41	14.17	0.69
		18-904	1005.90	B	—	—	—	—	—	—	—	—	—	—	—	—	—	—	—
T ?		18-915	631.30	B	57.27	0.11	0.22	2.91	1.61	0.20	0.28	-2.35	1.25	1.16	4.51	0.15	36.10	8.52	1.33

In this study, $CIA_{corrected} = [Al_2O_3 / (Al_2O_3 + CaO^* + Na_2O) \times (100 - 8.5)]$ for the Cenozoic mudstones, where Na_2O, Al_2O_3, and CaO^* are molar concentrations, and 8.5 represents the molecular percent of K_2O of the unweathered Cenozoic source rocks in the Qaidam Basin (Jian et al., 2013). If the $CaO^* \leq Na_2O$, CaO^* is considered as the CaO of silicate fraction; while if the CaO^* greater than Na_2O, the proportion of Na_2O is considered as the proportion of CaO of silicate fraction (Nesbitt and Young 1982; McLennan 1993). Authigenic U = total U- Th/3 (Jones and Manning, 1994).

116

Table 5.3. Isotopic, elemental* and Rock-Eval data of the kerogen from Pleistocene biogenic gas source rocks in the central Qaidam Basin, China.

Sample ID	Well Interval	Depth (m)	Organic Facies	TOC (wt.%)	TIC (wt.%)	TS (wt.%)	C (%)	H (%)	N (%)	C/N (mass)	H/C (mass)	C/S (mass)	C/N (atom)	H/C (atom)	C/S (atom)	δ13C‰ (rock)	δ15N‰	S1 (mg HC/g rock)	S2 (mg HC/g rock)	Tmax (°C)	HI (mg HC/g rock)
18-853	K4	801.46	A	40.68	0.03	5.24	41.60	4.81	1.68	24.76	0.12	7.94	28.89	1.39	21.17	-28.49	2.58	6.78	116.07	396	285
18-857	K4	820.47	B	/	/	/	/	/	/	/	/	/	/	/	/	-24.10	/	/	/	377	105
18-861	K9 (S 1)	1279.40	A	48.16	0.03	5.06	48.02	5.21	2.22	21.63	0.11	9.49	25.24	1.30	25.31	-28.32	2.23	9.69	149.28	410	310
18-864	K10	1380.50	A	26.72	0.04	9.80	27.21	3.36	1.22	22.30	0.12	2.78	26.02	1.48	7.40	-27.16	4.16	2.45	75.80	422	284
18-867	K11 (T 1)	1697.30	A	22.44	0.07	5.57	23.31	3.13	1.08	21.58	0.13	4.18	25.18	1.61	11.16	-27.90	4.38	1.71	52.47	422	234
18-869	K11	1697.70	A	31.82	0.05	2.17	32.67	3.73	1.48	22.07	0.11	15.06	25.75	1.37	40.15	-27.56	4.23	3.10	87.27	415	274
18-872	K4 (Y 1)	124.69	B	/	/	/	/	/	/	/	/	/	/	/	/	-23.12	/	/	/	372	64
18-878	K2	543.80	A	30.92	0.05	4.79	31.83	3.89	1.10	28.94	0.12	6.65	33.76	1.47	17.72	-27.32	2.82	6.00	68.31	407	221
18-879	K3 (S 2)	555.10	B	/	/	/	/	/	/	/	/	/	/	/	/	-24.65	/	/	/	382	173
18-880	K3	566.10	B	/	/	/	/	/	/	/	/	/	/	/	/	-24.57	/	/	/	377	116
18-895	K6 (T 2)	1269.90	B	/	/	/	/	/	/	/	/	/	/	/	/	-23.34	/	/	/	371	92
18-897	K4	235.10	B	/	/	/	/	/	/	/	/	/	/	/	/	-22.50	/	/	/	372	86
18-904	K13 (H 1)	1005.90	B	/	/	/	/	/	/	/	/	/	/	/	/	-23.62	/	/	/	373	97
18-916	K6 (T 3)	646.11	B	/	/	/	/	/	/	/	/	/	/	/	/	-23.11	/	/	/	/	111

*For facies B, only data which were not affected by precipitation of fluorinated compounds during HF treatment are presented.

117

5.5.2 Rock-Eval pyrolysis

The Rock-Eval results of the kerogen concentrates are listed in Table 5.3 for organic facies A only. For organic facies B, only the TOC normalized HI values as well as T_{max} values are listed due to problems with kerogen concentration (precipitation of fluorinated compounds). HI and T_{max}, however, are not affected. For organic facies A, S_1 and S_2 values range from 1.71 to 9.69 (mean value = 4.95) and from 52.47 to 116.07 (mean value = 91.53 mg HC/g rock), respectively. Average T_{max} values are 412 and 375 °C for facies A and B indicating immature organic matter, while average HI values are at 268 and 106 mg/g TOC, respectively, indicating the presence of type III kerogen.

5.5.3 Distribution pattern of GDGTs
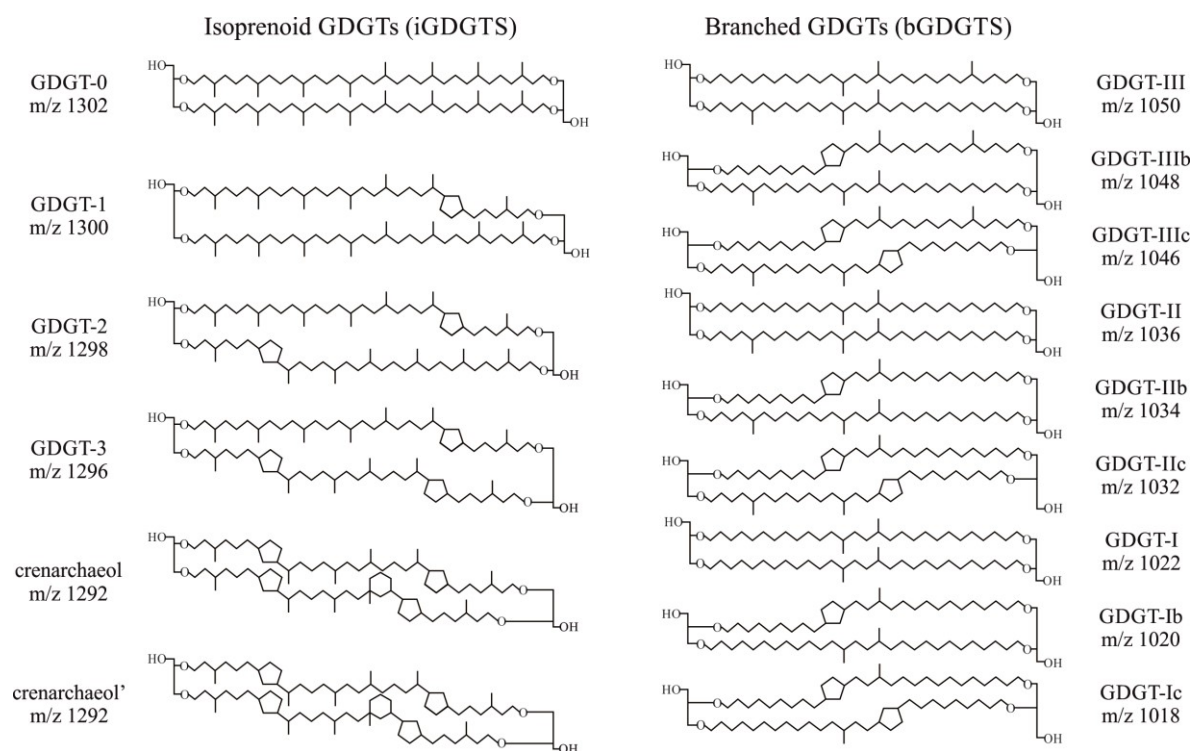
Fig. 5.4. tructures and molecular ion m/z values for glycerol dialkyl glycerol tetraethers (GDGTs) (taken from Li et al., 2016).

GDGTs have been detected in nine out of fourteen samples. Among them, three samples came from the organic facies A group and six samples from the organic facies B group. Unlike other parameters, the distribution patterns of GDGTs are very similar in both organic facies groups. GDGT numbers refer to structures shown in Li et al. (2016) (Fig. 5.4). In this study, both *b*GDGTs and *i*GDGTs can be recognized, and the concentrations of *b*GDGTs are higher than those of *i*GDGTs in most samples with $R_{i/b}$ index values of 0.77-3.35 (Table 5.4). The proportions of each *i/b*GDGT to all *i/b*GDGTs are listed in Table 5.4 ($R_{i/b}$).

Fig. 5.5. The ternary diagram of the bGDGTs type I, II, III (data from De Jonge et al., 2014; Sinninghe Damsté et al., 2016; Crampton-Flood et al., 2021).
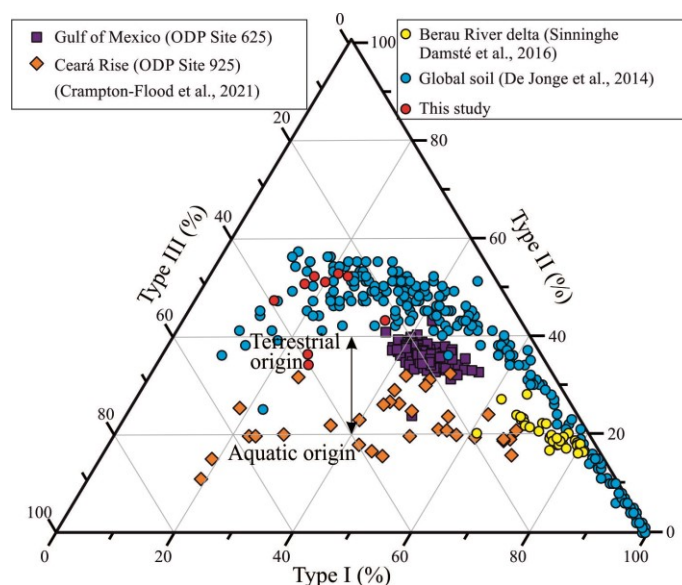
*b*DGDTs are mainly show as GDGT II followed by GDGT I and III (Fig. 5.5 and Fig. 5.6; Table 5.4). In addition, *b*GDGTs without cyclopentane moieties (*b*GDGTI, -II, and -III) were generally more abundant than cyclopentane ring-containing *b*GDGTs (Fig. 5.6). MBT indices are 0.17-0.34, and MBT' values are almost identical to MBT because of the low concentration of GDGTIIIb and -IIIc for all samples (Table 5.5). CBT and BIT values are 0.31-0.76 and 0.72-1.00, respectively (Table 5.5).

Five *i*GDGTs were detected. GDGT-0 is the most abundant *i*GDGT (56.82–85.22 % of *i*GDGTs) (Table 5.4). The concentrations of *i*GDGTs with cyclopentane(s) moieties (*i*GDGT 1–3) decrease from *i*GDGT 1 to *i*GDGT 3 with overall low concentrations (Fig. 5.6). The relative abundance of crenarchaeol shows a complex pattern (Table 5.4). *i*GDGTs 1–3 is generally more abundant than crenarchaeol , but the proportion of *i*GDGT-1 is lower than that of crenarchaeol in samples 18-872, 18-879 and 18-880 (Table 5.4). Furthermore, crenarchaeol concentrations are lower than *i*GDGTs 0–3 in samples 18-853, 18-867, 18-878 and 18-897 (Table 5.4). The related proxy of TEX_{86} ranging from 0.35 to 0.54 (avg. 0.47) shows little variations (Table 5.5).
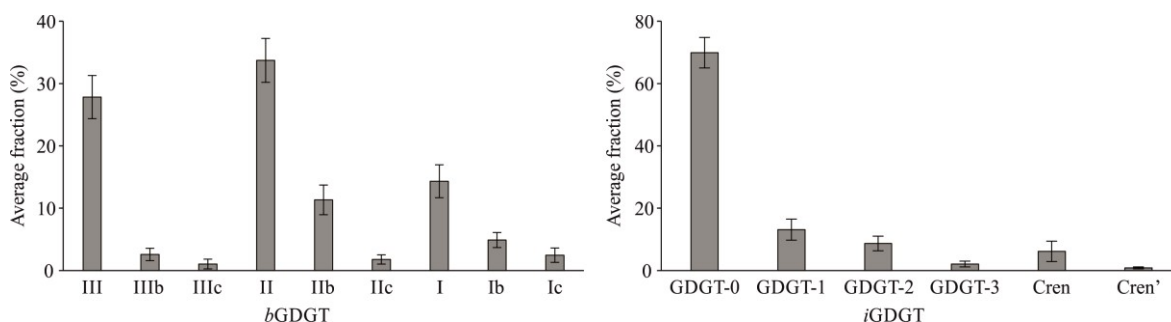

Fig. 5.6. Fractional abundance of GDGT I–III GDGT 0–3, crenarchaeol, crenarchaeol', as fractions of the sum of all pictured GDGTs (bGDGTs as well as iGDGTs).

Table 5.4. Fractional abundance of iGDGTs and bGDGTs

Sample ID	Well	Interval	Depth (m)	Organic Facies	iGDGTs						bGDGTs									
					GDGT-0	GDGT-1	GDGT-2	GDGT-3	Crenarchaeol	Crenarchaeol'	GDGT-III	GDGT-IIIb	GDGT-IIIc	GDGT-II	GDGT-IIb	GDGT-IIc	GDGT-I	GDGT-Ib	GDGT-Ic	$R_{i/b}$
18-853	S 1	K4	801.46	A	78.66	13.88	6.86	0.49	0.08	0.04	29.76	2.48	0.27	35.91	13.88	1.04	9.83	6.47	0.36	0.77
18-857		K4	820.47	B	70.29	10.28	8.17	2.48	8.78	1.61	23.54	0.93	0.00	40.17	11.00	1.17	17.45	4.09	1.64	3.35
18-867	T 1	K11	1697.30	A	57.38	20.01	14.07	6.55	1.98	1.62	28.60	6.87	4.70	23.37	6.34	4.57	18.01	4.37	3.17	1.66
18-872	Y 1	K4	124.69	B	78.49	5.57	3.33	1.25	11.36	0.68	24.25	2.88	1.73	40.92	6.74	3.54	14.84	2.88	2.21	1.04
18-878		K2	543.80	A	56.82	25.42	16.64	1.07	0.06	0.02	22.26	2.92	0.52	38.93	13.61	0.78	11.27	8.53	1.18	1.55
18-879	S 2	K3	555.10	B	68.55	9.36	6.48	2.13	13.48	1.08	37.82	1.16	0.37	34.84	11.31	1.33	6.39	5.06	1.72	1.17
18-880		K3	566.10	B	63.47	10.97	6.99	1.58	16.99	1.54	27.01	2.49	0.64	30.25	20.27	1.83	15.64	0.88	0.99	1.70
18-897	H 1	K4	235.10	B	70.22	14.64	11.38	2.39	1.38	0.75	19.39	2.74	0.57	35.47	6.35	1.51	23.90	7.25	2.82	2.37
18-916	T 3	K6	646.11	B	85.22	7.89	4.44	0.95	1.50	0.54	37.87	0.67	0.67	23.66	12.61	0.16	11.71	4.59	8.05	0.81

Table 5.5. Calculated proxies based on iGDGTs and bGDGTs.

Sample ID	Well	Interval	Depth (m)	Organic Facies	TEX$_{86}$	CBT	MBT	MBT'	BIT	#ringstetra
18-853	S 1	K4	801.46	A	0.35	0.35	0.17	0.17	1.00	0.43
18-857		K4	820.47	B	0.54	0.58	0.23	0.23	0.73	0.32
18-867	T 1	K11	1697.30	A	0.53	0.59	0.26	0.29	0.96	0.42
18-872	Y 1	K4	124.69	B	0.49	0.76	0.20	0.21	0.87	0.37
18-878		K2	543.80	A	0.41	0.36	0.21	0.22	1.00	0.52
18-879	S 2	K3	555.10	B	0.51	0.40	0.13	0.13	0.83	0.65
18-880		K3	566.10	B	0.48	0.34	0.18	0.18	0.72	0.16
18-897	H 1	K4	235.10	B	0.50	0.64	0.34	0.35	0.96	0.38
18-916	T 3	K6	646.11	B	0.43	0.31	0.24	0.25	0.98	0.85

120

5.5.4 Carbon and nitrogen isotope

Carbon isotope data in the kerogen concentrates clearly differ in the samples of the two organic facies. $\delta^{13}C$ values vary from –27.16 to –28.49 ‰ VPDB (avg. –27.79 ‰ VPDB) and $\delta^{15}N$ values from 2.23 to 4.38 ‰ air (avg. 3.40 ‰ air) in organic facies A samples. For organic facies B samples, $\delta^{13}C$ values vary from –22.50 to –24.65 ‰ VPDB (avg. –23.63 ‰ VPDB) while $\delta^{15}N$ values could not be measured accurately due to the low N concentrations and are thus not reported here (Table 5.3).

5.6 Discussion

5.6.1 Origin of organic matter
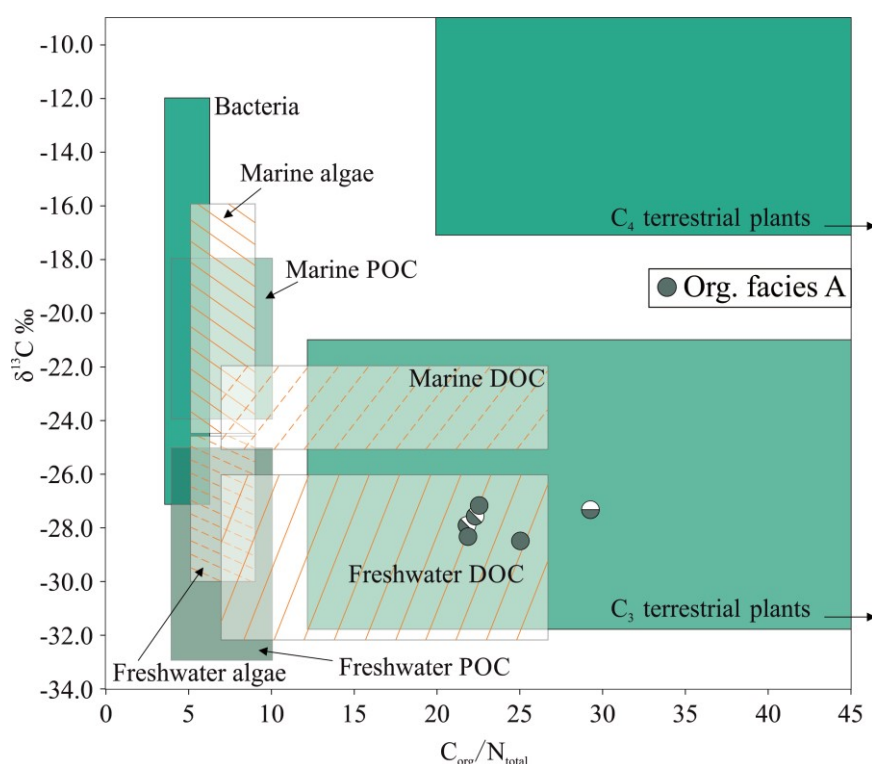
Fig. 5.7. Typical $\delta^{13}C$ and C/N ranges for organic inputs (after Lamb et al., 2006). Note: sample symbols represent sample locations (Fig. 5.1b).

$\delta^{13}C_{org}$ can be used to distinguish continental and marine plant sources of OM and even to identify types of land plants as well (Meyers, 1997). Lamb et al. (2006) proposed that $\delta^{13}C$ and C/N ratios in organic material are useful indicators to deduce depositional environments and OM origin. Fig. 5.7 indicates that the OM of organic facies A is mainly derived from a mixture of C_3 higher plants and freshwater dissolved organic carbon (DOC) which indicates a mixture of higher plants and phytoplankton in lacustrine environments (Rashid, 1985; Lamb et al., 2006). In addition, the $\delta^{15}N_{org}$ value is an indicator distinguishing land-plant and algal sources of OM, because $\delta^{15}N_{org}$ values of plankton ($\delta^{15}N_{org}$ of +8.6‰) are higher than those of C_3 plants ($\delta^{15}N_{org}$ of +0.4‰) (Peterson and Howarth,

1987). $\delta^{15}N$ values between 2 and 4‰ in organic facies A samples thus also indicate a mixture of C_3 plants and phytoplankton. These findings are basically in agreement with petrographic and biomarker data as well as Rock-Eval data (Qiao et al., 2021a), indicating the OM in organic facies A samples mainly derives from macrophytes growing at the lake margin, such as submerged angiosperms, freshwater mosses, non-marine algae, and lichens. This conclusion is also consistent with the C_3 plant distribution during the late Pliocene and the current dominance of C_3 vegetation in the TP (Wang et al., 2008). It should be noticed that the OM is in reality derived from multiple sources; thus the average $\delta^{13}C_{org}$ value of each sample indicates the major origin of OM and cannot exclude other minor sources, such as bacteria.

5.6.2 Depositional conditions within the water column
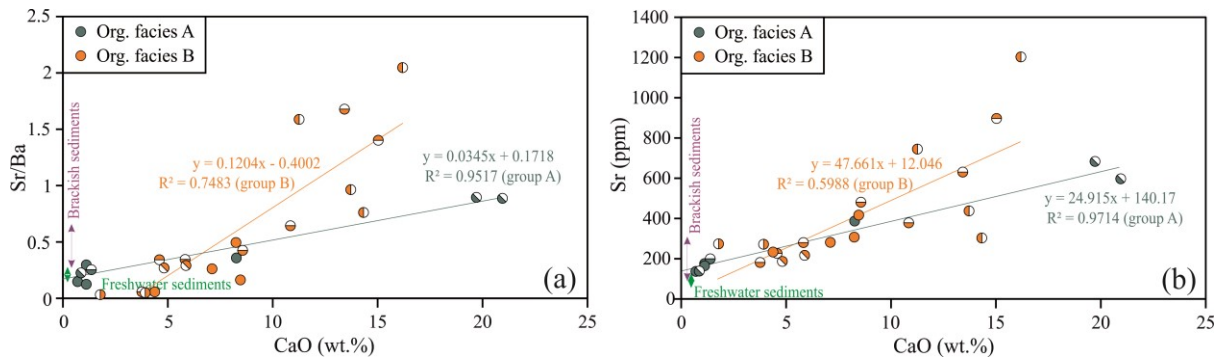
Fig. 5.8. (a) Sr/Ba and (b) Sr vs. CaO indicating paleo-salinity of the Pleistocene source rocks from the Qaidam Basin, China. Note: sample symbols represent sample locations (Fig. 5.1b).

Salinity plays an important role in aquatic organism community composition in lake systems (Romero-Viana et al., 2012). Organic facies A was deposited in a shallow freshwater environment, probably without stratification, which is supported by the moderate H/C ratios in combination with high C/S ratios for organic facies A kerogen (Table 5.3) and the relatively low $\delta^{13}C$ values (Lamb et al., 2006). By contrast, organic facies B developed in a hypersaline depositional environment; a first indicator are the rather high $\delta^{13}C$ values (Lamb et al., 2006). Moreover, different paleo-salinities during deposition of the two organic facies are also indicated by Sr/Ba ratios. Wei and Algeo (2020) considered that it is necessary to exclude carbonate-hosted Sr when using Sr/Ba ratios as a paleo-salinity proxy. In this study, around 140 ppm are bound to silicates rather than carbonate based on the y-intercept in Fig. 5.8b. For organic facies A samples this finding indicates freshwater conditions (silicate-bound Sr/Ba ratios are 0.11-0.24) (Fig. 5.8a; Wei and Algeo, 2020). However, almost all Sr is carbonate-hosted in organic facies B samples (Fig. 5.8b), and thus cannot be used as an indicator of paleo-salinity. The above conclusion supports the results based on the TOC/TS ratios and biomarker characters in a previous study (Qiao et al., 2021a).
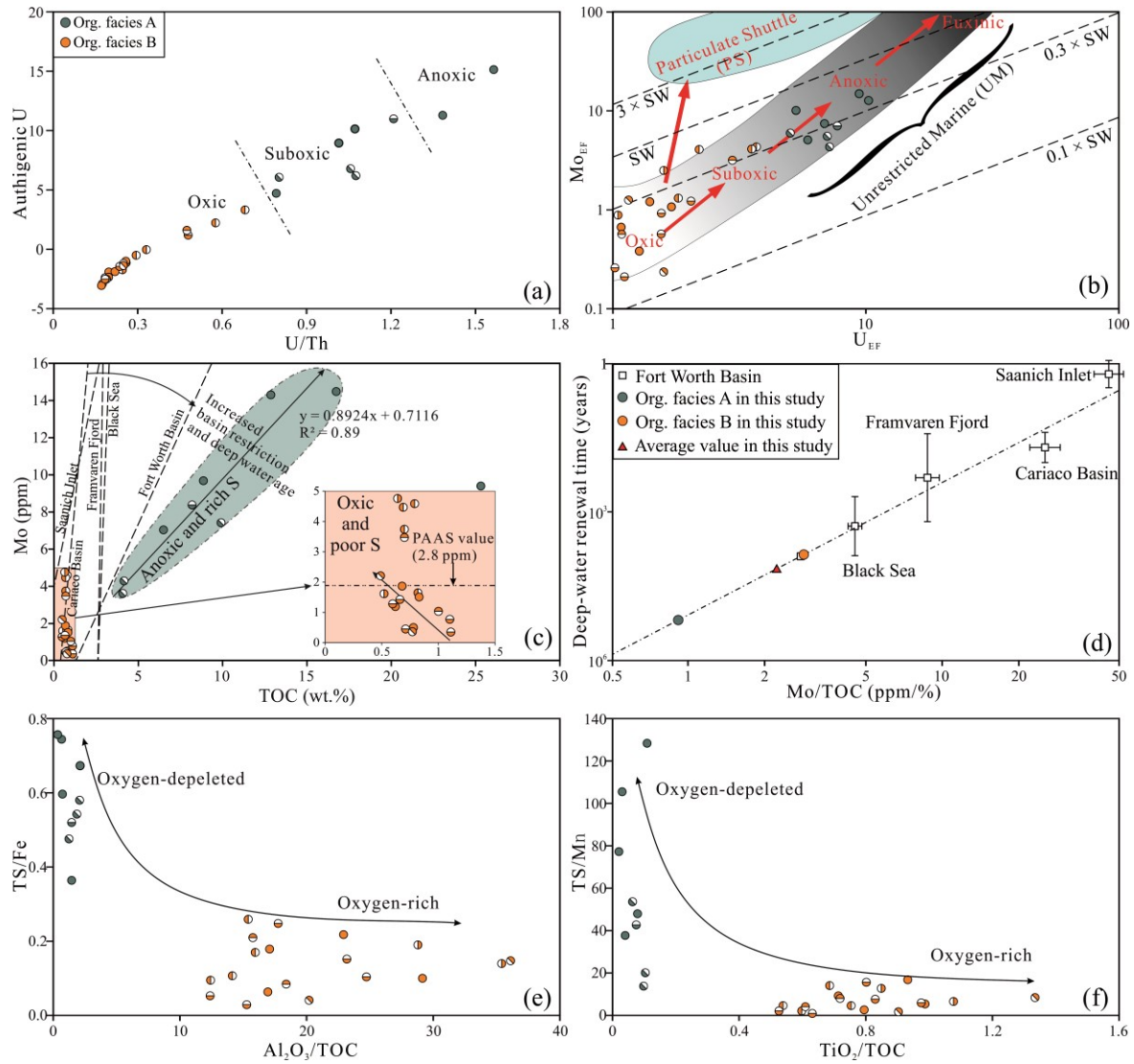
Fig. 5.9. (a) U/Th ratio vs. authigenic U to interpret paleo-redox conditions. (b) U_{EF} vs. Mo_{EF} (General patterns of U_{EF} vs. Mo_{EF} covariation is modified after Tribovillard et al. (2012)). (c) Comparison of TOC–Mo relationship between results of this study, Barnett Formation in the Fort Worth Basin and those of modern anoxic silled-basin environments (The TOC–Mo regression line slopes and previous studies data are given in Rowe et al. (2008). Note: the TOC contents used in Rowe et al. (2008) are original TOC_o ($TOC_o = TOC_{meas}/(1-0.363)$, so the slope for the Fort Worth Basin should be a little bit steeper). (d) Estimation of deep-water renewal time (years) during Pleistocene source rocks deposition using estimates from modern anoxic silled basins and the Barnett Formation in the Fort Worth Basin. Note: sample symbols represent sample locations (Fig. 5.1b). (e)TS/Fe vs. Al_2O_3/TOC and (f) TS/Mn vs. TiO_2/TOC to interpret paleo-redox conditions (modified after Cichon-Pupienis, et al., 2020). Note: sample symbols represent sample locations (Fig. 5.1b).

Besides paleo-salinity, paleo-redox conditions can also affect productivity and preservation of OM. The plot of U/Th ratios vs. authigenic U values (authigenic U = total U–Th/3; Jones and Manning, 1994; Fig. 5.9a) indicates dysoxic to slightly anoxic bottom water conditions for organic facies A samples and oxic conditions for organic facies B samples (Fig. 5.9a), i.e. there is a major difference between organic facies A and B, separating them clearly. The same results are inferred from Mo_{EF} vs. U_{EF} co-variation (Fig. 5.9b; see results for calculation of enrichment factors). Both U and Mo are enriched under oxygen-

depleted and even more under anoxic conditions. However, enrichment of Mo relative to U is enhanced under sulfidic conditions, i.e. when bottom water contains hydrogen sulfide (Algeo and Tribovillard, 2009; Tribovillard et al., 2012). The grey zone (Fig. 5.9b) indicates the "unrestricted marine" (UM) trend where the Mo_{EF} vs. U_{EF} co-variation is controlled by redox conditions at the sediment/water interface. Facies B samples plot clearly in the oxic zone, where little or no enrichment of Mo and U takes place, while facies A samples follow the trend of suboxic to anoxic conditions showing modest enrichment factors for both elements (Fig. 5.9b). It is interesting to note that the principles developed for marine settings can also be applied for the lacustrine setting of the Pleistocene in the Qaidam Basin. Differences, however, exist as well, e.g. Mo/TOC and U/TOC ratios are much lower in the Qaidam Basin sediments, which is certainly related to lake water chemistry (lower U and Mo concentrations compared to sea water) and high bioproductivity.

Anoxic environments are also indicated by the clear positive relationship between Mo and TOC contents in most organic facies A samples (Fig. 5.9c), because the presence of H_2S can prompt Mo to be easily sorbed by OM (Helz et al., 1996; Zheng et al., 2000; Tribovillard et al., 2012). It should be noted that the Mo/TOC ratios in both organic facies A and B samples are even lower than those in recent Black Sea sediments (Fig. 5.9c and d) indicating strongly restriction conditions. However, this conclusion is not necessarily valid here due to the different Mo concentrations in the non-marine setting and also by the high sedimentation rate in the basin (0.65 to 0.8 km/Ma on average; Dang et al., 2008; Shuai et al., 2013; Zhang et al., 2013a). Low Mo/TOC ratios giving misleading information related to basinal restriction are also reported for Telychian sediments recently (Cichon-Pupienis et al., 2021). This anomaly may be due to three reasons. First, the high sedimentation rate may lead to faster removal of sediments from the contact of the overlying water column (Liu and Algeo; 2020) during periodic/occasional fresh-water influxes carrying large amounts of terrigenous debris, i.e., relatively well ventilated bottom waters was not favorable for trace metal uptake in sediments. Second, terrestrial debris supply was limited during periods of high water evaporation, thus limiting the amount of e.g. Mo and U that was transported towards the sediment/water interface, therefore, leading to a relative depletion of such elements per unit volume of OM. Third, the study area did not develop a persistent and extensive H_2S rich bottom water. Conversely, the positive relationship between Mo and TOC contents is not observed in organic facies B (Fig. 5.9c), indicating an oxic depositional environment. Ghassal et al. (2018) proposed using the TS/Fe vs. Al_2O_3/TOC ratios and TS/Mn vs. TiO_2/TOC ratios as proxies to indicate terrigenous input and redox conditions. Later, Cichon-Pupienis et al. (2020) used these proxies to interpret redox conditions at the sediment-sea water interface. For our Pleistocene samples, the TS/Fe vs. Al_2O_3/TOC (Fig. 5.9e) and TS/Mn vs. TiO_2/TOC (Fig. 5.9f) diagrams indicate oxygen-depleted conditions for organic facies A samples and oxygen-rich bottom water conditions for organic facies B samples (i.e., higher Al_2O_3/TOC and TiO_2/TOC ratios), which is in accordance with the other parameters discussed above. Moreover, a reducing sediment/water interface is also indicated for organic facies A by high C_{org}/P ratios (108.11-1375.11) and an oxidizing environment for organic

facies B by low C_{org}/P ratios (31.53-82.95) (Table 5.2), respectively (Algeo and Ingall, 2007; Algeo and Li, 2020). The above results are consistent with the relative concentrations of TOC, TS and iron (Qiao et al., 2021a).

5.6.3 Factors controlling OM preservation and accumulation

Paleo-redox conditions and paleo-productivity are the most important factors controlling OM preservation in source rocks (Pedersen and Calvert, 1990). In addition, lateral variability in thickness and facies of source rocks depend on interacting complex physical and chemical processes not only related to OM quantity and quality. The very high sediment accumulation rates characterizing the Pleistocene section in the Qaidam Basin have been discussed in Qiao (2021a). Here we report additional evidence based on calculated source potential index. The hydrocarbon generation potential of a given formation is determined by the thickness of the source rock and its kerogen maturity, quantity as well as quality. Based on Demaison and Huizinga (1991) a source potential index (SPI; t HC/m^2) can be calculated as

$$\text{SPI} = \frac{h \times \overline{(S_1 + S_2)} \times \rho}{1000} \quad (5.30)$$

In which h (m) and ρ (t/m^3) are thickness and density of source rock, respectively. $\overline{(S_1 + S_2)}$ (kg HC/t rock) are average values of Rock-Eval parameters (data published in Qiao et al., 2021a).

Table 5.6 shows the calculated SPI values for the different wells under the assumption of an average density of different organic facies (the mean density is 2.10 g/cm^3 for organic facies A samples and 2.22 g/cm^3 for organic facies B samples; Qiao et al., 2021a). Except for the T2 Well which is close to Sebei 1 Gas Field (SPI value = 1.49 t HC/m^2), the wells located above the gas fields show moderate to high SPI values ranging from 2.24 to 25.66 t HC/m^2 (Table 5.6). It should be noted that there is a rather high uncertainty with respect to the absolute values, because there the sample number is small compared to the thickness of the formation. Sampling of source rocks is often biased towards organic matter-rich layers; therefore the average $S_1 + S_2$ value might be overestimated by more than 10 % of the value. Nevertheless, the data indicate that the studied, thick Pleistocene sequence has overall a very high source potential index. Although the periodic oxic conditions in bottom water were not in favor of OM preservation, the overall high sedimentation rates exceeding those of most marine settings by far (Qiao et al., 2021a) were the key factor for developing a very good source rock sequence (Hunt, 1996; Demaison and Moore, 1980).

The relative importance of paleo-redox conditions and paleo-productivity as control factors on OM preservation can be evaluated via the relationship between TOC content and $\delta^{13}C_{org}$ value (Harris et al., 2004). If bioproductivity is the controlling factor, $\delta^{13}C_{org}$ values should be positively correlated to TOC content (Hollander and McKenzie, 1991); where OM preservation is controlled by paleo-redox conditions, the relationship generally shows a negative correlation (Freeman et al., 1990, 1994; Wachniew and Różański, 1997). Fig. 5.10 indicates that the OM preservation in both organic facies A and B was primarily controlled by the paleo-redox conditions, i.e., the dysoxic to slightly anoxic bottom

water conditions for organic facies A samples and oxic conditions for organic facies B samples might be the most important factor controlling their low and high TOC content, respectively.
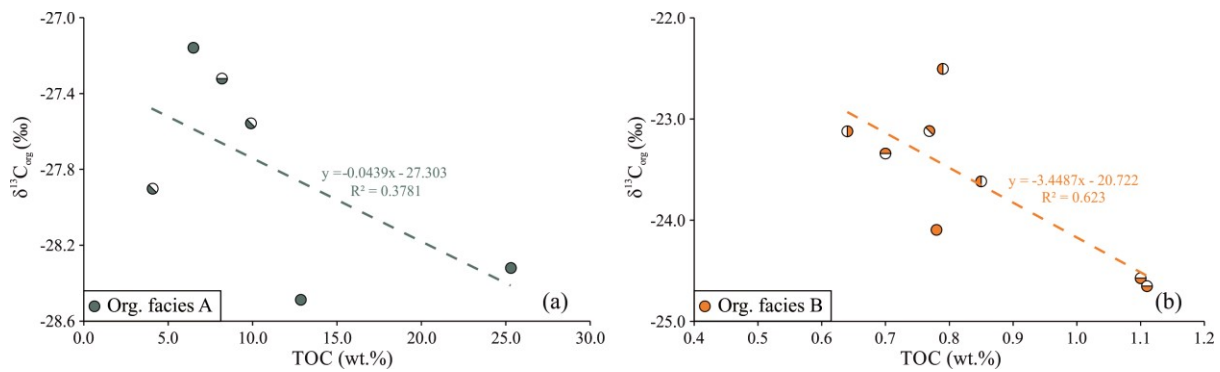
Fig. 5.10. Cross plot of the carbon isotopic composition of kerogen ($\delta^{13}C_{org}$) vs. total organic carbon content (TOC). $\delta^{13}C_{org}$ shows a significant negative correlation with TOC in both facies A and B samples, indicating organic carbon deposition was controlled by redox conditions. Note: sample symbols represent sample locations (Fig. 5.1b).

Table 5.6. SPI calculated based on our studied wells.

Gas field	Well	Calculated accumulation thickness	$\overline{(S_1 + S_2)}$ (kg HC/t rock)	ρ (t/m³)	SPI (t HC/m²)
Seibei 1	S 1	1215	10.7	2.19	25.66
	T 2	1215	0.69	2.22	1.49
Tainan	T 1	1170	7.45	2.19	15.3
Yanhu	Y 1	1080	2.25	2.22	4.32
Seibei 2	S 2	1197	4.75	2.19	9.98
Tuofengshan	T 3	1080	1.17	2.22	2.24

5.6.4 Paleoclimate

5.6.4.1 Evidence from major and trace elements

The Asian inland began drying in the Miocene, or even late Oligocene (An et al., 2001), intensified at the early Pleistocene, which may be related to the global cooling and the TP uplift (Fang et al., 2007; Wu et al., 2011). The Chemical Index of Alteration (CIA, Nesbitt and Young, 1982) is a measure of the relative contribution of feldspars and their chemical alteration products (clay minerals) in a rock and, thus, serves as an indicator for the degree of weathering (e.g. Fedo et al., 1995; Roy and Roser, 2013). It can be applied for both, igneous as well as sedimentary rocks, whereby it rather represents the general weathering conditions of a larger provenance region for the latter ones. Fig. 5.11a shows a triangular plot of the relative composition of different oxides with Al_2O_3 representing their stable parts and K_2O and $CaO^* + Na_2O$ their labile parts. CaO^* represents only the fraction originating from silicates and not carbonates or apatite. It is calculated according to Fedo et al. (1995):

$$CaO^* = CaO - CO_{2 \text{ (calcite)}} - 0.5 \times CO_{2 \text{ (dolomite)}} - 10/3 \times P_2O_{5 \text{ (apatite)}} \quad (5.31)$$

Here, the ratio of dolomite/calcite is considered 0.8 (average ratio of the Qigequan Formation in the study area based on XRD data; Zhang et al., 2014) and CO_2 yields are obtained from TIC measurements.
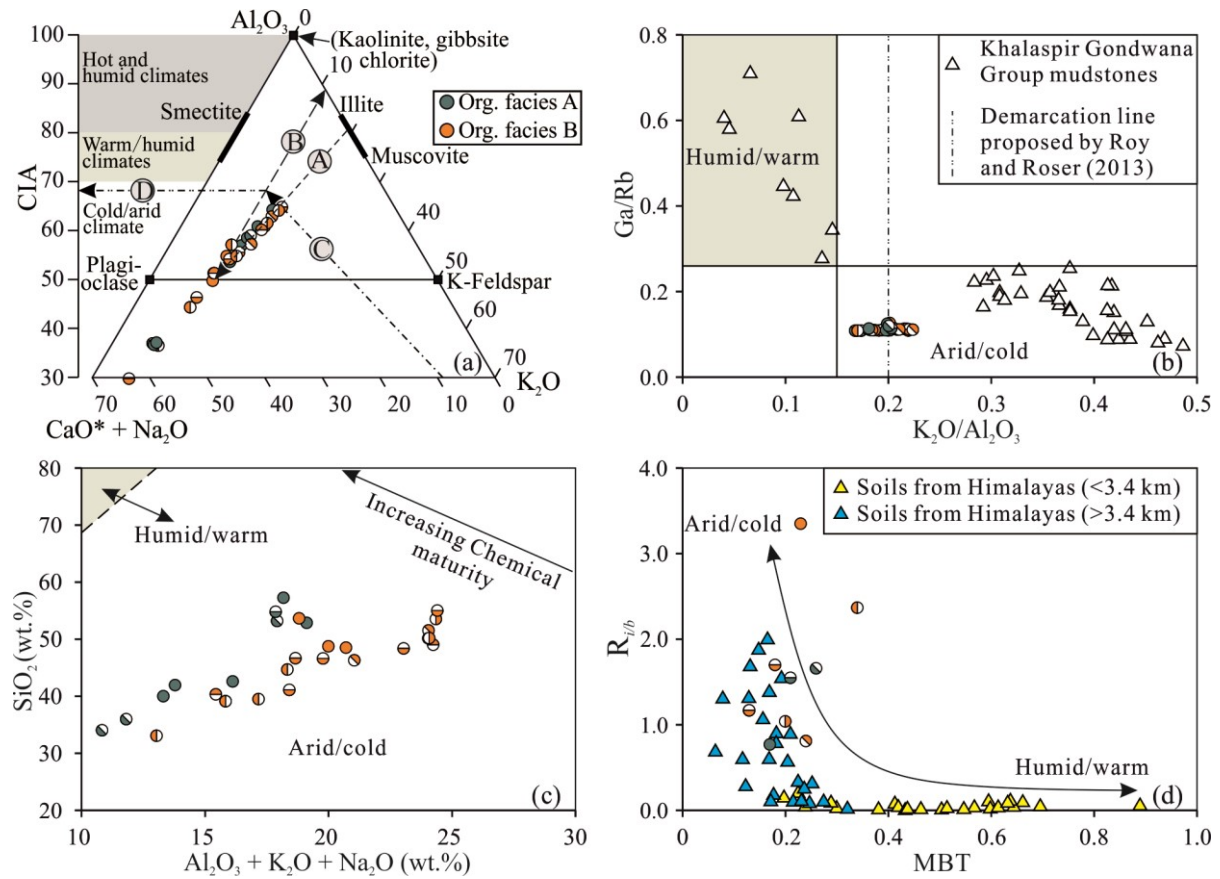
Fig. 5.11. (a) A–CN–K ternary diagrams for mudstones correction for K metasomatism is made by projecting data points back onto ideal weathering pathway from K-apex (Fedo et al., 1995). (b) Discrimination diagrams of SiO_2 vs. $(Al_2O_3 + K_2O + Na_2O)$ after Suttner and Dutta (1986) and (c) Ga/Rb vs. K_2O/Al_2O_3 (Roy and Roser, 2013) for the Pleistocene source rocks from the Qaidam Basin. (d) The distribution of soil sample GDGTs at low altitudes (<3,400 m asl) in the central Himalayas is characterized by high MBT and low $R_{i/b}$ values, opposite to the pattern observed for high altitudes (after Chen, et al.,2020). The characteristics of the MBT and high $R_{i/b}$ values for the studied samples are similar to those for higher altitudes. Note: samples symbols represent sample locations (Fig. 5.1b).

The dashed line (arrow A in Fig. 5.11a) presents the regression through the studied samples, and its intersection with feldspar (Pl-Kfs) represents the unweathered rock. The solid-line (arrow B in Fig. 5.11a) represents the predicted weathering trend. CIA values are further corrected for the possible effects of diagenesis and K-metasomatism, which may cause some degree of K-enrichment in contrast to its general depletion (e.g. Nesbitt and Young, 1984; Fedo et al., 1995). This correction is performed by projecting each data point onto the Upper Archaean trend along a vector originating in the K_2O corner (arrow C in Fig. 5.11a), yielding the corrected, pre-metasomatized CIA values (arrow D in Fig. 5.11a). A detailed description of the correction procedure is given by Fedo et al. (1995). The here

analyzed samples show CIA$_{corrected}$ values of 30-65 (53 on average; Table 5.2) indicating arid/cold conditions with weak chemical weathering during the Pleistocene (Fig. 5.11a). Compared to the mean CIA values of Paleocene + Eocene (CIA 71), Oligocene (72), and Miocene (67) mudstones released by Jian et al. (2013), these new CIA values indicate a continuous cooling and aridification process.

The interpreted arid/cold conditions are further supported by Ga/Rb and K_2O/Al_2O_3 ratios (Roy and Roser, 2013): Both low Ga/Rb ratio < 0.15 and high K_2O/Al_2O_3 ratios > 0.17-0.22 suggest abundant illite and dry/cold climatic conditions (Roy and Roser, 2013). Meanwhile, the K_2O/Al_2O_3 ratios in this study are higher than 0.17; we thus propose that values higher than 0.15 to 0.17 mark arid/cold conditions, rather than 0.2 defined for the Khalaspir Gondwana Group mudstones by Roy and Roser (2013) (Fig. 5.11b). The same result is affirmed by the binary diagram between SiO_2 and $Al_2O_3 + K_2O + Na_2O$ (Fig. 5.11c). Interestingly, there is no significant difference between organic facies A and B samples with respect to these paleoclimate proxies. Our conclusions on an arid and cold climate are in line with previous publications based on evaporite minerals (Luo et al., 2018), sporopollen (Wu et al., 2011), carbonate contents and salt ion records (Zhang et al., 2013b), as well as stable hydrogen isotopic composition of leaf-wax n-alkanes (Zhuang et al., 2011) on rocks of the same age in the basin.

5.6.4.2 Evidence from GDGTs
5.6.4.2.1 GDGTs as indicator of palaeo-temperature

The current climate of the Qaidam Basin is extremely arid with the MAAT (mean annual air temperature) ranging from -2.5 to 5 °C (Herb et al., 2013; Günther et al., 2014). Considering the continuing cooling of the paleo-climate in the Qaidam Basin since the Pleistocene (Fig. 5.12; Cai et al., 2012), the Pleistocene MAAT value should be warmer than -2.5-5 °C. Such a tendency is visible for the calculated MAATs (Fig. 5.13), but there is quite some range in the Pleistocene values, depending on the adopted equation.
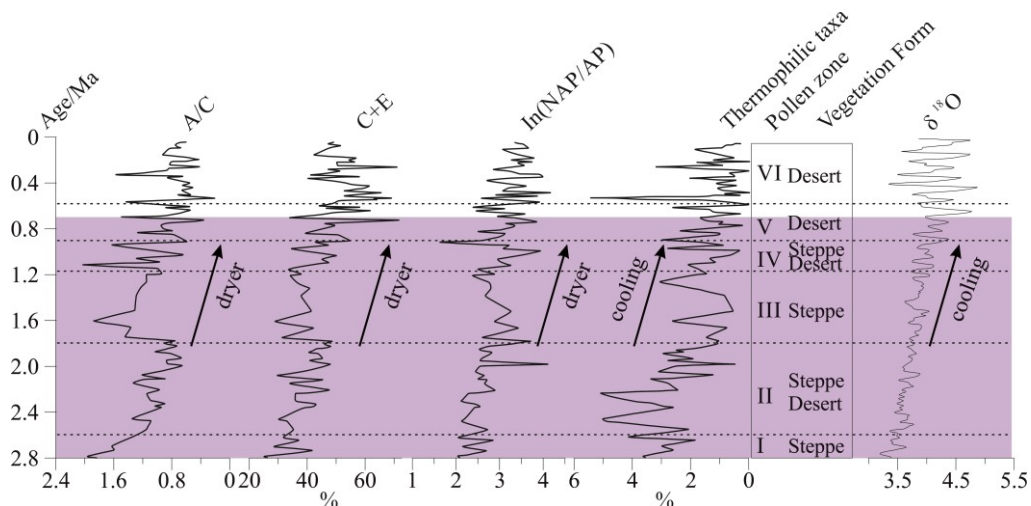
Fig. 5.12. Sporopollen variations and implications for climatic conditions in the Quaidam Basin from Cai et al. (2012) with isotope data from (Lisiecki and Raymo, 2005 as shown in Cai et al., 2012). A/C: Artemisia/Chenopodiaceae; C+E: Xerophytic taxa (Chenopodiaceae+Ephedraceae) (%); ln(NAP/AP): ln ratios of Non Arboreal Pollen (NAP) to Arboreal Pollen; Thermophilic taxa: Betula+Quercus+Castanea+Juglans (%).

Table 5.7 Related calculated results based on iGDGTs and bGDGTs.

Sample ID	Well	Interval	Depth (m)	Organic facies	MAAT (based on soil)					MAAT (based on lake)					LST						pH				
					MAAT Weijers 2007	MAAT Peterse 2012	MAAT Günther 2014	MAAT De Jonge 2014	MAAT De Jonge 2014'	MAAT Loomis 2012	MAAT Sun 2011	MAAT Pearson 2011	MAAT Tierney 2010	MAAT Tierney 2010'	LST Powers 2010	LST Castaneda 2011	LST Tierney 2010	LST Kim 2008	WLST	SLST	pH Tierney 2010	pH De Jonge 2014	pH Günther 2014	pH Weijers 2007	pH Sun 2011
18-853	S 1	K4	801.46	A	-1.01	4.21	0.64	0.38	-2.76	9.41	8.40	16.84	13.98	13.69	7.24	5.70	10.00	8.74	2.40	10.58	9.25	7.21	8.77	7.84	8.37
18-857		K4	820.47	B	0.06	4.88	3.27	0.29	-0.79	8.32	9.60	15.27	13.96	14.32	17.24	16.51	17.65	19.80	13.68	19.76	8.56	6.75	9.41	7.23	7.98
18-867	T 1	K11	1697.30	A	1.20	6.58	3.65	5.79	0.94	-5.18	10.47	16.52	14.68	15.67	16.34	15.54	16.96	18.81	12.67	18.93	8.54	6.74	9.42	7.22	7.97
18-872	Y 1	K4	124.69	B	-3.28	3.07	4.91	-0.49	-1.58	-2.97	7.34	13.85	11.22	14.47	14.29	13.32	15.39	16.53	10.35	17.05	8.01	6.40	9.91	6.76	7.67
18-878		K2	543.80	A	1.12	5.64	0.94	0.58	-1.31	14.41	10.03	20.04	15.36	17.81	10.47	9.19	12.47	12.31	6.04	13.54	9.24	7.20	8.78	7.83	8.37
18-879	S 2	K3	555.10	B	-3.22	2.75	0.90	0.20	-3.94	4.40	6.79	13.93	12.39	9.24	15.45	14.57	16.28	17.81	11.65	18.11	9.10	7.11	8.91	7.71	8.29
18-880		K3	566.10	B	-0.44	4.60	0.54	1.76	-2.47	2.90	8.80	12.59	14.40	15.51	13.95	12.95	15.13	16.16	9.97	16.74	9.30	7.24	8.73	7.88	8.40
18-897	H 1	K4	235.10	B	4.90	8.25	4.54	3.96	2.90	11.64	13.39	19.78	16.93	16.64	14.90	13.97	15.86	17.21	11.04	17.61	8.38	6.64	9.57	7.08	7.88
18-916	T 3	K6	646.11	B	3.21	6.81	0.70	6.37	-0.38	10.30	11.55	14.80	16.85	10.89	11.41	10.20	13.19	13.35	7.10	14.41	9.37	7.28	8.66	7.94	8.44

*b*GDGTs can be produced by organisms in peats, soils, water columns and lake sediments. As a result, it is important to investigate the sources of *b*GDGTs before attempting to reconstruct the paleo-climate. Temperature reconstruction functions based on the *b*GDGTs generated from soils are shown in Fig. 5.13 and Table 5.7. $MAAT_{Weijers2007}$ and $MAAT_{De\ Jonge2014}$ values show the coolest conditions, while $MAAT_{Peterse2012}$ values show warmer conditions (Fig. 5.13). Günther et al. (2014) found that most soil calibrations are invalid in the Tibetan Plateau because the Tibetan Plateau was not included in these soil calibrations, although Günther et al. (2014) found that $MAAT_{Peterse2012}$ values were close to observed MAAT for the plateau. The equation proposed by Günther et al. (2014) was used to predict Tibetan MAAT for the studied samples, showing the Pleistocene MAAT were slightly higher than the present temperature. The prediction was similar with $MAAT_{De\ Jonge2014'}$ values (Fig. 5.13 and Table 5.7), indicating the temperature is cooling from Pleistocene to present.

Temperature reconstruction functions based on the GDGTs generated from organisms within water are different from those derived from organisms within soils. Thus, the origin of GDGTs can affect the reliability of reconstruction of temperature (De Jonge et al., 2014; Sinninghe Damsté, 2016). Generally, the MAAT is based on lake calibrations (Tierney et al., 2010b; Pearson et al., 2011; Sun et al., 2011; Loomis et al; 2012) were substantially higher MAAT values than observed in present days. The calibration of *b*GDGTs based on lake sediments (i.e. aquatic origin GDGTs) including $MAAT_{Tierney2010}$, $MAAT_{Tierney2010'}$, $MAAT_{Sun2011}$, $MAAT_{Pearson2011}$, $MAAT_{Loomis2012}$, $MAAT_{Loomis2012}$ values were clearly higher than soil-based calibrations with large variation. By comparison of India's west Berau delta sediments with global soil I/II/III *b*GDGTs type triangle distribution, Sinninghe Damsté (2016) found that *b*GDGTs of aquatic origin or mixed with aquatic origin were located below the soil samples in the triangular map (Fig. 5.5). As shown in Fig. 5.5, most of the studied samples show a pattern similar to the distribution of *b*GDGTs in modern global soil (De Jonge et al., 2014). The *b*GDGT-II abundances are higher than those of mixed terrestrial/aquatic origin in the Ceará Rise (ODP Site 925) and aquatic origin in the Gulf of Mexico (ODP Site 625) (Crampton-Flood et al., 2021), indicating that the GDGTs are mainly derived from terrestrial soil input. The same conclusion can be drawn from the lower abundances of *b*GDGT-IIIa and higher abundances of *b*GDGT-II (Fig. 5.6; Günther et al., 2014). The #rings$_{tetra}$ index was used to evaluate the relative contribution of cyclic *b*GDGTs (Sinninghe Damsté, 2016). In general, #ring$_{stetra}$ is increasing with the increase of distance from the coast (Sinninghe Damsté, 2016). If the mean value of #ring$_{stetra}$ is greater than 0.7, *b*GDGTs cannot be completely originating from soil (Sinninghe Damsté, 2016). #ring$_{stetra}$ values from the studied samples are 0.16-0.85 (avg. 0.45; Table 5.5), indicating that *b*GDGTs in the studied sediments mainly derive from soil. In addition, the high BIT values ranging from 0.72 to 1.00 (avg. 0.89; Table 5.5) indicate the shallow water depth in the study area as well (Sinninghe Damsté, 2016). The phenomenon that most of the *b*GDGTs are catchment soil-derived in some Tibetan lake systems has been observed before (Günther et al., 2014). Combining with the above discussion, *b*GDGT in Tibetan lakes originated mainly from surrounding soils, although the studied samples were sampled from lake sediments. Thus

the MAAT values based on calibration of soil-derived GDGTs are probably more reliable than those based on calibration by lake sediments. According to spore and pollen data as well as oxygen isotopes, there is a cooling trend from 2.8 Ma to present-day (Fig.12) with quite some variability in each time interval. The MAAT fluctuation within the Pleistocene interval is also significant based on our data, e.g. the well calibrated $MAAT_{Günther\ 2014}$ ranging from 0.54 ˚C to 4.91 ˚C with an average of 2.23 ˚C. This is slightly higher than at present-day, but the Pleistocene variability (4.5 °C between coolest and warmest temperature) is greater than the cooling since then.
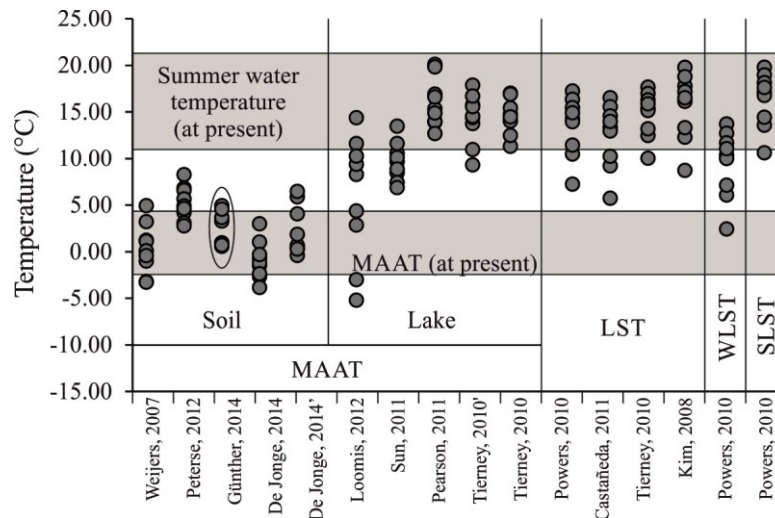
Fig. 5.13. Comparison of reconstructed temperatures based on soil calibrations in soils and lake sediments as obtained from Eqs. 5.6 to 5.21.

The TEX_{86} proxy was used to reconstruct LST (lake surface temperature). A lacustrine (compiled by Castañeda and Schouten, 2011) and a marine calibration (Kim et al., 2008) were used to evaluate the obtained data. Moreover, seasonal influence was estimated by using a study of Powers et al. (2010). The reconstructed $LST_{Kim2008}$, $LST_{Castañeda2011}$ and SLST were in agreement with the current measured summer surface water temperature (SLST; Fig. 5.13 and Table 5.7); thus the temperature during the Pleistocene was probably warmer than at present-day. Only the WLST significantly differed from the measured mean water temperature, which is expected, because it reflects the cooler winter temperature (Fig. 5.13 and Table 5.7). Generally, LST has a high correlation with MAAT. However, such a close relationship between both parameters cannot be detected in recent Tibetan lakes due to glacial meltwater input substantially reducing LST, or circulation of warm or cold water volumes within the lakes (Günther et al., 2014). The TEX_{86} is affected by a variety of factors (e.g. Schouten et al., 2013); for example TEX_{86} is not suitable to calculate temperatures for lacustrine environments, if the lakes were strongly influenced by methanogenesis (Blaga et al., 2009), or if the sediments contain a large number of soil-derived *i*GDGTs (Blaga et al., 2009; Powers et al., 2010). All major groups of archaea except halophilic archaea can generate *i*GDGT-0 (Schouten et al., 2013 and references therein). In most cases, they are regarded as terrestrially sourced biomarkers, even if in situ production of *i*GDGT-0 cannot be

excluded as suggested in previous studies (e.g. Blaga et al., 2009; Bechtel et al., 2010). By contrast, crenarchaeol and iGDGTs 1–3 are produced in situ in lake environments (Günther et al., 2014) and are thus used for the TEX_{86} calculation. In this study, the TEX_{86} reveals LST ranging from 5.7 to 19.6 ˚C (WLST were 2.4-13.7 ˚C) (Fig. 5.13 and Table 5.7). Interestingly, MAATs calculated based on lake calibrations (Powers et al., 2010; Tierney et al., 2010a; Castaneda and Schouten, 2011) show strong agreement with the SLT.

5.6.4.2.2 GDGTs as indicator of palaeo-pH and moist/arid conditions

According to Günther et al. (2014) pH and salinity were probably the most influential environmental factors for the relative distribution of bGDGTs in the lake sediments, while archaeal lipid distributions were related mainly to temperature (and to a lesser extent pH and conductivity). At present, the mean annual precipitation (MAP) ranges between around 50 mm at the margin to about 25 mm in the central basin with a mean annual potential evaporation of > 3000 mm (Chen and Bowler, 1986; Yang et al., 1995; Jiang and Robbins, 2000); conditions are dry.

Xie et al. (2012) and Yang et al. (2014) found that the high $R_{i/b}$ values (>0.5) in soil only can be observed in areas where MAP is less than 600 mm and alkaline soils (pH > 7.5) exist. Alkaline soils provide a favorite environment for soil Thaumarchaeota which is a major source organism for iGDGTs, thus leading to higher concentrations of iGDGTs there (Kim et al., 2012). However, microbes producing bGDGTs find best conditions at low pH, e.g. in acidic soils (Weijers et al., 2007b). The high $R_{i/b}$ values measured on our samples ranging from 0.77-3.40 (1.62 on average) indicate arid and alkaline soils conditions.

There is a close link between the aridity in Central Asia, the major uplift of the plateau, and the development of alkaline sediments in this region that occurred during the Late Miocene (around 8-9 Ma ago) (An et al., 2001; Xie et al., 2012). This corresponds to the first stages of evolution of Asian climates, i.e. the Asian interior drought intensified, and the Indian and East Asian monsoon began, as well as the initial uplift period of the TP. The continued intensification of the east Asian summer and winter monsoons occurred about 3.6–2.6 Ma ago followed by more intense and continuous East Asian winter monsoon conditions and increased variability and possible weakening of the Indian and east Asian summer monsoons since around 2.6 Ma ago (An et al., 2001), resulting in the aridity in Central and East Asia. This evolution is also reflected by the obviously higher Pleistocene $R_{i/b}$ values derived from this study as compared to those of the Late Miocene on the Tibetan Plateau (Xie et al., 2012). Due to the continuous uplift of the Tibetan Plateau since the Holocene, the Pleistocene $R_{i/b}$ values are clearly lower than those of the modern northeastern Tibetan Plateau (Sun et al., 2016), indicating a continuous aridification process. The low MBT values for high-altitude areas usually coexist with high $R_{i/b}$ values, representing a cold and dry environment, as opposed to the high MBT and low $R_{i/b}$ values, which represent a low-altitude warmer and more humid environment (Fig. 5.11d). The low MBT and high $R_{i/b}$ values in the studied samples would therefore indicate a cold and dry environment (Fig. 5.11d). Hence, the paleo environment during the Pleistocene period was likely arid and cold. Considering the current

elevation of the Qaidam Basin (2.7-3.5 km) and rapid uplift after the Pleistocene, the high Pleistocene $R_{i/b}$ values (Fig. 5.11d) probably indicate arid conditions caused by the inland location rather than by very high altitude.

Generally, high pH values indicate an arid environment. Relationships between CBT (cyclisation of branched tetraethers) and pH values were observed for soils samples (Weijers et al., 2007b; Peterse et al., 2010; Xie et al., 2012). For global soils CBT and pH values show a negative relationship (Weijers et al., 2007b; Peterse et al., 2010). Xie et al. (2012) argued that this relationship would be negative in acid environment (Ph < 7) and that there should be a slightly positive correlation or a flattening off in alkaline environment (7 < Ph < 9) for all soils collected from different climate zones of China. This positive correlation in soils and surface sediments of Tibetan saline lakes with pH > 8 was also observed by Günther et al. (2014).

In this study, calculated $pH_{Günther2014}$ values are highest, ranging 8.66 from 9.91 (mean value = 9.13), followed by $pH_{Tierney2010}$ (8.00-9.37) and $pHsun_{2011}$ (7.67-8.37) (Table 5.7). All of these values, however, indicate an arid environment. The pH values based on soil-derived GDGTs (Weijers et al., 2007b) show alkaline environment as well with $pH_{Weijers2007}$ values ranging from 6.75 to 7.92 (7.5 on average). These new results are consistent with those of previous studies indicating that soils on the Tibetan Plateau tend to be alkaline with pH varying between 6 and 10 (8 on average; Wang et al., 2012; Günther et al., 2014).

5.7 Conclusion

This study combines major and trace elements, GDGTs, and stable isotopes of two organic facies from Pleistocene, microbial gas source rocks in the central Qaidam Basin in order to achieve an overview on climatic conditions during that time. The following conclusions concerning origin of organic matter, depositional conditions within the water column, factors controlling OM quantity and quality, and paleo-climatic conditions are drawn:

1) The OM of organic facies A is mainly derived from a mixture of C3 higher plants and phytoplankton growing in marginal parts of the lake. This facies is characterized by high TOC contents and abundant terrigenous organic matter.

2) Organic facies A were deposited in a shallow freshwater environment under dysoxic to anoxic bottom water conditions, while organic facies B developed in a hypersaline lake environment under oxic bottom water conditions. Based on TOC contents and carbon isotope data, the OM preservation in both organic facies A and B was primarily controlled by the paleo-redox conditions, i.e., the dysoxic to anoxic bottom water conditions for organic facies A and oxic conditions for organic facies B might be the most important factors controlling their high and low TOC content, respectively.

3) Due to the high sedimentation rates, organic carbon accumulation was fast due to rapid burial and thus good preservation of organic matter. According to the negative correlation between TOC content and $\delta^{13}C_{org}$ values, OM preservation was controlled by paleo-redox conditions.

4) There is no significant difference between organic facies A and B with respect to the paleoclimate proxies. Related major and trace elements indicate arid/cold conditions with weak chemical weathering during the Pleistocene. Combined with the published data, the CIA and $R_{i/b}$ values indicate a rather continuous cooling and aridification process from Miocene to Pleistocene and recent.

5) The bGDGTs of the studied samples are mainly derived from terrestrial soil input, and the Pleistocene calculated MAAT based on bGDGTs (0.54-4.91 ˚C, 2.23 ˚C on average according to the most reasonable calibration) were slightly higher than the present temperature. The reconstructed lake surface temperature ranges from 5.7 to 19.6 ˚C (WLST were 2.4-13.7 ˚C). The Pleistocene soils on the Tibetan Plateau were alkaline.

6 General discussion and outlook

6.1 General discussion

This thesis covers basic non-marine source rock characterization and investigations of hydrocarbon potential for shale gas, shale oil and microbial gas. Concerning the Paleozoic gas shales and Triassic oil shale in the Ordos Basin as well as microbial gas mudstones in the Qaidam Basin, depositional environment, thermal maturity and hydrocarbon potential were analyzed. In addition, factors controlling organic matter (OM) accumulation and records of paleo -environment and -climate evolution in mudstone/shale have been analyzed. The characteristics of the non-marine source rocks covering stages from immature to over mature are investigated within this thesis. Part of the results are in good accordance with those documented in other publications, but some new ideas have been proposed as well. Major conclusions are summarized as follows:

• **Thermal maturity and depositional conditions of Upper Paleozoic shales from the Ordos Basin:**
The Upper Paleozoic gas shales presented in this thesis have over thermal maturities with maturity ranging from 2.35 to 2.97%. The results are similar to the other publications in the similar area showing the maturity of 2.3-3.12% (Ding et al., 2013; Xiong et al., 2017; Yang et al., 2017b). This relatively homogeneous maturity over a wide area corresponds to the rather equal thickness of the over formations along the whole basin. Both in terms of lithology and mineral content, rocks show strong variability, related to variable depositional settings. The values of TOC/TS of the samples studied cover a wide range and indicate the shift from marine to terrigenous environments as well. The observation of abundant vitrinite and inertinite particles, and even coal fragments and roots, indicates the terrestrial origin of most OM. This material certainly represents a former type III kerogen, now strongly converted towards carbon-rich residues, which is consistent with conclusions from previous studies (Yang et al., 2016, 2017b; Xiong et al., 2017). While most samples have a high content of clay minerals, samples B-3 and B-4 show high contents of carbonate. These samples also have low TOC/TS ratios indicating a marine depositional environment. For our sample set, strong marine influence is indicated for Benxi Formation (in agreement with e.g. Ding et al. (2013) and Xiong et al. (2013)), but not for Shanxi Formation where the studied samples do not show any marine influence. Clay minerals are clearly dominated by I/S mixed layer in Shanxi Formation, while Benxi Formation shales are characterized by a mixture of both I/S mixed layer and kaolinite. This non-uniform distribution of clay minerals is consistent with previously published data (Ding et al., 2013; Yang et al., 2016, 2017b; Xiong et al., 2017).

• **Controls on gas storage characteristics of Upper Paleozoic shales from the Ordos Basin:** Both the Benxi and Shanxi shales are characterized by comparatively low porosities, sorption capacities and gas storage capacities compared to producing marine shale gas systems. Excess

sorption capacity and porosity of over-mature Benxi and Shanxi transitional shales are controlled by their high clay mineral content (up to 80%). In contrast to other shales (e.g. Gasparik et al., 2014; Merkel et al., 2015, 2016; Shabani et al., 2018), TOC has a minor effect on gas sorption because of its low content (smaller than 2.3%). The volumetric "free" gas storage prevails in deeper Benxi and Shanxi reservoirs whereas excess sorptive storage generally dominates the total storage capacity of these shale reservoirs at shallow depths. Methane sorption does not have a positive effect on gas production at high pressure. Only when the pore pressure in the matrix is reduced significantly will "excess sorbed" gas contribute to production. This has major implications for deep reservoirs, where pore pressures in the matrix may not be sufficiently reduced before production ceases. Combined with the large amount of clay minerals that make hydraulic fracturing more difficult, these formations are regarded unfavourable for shale gas exploitation.

- **Depositional environment and organic matter composition of shales from the Triassic Chang 7 Member in the Ordos Basin:** The Chang 7 member is a typical clay-rich source rock deposited and preserved in a sulphate-poor lacustrine environment in the center of the basin (MW 16 well) and a fluvio-deltaic environment northwestward (MW 1 well) under fresh water and oxic to sub-oxic conditions. The MW 16 well situated close to the center of the former lake shows, however, slightly reducing conditions. The same result can be drawn from the pyrite size and elemental composition data in the similar area, which were previously published (Yuan et al., 2016). OM is composed of a type II-III kerogen. A mixture of lacustrine aquatic algal-bacterial-macrophytic organisms and terrigenous higher plants (mainly composed of conifers) was the main source of OM based on combined organic petrography and biomarker results. Due to the large area of the basin, the composition of OM shows large variation. For example, the OM is composed of a type I-II kerogen in the southern area (Zhang et al., 2020; Fig. 6.1).
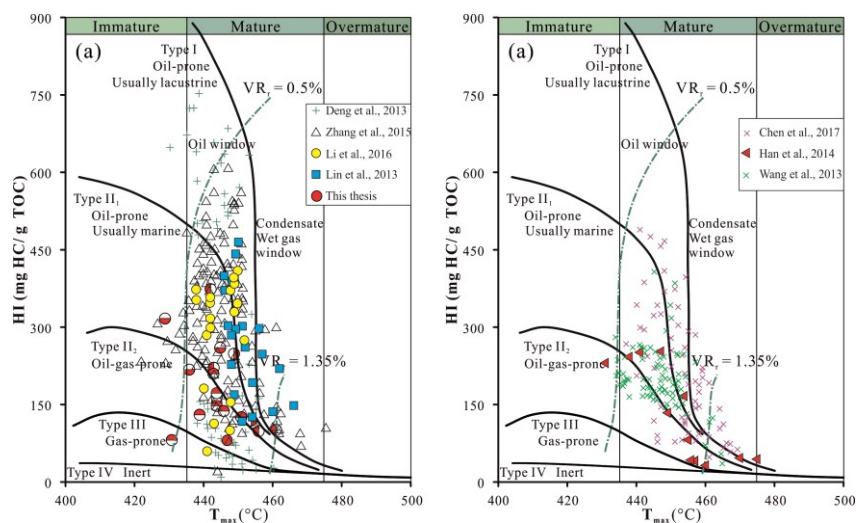
Fig. 6.1. Rock-Eval data on the Chang 7 member in the Ordos Basin: comparison of our results and other data from publications (see Chen et al., 2017).

- **Maturity of organic matter-rich shales from the Triassic Chang 7 Member in the Ordos Basin:** The thermal maturity of the Chang 7 Member source rocks reaches the main phase of oil generation based on vitrinite reflectance, Rock-Eval and most molecular geochemical data. The T_{max} values are quite similar to those from previous publications (Chen et al., 2016; Fig. 6.1). This small range of maturity accords with the thickness distribution of the Triassic, Jurassic and Lower Cretaceous rocks in the study area. The study reveals that these source rocks possess good to very good potential for liquid hydrocarbon generation, based on the moderate to very high total OM content, thickness (up to 100 m of source rock within the 60–120 m Chang 7 Member) and Rock-Eval results. The quality of the source rocks is not as good as previously reported (e.g. Xu et al., 2019), which might be caused by the sampling locations further towards the margin of the basin. Best source rock properties are expected in the area of the former central lake.

- **Classification of Pleistocene microbial gas source rocks in the Qaidam Basin:** These sediments are generally rich in OM, but contain two vastly different organic facies (A and B), which are interlayered with each other. These two organic facies both represent lacustrine systems. Periodically, shallow freshwater fluvio-lacustrine environments similar developed during high water levels at the lake margins with suboxic to anoxic redox conditions in bottom water favoring the development of OM-rich (4.1–25.3 wt.% TOC) and sulphur-rich (1.5–3.7 wt.% TS) sediments. They represent organic facies A, which, however, accounts for only a small proportion of the whole sedimentary sequence. More common is organic facies B, represented by samples with moderate TOC content of 0.5–1.1 wt.% and TS content of 0.1–1.0 wt.%, which were deposited under more oxic bottom waters in more distal parts of the lake.

- **Depositional environment of Pleistocene microbial gas source rocks in the Qaidam Basin:** The depositional environment of Pleistocene microbial gas source rocks was interpreted based on the TOC/TS ratios, biomarker characters, C_{org}/P ratios, trace elements, relative concentrations of TOC, TS and iron, H/C and C/S ratios of kerogen samples. Organic facies A samples were deposited in a shallow freshwater environment without stratification, but organic facies B samples developed in hypersaline depositional environments and partly even in lakes with water column stratification. Moreover, organic facies A samples were deposited under dysoxic to slightly anoxic bottom water conditions, while organic facies B samples were deposited under oxic conditions. However, reducing conditions indicated by biomarker data were probably sometimes present in the sediments caused by the "mat-seal effect".

- **Composition and maturity of organic matter of microbial gas source rocks in the Qaidam Basin:** The kerogen type is gas prone mixed type II-III in most samples, which are thermally immature. A large part of it is originated from aquatic higher plants in sediments representing organic facies A, i.e. submerged angiosperms and macrophytes that were growing at the lake margin. In contrast, organic facies B samples mainly developed from algae living in salt water.

Cyanobacteria contributed to the kerogen in both organic facies, while other microbial contribution was more pronounced for organic facies B than organic facies A. Terrestrial higher land plants only provided a minor part of the kerogen.

• **Organic carbon accumulation rate of microbial gas source rocks in the Qaidam Basin:** Both organic facies A (75-450 g C m^{-2}a^{-1}) and organic facies B (8-40g C m^{-2}a^{-1}) show high calculated organic carbon accumulation rates, which are favorable for rapid burial of kerogen into the methanogenesis zone. They are distinctly higher than e.g. in OM-rich Quaternary marine sediments sites drilled by ODP such as Baffin Bay, Labrador Sea (0.1–3 g C m^{-2}a^{-1}; Stein, 1991). Furthermore, they are greater or close to upwelling areas offshore Peru and Oman (0.4–15.9 g C m^{-2}a^{-1} with an average value of 3.69 g C m^{-2}a^{-1}; Lückge et al., 1996) and open-ocean gyres (0.026–378 g C m^{-2}a^{-1} with an average value of 55.85 g C m^{-2}a^{-1}; Suess, 1980), respectively (Fig. 6.2). This is due to the tectonic setting leading to strong erosion in the hinterland and thus high sediment accumulation rates, combined with lake environments favorable for OM production and preservation. Compared to other lake systems, the values of organic facies B samples are slightly lower and those of facies A are slightly higher than those in Brazilian lakes, such as Feia (43 g C m^{-2}a^{-1}; lake altitude is 850 m) and Agua Preta de Baixo (22 g C m^{-2}a^{-1}; lake altitude is 240 m), where also large populations of floating macrophytes developed during the Holocene (Turcq et al., 2002). In addition, the wells located above the gas fields show moderate to high SPI (source potential index) values ranging from 2.24 to 25.66 t HC/m^2, but the T2 Well which is close to Sebei 1 Gas Field shows a lower SPI value (1.49 t HC/m^2).
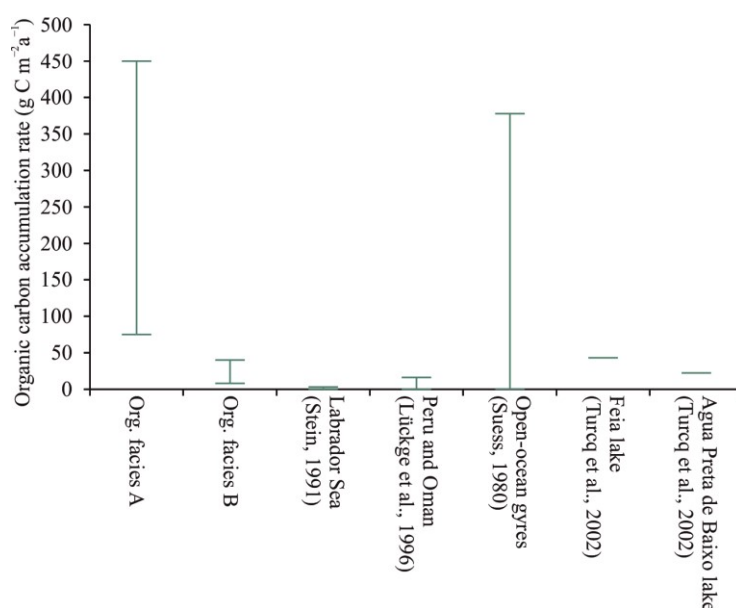
Fig. 6.2. Organic carbon accumulation rate in the microbial gas source rocks in the Qaidam Basin: comparison of our results and data on other data from publications.

- **Factors controlling OM organic matter accumulation of microbial gas source rocks in the Qaidam Basin:** The relative importance of palaeoredox conditions and palaeoproductivity as control factors on OM preservation can be evaluated via the relationship between TOC content and $\delta^{13}C_{org}$ value. The OM accumulation in both organic facies A and B was primarily controlled by the palaeoredox conditions, i.e., the dysoxic to slightly anoxic bottom water conditions for organic facies A samples and oxic conditions for organic facies B samples might be the most important factor controlling their high and low TOC content, respectively.

- **Climatic conditions during the Pleistocene in the Central Qaidam Basin:** There is no significant difference between organic facies A and B samples with respect to the paleoclimate proxies. These sediments were deposited under arid/cold conditions with weak chemical weathering during the Pleistocene period. Combined to the mean CIA values of J_1 (88), J_2 (87), J_3 (75), K_1 (71), E_{1+2} (68), E_3 (71), N_1 (72), and N_{21} (67) mudstones released by Jian et al. (2013), the CIA values indicate a continuous cooling and aridification process (Fig. 6.3). The Pleistocene MAAT (mean annual air temperatures; 0.54-4.91 °C, 2.23 °C on average) were slightly higher than the present temperature. The Pleistocene $R_{i/b}$ values are located between the higher modern $R_{i/b}$ (Sun et al., 2016) values in northeastern TP and the lower Late Miocene $R_{i/b}$ values in the TP (Xie et al., 2012), indicating arid and alkaline soil conditions and a continuous aridification process. Moreover, soils at the Tibetan Plateau tended to become more alkaline with pH varying between 6 and 10.
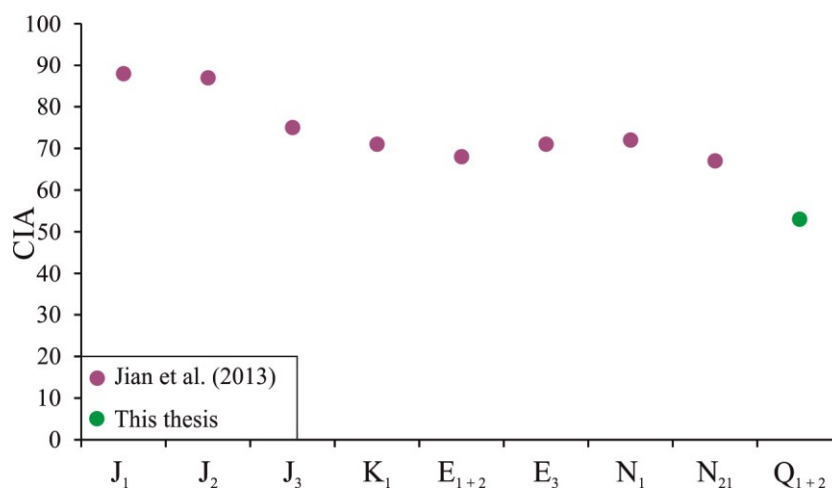
Fig. 6.3. CIA values for different source rocks in the Qaidam Basin from old (left) to young (right): comparison of our results and data on other data from Jian et al. (2013).

6.2 Outlook

During my PhD study, different source rocks in northern China and their hydrocarbon generation potential were investigated. Several topics which remain worth investigating are listed as follows:

- Controls on gas storage characteristics of Upper Paleozoic shales from the Ordos Basin were studied. However, the analysis of the depositional environment using organic geochemical methods of

these non-marine Paleozoic gas shales in the Ordos Basin was limited due to their high thermal maturity. More systematic inorganic geochemical analysis, e.g. using major and trace elements and isotopic studies should be performed as well on these shales. Thermal maturity can be determined accurately by using vitrinite reflectance for such terrestrial shales with very high maturity. In addition, some molecular compounds, e.g. diamondoids, might provide valuable geochemical thermal maturity data and clay mineralogy (e.g. illite crystallinity) would be useful as well.

• The Ordos Basin is the second-largest basin in China. The Triassic Chang 7 Member is the most important source rock for the Mesozoic hydrocarbons in the basin. These source rocks developed a Type II-III kerogen from a typical fresh water lacustrine environment based on the data of molecular geochemistry and Rock-Eval pyrolysis as well as petrographical observations. However, the molecular structures of these kerogens in this area are not studied until now. In the next step, kerogen should be studied comprehensively using FT-IR-spectroscopy, Curie Point-pyrolysis-GC-/MS, X-ray diffraction (XRD), XRF, and ICP-MS to 1) gain new insights into the depositional environment of Chang 7 Member source rocks throughout the mid-western area of the Ordos Basin, and 2) obtain detailed information on structure and chemistry of Triassic lacustrine kerogen in the basin.

7 References

Abanda, P.A., Hannigan, R.E., 2006. Effect of diagenesis on trace element partitioning in shales. Chem. Geol. 230, 42–59.

Adegoke, A.K., Abdullah, W.H., Hakimi, M.H., Yandoka, B.M.S., 2014. Geochemical characterisation of Fika Formation in the Chad (Bornu) Basin, northeastern Nigeria: implications for depositional environment and tectonic setting. Appl. Geochem. 43, 1–12.

Al-Arouri, K.R., Mckirdy, D.M., Boreham, C.J., 1998. Oil-source correlations as a tool in identifying the petroleum systems of the southern Taroom Trough, Australia. Org. Geochem. 29 (1–3), 713–734.

Alexander, R., Bastow, T.P., Fisher, S.J., Kagi, R.I., 1995. Geosynthesis of organic compounds: II. Methylation of phenanthrene and alkylphenanthrenes. Geochim. Cosmochim. Acta 59 (20), 4259–4266.

Alexander, R., Cumbers, K.M., Kagi, R.I., 1986. Alkylbiphenyls in ancient sediments and petroleums. Organ. Geochem. 10, 841–845.

Alexander, R., Kagi, R.I., Noble, R., Volkman, J.K., 1984. Identification of some bicyclic alkanes in petroleum. Org. Geochem. 6, 63–72.

Alexander, R., Kagi, R.I., Rowland, S.J., Sheppard, P.N., Chirila, T.V., 1985. The effects of thermal maturity on distributions of dimethylnaphthalenes and trimethylnaphthalenes in some ancient sediments and petroleums. Geochim. Cosmochim. Acta 49 (2), 385–395.

Alexander, R., Kagi, R.I., Woodhouse, G.W., Volkman, J.K., 1983. The geochemistry of some biodegraded Australian oils. Aust. Petrol. Explor. Assoc. J. 23, 53–63.

Alexander, R., Larcher, A.V., Kagi, R.I., Price, P.L., 1988. The use of plant derived biomarkers for correlation of oils with source rocks in the Cooper/Eromanga Basin System, Australia. APEA J. 28, 310–324.

Algeo, T.J., Ingall, E., 2007. Sedimentary Corg:P ratios, Paleocean ventilation, and Phanerozoic atmospheric pO2. Palaeogeogr. Palaeoclimatol. Palaeoecol. 256,130–155.

Algeo, T.J., Li, C., 2020. Redox classification and calibration of redox thresholds in sedimentary systems. Geochim. Cosmochim. Acta. 287, 8–26.

Algeo, T.J., Maynard, J.B., 2004. Trace-element behavior and redox facies in core shales of Upper Pennsylvanian Kansas-type cyclothems. Chem. Geol. 206, 289–318.

Algeo, T.J., Tribovillard, N., 2009. Environmental analysis of paleoceanographic systems based on molybdenum–uranium covariation. Chem. Geol. 268(3–4), 211–225.

An, Z., Kutzbach, J.E., Prell, W.L., Porter, S.C., 2001. Evolution of Asian monsoon and phased uplift of the Himalaya–Tibetanplateau since late Miocene time. Nature 411, 62–66.

Anderson, V.J., Shanahan, T.M., Saylor, J.E., Horton, B.K., Mora, A.R., 2014. Sources of local and regional variability in the MBT′/CBT paleotemperature proxy: Insights from a modern elevation transect across the Eastern Cordillera of Colombia. Org. Geochem. 69, 42–51.

Aravena, R., Harrison, S.M., Barker, J.F., Abercrombie, H., Rudolph, D., 2003. Origin of methane in the Elk Valley coalfield, southeastern British Columbia, Canada. Chem. Geol. 195, 219–227.

Arouri, K.R., McKirdy, D.M., 2005. The behaviour of aromatic hydrocarbons in artificial mixtures of Permian and Jurassic end-member oils: application to in-reservoir mixing in the Eromanga Basin, Australia. Org. Geochem. 36 (1), 105–115.

Bai, J., Fengyan, D., 1996. The early Precambrian crustal evolution of China. J. Southeast Asian Earth Sci. 13(3–5), 205–214.

Baniasad, A., Rabbani, A.R., Moallemi, S.A., Soleimany, B., Rashidi, M., 2017. Petroleum system analysis of the northwestern part of the Persian Gulf, Iranian sector. Org. Geochem. 107, 69–85.

Bao, J., Wang, Y., Song, C., Feng, Y., Hu, C., Zhong, S., Yang, J., 2017. Cenozoic sediment flux in the Qaidam Basin, northern Tibetan Plateau, and implications with regional tectonics and climate. Glob. Planet. Chang. 155, 56–69.

Barakat, A.O., Rullkötter, J., 1999. Origin of organic sulfur compounds in sediments from the Nördlinger Ries (southern Germany). J. Petrol. Sci. Eng. 22 (1–3), 103–119.

Bastow, T.P., Singh, R.K., van Aarssen, B.G.K., Alexander, R., Kagi, R.I., 2001. 2-Methylretene in sedimentary material: a new higher plant biomarker. Org. Geochem. 32, 1211–1217.

Bauersachs, T., Kremer, B., Schouten, S., Sinninghe Damsté, J.S., 2009. A biomarker and d15 N study of thermally altered Silurian cyanobacterial mats. Org. Geochem. 40, 149–157.

Baydjanova, S., George, S.C., 2019. Depositional environment, organic matter sources, and variable 17α (H)-diahopane distribution in early Permian samples, southern Sydney Basin, Australia. Org. Geochem. 131, 60–75.

Bechtel, A., Smittenberg, R.H., Bernasconi, S.M., Schubert, C.J., 2010. Distribution of branched and isoprenoid tetraether lipids in an oligotrophic and a eutrophic Swiss lake: insights into sources and GDGT-based proxies. Org. Geochem. 41(8), 822–832.

Bechtel, A., Widera, M., Sachsenhofer, R., Gratzer, R., Lücke, A., Woszczyk, M., 2007. Biomarker and stable carbon isotope systematics of fossil wood from the second Lusatian lignite seam of the Lubstów deposit (Poland). Org. Geochem. 38 (11), 1850–1864.

Behar, F., Beaumont, V., Penteado, H.D.B., 2001. Rock-Eval 6 technology: performances and developments. Oil Gas Sci. Technol. 56 (2), 111–134.

Berner, R.A., Raiswell, R., 1983. Burial of organic carbon and pyrite sulfur in sediments over Phanerozoic time: a new theory. Geochim. Cosmochim. Acta 47 (5), 855–862.

Berner, R.A., Raiswell, R., 1984. C/S method for distinguishing freshwater from marine sedimentary rocks. Geology 12, 365–368.

Beti, D.R., Garel, S., Setoyama, E., Behar, F., Ring, T.A., Kanungo, S., 2021. A new resource assessment workflow to achieve gas risk and phase-specific source potential indices. Mar. Petrol. Geol. 105136.

Bingham, E.M., McClymont, E.L., Valiranta, M., Mauquoy, D., Roberts, Z., Chambers, F. M., Pancost, R.D., Evershed, R.P., 2010. Conservative composition of n-alkane biomarkers in Sphagnum species: implications for palaeoclimate reconstruction in ombrotrohic peat bogs. Org. Geochem. 41, 214–220.

Blaga, C.I., Reichart, G.J., Heiri, O., Sinninghe Damsté, J.S., 2009. Tetraether membrane lipid distributions in water-column particulate matter and sediments: a study of 47 European lakes along a north–south transect. J. Paleolimnol. 41(3), 523–540

Blumenberg, M., Krüger, M., Nauhaus, K., Talbot, H.M., Oppermann, B.I., Seifert, R., Pape, T., Michaelis, W., 2006. Biosynthesis of hopanoids by sulfate-reducing bacteria (genus Desulfovibrio). Environ. Microbiol. 8, 1220–1227.

Blumenberg, M., Thiel, V., Reitner, J., 2015. Organic matter preservation in the carbonate matrix of a recent microbial mat–is there a 'mat seal effect'? Org. Geochem. 87, 25–34.

Blumer, M., Ehrhardt, M., Jones, J., 1973. The environmental fate of stranded crude oil. Deep-Sea Res. 20, 239–259.

Böcker, J., Littke, R., Hartkopf-Fröder, C., Jasper, K., Schwarzbauer, J., 2013. Organic geochemistry of Duckmantian (Pennsylvanian) coals from the Ruhr Basin, western Germany. Int. J. Coal Geol. 107, 112–126.

Bottari, F., Marsili, A., Morelli, I., Pacchiani, M., 1972. Aliphatic and triterpenoid hydrocarbons from ferns. Phytochemistry 11, 2519–2523.

Bou Daher, S., Nader, F.H., Müller, C., Littke, R., 2015. Geochemical and petrographic characterization of Campanian–lower Maastrichtian calcareous petroleum source rocks of Hasbayya, South Lebanon. Mar. Petrol. Geol. 64, 304–323.

Bourbonniere, R.A., Meyers, P.A., 1996. Anthropogenic influences on hydrocarbon contents of sediments deposited in eastern Lake Ontario since 1800. Environ. Geol. 28, 22–28.

Bradley, W.H., 1964. Geology of Green River Formation and associated Eocene rocks in southwestern Wyoming and adjacent parts of Colorado and Utah (No. 496–A).

Bray, E.E., Evans, E.D., 1961. Distribution of n-paraffins as a clue to recognition of source beds. Geochim. Cosmochim. Acta 22, 2–15.

Brooks, J.D., Gould, K., Smith, J.W., 1969. Isoprenoid hydrocarbons in coal and petroleum. Nature 222, 257–259.

Bruns, B., Littke, R., Gasparik, M., Wees, J.D., Nelskamp, S., 2016. Thermal evolution and shale gas potential estimation of the Wealden and Posidonia Shale in NWGermany and The Netherlands: a 3D basin modelling study. Basin Res. 28, 2–33.

Bustin, R.M., Bustin, A.M., Cui, A., Ross, D., Pathi, V.M., 2008. Impact of shale properties on pore structure and storage characteristics. SPE Shale Gas Production Conference Society of Petroleum Engineers, pp. 1–28.

Cai, M., Fang, X., Wu, F., Miao, Y., Appel, E., 2012. Pliocene–Pleistocene stepwise drying of Central Asia: evidence from paleomagnetism and sporopollen record of the deep borehole SG-3 in the western Qaidam Basin, NE Tibetan Plateau. Glob. Planet. Chang. 94, 72–81.

Cane, R.F., 1976. The origin and formation of oil shale. In: Yen, T.F., Chilingarian, G.V. (Eds.), Oil Shale, Developments in Petroleum Science, vol. 5. Elsevier, Amsterdam, pp. 27–60.

Canfield, D.E., Raiswell, R., Bottrell, S., 1992. The reactivity of sedimentary iron minerals toward PA. Am. J. Sci. 292, 659–683.

Carlson, R.E., Simpson, J., 1996. A coordinator's guide to volunteer lake monitoring methods. North American Lake Management Society, 96, 305.

Carroll, A.R., Bohacs, K.M., 1999. Stratigraphic classifcation of ancient lakes: balancing tectonic and climatic controls. Geology 27, 99–102.

Cassani, F., Gallango, O., Talukdar, S., Vallejos, C., Ehrmann, U., 1988. Methylphenanthrene maturity index of marine source rock extracts and crude oils from the Maracaibo Basin. Org. Geochem. 13, 73–80.

Castañeda, I. S., Schouten, S., 2011. A review of molecular organic proxies for examining modern and ancient lacustrine environments. Quaternary Sci. Rev. 30(21–22), 2851–2891.

Cesar, J., Grice, K., 2017. $\delta^{13}C$ of polycyclic aromatic hydrocarbons to establish the facies variations in a fluvial deltaic Triassic record (Dampier sub-Basin, Western Australia). Org. Geochem. 107, 59–68.

Chaffee, A.L., Fookes, C.J.R., 1988. Polycyclic aromatic hydrocarbons in Australian coals—III, Structural elucidation by proton nuclear magnetic resonance spectroscopy. Org. Geochem. 12, 261–271.

Chaffee, A.L., Johns, R.B., 1983. Polycyclic aromatic hydrocarbons in Australian coals, I. Angularly fused pentacyclic tri-and tetraaromatic components of Victorian brown coal. Geochim. Cosmochim. Acta 47, 2141–2155.

Chalmers, G.R., Bustin, R.M., 2007. The organic matter distribution and methane capacity of the Lower Cretaceous strata of Northeastern British Columbia, Canada. Int. J. Coal Geol. 70 (1–3), 223–239.

Chalmers, G.R., Bustin, R.M., 2008. Lower Cretaceous gas shales in northeastern British Columbia, Part I: geological controls on methane sorption capacity. Bull. Can. Petrol. Geol. 56 (1), 1–21.

Chen, C., Bai, Y., Fang, X., Xu, Q., Zhang, T., Deng, T., He, J., Chen, Q., 2020. Lower-altitude of the Himalayas before the mid-Pliocene as constrained by hydrological and thermal conditions. Earth Planet. Sci. Lett. 545, 116422.

Chen, D., Pang, X., Jiang, Z., Zeng, J., Qiu, N., Li, M., 2009. Reservoir characteristics and their effects on hydrocarbon accumulation in lacustrine turbidites in the Jiyang Super-depression, Bohai Bay Basin, China. Mar. Petrol. Geol. 26 (2), 149–162.

Chen, J., Summons, R.E., 2001. Complex patterns of steroidal biomarkers in Tertiary lacustrine sediments of the Biyang Basin, China. Org. Geochem. 32, 115–126.

Chen, J.F., Jahn, B.M., 1998. Crustal evolution of south eastern China: Nd and Sr isotopic evidence: Tectono physics, v. 284.

Chen, K.Z., Bowler, J.M., 1986. Late pleistocene evolution of salt lakes in the Qaidam Basin, Qinghai province, China. Palaeogeogr. Palaecolimatol. Palaeoecol. 54, 87–104.

Chen, R., Liu, G., Shang, F., Cao, Y., 2019a. Nitrogen isotope compositions of the Upper Triassic Chang 7 Shale, Ordos Basin, North China: Implications for depositional redox conditions. Mar. Petrol. Geol. 109, 279–290.

Chen, Y., Zhu, Z., Zhang, L., 2019b. Control actions of sedimentary environments and sedimentation rates on lacustrine oil shale distribution, an example of the oil shale in the Upper Triassic Yanchang Formation, southeastern Ordos Basin (NW China). Mar. Petrol. Geol. 102, 508–520.

Chen, Z., Guo, Q., Jiang, C., Liu, X., Reyes, J., Mort, A., Jia, Z., 2017. Source rock characteristics and rock-eval-based hydrocarbon generation kinetic models of the lacustrine Chang-7 shale of Triassic Yanchang Formation, Ordos Basin. China. Int. J. Coal Geol. 182, 52–65.

Chen, Z., Jiang, C., 2016. A revised method for organic porosity estimation in shale reservoirs using Rock-Eval data: example from Duvernay Formation in the Western Canada Sedimentary Basin. AAPG Bull. 100 (3), 405–422.

Chukwuma, K., Bordy, E.M., Coetzer, A., 2018. Evolution of porosity and pore geometry in the Permian Whitehill Formation of South Africa – a FE-SEM image analysis study. Mar. Petrol. Geol. 91, 262–278.

Cichon-Pupienis, A., Littke, R., Froidl, F., Lazauskienė, J., 2020. Depositional history, source rock quality and thermal maturity of Upper Ordovician-Lower Silurian organic-rich sedimentary rocks in the central part of the Baltic Basin (Lithuania). Mar. Petrol. Geol. 112, 104083.

Cichon-Pupienis, A., Littke, R., Lazauskienė, J., Baniasad, A., Pupienis, D., Radzevičius, S., Šiliauskas, L., 2021. Geochemical and sedimentary facies study–Implication for driving mechanisms of organic matter enrichment in the lower Silurian fine-grained mudstones in the Baltic Basin (W Lithuania). Int. J. Coal Geol. 103815.

Coetzee, J.A., 1967. Pollen analytical studies in East and Southern Africa. Palaeoecol. Afr. 3, 1–146.

Coleman, D.D., Liu, C.L., Riley, K.M., 1988. Microbial methane in the shallow Paleozoic sediments and glacial deposits of Illinois, USA. Chem. Geol. 71 (1–3), 23–40.

Connan, J., Cassou, A.M., 1980. Properties of gases and petroleum liquids derived from terrestrial kerogen at various maturation levels. Geochim. Cosmochim. Acta 44, 1–23.

Crampton-Flood, E.D., van der Weijst, C.M., van der Molen, G., Bouquet, M., Yedema, Y., Donders, T. H., Peterse, F., 2021. Identifying marine and freshwater overprints on soil-derived branched GDGT temperature signals in Pliocene Mississippi and Amazon River fan sediments. Org. Geochem. 154, 104200.

Cui, J., Li, S., Mao, Z., 2019. Oil-bearing heterogeneity and threshold of tight sandstone reservoirs: a case study on Triassic Chang7 member, Ordos Basin. Mar. Petrol. Geol. 104, 180–189.

Cumbers, K.M., Alexander, R., Kagi, R.I., 1987. Methylbiphenyl, ethylbiphenyl and dimethylbiphenyl iso mer distributions in some crude oils. Geochim. Cosmochim. Acta 51, 3105–3111.

Curiale, J.A., 1986. Origin of solid bitumens, with emphasis on biological marker results. Org. Geochem. 10, 559–580.

Curtis, J.B., 2002. Fractured shale-gas systems. AAPG Bull. 86 (11), 1921–1938.

Dang, X., Yang, H., Naafs, B.D.A., Pancost, R. D., Xie, S., 2016. Evidence of moisture control on the methylation of branched glycerol dialkyl glycerol tetraethers in semi-arid and arid soils. Geochim. Cosmochim. Acta 189, 24–36.

Dang, Y.Q., Zhao, W.Z., Su, A.G., Zhang, S.C., Li, M.W., Guan, Z.Q., Ma, D.D., Chen, X.L., Shuai, Y.H., Wang, H.T., Tan, Y.H., Xu, Z.Y., 2008. Biogenic gas systems in eastern Qaidam Basin. Mar. Petrol. Geol. 25, 344–356.

De Jonge, C., Hopmans, E.C., Zell, C.I., Kim, J.H., Schouten, S., Sinninghe Damsté, J.S., 2014. Occurrence and abundance of 6-methyl branched glycerol dialkyl glycerol tetraethers in soils: Implications for palaeoclimate reconstruction. Geochim. Cosmochim. Acta 141, 97–112.

Dean, W.E., Leinen, M., Stow, D.A., 1985. Classification of deep-sea, fine-grained sediments. J. Sediment. Res. 55(2), 250–256.

Demaison, G., Huizinga, B.J., 1991. Genetic classification of petroleum systems. AAPG Bull. 75, 1626–1643.

Demaison, G.J., Moore, G.T., 1980. Anoxic environments and oil source bed genesis. AAPG Bull. 64 (8), 1179–1209.

Deng, H.W., Qian, K, 1990. The genetic types and association evolution of deep lacustrine facies mudstones. Acta Sedimentologica Sinica, 8(3), 1–20.

Deng, L., Jia, G., Jin, C., Li, S., 2016. Warm season bias of branched GDGT temperature estimates causes underestimation of altitudinal lapse rate. Org. Geochem. 96, 11–17.

DePaolo, D.J., Wasserburg, G. J., 1976a. Nd isotopic variations and petrogenetic models. Geophys. Res. Lett. 3, 249–252.

DePaolo, D.J., Wasserburg, G. J., 1976b. Inferences about magma sources and mantle structure from variations of 143Nd/144Nd. Geophys. Res. Lett.3, 743–746.

Derenne, S., Largeau, C., Hetényi, M., Brukner-Wein, A., Connan, J., Lugardon, B., 1997. Chemical structure of the organic matter in a Pliocene maar-type shale: implicated Botryococcus race strains and formation pathways. Geochim. Cosmochim. Acta 61, 1879–1889.

Derry, L.A., France-Lanord, C., 1996. Neogene Himalayan weathering history and river 87Sr 86Sr: impact on the marine Sr record. Earth Planet. Sci. Lett. 142(1–2), 59–74.

Dettman, D.L., Fang, X., Garzione, C.N., Li, J., 2003. Uplift-driven climate change at 12 Ma: a long δ18O record from the NE margin of the Tibetan plateau. Earth Planet. Sci. Lett. 214(1–2), 267–277.

Didyk, B.M., Simoneit, B.R.T., Brassell, S.C., Eglinton, G., 1978. Organic geochemical indicators of paleoenvironmental conditions of sedimentation. Nature 272, 216–222.

Dimberline, A.J., Bell, A., Woodcock, N.H., 1990. A laminated hemipelagic facies from the Wenlock and Ludlow of the Welsh Basin. J. Geol. Soc. 147(4), 693–701.

Ding, S., Schwab, V.F., Ueberschaar, N., Roth, V.N., Lange, M., Xu, Y., Gleixner, G., Pohnert, G., 2016. Identification of novel 7-methyl and cyclopentanyl branched glycerol dialkyl glycerol tetraethers in lake sediments. Org. Geochem. 102, 52–58.

Ding, W., Zhu, D., Cai, J., Gong, M., Chen, F., 2013. Analysis of the developmental characteristics and major regulating factors of fractures in marine–continental transitional shale-gas reservoirs: a case study of the Carboniferous–Permian Strata in the southeastern Ordos Basin, central China. Mar. Petrol. Geol. 45 (4), 121–133.

Duan, Y., Wang, C.Y., Zheng, C.Y., Wu, B.X., Zheng, G.D., 2008. Geochemical study of crude oils from the Xifeng oilfield of the Ordos basin, China. J. Asian Earth Sci. 31, 341–356.

Duggen, S., Croot, P., Schacht, U., Hoffmann, L., 2007. Subduction zone volcanic ash can fertilize the surface ocean and stimulate phytoplankton growth: evidence from biogeochemical experiments and satellite data. Geophys. Res. Lett. 34, L01612.

Edmond, J.M., 1992. Himalayan tectonics, weathering processes, and the strontium isotope record in marine limestones. Science 258(5088), 1594–1597.

Eglinton, G., Hamilton, R.J., 1967. Leaf epicuticular waxes. Science 156, 1322–1335.

EIA, 2019. Annual Energy Outlook.

EIA, 2020. Annual Energy Outlook.

Erbacher, J., Thurow, J., Littke, R., 1996. Evolution patterns of radiolaria and organic matter variations: a new approach to identify sea-level changes in mid-cretaceous pelagic environments. Geology 24 (6), 499–502.

Espitalié, J., Deroo, G., Marquis, F., 1985. La pyrolyse Rock-Eval et ses applications. Deuxième partie. Revue de l'Institut français du Pétrole, 40(6), 755–784.

Fan, E., Tang, S., Zhang, C., Guo, Q., Sun, C., 2014. Methane sorption capacity of organics and clays in high-over matured shale-gas systems. Energy Explor. Exploit. 32 (6), 927–942.

Fan, P., Philp, R.P., Li, Z.X., Yu, X.K., Ying, G.G., 1991. Biomarker distributions in crude oils and source rocks from different sedimentary environments. Chem. Geol. 93, 61–78.

Fan, P., Philp, R.P., Zhenxi, Li, Guangguo, Ying, 1990. Geochemical characteristics of aromatic hydrocarbons of crude oils and source rocks from different sedimentary environments. In advances in Org. Geochem. 1989 (ed. B. Durand and F. Be'har). Org. Geochem. 16, 427–435.

Fang, X.M., Zhang, W.L., Meng, Q.Q., Gao, J.J., Wang, X.M., King, J., Song, C.H., Dai, S., Miao, Y.F., 2007. High-resolution magnetostratigraphy of the Neogene Huaitoutala section in the eastern Qaidam Basin on the NE Tibetan Plateau, Qinghai Province, China and its implication on tectonic uplift of the NE Tibetan Plateau. Earth Planet. Sci. Lett. 258, 293–306.

Farrimond, P., Taylor, A., Telnaes, N., 1998. Biomarker maturity parameters: the role of generation and thermal degradation. Org. Geochem. 29, 1181–1197.

Fedo, C.M., Wayne Nesbitt, H., Young, G. M., 1995. Unraveling the effects of potassium metasomatism in sedimentary rocks and paleosols, with implications for paleoweathering conditions and provenance. Geology 23, 921–924.

Ficken, K.J., Li, B., Swain, D.L., Eglinton, G., 2000. An n-alkane proxy for the sedimentary input of submerged/floating freshwater aquatic macrophytes. Org. Geochem. 31, 745–749.

Fink, R., Amann-Hildenbrand, A., Bertier, P., Littke, R., 2018. Pore structure, gas storage and matrix transport characteristics of lacustrine Newark Shale. Mar. Petrol. Geol. 97, 525–539.

Formolo, M., Martini, A., Petsch, S., 2008. Biodegradation of sedimentary organic matter associated with coalbed methane in the Powder River and San Juan Basins, USA. Int. J. Coal Geol. 76, 86–97.

Freeman, K.H., Hayes, J.M., Trendel, J.M., Albrecht, P., 1990. Evidence from carbon isotope measurements for diverse origins of sedimentary hydrocarbons. Nature 343(6255), 254.

Freeman, K.H., Wakeham, S.G., Hayes, J.M., 1994. Predictive isotopic biogeochemistry: hydrocarbons from anoxic marine basins. Org. Geochem. 21(6–7), 629–644.

Fu, S., J. Tian, H. Chen, Z. Hou, H. Yang, J. Fu, Z. Fan, X. Shi, 2003, The delta depositional system distribution of late Paleozoic era in Ordos basin (in Chinese): Journal of Chengdu University of Technology, v. 30, p. 235–241

Garzione, C.N., Dettman, D.L., Quade, J., DeCelles, P.G., Butler, R.F., 2000b. High times on the Tibetan Plateau: Paleoelevation of the Thakkhola graben, Nepal. Geology 28(4), 339–342.

Garzione, C.N., Quade, J., DeCelles, P.G., English, N.B., 2000a. Predicting paleoelevation of Tibet and the Himalaya from δ18O vs. altitude gradients in meteoric water across the Nepal Himalaya. Earth Planet. Sci. Lett. 183(1–2), 215–229.

Gasparik, M., Bertier, P., Gensterblum, Y., Ghanizadeh, A., Krooss, B.M., Littke, R., 2014. Geological controls on the methane storage capacity in organic-rich shales. Int. J. Coal Geol. 123, 34–51.

Gasparik, M., Gensterblum, Y., Ghanizadeh, A., Weniger, P., Krooss, B.M., 2015. Highpressure/high-temperature methane-sorption measurements on carbonaceous shales by the manometric method: experimental and data-evaluation considerations for improved accuracy. SPE J. 20, 790–809.

Gasparik, M., Ghanizadeh, A., Bertier, P., Gensterblum, Y., Bouw, S., Krooss, B.M., 2012. High-pressure methane sorption isotherms of black shales from The Netherlands. Energy Fuel. 26 (8), 4995–5004.

Gasparik, M., Ghanizadeh, A., Gensterblum, Y., Krooss, B.M., 2013. "Multi-temperature" method for high-pressure sorption measurements on moist shales. Rev. Sci. Instrum. 84 (8), 085116.

Gaus, G., Fink, R., Amann-Hildenbrand, A., Krooss, B.M., Littke, R., 2021. Experimental determination of porosity and methane sorption capacity of organic-rich shales as a function of effective stress: Implications for gas storage capacity. AAPG Bull. 105(2), 309–328.

Gehrels, G., Kapp, P., DeCelles, P., Pullen, A., Blakey, R., Weislogel, A., Ding, L., Guynn, J., Martin, A., McQuarrie, N., Yin, A., 2011. Detrital zircon geochronology of pre-Tertiary strata in the Tibetan–Himalayan orogen. Tectonics 30, TC5016.

Geng, Y.S. 1998. Archaean granite pluton events ofQianan area, East Hebei province and its evolution.In:CHEN, Y. Q. (ed.)Corpus on Early PrecambrianResearch of the North China Craton. Geological Publishing House, Beijing, 105–121.

George, S.C., Ahmed, M., 2002. Use of aromatic compound distributions to evaluate organic maturity of the Proterozoic middle Velkerri Formation, McArthur Basin, Australia. In: Keep, M., Moss, S.J. (Eds.), Proceedings of the Petroleum Exploration Society of Australia Symposium, The Sedimentary Basins of Western Australia, vol. 3, pp. 253–270.

George, S.C., Lisk, M., Eadington, P.J., Quezada, R.A., Krieger, F.W., Greenwood, P.F., Wilson, M.A., 1996. Comparison of Palaeo Oilcharges with Currently Reservoired Hydrocarbons Using Thegeochemistry of Oil-Bearing Fluid Inclusions, Society of Petroleum Engineers, Paper 36980, Adelaide, pp. 159–171.

George, S.C., Ruble, T.E., Dutkiewicz, A., Eadington, P.J., 2001. Assessing the maturity of oil trapped in fluid inclusions using molecular geochemistry data and visuallydetermined fluorescence colours. Appl. Geochem. 16 (4), 451–473.

George, S.C., Volk, H., Dutkiewicz, A., Ridley, J., Buick, R., 2008. Preservation of hydrocarbons and biomarkers in oil trapped inside fluid inclusions for> 2 billion years. Geochim. Cosmochim. Acta 72 (3), 844–870.

Ghanizadeh, A., Clarkson, C.R., Aquino, S., Ardakani, O.H., Sanei, H., 2015. Petrophysical and geomechanical characteristics of Canadian tight oil and liquid-rich gas reservoirs: I, pore network and permeability characterization. Fuel 153, 664–681.

Ghanizadeh, A., Gasparik, M., Amann-Hildenbrand, A., Gensterblum, Y., Krooss, B.M., 2014. Experimental study of fluid transport processes in the matrix system of the European organic-rich shales: I. Scandinavian Alum Shale. Mar. Petrol. Geol. 51, 79–99.

Ghassal, B.I., Littke, R., El Atfy, H., Sindern, S., Scholtysik, G., El Beialy, S., El Khoriby, E., 2018. Source rock potential and depositional environment of Upper cretaceous sedimentary rocks, Abu Gharadig Basin, Western Desert, Egypt: an integrated palynological, organic and inorganic geochemical study. Int. J. Coal Geol. 186, 14–40.

Ghazwani, A., Littke, R., Gaus, G., Hartkopf-Fröder, C., 2018. Assessment of unconventional shale gas potential of organic-rich Mississippian and lower Pennsylvanian sediments in western Germany. Int. J. Coal Geol. 198, 29–47.

Gonzales, L.D., Mastalerz, M., Mendonca Filho, J.G., 2020. Application of organic facies and biomarkers in characterization of paleoenvironmental conditions and maturity of sediments from the Codo Formation in the west central part of the Sao Luis Basin, Brazil. Int. J. Coal Geol. 225, 103482.

Grice, K., Nabbefeld, B., Maslen, E., 2007. Source and significance of selected polycyclic aromatic hydrocarbons in sediments (Hovea-3 well, Perth Basin, Western Australia) spanning the Permian–Triassic boundary. Org. Geochem. 38 (11), 1795–1803.

Grice, K., Schouten, S., Nissenbaum, A., Charrach, J., Sinninghe Damsté, J.S., 1998. A remarkable paradox: sulfurised freshwater algal (Botryococcus braunii) lipids in an ancient hyper saline euxinic ecosystem. Org. Geochem. 28, 195–216.

Grohmann, S., Romero-Sarmiento, M.F., Nader, F.H., Baudin, F., Littke, R., 2019. Geochemical and petrographic investigation of Triassic and late Miocene organicrich intervals from onshore Cyprus, Eastern Mediterranean. Int. J. Coal Geol. 209, 94–116.

Guenther, F., Aichner, B., Siegwolf, R., Xu, B., Yao, T., Gleixner, G., 2013. A synthesis of hydrogen isotope variability and its hydrological significance at the Qinghai–Tibetan Plateau. Quat. Int. 313–314, 3–6.

Günther, F., Thiele, A., Gleixner, G., Xu, B., Yao, T., Schouten, S., 2014. Distribution of bacterial and archaeal ether lipids in soils and surface sediments of Tibetan lakes: implications for GDGT-based proxies in saline high mountain lakes. Org. Geochem. 67, 19–30.

Guo, J.H., Sun, M., Chen, F.K., Zhai, M.G., 2005. Sm–Nd and SHRIMP U–Pb zircon geochronology of high-pressure granulites in the Sanggan area, North China Craton: timing of Paleoproterozoic continental collision. J. Asian Earth Sci. 24(5), 629–642.

Guo, Z., J. Zhang, Z. Yu, 1994, The evolutional characteristics of structure of the oil and gas bearing areas in Ordos massif: Petrol. Explor. Dev. v. 21, no. 2, p. 22 –29.

Guo, Z., Ma, Y., Liu, W., Wang, L., Tian, J., Zeng, X., Ma, F., 2017. Main factors controlling the formation of basement hydrocarbon reservoirs in the Qaidam Basin, western China. J. Petrol. Sci. Eng. 149, 244–255.

Gustavsson, L., Sathre, R., 2006. Variability in energy and carbon dioxide balances of wood and concrete building materials. Build. Environ. 41 (7), 940–951.

Haberer, R.M., Mangelsdorf, K., Wilkes, H., Horsfield, B., 2006. Occurrence and palaeoenvironmental significance of aromatic hydrocarbon biomarkers in Oligocene sediments from the Mallik 5L-38 Gas Hydrate Production Research well (Canada). Org. Geochem. 37 (5), 519–538.

Hanson, A.D., Ritts, B.D., Moldowan, J.M., 2007. Organic geochemistry of oil and source rock strata of the Ordos basin, north-Central China. AAPG Bull. 91 (9), 1273–1293.

Harris, N.B., Freeman, K.H., Pancost, R.D., White, T.S., Mitchell, G.D., 2004. The character and origin of lacustrine source rocks in the Lower Cretaceous synrift section, Congo Basin, west Africa. AAPG Bull. 88(8), 1163–1184.

Harrison, T.M., Copeland, P., Kidd, W.S.F., Yin, A., 1992. Raising Tibet. Science 255, 1663–1670.

He, D., Ladd, S.N., Saunders, C.J., Mead, R.N., Jaffé, R., 2020. Distribution of n-alkanes and their d 2 H and d 13 C values in typical plants along a terrestrial-coastal-oceanic gradient. Geochim. Cosmochim. Acta 281, 31–52.

Hedges, J.I., Eglinton, G., Hatcher, P.G., Kirchman, D.L., Arnosti, C., Derenne, S., Evershed, R.P., Kögel-Knabnerh, I., Wde Leeuw, J., Littke, R., Michaelisk, W., Rullkötter, J., 2000. The molecularly-uncharacterized component of nonliving organic matter in natural environments. Org. Geochem. 31(10), 945–958.

Helz, G.R., Miller, C.V., Charnock, J.M., Mosselmans, J.F.W., Pattrick, R.A.D., Garner, C.D., Vaughan, D.J., 1996. Mechanism of molybdenum removal from the sea and its concentration in black shales: EXAFS evidence. Geochim. Cosmochim. Acta 60(19), 3631–3642.

Herb, C., Zhang, W., Koutsodendris, A., Appel, E., Fang, X., Pross, J., 2013. Environmental implications of the magnetic record in Pleistocene lacustrine sediments of the Qaidam Basin, NE Tibetan Plateau. Quatern. Int. 313, 218–229.

Herron, M.M., 1988. Geochemical classification of terrigenous sands and shales from coreor log data. J. Sediment. Petrol. 58, 820–829.

Hollander, D.J., McKenzie, J. A., 1991. CO2 control on carbon-isotope fractionation during aqueous photosynthesis: A paleo-pCO2 barometer. Geology 19(9), 929–932.

Hopmans, E.C., Weijers, J.W., Schefuß, E., Herfort, L., Sinninghe Damsté, J.S., Schouten, S., 2004. A novel proxy for terrestrial organic matter in sediments based on branched and isoprenoid tetraether lipids. Earth Planet. Sci. Lett. 224(1–2), 107–116.

Hu, G., Li, J., Hu, S., Chen, Z., 2015. The origin of low molecular weight hydrocarbons associated with biogenic gas from the Eastern Depression in Qaidam Basin, China. B. Can. Petrol. Geol. 63 (1), 96–107.

Hu, G., Luo, X., Li, Z., Zhang, Y., Yang, C., Li, J., Ni, Y.Y., Tao, X., 2010. Geochemical characteristics and origin of light hydrocarbons in biogenic gas. Sci. China-Earth Sci. 53, 832–843.

Huang, D., Shang, H., Li, J., 1984. Advances in theoretical research on continental oil generation in China, Beijing Petroleum Symposium 20-24th Sept. 1984, Beijing China, Preprint 38 p.

Huang, H., Zhang, S., Su, J., 2015. Pyrolytically derived polycyclic aromatic hydrocarbons in marine oils from the Tarim Basin, NW China. Energ. Fuel 29, 5578–5586.

Huang, W.Y., Meinschein, W.G., 1979. Sterols as ecological indicators. Geochim. Cosmochim. Acta 43, 739–745.

Huc, A.Y., 1988. Aspects of depositional processes of organic matter in sedimentary basins. In: Organic Geochemistry in Petroleum Exploration (pp. 263–272). Pergamon.

Hughes, W.B., 1984. Use of thiophenic organic sulphur compounds in characterizing of oils derived from carbonate versus siliciclastic sources. In: Palacas, G. (Ed.), Petroleum Geochemistry and Source Rock Potential of Carbonate Rocks, vol. 18. AAPG Studies in Geology, pp. 181–196.

Hughes, W.B., Holba, A.G., Dzou, L.I.P., 1995. The ratio of dibenzothiophene to phenanthrene and pristane to phytane as indicators of depositional environment and lithology of petroleum source rocks. Geochim. Cosmochim. Acta 59, 3581–3598.

Hunt, J.M., 1979. Petroleum Geochemistry and Geology. New York: Freman. 261–273

Hunt, J.M., 1996. Petroleum Geochemistry and Geology. W.H. Freeman and Company, New York.

Hutchinson, G. E., 1957. A Treatise on Limnology I -- Geography, Physics and Chemistry Wiley New York, 1015 p.

ICCP, 1998. The new vitrinite classification (ICCP System 1994). Fuel 77, 349–358.

ICCP, 2001. The new inertinite classification (ICCP System 1994). Fuel 80, 459–471.

ICCP, 2017. Classification of liptinite – ICCP System 1994. Int. J. Coal Geol. 169, 40–61.

Innes, H.E., Bishop, A.N., Head, I.M., Farrimond, P., 1997. Preservation and diagenesis of hopanoids in recentlacustrine sediments of Priest Pot, England. Org. Geochem. 26, 565–576.

Jahn, B.M., Auvray, B., Cornichet, J., Bai, Y.L., Shen, Q.H., Liu, D.Y., 1987. 3.5 Ga old amphibolites from eastern Hebei Province, China: field occurrence, petrography, Sm-Nd isochron age and REE geochemistry. Precambrian Res. 34(3–4), 311–346.

Jahn, B.M., Zhang, Z.Q., 1984a. Archean granulite gneisses from eastern Hebei Province, China: rare earth geochemistry and tectonic implications. Contrib. Mineral. Petr. 85(3), 224–243.

Jahn, B.M., Zhang, Z.Q., 1984b. Radiometric ages (Rb-Sr, Sm-Nd, U-Pb) and REE geochemistry of Archaean granulite gneisses from eastern Hebei province, China. In Archaean geochemistry (pp. 204–234). Springer, Berlin, Heidelberg.

Jaroszewicz, E., Bojanowski, M., Marynowski, L., Łoziński, M., Wysocka, A., 2018. Paleoenvironmental conditions, source and maturation of Neogene organic matter from the siliciclastic deposits of the Orava-Nowy Targ Basin. Int. J. Coal Geol. 169 196, 288–301.

Jarvie, D.M., 2012. Shale resource systems for oil and gas: part 1—shale-gas resource systems. In: AAPG Memoir, pp. 69–87.

Jarvie, D.M., Hill, R.J., Ruble, T.E., Pollastro, R.M., 2007. Unconventional shale-gas systems: the Mississippian Barnett Shale of north-central Texas as one model for thermogenic shale-gas assessment. AAPG Bull. 91 (4), 475–499.

Ji, L., Zhang, T., Milliken, K.L., Qu, J., Zhang, X., 2012. Experimental investigation of main controls to methane adsorption in clay-rich rocks. Appl. Geochem. 27 (12), 2533–2545.

Ji, L.M., Meng, F.W., 2006. Palynology of Yanchang Formation of Middle and late Triassic in Eastern Gansu Province and its paleoclimatic significance. J. China Univ. Geosci. 17, 209–220.

Ji, L.M., Yan, K., Meng, F.W., Zhao, M., 2010. The oleaginous Botryococcus from the Triassic Yanchang Formation in Ordos Basin, Northwestern China, Morphology and its paleoenvironmental significance. J. Asian Earth Sci. 38, 175–185.

Jian, X., Guan, P., Zhang, W., Feng, F., 2013. Geochemistry of Mesozoic and Cenozoic sediments in the northern Qaidam basin, northeastern Tibetan Plateau: implications for provenance and weathering. Chem. Geol. 360, 74–88.

Jiang, C., Alexander, R., Kagi, R.I., Murray, A.P., 1998. Polycyclic aromatic hydrocarbons in ancient sediments and their relationships to palaeoclimate. Org. Geochem. 29, 1721–1735.

Jiang, D., 1988. Spores and pollen in oils as indicators of lacustrine source rocks. Geological Society, London, Special Publications, 40(1), 159–169.

Jiang, D.X., Robbins, E.I., 2000. Quaternary palynofloras and paleoclimate of the Qaidam Basin, Qinghai Province, northwestern China. Palynology 24, 95–112.

Jiang, L., George, S.C., 2019. Biomarker signatures of Upper cretaceous Latrobe Group petroleum source rocks, Gippsland Basin, Australia: distribution and geological significance of aromatic hydrocarbons. Org. Geochem. 138, 103905.

Jones, B., Manning, D.A.C., 1994. Comparison of geochemical indices used for the interpretation of palaeoredox conditions in ancient mudstones. Chem. Geol. 111, 111–129.

Katz, B., Lin, F., 2014. Lacustrine basin unconventional resource plays: key differences. Mar. Petrol. Geol. 56, 255–265.

Katz, B.J., 1983. Limitations of 'Rock-Eval'pyrolysis for typing organic matter. Org. Geochem. 4 (3–4), 195–199.

Katz, B.J., 2001. Lacustrine basin hydrocarbon exploration-current thoughts. J. Paleolimnol. 26, 161–179.

Kenig, F., 2000. C16–C29 homologous series of monomethylalkanes in the pyrolysis products of a Holocene microbial mat. Org. Geochem. 31 (2–3), 237–241.

Killops, S., Killops, V., 2005. Introduction to Organic Geochemistry, second ed. Blackwell Publishing, Oxford.

Killops, S.D., Massoud, M.S., 1992. Polycyclic aromatic-hydrocarbons of pyrolytic origin in ancient sediments - evidence for Jurassic vegetation fires. Org. Geochem. 18, 1–7.

Kim, J.G., Jung, M.Y., Park, S.J., Rijpstra, W.I.C., Sinninghe Damsté, J.S., Madsen, E. L., Min, D., Kim, J.S., Kim, G.J., Rhee, S. K., 2012. Cultivation of a highly enriched ammonia-oxidizing archaeon of thaumarchaeotal group I. 1b from an agricultural soil. Environment. Microbiol. 14(6), 1528–1543.

Kim, J.H., Schouten, S., Hopmans, E.C., Donner, B., Sinninghe Damsté, J.S., 2008. Global sediment core-top calibration of the TEX86 paleothermometer in the ocean. Geochim. Cosmochim. Acta 72(4), 1154–1173.

Kolattukudy, P.E. (Ed.), 1976. Chemistry and Biochemistry of Natural Waxes. Elsevier, Amsterdam, p. 459.

Köster, J., Van Kaam-Peters, H.M., Koopmans, M.P., De Leeuw, J.W., Sinninghe Damsté, J.S., 1997. Sulphurisation of homohopanoids: effects on carbon number distribution, speciation, and 22s22r epimer ratios. Geochim. Cosmochim. Acta 61 (12), 2431–2452.

Kröner, A., Wilde, S. A., Li, J. H., Wang, K. Y., 2005a. Age and evolution of a late Archean to Paleoproterozoic upper to lower crustal section in the Wutaishan/Hengshan/Fuping terrain of northern China. J. Asian Earth Sci. 24(5), 577–595.

Kröner, A., Wilde, S. A., O'Brien, P. J., Li, J. H., Passchier, C. W., Walte, N. P., and Liu, D. Y., 2005b. Field relationships, geochemistry, zircon ages and evolution of a late Archaean to Palaeoproterozoic lower crustal section in the Hengshan Terrain of northern China. Acta Geol. Sin. 79(5), 605–629.

Krooss, B.V., Van Bergen, F., Gensterblum, Y., Siemons, N., Pagnier, H.J.M., David, P., 2002. High-pressure methane and carbon dioxide adsorption on dry and moistureequilibrated Pennsylvanian coals. Int. J. Coal Geol. 51 (2), 69–92.

Kruge, M.A., Hubert, J.F., Bensley, D.F., Crelling, J.C., Akes, R.J., 1990. Organic geochemistry of a lower Jurassic synrift lacustrine sequence, Hartford Basin, Connecticut, USA. Org. Geochem. 16, 689–701.

Krull, E., Haynes, D., Lamontagne, S., Gell, P., McKirdy, D., Hancock, G., McGowan, J., Smernik, R., 2009. Changes in the chemistry of sedimentary organic matter within the Coorong over space and time. Biogeochemistry 92 (1–2), 9.

Kunz, O., Wagner, W., 2012. The GERG-2008 wide-range equation of state for natural gases and other mixtures: an expansion of GERG-2004. J. Chem. Eng. Data 57 (11), 3032–3091.

Kusky, T., Li, J., Santosh, M., 2007. The Paleoproterozoic North Hebei orogen: North China craton's collisional suture with the Columbia supercontinent. Gondwana Res. 12(1–2), 4–28.

Kusky, T.M., Li, J., 2003. Paleoproterozoic tectonic evolution of the North China Craton. J. Asian Earth Sci. 22(4), 383–397.

Kusky, T.M., Li, J.H., Tucker, R.D., 2001. The Archean Dongwanzi ophiolite complex, North China Craton: 2.505-billion-year-old oceanic crust and mantle. Science, 292(5519), 1142–1145.

Kusky, T.M., Li, Z.H., Glass, A., Huang, H.A., 2004. Archean ophiolites and ophiolite fragments of the North China craton. Precambrian ophiolites and related rocks. Developments in Precambrian Geology, 13, 223–274.

Kutzbach, J.E., Prell, W.L., Ruddiman, W.F., 1993. Sensitivity of Eurasian climate to surface uplift of the Tibetan Plateau. J. Geol. 101(2), 177–190.

Kvalheim, O.M., Christy, A.A., Telnæs, N., Bjørseth, A., 1987. Maturity determination of organic matter in coals using the methylphenanthrene distribution. Geochim. Cosmochim. Acta 51 (7), 1883–1888.

Kvenvolden, K.A., 1988. Methane hydrate: a major reservoir of carbon in the shallow geosphere. Chem. Geol. 71, 41–51.

Lafargue, E., Marquis, F., Pillot, D., 1998. Rock-Eval 6 applications in Hydrocarbon Exploration, production, and Soil Contamination Studies. Oil Gas Sci. Tech. 53 (4), 421–437.

Lamb, A.L., Wilson, G.P., Leng, M.J., 2006. A review of coastal palaeoclimate and relative sea-level reconstructions using δ13C and C/N ratios in organic material. Earth-Sci. Rev. 75(1–4), 29–57.

Land, L.S., Mack, L.E., Milliken, K.L., Leo Lynch, F., 1997. Burial diagenesis of argillaceous sediment, south Texas Gulf of Mexico sedimentary basin: A reexamination. Geol. Soc. Am. Bull. 109(1), 2–15.

Lee, C., Love, G.D., Jahnke, L.L., Kubo, M.D., Des Marais, D.J., 2019. Early diagenetic sequestration of microbial mat lipid biomarkers through covalent binding into insoluble macromolecular organic matter (IMOM) as revealed by sequential chemolysis and catalytic hydropyrolysis. Org. Geochem. 132, 11–22.

Lehmkuhl, F., Haselein, F., 2000. Quaternary paleoenvironmental change on the Tibetan Plateau and adjacent areas (Western China and Western Mongolia). Quat. Int. 65, 121–145.

Lemons, D.R., Chan, M.A., 1999. Facies architecture and sequence stratigraphy of fine-grained lacustrine deltas along the eastern margin of late Pleistocene Lake Bonneville, northern Utah and southern Idaho. AAPG Bull. 83(4), 635–665.

Leventhal, J.S., 1983. An interpretation of carbon and sulfur relationships in Black Sea sediments as indicators of environments of deposition. Geochim. Cosmochim. Acta 47 (1), 133–137.

Lewan, M.D., 1994. Assessing natural oil expulsion from source rocks by laboratory pyrolysis. In: Magoon, L.B., Dow, W.G. (Eds.), The Petroleum System – From Source to Trap. AAPG Memoir, vol. 60, pp. 201–210.

Li, C., Zhu, S., Zhu, S., 1984. Sedimentary system and oil-bearing features of the small intermontane rift basin of Biyang, Beijing Petroleum Symposium 20-24 Sept. 1984, Beijing China Preprint 18 p.

Li, D., Li, R., Zhu, Z., Wu, X., Cheng, J., Liu, F., Zhao, B., 2017. Origin of organic matter and paleo-sedimentary environment reconstruction of the Triassic oil shale in Tongchuan City, southern Ordos Basin (China). Fuel 208, 223–235.

Li, J., Kusky, T., 2007. A late Archean foreland fold and thrust belt in the North China Craton: implications for early collisional tectonics. Gondwana Res. 12(1–2), 47–66.

Li, J., Pancost, R.D., Naafs, B.D. A., Yang, H., Zhao, C., Xie, S., 2016. Distribution of glycerol dialkyl glycerol tetraether (GDGT) lipids in a hypersaline lake system. Org. Geochem. 99, 113–124.

Li, J., Zhou, S., Li, Y., Ma, Y., Yang, Y., Li, C., 2016. Effect of organic matter on pore structure of mature lacustrine organic-rich shale: a case study of the Triassic yanchang shale, Ordos basin, China. Fuel 185, 421–431.

Li, J.H., Kroner, A., Xianglin, Q., Brien, P.O., 2000. Tectonic evolution of an Early Precambrian high-pressure granulite belt in the North China Craton. Acta Geol. Sin.-Engl. 74(2), 246–258.

Li, J.H., Qian, X.L., Huang, X.N., Liu, S.W., 2000a. The tectonic framework of the basement of North China Craton and its implication for the early Precambrian cratonization. Acta Petrol. Sin. 16(1), 1–10.

Li, M., Chen, Z., Cao, T., Ma, X., Liu, X., Li, Z., Jiang, Q., Wu, S., 2018. Expelled oils and their impacts on rock-eval data interpretation, Eocene Qianjiang Formation in Jianghan Basin, China. Int. J. Coal Geol. 191, 37–48.

Li, M., Wang, T., Liu, J., Zhang, M., Lu, H., Ma, Q., Gao, L., 2009. Biomarker 17α (H)-diahopane: a geochemical tool to study the petroleum system of a Tertiary lacustrine basin, Northern South China Sea. Appl. Geochem. 24 (1), 172–183.

Li, Q., Wu, S., Xia, D., You, X., Zhang, H., Lu, H., 2020. Major and trace element geochemistry of the lacustrine organic-rich shales from the Upper Triassic Chang 7 Member in the southwestern Ordos Basin, China: Implications for paleoenvironment and organic matter accumulation. Mar. Petrol. Geol. 111, 852–867.

Li, S.,S. Yang, T. Jerzykiewicz, 1995, Upper Triassic–Jurassic foreland sequences of the Ordos basin in China, in S. L. Dorobek and G. M. Ross, eds., Stratigraphic evolution of foreland basins: SEPM Special Publication 52, p. 233–241.

Lima, A.L.C., Farrington, J.W., Reddy, C.M., 2005. Combustion-derived polycyclic aromatic hydrocarbons in the environment—a review. Environ. Forensic 6, 109–131.

Lindgren, H., Jacobsen, H., Jakobsen, H.J., 1991. Diagenetic structural transformations in North Sea Jurassic illite/smectite. Clay Clay Miner. 39 (1), 54–69.

Lisiecki, L.E., Raymo, M.E., 2005. A Pliocene‐Pleistocene stack of 57 globally distributed benthic δ 18O records. Paleoceanography, 20(1), PA1003.

Littke, R., 1993. Deposition of organic matter-rich sediments. In: Deposition, Diagenesis and Weathering of Organic Matter-Rich Sediments, pp. 12–45.

Littke, R., Baker, D.R., Rullkötter, J., 1997. "Deposition of Petroleum Source rocks." Petroleum and Basin Evolution. Springer, Berlin, Heidelberg, pp. 271–333.

Littke, R., Krooss, B., Uffmann, A.K., Schulz, H.M., Horsfield, B., 2011. Unconventional gas resources in the Paleozoic of Central Europe. Oil Gas Sci. Technol. Revue d'IFP Energies nouvelles 66 (6), 953–977.

Liu, D., Yuan, P., Liu, H., Li, T., Tan, D., Yuan, W., He, H., 2013. High-pressure adsorption of methane on montmorillonite, kaolinite and illite. Appl. Clay Sci. 85 (1), 25–30.

Liu, H., Yang, H., Cao, Y., Leng, Q., Liu, W., 2018. Inter-molecular variations of fatty acid δD in algae and submerged plants from the north-eastern Tibetan Plateau. Org. Geochem. 122, 17–28.

Liu, J., Algeo, T.J., 2020. Beyond redox: control of trace-metal enrichment in anoxic marine facies by watermass chemistry and sedimentation rate. Geochim. Cosmochim. Acta 287, 296–317

Liu, S., Pan, Y., Xie, Q., Zhang, J., Li, Q., 2004. Archean geodynamics in the Central Zone, North China Craton: constraints from geochemistry of two contrasting series of granitoids in the Fuping and Wutai complexes. Precambrian Res. 130(1–4), 229–249.

Liu, S., Zhao, G., Wilde, S.A., Shu, G., Sun, M., Li,Q., Tian, W., Zhang, J., 2006. Th–U–Pb monazite geochronology of the Lüliang and Wutai Complexes: constraints on the tectonothermal evolution of the Trans-North China Orogen. Precambrian Res. 148(3–4), 205–224.

Liu, W., Li, X., An, Z., Xu, L., Zhang, Q., 2013. Total organic carbon isotopes: a novel proxy of lake level from Lake Qinghai in the Qinghai–Tibet Plateau, China. Chem. Geol. 347, 153–160.

Liu, W., Wang, H., Zhang, C. L., Liu, Z., He, Y., 2013. Distribution of glycerol dialkyl glycerol tetraether lipids along an altitudinal transect on Mt. Xiangpi, NE Qinghai-Tibetan Plateau, China. Org. Geochem. 57, 76–83.

Liu, Z., Pagani, M., Zinniker, D., DeConto, R., Huber, M., Brinkhuis, H., Shah, S.R., Leckie, R.M., Pearson, A., 2009. Global cooling during the Eocene-Oligocene climate transition. Science 323(5918), 1187–1190.

Loomis, S.E., Russell, J.M., Ladd, B., Street-Perrott, F.A., Sinninghe Damsté, J.S., 2012. Calibration and application of the branched GDGT temperature proxy on East African lake sediments. Earth Planet. Sci. Lett. 357, 277–288.

Loomis, S.E., Russell, J.M., Sinninghe Damsté, J.S., 2011. Distributions of branched GDGTs in soils and lake sediments from western Uganda: implications for a lacustrine paleothermometer. Org. Geochem. 42(7), 739–751.

Lückge, A., Boussafir, M., Lallier-Vergès, E., Littke, R., 1996. Comparative study of organic matter preservation in immature sediments along the continental margins of Peru and Oman. Part I: results of petrographical and bulk geochemical data. Org. Geochem. 24 (4), 437–451.

Lückge, A., Ercegovac, M., Strauss, H., Littke, R., 1999. Early diagenetic alteration of organic matter by sulfate reduction in Quaternary sediments from the northeastern Arabian Sea. Mar. Geol. 158 (1–4), 1–13.

Luo, Z., Su, Q., Wang, Z., Heermance, R.V., Garzione, C., Li, M., Ren, X., Song, Y., Nie, J., 2018. Orbital forcing of Plio-Pleistocene climate variation in a Qaidam Basin lake based on paleomagnetic and evaporite mineralogic analysis. Palaeogeogr. Palaeoclimatol. Palaeoecol. 510, 31–39.

MacIlvaine, J.C., Ross, D.A., 1973. Surface sediments of the Gulf of Panama. J. Sediment. Res. 43(1), 215–223.

Mackenzie, A., Patience, R., Maxwell, J., Vandenbroucke, M., Durand, B., 1980. Molecular parameters of maturation in the Toarcian shales, Paris Basin, France—I. changes in the configurations of

acyclic isoprenoid alkanes, steranes and triterpanes. Geochim. Cosmochim. Acta 44, 1709–1721.

Macquaker, J.H., Adams, A.E., 2003. Maximizing information from fine-grained sedimentary rocks: An inclusive nomenclature for mudstones. J. Sediment. Res. 73(5), 735–744.

Macquaker, J.H., Bentley, S.J., Bohacs, K.M., 2010b. Wave-enhanced sediment-gravity flows and mud dispersal across continental shelves: Reappraising sediment transport processes operating in ancient mudstone successions. Geology 38(10), 947–950.

Macquaker, J.H., Keller, M.A., Davies, S.J., 2010a. Algal blooms and "marine snow": Mechanisms that enhance preservation of organic carbon in ancient fine-grained sediments. J. sediment. Res. 80(11), 934–942.

Mastalerz, M., Schimmelmann, A., Drobniak, A., Chen, Y., 2013. Porosity of Devonian and Mississippian New Albany Shale across a maturation gradient: insights from organic petrology, gas adsorption, and mercury intrusion. AAPG Bull. 97 (10), 1621–1643.

Mattavelli, L., Ricchiuto, T., Grignani, D., Schoell, M., 1983. Geochemistry and habitat of natural gases in Po basin, northern Italy. AAPG Bull. 67 (12), 2239–2254.

McLennan, S.M., 1993. Weathering and global denudation. J. Geol. 101, 295–303.

Mead, R., Xu, Y., Chong, J., Jaffé, R., 2005. Sediment and soil organic matter source assessment as revealed by the molecular distribution and carbon isotopic composition of n-alkanes. Org. Geochem. 36 (3), 363–370.

Merkel, A., Fink, R., Littke, R., 2015. The role of pre-adsorbed water on methane sorption capacity of Bossier and Haynesville shales. Int. J. Coal Geol. 147, 1–8.

Merkel, A., Fink, R., Littke, R., 2016. High pressure methane sorption characteristics of lacustrine shales from the Midland Valley Basin. Scotland. Fuel 182, 361–372.

Meyers, P., Ishiwatari, R., 1993. Lacustrine organic geochemistry-an overview of indicators of organic matter sources and diagenesis in lake sediments. Org. Geochem. 20, 867–900.

Meyers, P.A., 1997. Organic geochemical proxies of paleoceanographic, paleolimnologic, and paleoclimatic processes. Org. Geochem. 27(5–6), 213–250.

Moldowan, J.M., Dahl, J., Huizinga, B.J., Fago, F.J., Hickey, L.J., Peakman, T.M., Taylor, D.W., 1994. The molecular fossil record of oleanane and its relation to angiosperms. Science 265, 768–771.

Moldowan, J.M., Sundararaman, P., Schoell, M., 1986. Sensitivity of biomarker properties to depositional environment and/or source input in the lower Toarcian of SW-Germany. Org. Geochem. 10, 915–926.

Molnar, P., England, P., Martinod, J., 1993. Mantle dynamics, uplift of the Tibetan Plateau, and the Indian monsoon. Rev. Geophys. 31(4), 357–396.

Montgomery, S.L., Jarvie, D.M., Bowker, K.A., Pollastro, R.M., 2005. Mississippian Barnett Shale, Fort Worth Basin, north-central Texas: gas-shale play with multi–-trillion cubic foot potential. AAPG Bull. 89 (2), 155–175.

Moore, T.A., 2012. Coalbed methane: a review. Int. J. Coal Geol. 101, 36–81.

Myers, A.L., Monson, P.A., 2002. Adsorption in porous materials at high pressure: theory and experiment. Langmuir 18 (26), 10261–10273.

Nakamura, H., Sawada, K., Takahashi, M., 2010. Aliphatic and aromatic terpenoid biomarkers in cretaceous and Paleogene angiosperm fossils from Japan. Org. Geochem. 41 (9), 975–980.

Nesbitt, H. W., Young, G. M., 1984. Prediction of some weathering trends of plutonic and volcanic rocks based on thermodynamic and kinetic considerations. Geochim. Cosmochim. Acta 48(7), 1523–1534.

Nesbitt, H.W., 1979. Mobility and fractionation of rare earth elements during weathering of a granodiorite. Nature 279, 206–210.

Nesbitt, H.W., Markovics, G., Price, R.C., 1980. Chemical processes affecting alkalis and alkaline earths during continental weathering. Geochim. Cosmochim. Acta 44, 1659–1666.

Nesbitt, H.W., Young, G.M., 1982. Early Proterozoic climates and plate motions inferred from major element chemistry of lutites. Nature 299, 715–717.

Nesbitt, H.W., Young, G.M., 1984. Prediction of some weathering trends of plutonic and volcanic rocks based on thermodynamic and kinetic considerations. Geochim. Cosmochim. Acta 48(7), 1523–1534.

Nesbitt, H.W., Young, G.M., 1989. Formation and diagenesis of weathering profiles. J. Geol. 97, 129–147.

Ni, Y., Dai, J., Zou, C., Liao, F., Shuai, Y., Zhang, Y., 2013. Geochemical characteristics of biogenic gases in China. Int. J. Coal Geol. 113, 76–87.

Nichols, J.E., Booth, R.K., Jackson, S.T., Pendall, E.G., Huang, Y., 2006. Paleohydrologic reconstruction based on n-alkane distributions in ombrotrophic peat. Org. Geochem. 37, 1505–1513.

Nytoft, H.P., Lutnæs, B.F., Johansen, J.E., 2006. 28-Nor-spergulanes, a novel series of rearranged hopanes. Org. Geochem. 37 (7), 772–786.

Olgun, N., Duggen, S., Andronico, D., Kutterolf, S., Croot, P. L., Giammanco, S., Censi, P., Randazzo, L. (2013). Possible impacts of volcanic ash emissions of Mount Etna on the primary productivity in the oligotrophic Mediterranean Sea: Results from nutrient-release experiments in seawater. Mar. Chem. 152, 32–42.

Oros, D.R., Standley, L.J., Chen, X., Simoneit, B.R., 1999. Epicuticular wax compositions of predominant conifers of western North America. Zeitschrift für Naturforschung C 54 (1–2), 17–24.

Oshima, M., Suzuki, K., Yoneda, J., Kato, A., Kida, M., Konno, Y., Tenma, N., 2019. Lithological properties of natural gas hydrate–bearing sediments in pressure-cores recovered from the Krishna–Godavari Basin. Mar. Petrol. Geol. 108, 439–470.

Otto, A., Wilde, V., 2001. Sesqui-, di-, and triterpenoids as chemosystematic markers in extant conifers—a review. Bot. Rev. 67, 141–238.

Pan, S., Horsfield, B., Zou, C., Yang, Z., Gao, D., 2017. Statistical analysis as a tool for assisting geochemical interpretation of the Upper Triassic Yanchang Formation, Ordos Basin, Central China. Int. J. Coal Geol. 173, 51–64.

Pang, X., Zhao, W., Su, A., Zhang, S., Li, M., Dang, Y., Xu, F., Zhou, R., Zhang, D., Xu, Z., Guan, Z., Chen, J., Li, S., 2005. Geochemistry and origin of the giant Quaternary shallow gas accumulations in the eastern Qaidam Basin, NW China. Org. Geochem. 36, 1636–1649.

Pawlowska, M.M., Butterfield, N.J., Brocks, J.J., 2013. Lipid taphonomy in the Proterozoic and the effect of microbial mats on biomarker preservation. Geology 41 (2), 103–106.

Pearson, E.J., Juggins, S., Talbot, H.M., Weckström, J., Rosén, P., Ryves, D.B., Roberts, S.J., Schmidt, R., 2011. A lacustrine GDGT-temperature calibration from the Scandinavian Arctic to Antarctic: renewed potential for the application of GDGT-paleothermometry in lakes. Geochim. Cosmochim. Acta 75, 6225–6238.

Peltonen, C., Marcussen, Ø., Bjørlykke, K., Jahren, J., 2009. Clay mineral diagenesis and quartz cementation in mudstones: the effects of smectite to illite reaction on rock properties. Mar. Petrol. Geol. 26 (6), 887–898.

Pepper, A.S., Corvi, P.J., 1995. Simple kinetic models of petroleum formation. Part I: oil and gas generation from kerogen. Mar. Petrol. Geol. 12, 291–319.

Peters, K.E., Moldowan, J.M., 1991. Effects of source, thermal maturity, and biodegradation on the distribution and isomerization of homohopanes in petroleum. Org. Geochem. 17, 47–61.

Peters, K.E., Moldowan, J.M., 1993. The Biomarker Guide: Interpreting Molecular Fossils in Petroleum and Ancient Sediments. Prentice Hall, Englewood Cliffs, NJ.

Peters, K.E., Walters, C.C., Moldowan, J.M., 2005. The Biomarker Guide: Volume II Biomarkers and Isotopes in Petroleum Exploration and Earth History. Cambridge University Press, United Kingdom.

Peterse, F., Nicol, G.W., Schouten, S., Sinninghe Damsté, J.S., 2010. Influence of soil pH on the abundance and distribution of core and intact polar lipid-derived branched GDGTs in soil. Org. Geochem. 41(10), 1171–1175.

Peterse, F., van der Meer, J., Schouten, S., Weijers, J.W., Fierer, N., Jackson, R.B., Kim, J.H., Sinninghe Damsté, J.S., 2012. Revised calibration of the MBT–CBT paleotemperature proxy based on branched tetraether membrane lipids in surface soils. Geochim. Cosmochim. Acta 96, 215–229.

Peterse, F., van Der Meer, M.T.J., Schouten, S., Jia, G., Ossebaar, J., Blokker, J., Sinninghe Damsté, J.S., 2009. Assessment of soil n-alkane δD and branched tetraether membrane lipid distributions as tools for paleoelevation reconstruction. Biogeosciences 6(12), 2799–2807.

Peterson, B.J., Howarth, R.W., 1987. Sulfur, carbon, and nitrogen isotopes used to trace organic matter flow in the salt-marsh estuaries of Sapelo Island, Georgia 1. Limnol. Oceanog. 32(6), 1195–1213.

Picard, M.D., 1971. Classification of fine-grained sedimentary rocks. J. Sediment. Res. 41(1), 179–195.

Picard, M.D., High, L.R., 1981. Physical stratigraphy of ancient lacustrine deposits (Eds. Etheridge, F.G. and Flores, R.M.) in: Recent and Ancient Non-marine Depositional Environments: Models for Exploration, Soc. Econ. Paleontol. Mineral. Spec. Publ. No 31 pp. 233–259

Pichevin, L., Bertrand, P., Boussafr, M., Disnar, J.R., 2004. Organic matter accumulation and preservation controls in a deep-sea modern environment: an example from Namibian slope sediments. Org. Geochem. 35, 543–559.

Pickel, W., Kus, J., Flores, D., Kalaitzidis, S., Christanis, K., Cardott, B.J., MiszKennan, M., Rodrigues, S., Hentschel, A., Hamor-Vido, M., Crosdale, P., Wagner, N., I.C.C.P., 2017. Classification of liptinite–ICCP System 1994. Int. J. Coal Geol. 169, 40–61.

Polat, A., Herzberg, C., Münker, C., Rodgers, R., Kusky, T., Li, J., Fryer, B., Delaney, J., 2006. Geochemical and petrological evidence for a suprasubduction zone origin of Neoarchean (ca. 2.5 Ga) peridotites, central orogenic belt, North China craton. Geol. Soc. Am. Bull. 118(7–8), 771–784.

Polat, A., Kusky, T., Li, J., Fryer, B., Kerrich, R., Patrick, K., 2005. Geochemistry of Neoarchean (ca. 2.55–2.50 Ga) volcanic and ophiolitic rocks in the Wutaishan greenstone belt, central orogenic belt, North China craton: implications for geodynamic setting and continental growth. Geol. Soc. Am. Bull. 117(11–12), 1387–1399.

Polat, A., Li, J., Fryer, B., Kusky, T., Gagnon, J., Zhang, S., 2006. Geochemical characteristics of the Neoarchean (2800–2700 Ma) Taishan greenstone belt, North China Craton: evidence for plume–craton interaction. Chem. Geol. 230(1–2), 60–87.

Pole, M., Wang, Y., Bugdaeva, E.V., Dong, C., Tian, N., Li, L., Zhou, N., 2016. The rise and demise of Podozamites in East Asia—an extinct conifer life style. Palaeogeogr. Palaeoclimatol. Palaeoecol. 464, 97–109.

Powell, T.G., 1986. Petroleum geochemistry and depositional setting of lacustrine source rocks. Mar. Petrol. Geol. 3(3), 200–219.

Powers, L., Werne, J.P., Vanderwoude, A.J., Sinninghe Damsté, J.S., Hopmans, E.C., Schouten, S., 2010. Applicability and calibration of the TEX86 paleothermometer in lakes. Org. Geochem. 41(4), 404–413.

Preston, J.C., Edwards, D.S., 2000. The petroleum geochemistry of oils and source rocks from the northern Bonaparte Basin, offshore northern Australia. The APPEA J. 40 (1), 257–282.

Prinz, L., Zieger, L., Littke, R., McCann, T., Lokay, P., Asmus, S., 2017. Syn-and postdepositional sand bodies in lignite–the role of coal analysis in their recognition. A study from the Frimmersdorf Seam, Garzweiler open-cast mine, western Germany. Int. J. Coal Geol. 179, 173–186.

Qiao, J., Baniasad, A., Zieger, L., Zhang, C., Luo, Q., Littke, R., 2021b. Paleo-depositional environment, origin and characteristics of organic matter of the Triassic Chang 7 Member of the Yanchang Formation throughout the mid-western part of the Ordos Basin, China. Int. J. Coal Geol. 237, 103636.

Qiao, J., Baniasad, A., Zieger, L., Zhang, C., Luo, Q., Littke, R., 2021a. High microbial gas potential of Pleistocene lacustrine deposits in the central Qaidam Basin, China: An organic geochemical and petrographic assessment. Int. J. Coal Geol. 103818.

Qiao, J., Littke, R., Zieger, L., Jiang, Z., Fink, R., 2020. Controls on gas storage characteristics of Upper Paleozoic shales from the southeastern Ordos Basin. Mar. Petrol. Geol. 117, 104377.

Qiu, N., Kang, Y., Jin, Z., 2003. Temperature and pressure field in the Tertiary succession of the western Qaidam basin, Northeast Qinghai-Tibet Plateau, China. Mar. Petrol. Geol. 20 (5), 493–507.

Raberg, J.H., Harning, D.J., Crump, S.E., de Wet, G., Blumm, A., Kopf, S., Geirsdóttir, Á., Miller, G.H., Sepúlveda, J., 2021. Revised fractional abundances and warm-season temperatures substantially improve brGDGT calibrations in lake sediments. Biogeosciences 18(12), 3579–3603.

Radke, M., 1984. Relationship between rank and composition of aromatic hydrocarbons for coals of different origins. Org. Geochem. 6 (84), 423–430.

Radke, M., 1988. Application of aromatic compounds as maturity indicators in source rocks and crude oils. Mari. Petrol. Geol. 5 (3), 224–236.

Radke, M., Rullkötter, J., Vriend, S.P., 1994. Distribution of naphthalenes in crude oils from the Java Sea: source and maturation effects. Geochim. Cosmochim. Acta 58 (17), 3675–3689.

Radke, M., Vriend, S.P., Ramanampisoa, L.R., 2000. Alkyldibenzofurans in terrestrial rocks: influence of organic facies and maturation. Geochim. Cosmochim. Acta 64 (2), 275–286.

Radke, M., Welte, D.H., 1983. The methylphenanthrene index (MPI): a maturity parameter based on aromatic hydrocarbons. In: Bjorøy, M., Albrecht, C., Cornford, C., et al. (Eds.), Adv. Org. Geochem., 10 New York, USA, John Wiley and Sons, pp. 504–512.

Radke, M., Welte, D.H., Willsch, H., 1986. Maturity parameters based on aromatic hydrocarbons: Influence of the organic matter type. Org. Geochem. 10 (1–3), 51–63.

Radke, M., Willsch, H., Leythaeuser, Teichmüller, 1982. Aromatic compounds of coal; relation of distribution pattern to rank. Geochim. Cosmochim. Acta 46, 1831–1848.

Raji, M., Gröcke, D.R., Greenwell, H.C., Gluyas, J.G., Cornford, C., 2015. The effect of interbedding on shale reservoir properties. Mar. Petrol. Geol. 67, 154–169.

Ramstein, G., Fluteau, F., Besse, J., Joussaume, S., 1997. Effect on orogeny, plate motion and land–sea distribution on Eurasian climate change over the past 30 million years. Nature 386, 788–795.

Randazzo, L., 2013. Possible impacts of volcanic ash emissions of Mount Etna on the primary productivity in the oligotrophic Mediterranean Sea: results from nutrientrelease experiments in seawater. Mar. Chem. 152, 32–42.

Rashid, M.A., 1985. Geochemistry of Marine Humic Compounds. Springer-Verlag, New York

Raymo, M.E., Ruddiman, W.F., 1992. Tectonic forcing of late Cenozoic climate. Nature 359(6391), 117–122.

Rea, D.K., Snoeckx, H., Joseph, L.H., 1998. Late Cenozoic eolian deposition in the North Pacific: Asian drying, Tibetan uplift, and cooling of the northern hemisphere. Paleoceanography 13(3), 215–224.

Renaut, R.W., Owen, R.B., Jones, B., Tiercelin, J.J., Tarits, C., Ego, J.K., Konhauser, K.O., 2013. Impact of Lake-level changes on the formation of thermogene travertine in continental rifts: evidence from Lake Bogoria, Kenya Rift Valley. Sedimentology 60, 428–468.

Requejo, A.G., Hieshima, G.B., Hsu, C.S., McDonald, T.J., Sassen, R., 1997. Short-chain (C21 and C22) diasteranes in petroleum and source rocks as indicators of maturity and depositional environment. Geochim. Cosmochim. Acta 61, 2653–2667.

Rexer, T.F., Mathia, E.J., Aplin, A.C., Thomas, K.M., 2014. High-pressure methane adsorption and characterization of pores in Posidonia shales and isolated kerogens. Energ. Fuel. 28 (5), 2886–2901.

Riboulleau, A., Schnyder, J., Riquier, L., Lefebvre, V., Baudin, F., Deconinck, J.F., 2007. Environmental change during the early cretaceous in the Purbeck-type Durlston Bay section (Dorset, Southern England): a biomarker approach. Org. Geochem. 38, 1804–1823.

Rice, D.D., Claypool, G.E., 1981. Generation, accumulation and resource potential of biogenic gas. AAPG Bull. 65, 5–25.

Rieser, A.B., Bojar, A., Neubauer, F., Genser, J., Liu, Y., Ge, X.-H., Friedl, G., 2009. Monitoring Cenozoic climate evolution of northeastern Tibet: stable isotope constraints from the western Qaidam Basin, China. Int. J. Earth Sci. 98, 1063–1075.

Rippen, D., Littke, R., Bruns, B., Mahlstedt, N., 2013. Organic geochemistry and petrography of lower cretaceous Wealden black shales of the Lower Saxony Basin: the transition from lacustrine oil shales to gas shales. Org. Geochem. 63, 18–36.

Rodrigues, B., Duarte, L.V., Mendonça Filho, J.G., Santos, L.G., de Oliveira, A.D., 2016. Evidence of terrestrial organic matter deposition across the early Toarcian recorded in the northern Lusitanian Basin. Portugal. Int. J. Coal Geol. 168, 35–45.

Rohmer, M., Ourisson, G., 1976. Dérivés du bactériohopane: variations structurales et répartition. Tetrahedron Lett. 17 (40), 3637–3640.

Romero-Sarmiento, M.F., Riboulleau, A., Vecoli, M., Versteegh, G., Défarge efarge, Fatima, 2011. Aliphatic and aromatic biomarkers from carboniferous coal deposits at Dunbar (east lothian, Scotland): palaeobotanical and palaeoenvironmental significance. Palaeogeogr. Palaeoclimatol. Palaeoecol. 309 (3), 309–326.

Romero-Viana, L., Kienel, U., Sachse, D., 2012. Lipid biomarker signatures in a hypersaline lake on Isabel Island (Eastern Pacific) as a proxy for past rainfall anomaly (1942–2006 AD). Palaeogeogr. Palaecolimatol. Palaeoecol. 350, 49–61.

Ross, D.J., Bustin, R.M., 2007. Shale gas potential of the lower Jurassic Gordondale member, northeastern British Columbia, Canada. Bull. Can. Petrol. Geol. 55, 51–75.

Ross, D.J., Bustin, R.M., 2009. The importance of shale composition and pore structure upon gas storage potential of shale gas reservoirs. Mar. Petrol. Geol. 26 (6), 916–927.

Rowe, H.D., Loucks, R.G., Ruppel, S.C., Rimmer, S.M., 2008. Mississippian Barnett Formation, Fort Worth Basin, Texas: Bulk geochemical inferences and Mo–TOC constraints on the severity of hydrographic restriction. Chem. Geol. 257(1–2), 16–25.

Roy, D.K., Roser, B.P., 2013. Climatic control on the composition of Carboniferous–Permian Gondwana sediments, Khalaspir basin, Bangladesh. Gondwana Res. 23(3), 1163–1171.

Royden, L.H., Burchfiel, B.C., van der Hilst, R.D., 2008. The geological evolution of the Tibetan plateau. Science 321, 1054–1058.

Rullkötter, J., Littke, R., Schaefer, R.G., 1990. Characterization of organic matter in sulfur-rich lacustrine sediments of Miocene age (Nördlinger, southern Germany). In: Orr, W.L., White, C.M. (Eds.), Geochemistry of Sulfur in Fossil Fuels, ACS Symposium Series, vol. 429, pp. 149–169.

Sachse, V.F., Delvaux, D., Littke, R., 2012b. Petrological and geochemical investigations of potential source rocks of the Central Congo Basin, Democratic Republic of Congo. AAPG Bull. 96 (2), 245–275.

Sachse, V.F., Littke, R., Heim, S., Kluth, O., Schober, J., Boutib, L., Jabou, H., Perssen, F., Sindern, S., 2011. Petroleum source rocks of the Tarfaya Basin and adjacent areas. Morocco. Org. Geochem. 42 (3), 209–227.

Sachse, V.F., Littke, R., Jabour, H., Schümann, T., Kluth, O., 2012a. Late cretaceous (late Turonian, Coniacian and Santonian) petroleum source rocks as part of an OAE, Tarfaya Basin. Morocco. Mar. Petrol. Geol. 29 (1), 35–49.

Sageman, B.B., Murphy, A.E., Werne, J.P., Ver Straeten, C.A., Hollander, D.J., and Lyons, T.W., 2003. A tale of shales: the relative roles of production, decomposition, and dilution in the accumulation of organic-rich strata, Middle–Upper Devonian, Appalachian basin. Chem. Geol. 195(1–4), 229–273.

Sakurovs, R., Day, S., Weir, S., Duffy, G., 2008. Temperature dependence of sorption of gases by coals and charcoals. Int. J. Coal Geol. 73 (3–4), 250–258.

Scheidt, G., Littke, R., 1989. Comparative organic petrology of interlayered sandstones, siltstones, mudstones and coals in the Upper Carboniferous Ruhr basin, Northwest Germany, and their thermal history and methane generation. Geol. Rundsch. 78 (1), 375–390.

Schieber, J., 2011. Reverse engineering mother nature—Shale sedimentology from an experimental perspective. Sediment. Geol. 238(1–2), 1–22.

Schoell, M., 1980. The hydrogen and carbon isotopic composition of methane from natural gases of various origins. Geochim. Cosmochim. Acta 44 (5), 649–661.

Schoell, M., 1988. Multiple origins of methane in the Earth. Chem. Geol. 71 (1–3), 1–10.

Schouten, S., Hopmans, E.C., Forster, A., van Breugel, Y., Kuypers, M.M., Sinninghe Damsté, J.S., 2003. Extremely high sea-surface temperatures at low latitudes during the middle Cretaceous as revealed by archaeal membrane lipids. Geology 31(12), 1069–1072.

Schouten, S., Hopmans, E.C., Schefuß, E., Sinninghe Damsté, J.S., 2002. Distributional variations in marine crenarchaeotal membrane lipids: a new tool for reconstructing ancient sea water temperatures?. Earth Planet. Sci. Lett. 204(1–2), 265–274.

Schouten, S., Hopmans, E.C., Sinninghe Damsté, J.S., 2013. The organic geochemistry of glycerol dialkyl glycerol tetraether lipids: A review. Org. Geochem. 54, 19–61.

Seifert, W.K., Moldowan, J.M., 1978. Applications of steranes, terpanes and monoaromatics to the maturation, migration and source of crude oils. Geochim. Cosmochim. Acta 42 (1), 77–95.

Seifert, W.K., Moldowan, J.M., 1986. Use of biological markers in petroleum exploration. Methods in geochemistry and geophysics 24, 261–290.

Shabani, M., Moallemi, S.A., Krooss, B.M., Amann-Hildenbrand, A., Zamani-Pozveh, Z., Ghalavand, H., Littke, R., 2018. Methane sorption and storage characteristics of organic-rich carbonaceous rocks, Lurestan province, Southwest Iran. Int. J. Coal Geol. 186, 51–64.

Shanmugam, G., 1985. Significance of Coniferous rain Forests and Related Organic Matter in Generating Commercial Quantities of Oil, Gippsland Basin, Australia1. AAPG Bull. 69 (8), 1241–1254.

Shiea, J., Brassell, S.C., Ward, D.M., 1990. Mid-chain branched mono-and dimethyl alkanes in hot spring cyanobacterial mats: a direct biogenic source for branched alkanes in ancient sediments? Org. Geochem. 15, 223–231.

Shuai, Y., Zhang, S., Grasby, S.E., Chen, Z., Ma, D., Wang, L., Li, Z., Wei, C., 2013. Controls on biogenic gas formation in the Qaidam Basin, northwestern China. Chem. Geol. 335, 36–47.

Shuai, Y., Zhang, S., Grasby, S.E., Hou, W., Chen, Z., Huang, L., Kui, M., Xu, Y., Wang, Y., 2016. Microbial consortia controlling biogenic gas formation in the Qaidam Basin of western China. J. Geophys. Res. Biogeosci. 121, 2296–2309.

Simoneit, B.R.T., 1977. Diterpenoid compounds and other lipids in deep-sea sediments and their geochemical significance. Geochim. Cosmochim. Acta 41, 463–476.

Sinninghe Damsté, J.S., 2016. Spatial heterogeneity of sources of branched tetraethers in shelf systems: The geochemistry of tetraethers in the Berau River delta (Kalimantan, Indonesia). Geochim. Cosmochim. Acta 186, 13–31.

Sinninghe Damsté, J.S., Kenig, F., Kock-van Dalen, A.C., Rijpstra, W.I.C., Huc, A.Y., de Leeuw, J.W., 1995a. Occurrence and origin of mono-, di-and trimethylalkanes in modern and Holocene cyanobacterial mats from Abu Dhabi, United Arab Emirates. Geochim. Cosmochim. Acta 59 (14), 2999–3016.

Sinninghe Damsté, J.S., Kenig, F., Koopmans, M.P., Koster, J., Schouten, S., Hayes, J.M., De Leeuw, J.W., 1995b. Evidence for gammacerane as an indicator of water column stratification. Geochim. Cosmochim. Acta 59, 1895–1900.

Sinninghe Damsté, J.S., Ossebaar, J., Schouten, S., Verschuren, D., 2008. Altitudinal shifts in the branched tetraether lipid distribution in soil from Mt. Kilimanjaro (Tanzania): Implications for the MBT/CBT continental palaeothermometer. Org. Geochem. 39(8), 1072–1076.

Sinninghe Damsté, J.S., Schouten, S., Volkman, J.K., 2014. C27–C30 neohop-13 (18)-enes and their saturated and aromatic derivatives in sediments: Indicators for diagenesis and water column stratification. Geochim. Cosmochim. Acta 133, 402–421.

Sinninghe Damsté, J.S., Van Duin, A.C.T., Hollander, D., Kohnen, M.E.L., De Leeuw, J. W., 1995a. Early diagenesis of bacteriohopanepolyol derivatives: formation of fossil homohopanoids. Geochim. Cosmochim. Acta 59, 5141–5147.

Sircar, S., 1999. Gibbsian surface excess for gas adsorption revisited. Ind. Eng. Chem. Res. 38 (10), 3670–3682.

Song, D., He, D., Qi, X., Wang, S., Li, D., 2015a. Occurrence and composition of solid bitumens from the Bulonggoer Devonian paleo-oil reservoir, North Xinjiang, China. Org. Geochem. 83, 1–15.

Song, J., Littke, R., Maquil, R., Weniger, P., 2014. Organic facies variability in the Posidonia Black Shale from Luxembourg: Implications for thermal maturation and depositional environment. Palaeogeogr. Palaeoclimatol. Palaeoecol. 410, 316–336.

Song, J., Littke, R., Weniger, P., 2017. Organic geochemistry of the lower Toarcian Posidonia Shale in NW Europe. Org. Geochem. 106, 76–92.

Song, J., Littke, R., Weniger, P., Ostertag-Henning, C., Nelskamp, S., 2015b. Shale oil potential and thermal maturity of the lower Toarcian Posidonia Shale in NW Europe. Int. J. Coal Geol. 150, 127–153.

Stein, R., 1991. Accumulation of organic carbon in marine sediments: results from the Deep Sea Drilling Project/Ocean Drilling Program (DSDP/ODP). In: Lecture Notes in Earth Sciences, 34. Berlin Springer Verlag, p. PP5.

Stock, A.T., Littke, R., Lücke, A., Zieger, L., Thielemann, T., 2016. Miocene depositional environment and climate in western Europe: the lignite deposits of the Lower Rhine Basin, Germany. Int. J. Coal Geol. 157, 2–18.

Stow, D. A., 1981. Fine-grained sediments: Terminology. Q. J. Eng. Geol. Hydroge. 14(4), 243–244.

Strachan, M.G., Alexander, R., Kagi, R.I., 1988. Trimethylnaphthalenes in crude oils and sediments: Effects of source and maturity. Geochim. Cosmochim. Acta 52, 1255–1264.

Strixrude, L., Peacor, D.R., 2002. First-principles study of illite–smectite and implications for clay mineral systems. Nature (London) 420 (6912), 165–168.

Suess, E., 1980. Particulate organic carbon flux in the oceans—surface productivity and oxygen utilization. Nature 288 (5788), 260–263.

Summons, R., Bradley, A., Jahnke, L., Waldbauer, J., 2006. Steroids, triterpenoids and molecular oxygen. Philos. Trans. R. Soc. Lond. B 361, 951–968.

Sun, C., Zhang, C., Li, F., Wang, H., Liu, W., 2016. Distribution of branched glycerol dialkyl glycerol tetraethers in soils on the Northeastern Qinghai-Tibetan Plateau and possible production by nitrite-reducing bacteria. Science in China Series D: Earth Sci. 59(9), 1834–1846.

Sun, D., An, Z., Shaw, J., Bloemendal, J. Sun, Y., 1998. Magnetostratigraphy and palaeoclimatic significance of Late Tertiary aeolian sequences in the Chinese Loess Plateau. Geophys. J. Int. 134(1), 207–212.

Sun, D., Liu, D., Chen, M., An, Z., John, S., 1997. Magnetostratigraphy and palaeoclimate of red clay sequences from Chinese Loess Plateau. Science in China Series D: Earth Sci. 40(4), 337–343.

Sun, Q., Chu, G., Liu, M., Xie, M., Li, S., Ling, Y., Wang, X., Shi, L., Jia, G., Lü, H., 2011. Distributions and temperature dependence of branched glycerol dialkyl glycerol tetraethers in recent lacustrine sediments from China and Nepal. J. Geophys. Res.: Biogeo. 116(G1).

Sun, Z., Xie, Q., Yang, J., 1989, Ordos basin— A typical example of an unstable cratonic interior superimposed basin, in X. Zhu and W. Xu, eds., Chinese sedimentary basins: Amsterdam, Elsevier, p. 148–168.

Surdam, R. C., Stanley, K. O., 1979. Lacustrine sedimentation during the culminating phase of Eocene lake Gosiute, Wyoming (Green River Formation). Geol. Soc. Am. Bull. 90(1), 93–110.

Suttner, L. J., Dutta, P. K., 1986. Alluvial sandstone composition and paleoclimate; I, Framework mineralogy. J. Sediment. Res. 56(3), 329–345.

Tao, S., Wang, C., Du, J., Liu, L., Chen, Z., 2015. Geochemical application of tricyclic and tetracyclic terpanes biomarkers in crude oils of NW China. Mar. Petrol. Geol. 67, 460–467.

Tapponnier, P., Xu, Z., Roger, F., Meyer, B., Arnaud, N., Wittlinger, G., Yang, J., 2001. Oblique stepwise rise and growth of the Tibet Plateau. Science 294, 1671–1677.

Taylor, G.H., Teichmüller, M., Davis, A., Diessel, C.F.K., Littke, R., Robert, P., 1998a. Organic Petrology. Gerbrüder Borntraeger, Berlin, Stuttgart.

Taylor, S.R., McLennan, S.M., 1985. The Continental Crust: Its Composition and Evolution. Blackwell, Oxford. (312 pp.).

ten Haven, H.L., De Leeuw, J.W., Peakman, T.M., Maxwell, J.R., 1986. Anomalies in steroid and hopanoid maturity indices. Geochim. Cosmochim. Acta 50 (5), 853–855.

ten Haven, H.L., De Leeuw, J.W., Rullkötter, J., Sinninghe Damsté, J.S., 1987. Restricted utility of the pristane/phytane ratio as a palaeoenvironmental indicator. Nature 330 (6149), 641.

ten Haven, H.L., de Leeuw, J.W., Schenk, P.A., 1985. Organic geochemical studies of a Messinian evaporitic basin, north ern Apennines (Italy). I. Hydrocarbon biological markers for a hypersaline environments. Geochim. Cosmochim. Acta 49, 2181–2191.

Tian, Z., Chang, C., Huang, D., Wu, C., 1983. Sedimentary facies, oil generation in Meso-Cenozoic continental basins in China, Oil Gas J. 81 (20), 120–126.

Tian, Z., Q. Zhang, 1997, Lithofacies, paleogeography and hydrocarbon in Chinese petroliferous basins (in Chinese): Beijing, Chinese Geology Press, 260 p.

Tierney, J.E., Mayes, M.T., Meyer, N., Johnson, C., Swarzenski, P.W., Cohen, A.S., Russell, J.M., 2010a. Late-twentieth-century warming in Lake Tanganyika unprecedented since AD 500. Nat. Geosci. 3, 422–425.

Tierney, J.E., Russell, J.M., Eggemont, H., Hopmans, E.C., Verschuren, D., Sinninghe Damsté, J.S., 2010b. Environmental controls on branched tetraether lipid distributions in tropical East African lake sediments: a new lacustrine paleothermometer? Geochim. Cosmochim. Acta 74, 4902–4918.

Tribovillard, N.P., Algeo, T.J., Baudin, F., Riboulleau, A., 2012. Analysis of marine environmental conditions based onmolybdenum–uranium covariation—Applications to Mesozoic paleoceanography. Chem. Geol. 324, 46–58.

Tribovillard, N.P., Algeo, T.J., Lyons, T., Riboulleau, A., 2006. Trace metals as paleoredox and paleoproductivity proxies: An update. Chem. Geol. 232, 12–32.

Turcq, B., Albuquerque, A.L.S., Cordeiro, R.C., Sifeddine, A., Simoes Filho, F.F.L., Souza, A.G., Abr˜ ao, J.J., Oliveirab, F.B.L., Silvab, A.O., Capitˆ aneo, J., 2002. Accumulation of organic carbon in five Brazilian lakes during the Holocene. Sediment. Geol. 148 (1–2), 319–342.

Ufer, K., Stanjek, H., Roth, G., Dohrmann, R., Kleeberg, R., Kaufhold, 2008. Quantitative phase analysis of bentonites by the Rietveld method. Clay Clay Miner. 56 (2), 272–282.

Uffmann, A.K., Littke, R., Rippen, D., 2012. Mineralogy and geochemistry of Mississippian and lower Pennsylvanian black shales at the northern margin of the variscan mountain Belt (Germany and Belgium). Int. J. Coal Geol. 103, 92–108.

van Aarssen, B., Alexander, R., Kagi, R., 2000. Higher plant biomarkers reflectpalaeovegetation changes during Jurassic times. Geochim. Cosmochim. Acta 64, 1417–1424.

van Aarssen, B.G., Bastow, T.P., Alexander, R., Kagi, R.I., 1999. Distributions of methylated naphthalenes in crude oils: indicators of maturity, biodegradation and mixing. Org. Geochem. 30 (10), 1213–1227.

Vieth, A., Wilkes, H., 2006. Deciphering biodegradation effects on light hydrocarbons in crude oils using their stable carbon isotopic composition: A case study from the Gullfaks oil field, offshore Norway. Geochim. Cosmochim. Acta 70(3), 651–665.

Volk, H., George, S.C., Middleton, H., Schofield, S., 2005. Geochemical comparison of fluid inclusion and present-day oil accumulations in the Papuan Foreland – evidence for previously unrecognised petroleum source rocks. Org. Geochem. 36, 29–51.

Volkman, J.K., 1986. A review of sterol markers for marine and terrigenous organic matter. Org. Geochem. 9 (2), 83–99.

Volkman, J.K., 2003. Sterols in microorganisms. Appl. Microbiol. Biotechnol. 60, 495–506.

Volkman, J.K., Alexander, R., Kagi, R.I., Woodhouse, G.W., 1983. Demethylated hopanes in crude oils and their application in petroleum geochemistry. Geochim. Cosmochim. Acta 47, 785–794.

Volkman, J.K., Zhang, Z., Xie, X., Qin, J., Borjigin, T., 2015. Biomarker evidence for Botryococcus and a methane cycle in the Eocene Huadian oil shale, NE China. Org. Geochem. 78, 121–134.

Wachniew, P., Różański, K., 1997. Carbon budget of a mid-latitude, groundwater-controlled lake: isotopic evidence for the importance of dissolved inorganic carbon recycling. Geochim. Cosmochim. Acta 61(12), 2453–2465.

Wakeham, S.G., 1990. Algal and bacterial hydrocarbons in particulate matter and interfacial sediment of the Cariaco Trench. Geochim. Cosmochim. Acta 54, 1325–1336.

Wang, G., Chang, X., Wang, T.G., Simoneit, B.R., 2015. Pregnanes as molecular indicators for depositional environments of sediments and petroleum source rocks. Org. Geochem. 78, 110–120.

Wang, H., Dong, H., Zhang, C.L., Jiang, H., Liu, Z., Zhao, M., Liu, W., 2015. Deglacial and Holocene archaeal lipid-inferred paleohydrology and paleotemperature history of Lake Qinghai, northeastern Qinghai–Tibetan Plateau. Quaternary Res. 83(1), 116–126.

Wang, H., Liu, W., Zhang, C.L., Jiang, H., Dong, H., Lu, H., Wang, J., 2013a. Assessing the ratio of archaeol to caldarchaeol as a salinity proxy in highland lakes on the northeastern Qinghai–Tibetan Plateau. Org. Geochem. 54, 69–77.

Wang, H., Liu, W., Zhang, C.L., Liu, Z., He, Y., 2013b. Branched and isoprenoid tetraether (BIT) index traces water content along two marsh-soil transects surrounding Lake Qinghai: Implications for paleo-humidity variation. Org. Geochem. 59, 75–81.

Wang, H., Liu, W., Zhang, C.L., Wang, Z., Wang, J., Liu, Z., Dong, H., 2012. Distribution of glycerol dialkyl glycerol tetraethers in surface sediments of Lake Qinghai and surrounding soil. Org. Geochem. 47, 78–87

Wang, J., Wang, Y.J., Liu, Z.C., Li, J.Q., Xi, P., 1999. Cenozoic environmental evolution of the Qaidam Basin and its implications for the uplift of the Tibetan Plateau and the drying of Central Asia. Palaeogeogr. Palaeoclimatol. Palaeoecol. 152, 37–47.

Wang, K.Y., 1991. The preliminary study of Luyashang Paleoproterozoic quartz-monzonite. Shanxi Bull. Sci, 36, 685–687.

Wang, K.Y., Li, J.L., Hao, J., Li, J.H., Zhou, S.P., 1997. Late Archean mafic-ultramafic rocks from the Wuatishan, Shanxi Province: a possible ophiolite melange. Acta Petrol. Sin. 13(2), 139–151.

Wang, Q.C., Zhang, S.Q., 1995. The age of the Hongqiyingzi Group: a further discussion. Regional Geology of China, 2, 173–180.

Wang, T., Yang, S., Duan, S., Chen, H., Liu, H., Cao, J., 2015. Multi-stage primary and secondary hydrocarbon migration and accumulation in lacustrine jurassic petroleum systems in the northern Qaidam Basin, NW China. Mar. Petrol. Geol. 62, 90–101.

Wang, Y., Wang, X., Xu, Y., Zhang, C., Li, Q., Tseng, Z.J., Takeuchib, G, Deng, T., 2008. Stable isotopes in fossil mammals, fish and shells from Kunlun Pass Basin, Tibetan Plateau: paleo-climatic and paleo-elevation implications. Earth Planet. Sci. Lett. 270(1–2), 73–85.

Waples, D.W., Machihara, T.M., 1991. Biomarkers for Geologists. AAPG Methods in Exploration Series No. 9. American Association of Petroleum Geologists, Tulsa, Oklahoma.

Warren, J.K., 1986. Shallow-water evaporitic environments and their source rock potential. J. Sediment. Petrol. 56, 442–454.

Waseda, A., Nishita, H., 1998. Geochemical characteristics of terrigenous- and marinesourced oils in Hokkaido, Japan. Org. Geochem. 28, 27–41.

Watson, M.P., Hayward, A.B., Parkinson, D.N., Zhang, Z.M., 1987. Plate tectonic history, basin development and petroleum source rock deposition onshore China. Mar. Petrol. Geol. 4, 205–225.

Wei, W., Algeo, T.J., 2020. Elemental proxies for paleosalinity analysis of ancient shales and mudrocks. Geochim. Cosmochim. Acta 287, 341–366.

Weijers, J.W., Schefuß, E., Schouten, S., Sinninghe Damsté, J.S., 2007a. Coupled thermal and hydrological evolution of tropical Africa over the last deglaciation. Science 315(5819), 1701–1704.

Weijers, J.W., Schouten, S., Hopmans, E. C., Geenevasen, J.A., David, O.R., Coleman, J.M., Pancost, R.D., Sinninghe Damsté, J.S., 2006b. Membrane lipids of mesophilic anaerobic bacteria thriving in peats have typical archaeal traits. Environ. Microbiol. 8(4), 648–657.

Weijers, J.W., Schouten, S., Spaargaren, O.C., Sinninghe Damsté, J.S., 2006a. Occurrence and distribution of tetraether membrane lipids in soils: Implications for the use of the TEX86 proxy and the BIT index. Org. Geochem. 37(12), 1680–1693.

Weijers, J.W., Schouten, S., van den Donker, J.C., Hopmans, E.C., Sinninghe Damsté, J.S., 2007b. Environmental controls on bacterial tetraether membrane lipid distribution in soils. Geochim. Cosmochim. Acta 71(3), 703–713.

Weniger, P., Franců, J., Krooss, B.M., Bůzek, F., Hemza, P., Littke, R., 2012. Geochemical and stable carbon isotopic composition of coal-related gases from the SW Upper Silesian Coal Basin, Czech Republic. Org. Geochem. 53, 153–165.

Werne, J.P., Sageman, B.B., Lyons, T.W., Hollander, D.J., 2002. An integrated assessment of a "type euxinic" deposit: evidence for multiple controls on black shale deposition in the Middle Devonian Oatka Creek Formation. Am. J. Sci. 302(2), 110–143.

Whiticar, M.J., 1999. Carbon and hydrogen isotope systematics of bacterial formation and oxidation of methane. Chem. Geol. 161, 291–314.

Whiticar, M.J., 2020. The biogeochemical methane cycle. In: Wilkes, H. (Ed.), Hydrocarbons, Oils and Lipids: Diversity, Origin, Chemistry and Fate. Handbook of Hydrocarbon and Lipid Microbiology. Springer, Cham, pp. 2–49.

Wilkin, R.T., Barnes, H.L., Brantley, S.L., 1996. The size distribution of framboidal pyrite in modern sediments: an indicator of redox conditions. Geochim. Cosmochim. Acta 60, 3897–3912.

Wu, C., S. Xue, 1992, Sedimentology of Chinese petroliferous basins (in Chinese): Beijing, Petroleum Industry Press, p. 268–293.

Wu, F.L., Fang, X.M., Herrmann, M., Mosbrugger, V., Miao, Y.F., 2011. Extended drought in the interior of Central Asia since the Pliocene reconstructed from sporopollen records. Glob. Planet. Chang. 76 (1), 16–21.

Wu, F.Y., Ge, W.C., Sun, D.Y., 2003a. Discussions on the lithospheric thinning in eastern China. Earth Sci. Front. 10(3), 51–60.

Wu, F.Y., Walker, R.J., Ren, X.W., Sun, D.Y., Zhou, X.H., 2003b. Osmium isotopic constraints on the age of lithospheric mantle beneath northeastern China. Chem. Geol. 196(1–4), 107–129.

Wu, X., Liu, Q., Zhu, J., Li, K., Liu, G., Chen, Y., Ni, C., 2017. Geochemical characteristics of tight gas and gas-source correlation in the Daniudi gas field, the Ordos Basin, China. Mar. Petrol. Geol. 79, 412–425.

Xie, S., Pancost, R.D., Chen, L., Evershed, R.P., Yang, H., Zhang, K., Huang, J., Xu, Y, 2012. Microbial lipid records of highly alkaline deposits and enhanced aridity associated with significant uplift of the Tibetan Plateau in the Late Miocene. Geology 40(4), 291–294.

Xiong, F., Jiang, Z., Li,P., Wang, X., Bi,H., Li,Y., Moortgat, J., 2017. Pore structure of transitional shales in the Ordos Basin. NW China: effects of composition on gas storage capacity. Fuel 206, 504–515.

Xu, Z., Liu, L., Liu, B., Wang, T., Zhang, Z., Wu, K., Feng, C., Dou, W., Wang, Y., Shu, Y., 2019. Geochemical characteristics of the Triassic Chang 7 lacustrine source rocks, Ordos Basin, China: Implications for paleoenvironment, petroleum potential and tight oil occurrence. J. Asian Earth Sci. 178, 112–138.

Yang, C., Zhang, J., Han, S., Wang, X., Wang, L., Yu, W., Wang, Z., 2016. Compositional controls on pore-size distribution by nitrogen adsorption technique in the lowerPermian Shanxi shales, Ordos Basin. J. Nat. Gas Sci. Eng. 34, 1369–1381.

Yang, C., Zhang, J., Tang, X., Ding, J., Zhao, Q., Dang, W., Dang, W., Chen, H., Su, Y., Li, B., Lu, D., 2017b. Comparative study on micro-pore structure of marine, terrestrial, and transitional shales in key areas, China. Int. J. Coal Geol. 171, 76–92.

Yang, F., Ning, Z., Zhang, R., Zhao, H., Krooss, B.M., 2015. Investigations on the methane sorption capacity of marine shales from Sichuan Basin, China. Int. J. Coal Geol. 146, 104–117.

Yang, F., Xie, C., Ning, Z., Krooss, B.M., 2017a. High-pressure methane sorption on dry and moisture-equilibrated shales. Energ. Fuel. 31 (1), 482–492.

Yang, H., Lü, X., Ding, W., Lei, Y., Dang, X., Xie, S., 2015b. The 6-methyl branched tetraethers significantly affect the performance of the methylation index (MBT′) in soils from an altitudinal transect at Mount Shennongjia. Org. Geochem. 82, 42–53.

Yang, H., Pancost, R. D., Dang, X., Zhou, X., Evershed, R. P., Xiao, G., Tang, C., Gao, L., Guo, Z., Xie, S., 2014. Correlations between microbial tetraether lipids and environmental variables in Chinese soils: Optimizing the paleo-reconstructions in semi-arid and arid regions. Geochim. Cosmochim. Acta 126, 49–69.

Yang, H., Xiao, W., Jia, C., Xie, S., 2015a. Paleoaltimetry proxies based on bacterial branched tetraether membrane lipids in soils. Front. Earth Sci. 9(1), 13–25.

Yang, J.J. (Ed.), 2002. Tectonic Evolution and Oil–Gas reservoirsDistribution in Ordos Basin. Petroleum Industry Press, Beijing.

Yang, L., Tang, X., Zhang, J., Mo, X., Huang, H., Liu, Z., 2018. Geochemical characteristics of the extremely high thermal maturity transitional shale gas in the southern North China Basin (SNCB) and its differences with marine shale gas. Int. J. Coal Geol. 194, 33–44.

Yang, M., Liu, C., Tang, X., Zheng, X., 2008. The Chang 7 member of the upper Triassic in the Southwest Ordos Basin: Carbon isotope study of dispersed organic matter and its paleoclimate significance. Petrol. Sci. 5 (1), 20–23.

Yang, W.B., Spencer, R.J., Krouse, H.R., Lowenstein, T.K., Casas, E., 1995. Stable isotopes of lake and fluid inclusion brines, Dabusun Lake, Qaidam Basin, western China: hydrology and paleoclimatology in arid environments. Palaeogeogr. Palaeoclimatol. Palaeoecol. 117, 279–290.

Yang, Y., Li, W., Ma, L., 2005. Tectonic and stratigraphic controls of hydrocarbon systems in the Ordos basin: a multicycle cratonic basin in Central China. AAPG Bull. 89 (2), 255–269.

Yu, Q., Ren, Z., Li, R., Wang, B., Qin, X., Tao, N., 2017. Paleogeo temperature and maturity evolutionary history of the source rocks in the Ordos Basin. Geol. J. 52 (S1), 97–118.

Yuan, W., Liu, G., Stebbins, A., Xu, L., Niu, X., Luo, W., Li, C., 2017. Reconstruction of redox conditions during deposition of organic-rich shales of the Upper Triassic Yanchang Formation, Ordos Basin, China. Palaeogeogr. Palaeoclimatol. Palaeoecol. 486, 158–170.

Yue, Y., G.J. Liou, Graham, S.A., 2001, Tectonic correlation of Beishan and Inner Mongolia orogens and its implications for the palinspastic reconstruction of north China, in M. S. Hendrix and G. A. Davis, eds., Paleozoic and Mesozoic tectonic evolution of central Asia: From continental assembly to intracontinental deformation: Geol. Soc. Am. Memoir 194, p. 101–116.

Zhai, G., 1990, The petroleum geology of China (in Chinese): Beijing, Petroleum Industry Press, v. 12, p. 3–330.

Zhai, G., Wang, S., Li, G., 1984. Characteristics of sedimentary basins in China and its oil and gas distribution, Beijing Petroleum Symposium 20-24th Sept. 1984, Beijing China, Preprint 37 p.

Zhai, M., Liu, W., 2003. Palaeoproterozoic tectonic history of the North China craton: a review. Precambrian Res. 122(1–4), 183–199.

Zhang, F., Zhong, J. Ma, J. 1998. A tentative discussion of the Carlin-type gold deposits in Qinling and related problems (in Chinese). Mineral Deposit 17, 172–184.

Zhang, K., Liu, R., Liu, Z., Li, B., Han, J., Zhao, K., 2020. Influence of volcanic and hydrothermal activity on organic matter enrichment in the Upper Triassic Yanchang Formation, southern Ordos Basin, Central China. Mar. Petrol. Geol. 112, 104059.

Zhang, S.C, Shuai, Y.H., Huang, L., Wang, L.Q., Su, J., Huang, H.P., Ma, D.D., Li, M.W., 2013a. Timing of biogenic gas formation in the eastern Qaidam Basin, NW China. Chem. Geol. 352, 70–80.

Zhang, S.C., Li, M.W., Shuai, Y.H., Huang, L., Su, A.G., Li, Z.X., 2014. Biogeochemical identification of the Quaternary biogenic gas source rock in the Sanhu Depression, Qaidam Basin. Org. Geochem. 73, 101–108.

Zhang, S.C., Shuai, Y.H., Huang, L., Wang, L.Q., Su, J., Huang, H.P., Ma, D.D., Li, M.W., 2013a. Timing of biogenic gas formation in the eastern Qaidam Basin, NW China. Chem. Geol. 352, 70–80.

Zhang, T., Ellis, G.S., Ruppel, S.C., Milliken, K., Yang, R., 2012. Effect of organic-matter type and thermal maturity on methane adsorption in shale-gas systems. Org. Geochem. 47, 120–131.

Zhang, W., Yang, H., Yang, W., Wu, K., Liu, F., 2015. Assessment of geological characteristics of lacustrine shale oil reservoir in Chang7 Member of Yanchang Formation, Ordos Basin. Geochimica. 44 (5), 505–515.

Zhang, W., Yang, W., Xie, L., 2017. Controls on organic matter accumulation in the Triassic Chang 7 lacustrine shale of the Ordos Basin, Central China. Int. J. Coal Geol. 183, 38–51.

Zhang, X., Hu, Y., Duan, Y., Ma, L., Meng, Z., He, P., Zhou, S., Peng, D., 2003. Geochemical characteristics and origin of natural gases in the Qaidam Basin, China. Acta Geol. Sin. 77 (1), 103–115.

Zhang, Y., 1997, Prototype analysis of Chinese petroliferous basin (in Chinese): Nanjing, China, Nanjing University Press, p. 262–294.

Zhang, Z.G., Han, W.X., Fang, X.M., Song, C.H., Li, X.Y., 2013b. Late Miocene–Pleistocene aridification of Asian inland revealed by geochemical records of lacustrine-fan delta sediments from the western Tarim Basin, NW China. Palaeogeogr. Palaeoclimatol. Palaeoecol. 377 (2), 52–61.

Zhao, G., Sun, M., Wilde, S. A., Sanzhong, L., 2005. Late Archean to Paleoproterozoic evolution of the North China Craton: key issues revisited. Precambrian Res. 136(2), 177–202.

Zhao, G., Sun, M., Wilde, S. A., Sanzhong, L., Liu, S., Zhang, J., 2006. Composite nature of the North China Granulite-Facies Belt: tectonothermal and geochronological constraints. Gondwana Res. 9(3), 337–348.

Zhao, G., Wilde, S. A., Cawood, P. A., Sun, M., 2001. Archean blocks and their boundaries in the North China Craton: lithological, geochemical, structural and P–T path constraints and tectonic evolution. Precambrian Res. 107(1–2), 45–73.

Zhao, H., Liu, C., Wang, J., Gui, X., Qiao, J., Wang, H., 2011. Characteristics of later different reformation and its significance in occurrence of multi-energy deposits in Ordos Basin. Petrol. Explor. Dev. 29(4), 435–453.

Zhao, J., Mountney, N.P., Liu, C., Qu, H., Lin, J., 2015. Outcrop architecture of a fluviolacustrine succession: Upper Triassic Yanchang Formation, Ordos Basin, China. Mar. Petrol. Geol. 68, 394–413.

Zheng, Y., Anderson, R.F., van Geen, A., Kuwabara, J., 2000. Authigenic molybdenum formation in marine sediments: a link to pore water sulfide in the Santa Barbara Basin. Geochim. Cosmochim. Acta 64, 4165–4178.

Zhou, J., Xu, F., Wang, T., Cao, A., Yin, C., 2006. Cenozoic deformation history of the Qaidam Basin, NW China: Results from cross-section restoration and implications for Qinghai–Tibet Plateau tectonics. Earth Planet. Sci. Lett. 243(1–2), 195–210.

Zhuang, G.S., Hourigan, J.K., Koch, P.L., Ritts, B.D., Kent-Corson, M.L., 2011. Isotopic constraints on intensified aridity in Central Asia around 12Ma. Earth Planet. Sci. Lett. 312 (1–2), 152–163.

Zieger, L., Littke, R., 2019. Bolsovian (Pennsylvanian) tropical peat depositional environments: the example of the Ruhr Basin, Germany. Int. J. Coal Geol. 103–209.

Zou, C., Dong, D., Wang, S., Li, J., Li, X., Wang, Y., Li, D., Cheng, K., 2010. Geological characteristics and resource potential of shale gas in China. Petrol. Explor. Dev. 37 (6), 641–653.

Zou, C., Zhu, R., Chen, Z. Q., Ogg, J. G., Wu, S., Dong, D., Qiu, Z., Wang, Y., Wang, L., Lin, S., Cui, J., Su, L., Yaninternationalg, Z., 2019. Organic-matter-rich shales of China. Earth-Sci. Rev. 189, 51–78.

Curriculum Vitae

Name:	**Jinqi Qiao**
Tel:	**+49 1637500511**
E-mail address:	**jinqi.qiao@emr.rwth-aachen.de**

PERSONAL INFORMATION

Gender:	**Male**
Date of birth:	**29/10/1992**
Birthplace:	**Gansu Province (China)**
Nationality	**Chinese**
Major:	**Geology**
Ranking:	**1/133 (Master period) and 4/27 (Bachelor period)**

EDUCATION

09/2017 – present	**Applied Geosciences, RWTH Aachen university, Phd. (with Prof. Dr. Littke Ralf);**
09/2014 – 06/2017	**Geological Engineering, China University of Petroleum (Beijing), M.Sc. (with Prof. Dr. Luofu Liu);**
09/2010 – 06/2014	**Geochemistry, Lanzhou University, B.S.**

RESEARCH PAPERS

1, **Qiao, J.Q.,** Sebastian, G., Baniasad, A., Zhang, C., Jiang, Z., Littke, R., 2021. High microbial gas potential of Pleistocene lacustrine deposits in the central Qaidam Basin, China: An organic geochemical and petrographic assessment. International Journal of Coal Geology, 103818. (SCI);

2, **Qiao, J.Q.,** Baniasad, A., Zieger, L., Zhang, C., Luo, Q., Littke, R., 2021. Paleo-depositional environment, origin and characteristics of organic matter of the Triassic Chang 7 Member of the Yanchang Formation throughout the mid-western part of the Ordos Basin, China. International Journal of Coal Geology, 237, 103636. (SCI);

3, **Qiao, J.Q,** Littke, R., Zieger, L., Jiang, Z., Fink, R., 2020. Controls on gas storage characteristics of Upper Paleozoic shales from the southeastern Ordos Basin. Marine and Petroleum Geology, 117, 104377. (SCI);

4, **Qiao, J.Q.,** Liu, L.F., An, F.L., Xiao, F., Wang, Y., Wu, K.J., Zhao, Y.Y., 2016. Hydrocarbon potential evaluation of the source rocks from the Abu Gabra Formation in the Sufyan Sag, Muglad Basin, Sudan. Journal of African Earth Sciences. 118: 301-312. (SCI);

5, **Qiao, J.Q.,** Liu, L.F., Shen, B.J., et al., 2016. Formation of Ordovician Shale Gas and Prediction of Favorable Zones in Tarim Basin. Xinjiang Petroleum Geology. 37(4): 409-416 (in Chinese with English abstract);

6, **Qiao, J.Q.,** Liu, L.F., Shang, X.Q., et al., 2016. The Relationship Between V, Ni or V /Ni Ration and Each of Organic Matter Abundance and Diagenetic Evolution Stages in Shales: Taking the Shales in Fukang Sag of Junggar Basin for Example. Bulletin of Mineralogy Petrology and Geochemistry. 35(4): 757-769 (in Chinese with English abstract);

7, Liu, L.F., **Qiao, J.Q.,** Shen, B.J., Lu, X.Y., Yang, Y.S., 2017. Geological Characteristics and Shale Gas Distribution of Carboniferous Mudstones in the Tarim Basin, China. Acta Geochimica. 36(2), 260-275. (ESCI/EI).

8, Cheng, P., Meng, Q.Q., **Qiao, J.Q.,** et al. 2014. Quantitative Representation of the Leaching Properties of Chemical Elements. Acta Sedimentologica Sinica. 32(4):663-668 (in Chinese with English abstract);

9, Liu, L.F., Luo, Q., **Qiao, J.Q.,** et al. 2018. The studies of Carboniferous structure characteristics and the reservoir forming conditions in the Xincun Oilfield, Chepaizi area, Junggar Basin. Geological Bulletin of China. 37 (1): 70-82 (in Chinese with English abstract).

SCHOLARSHIPS AND AWARDS

09/2016 – 06/2017	• **First-class Academic Scholarship, China University of Petroleum (Beijing)** • **National Scholarship, The Ministry of Education of the People's Republic of China** • **Outstanding Graduate of Beijing, Beijing Municipal Education Commission**
09/2015 – 06/2016	• **First-class Academic Scholarship, China University of Petroleum (Beijing)**
09/2014 – 06/2015	• **First-class Academic Scholarship, China University of Petroleum (Beijing)** • **Outstanding Students Scholarships, China University of Petroleum (Beijing)**
09/2013 – 06/2014	• **Second-class Scholarship, Lanzhou University** • **Student Pacemaker, Lanzhou University** • **Excellent project The Influence of Atmospheric Precipitation on the Loess Element Distribution (Person in charge), The National College Students' Innovative Entrepreneurial Training Program**
09/2012 – 06/2013	• **National Encouragement Scholarship, The Ministry of Education of the People's Republic of China** • **Student Pacemaker, Lanzhou University** • **Excellent Student Cadre, Lanzhou University**